



**UNIVERSITY of the
WESTERN CAPE**

**RAINFALL INDUCED TRANSIENT PRESSURE WAVE
MECHANISMS AND PORE WATER PRESSURE
DYNAMICS IN TAILINGS**

BY

CHARNÉ THERON

STUDENT NUMBER: 4115487

**A thesis submitted in fulfillment of the requirements for the degree of
Doctor of Philosophy in the Department of Earth Sciences,
Faculty of Natural Sciences, University of the Western Cape**

**SUPERVISOR:
PROF. YONGXIN XU**

**CO-SUPERVISOR
PROF. SIMON A. LORENTZ**

4 NOVEMBER 2023

KEYWORDS

Climate change

Tailings dams

Pore air propagation

Transient pressure wave mechanisms

Groundwater Ridging

Lisse Effect

Rainfall induced slope instability



UNIVERSITY *of the*
WESTERN CAPE

ABSTRACT

Rainfall Induced Pore Pressure Dynamics in Tailings Dams

C. Theron

PhD Thesis, Department of Earth Sciences, University of the Western Cape, South Africa

Tailings Storage Facilities are some of the largest engineered structures responsible for the containment of mining waste, yet some physical/hydrological processes causing slope instability are still poorly understood. Previous studies conducted on the causes of failure of TSFs indicate rainfall-induced slope instability as the main trigger. However, the generation of certain physical/hydrological processes and the behaviour of soil hydraulic properties in the vadose zone when exposed to high intensity rainfall events, have only been considered on natural hillslopes.

The purpose of this study is to investigate one such process resulting from high rainfall intensities on partially saturated conditions. In particular, it is hypothesised in this work that the wetting front advance from high rainfall intensities, anticipated under the force of climate change, may cause transient air pressure waves to change pore water suction and elevate the phreatic surface, subsequently impacting on the effective stress. The mechanisms that lead to the mobilisation of pre-event water through transient air pressure waves are known as Groundwater Ridging and the Lisse Effect. In this study, it was hypothesized that these phenomena contribute significantly to slope instability. In order to quantify the processes and predict these phenomena and their resultant impact on stability, specific experiments were set up. Laboratory experimentation included a large leak-proof column (600 mm ID x 3,0 m tall) filled up to 2,65 m with tailings at *in-situ* dry bulk density of 1 675 kg/m³. The PVC column was instrumented with seven data ports, vertically spaced down the column. Each port consisted of a time domain reflectometry probe to measure volumetric water content, a mini tensiometer to sense pore water suction and a pore air pressure probe. An external manometer tube measured the phreatic surface created near the base. The experimental setup allowed for the application of artificial rainfall at different intensities and controlled boundary conditions, during automatic logging of the hydraulic state variables, recorded at twenty-second intervals. Recorded observations were used to determine phreatic surface dynamics, the soil moisture

profile and general pore water/air pressure responses. The experiment was specifically designed to differentiate between pore water migration due saturated/unsaturated Darcy flow, from pore water responses to pneumatic pressure transfers. This study also examined the anticipated impact of climate change on rainfall parameters and quantified geotechnical characteristics of the tailings porous medium under variably saturated states. The results demonstrated that after the application of water to the soil surface, pore air pressure ahead of the wetting front increased, causing higher water content levels and a decrease in pore water suction. This led to the conclusion that high intensity rainfall events generate transient air pressure waves in tailings porous medium, thereby inducing the transmission of pore air pressure head to a potential failure plane. Since air pressure in the unsaturated zone affects pore water pressure, water content and subsequently shear strength, it also contributes indirectly to slope instability.

November 2023



DECLARATION

I hereby declare that this PhD thesis entitled *Rainfall induced transient pressure wave mechanisms and pore water pressure dynamics in tailings* is my own work and that I have not previously submitted it to any university for a degree or examination. All sources that I have quoted have been indicated and duly acknowledged by means of complete references.

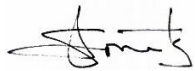


04/11/2023

Charné Theron

Date

This dissertation has been submitted for examination with my approval as a supervisor.



04/11/2023

Prof. Simon A. Lorentz (CO-SUPERVISOR)

Date



04/11/2023

Prof. Yongxin Xu (SUPERVISOR)

Date

ACKNOWLEDGMENTS

Thank you to my wonderful parents for your prayers, unwavering support and believing in my every effort. To my children, Tristan and Morgan, without whom there would have been no reason. And finally, our heavenly Father, for having a plan much better than I could ever have imagined myself but also for giving me the strength, good health and perseverance to never give up.

I thank the following persons for their support during this study:

- Prof. Simon A. Lorentz, for introducing me to this topic, his enthusiastic and dedicated support, willingness to travel, both locally and internationally, for providing crucial laboratory instruments, for meetings and laboratory experimentation and for actively providing various opportunities to partake in conferences.
- Prof. Yongxin Xu, for his guidance, support and generous inputs.
- Laboratory staff at the Cape Peninsula University of Technology, Dr. Peter Kainda, Luvo Maduna and Wesley Snell, for always being willing to give a helping hand and an encouraging word.
- Mr. Johan Veldsman of Burger and Wallace Construction Pty (Ltd) for providing the PVC column.
- Mr. James Tempers from Mesh Cape for donating materials.
- Mr. Neil Hoy from Campbell Scientific in Stellenbosch for his help setting up laboratory equipment, prompt responses and guidance in writing programs and deciphering data.
- My colleagues and friends at the Rijks University of Groningen, Netherlands, for your encouragement and guidance.
- The Rijks University of Groningen, Netherlands, for providing me with a travel grant as part of the sub-Saharan Africa (SSA) Strategy. This will be utilised towards further research in the field.
- The examiners for their substantial contribution and valuable feedback.

DEDICATION

TO MY DAD

Jeremiah 29:11



UNIVERSITY *of the*
WESTERN CAPE

PUBLICATIONS

Theron, C, Lorentz, S.A., and Xu, Y. 2022. Rainfall-induced groundwater ridging and the Lisse effect on tailings storage facilities: A literature review. *Journal of the Southern African Institute of Mining and Metallurgy*, vol. 122, no. 2, 37-44

Conference Proceedings: Papers

Theron, C. and Lorentz, S.A. (2023) ‘Rainfall induced transient pressure wave mechanisms and pore water pressure dynamics in tailings’. Proceedings of the International Mine Water Association (IMWA) Congress. Newbury, Wales.

Conference Proceedings: Presentations

Theron, C. and Lorentz, S.A. (2021) ‘Possible porous medium mechanisms causing instability in platinum tailings’, Kirkham Virtual Conference: Soil Physics in Agricultural Production, Water Resources and Waste Management, 30 Augustus 2021

Theron, C. and Lorentz, S.A. (2021) ‘Rainfall induced transient pressure wave mechanisms and pore water pressure dynamics in tailings’, South African Institute for Mining and Metallurgy (SAIMM) Conference, Rustenburg, South Africa, 8 – 9 November 2021

Conference Proceedings: Posters

Theron, C. and Lorentz, S.A. (2022) ‘Transient pressure wave mechanisms and pore water pressure dynamics in tailings’, Kirkham Conference, Kruger National Park, South Africa, 28 Augustus – 2 September 2022



UNIVERSITY *of the*
WESTERN CAPE

Contents

ABSTRACT.....	iii
DECLARATION	v
ACKNOWLEDGMENTS	vi
DEDICATION	vii
PUBLICATIONS.....	viii
CHAPTER 1	24
1.1 Introduction.....	24
1.1.1 Background to the Study	25
1.2 General importance.....	26
1.3 Problem statement and research question.....	26
1.4 Research objectives	27
1.5 Specific aim of study	27
1.6 Research hypotheses.....	28
1.7 Overview of the methodologies.....	28
1.8 Significance of the thesis	29
1.8.1 Contribution of this research to the State of Knowledge.....	29
1.8.2 Contribution of this research to the broader scientific community, the mining industry and society as a whole	29
1.9 Outline of the thesis	30
CHAPTER 2	32
2.1 Literature review.....	32
2.1.1 Background studies and problem statement	32
2.1.2 Tailings dam failures	33
2.1.3 Historical TSFs Disasters	37
2.1.3.1 Recent International Tailings Dam Failures	39

2.1.3.2	South African Tailings Dam Failures	42
2.1.4	Method of construction and relationship with failure.....	46
2.2	Climate Change	49
2.2.1	Climate Change and Rainfall.....	50
2.2.1.1	Possible impacts of climate change on Tailings Storage Facilities	51
2.2.2	Determining future climates	52
2.2.2.1	General Circulation Models and Regional Climate Models.....	52
2.2.2.2	Concentration scenario: Intergovernmental Panel on Climate (IPCC).....	53
2.3	Characteristics of rainfall events during which failure occur	55
2.3.1	Pre-event water in the stream stormflow hydrograph.....	59
2.4	Fundamental principles related to porous medium conditions	60
2.4.1	The geotechnical stability of tailings dams	63
2.5	Rapid mobilization of pre-event water	63
2.5.1	Transient Pressure Wave Mechanisms	64
2.5.1.1	Groundwater Ridging	65
2.5.1.2	Lisse Effect	68
2.6	Summary and Conclusions	73
CHAPTER 3		75
3.1	Research Design and Methodology.....	75
3.1.1	Site selection and study area.....	75
3.1.1.1	Location	75
3.1.1.2	Local Geology	76
3.1.1.3	Operational activities	76
3.1.1.4	Climatic classification	77
3.2	Data collection and analysis	78
3.2.1	Climate change	79
3.2.2	Tailings characteristics and geohydrological properties.....	80

3.2.3	Laboratory experiments	81
3.2.3.1	Laboratory apparatus	82
3.2.3.2	Sensor development.....	84
3.2.3.3	Material parameters	87
3.2.3.4	Experimental Procedure.....	88
CHAPTER 4		92
4.1	Results.....	92
4.1.1	Climate change	92
4.1.1.1	Temperature trends	92
4.1.1.2	Rainfall data.....	96
4.1.1.2.1	Summary of rainfall trends	97
4.1.2	Physical characteristics	99
4.1.2.1	Soil classification and particle size distribution	99
4.1.2.2	Hydraulic characteristics	100
4.1.2.3	Estimation of the Water Retention Curve.....	103
4.1.3	Results from laboratory experiments.....	103
4.2	Conclusion	112
CHAPTER 5		115
5.1	Theoretical Approach	115
5.2	Assumptions	115
5.3	Rainfall induced pore air pressure diffusion and transient pressure wave generation through porous soil media: Theories	115
5.3.1	Soil Water Characteristic Curves for Unsaturated Soils.....	122
5.3.2	Pore air pressure and slope stability of tailings dams.....	125
5.3.3	The phreatic surface and slope stability of tailings dams	128
5.4	Numerical modelling for unsaturated water flow	130
5.4.1	HYDRUS 1D Numerical Model.....	131

5.4.2	Variable parameters as input data for HYDRUS 1D.....	132
5.4.3	Output results.....	135
5.5	Conclusion	142
CHAPTER 6		145
6.1	Interpretation and discussion of results	145
6.1.1	Climate change	145
6.1.1.1	Temperature trends and predicted future temperature characteristics.....	145
6.1.1.2	Interpretation of rainfall data and predicted future rainfall characteristics	145
6.1.1.3	Intensity-Duration-Frequency Curves	147
6.1.2	Climate change conclusions	150
6.2	Interpretation of soil behavior based on characterisation	151
6.3	Interpretation of laboratory results	154
6.4	Risk assessment	161
6.5	Conclusion	165
CHAPTER 7		168
7.1	Conclusion	168
7.2	Recommendations for policy and engineering design.....	170
7.3	Limitations.....	173
7.4	Future Perspectives and Recommendation for Further Research.....	174
REFERENCES		176
APPENDIX A.....		197
APPENDIX B		201
APPENDIX C		209

LIST OF NOTATIONS AND ABBREVIATIONS

A	cross sectional area
AEV	Air Entry Value
B-C	Brooks-Corey
BSh	Warm semi-arid climate
Bsk	Cold semi-arid climate
C	Specific water capacity
c'	Effective soil cohesion
cdf	cumulative distribution function
CF	Capillary Fringe
CS	Coarse sand (0.50 – 2.00 mm)
CSAG	Climate Systems Analysis Group
Csb	Temperate Mediterranean climate
d_h	Water table rise
DJF	December January February
EWS	Early warning systems
f	Porosity of the porous medium
FS	Fine sand (0.053 – 0.25 mm)
g	Gravitational acceleration
GCM	Global Circulation Model
GEV	Generalised extreme value distribution
GPD	Generalised Pareto distribution
GW	Groundwater
GWR	Groundwater ridging
h	Matric potential in cm
H	Hydraulic head
h_a	Pore air pressure
h_b	Pore air entry pressure of the soil
HOF	Hortonian overland flow
H_w	Dimensionless pore water pressure
i	hydraulic gradient ($\frac{\Delta h}{\Delta L}$)
ID	Internal diameter

IDF	Intensity Duration Frequency curves
IPCC	Intergovernmental Panel on Climate Change
JJA	June July August
K_{sat}	Saturated hydraulic conductivity
$K(\theta)$	Unsaturated hydraulic conductivity (a function of soil water content)
$K(h)$	unsaturated hydraulic conductivity cm/d^{-1}
kg	Kilograms
km	kilometer
l	Pore size distribution index in Brooks-Corey equation
L	length
L	The operator in the Laplace transform
LE	Lisse Effect
L^{-1}	The operator in the inverse Laplace transform
MAM	March April May
MAP	Mean Annual Precipitation
MGM	Modified van Genuchten-Mualem
MIG	Mainstream inert grinding
MME	Multi Model Ensemble
MS	Medium sized sand (0.25 – 0.50 mm)
n	pore size distribution
N	Newton
P_a	atmospheric pressure
P_c	capillary pressure (internal)
Pdf	Probability density function
ppm	Parts per million
PGM	primary platinum group metals
PTFs	Pedo transfer functions
PVC	polyvinyl chloride
P_w	water pressure
P_{wc}	atmospheric pressure in form of water column height
ΔP	pressure difference
P_0	atmospheric pressure (external)

q	quantity flowing in unit time
R	radius of curvature of the surface along any two orthogonal tangents
RCM	Regional circulation model
RCP	Representative concentration pathway
s	Time parameter (complex number) in the Laplace transform
S	Saturation content (%)
SDG	Sustainable development goals
SDR	Short duration rainfall
SOF	Saturated overland flow
SON	September October November
SMI	Soil moisture index
SSP	Shared socioeconomic pathway
SW	Soil water
t	Time coordinate
T	Dimensionless time coordinate
tp	Time to peak response of the potential pressure
tr	Time lapse
TDR	Time Domain Reflectometry
TSF	Tailings storage facilities
U	Unit cross-sectional area of the capillary fringe
u_a	Pore air pressure
UFG	Ultrafine grinding technology
USPF	unsaturated soil property functions
$u(t)$	Heaviside unit step function
u_w	pore water pressure
UZ	Unsaturated zone
V	Volume
y_{cf}	Depth of the capillary fringe
y_{uz}	Depth of unsaturated zone
y_w	Depth of ponded water on the soil surface
VWC	Volumetric Water Content
y	Vertical space coordinate
Y	Dimensionless space coordinate

z	Elevation head/depth
α	inverse of the air entry suction
η	osmotic suction
κ	Energy conductivity of soil pore water
σ	surface tension of the liquid-vapour interface
\emptyset	Diameter
φ'	Effective friction angle
γ_s	Solid surface tension
γ_L	Liquid surface tension
γ_{sL}	Solid-liquid boundary tension
γ_w	Unit weight of water
γ_t	Unit weight of soil
θ	Slope angle
θ_r	Residual volumetric water content in $\text{cm}^3.\text{cm}^{-3}$
θ_s	Saturated volumetric water content in $\text{cm}^3.\text{cm}^{-3}$
$\theta(\Psi)$	Water retention curve
$ \psi $	Suction pressure
λ	Pore size distribution



UNIVERSITY *of the*
WESTERN CAPE

LIST OF TABLES

Table 2.1: Examples of global tailings dam failures (Lyu <i>et al.</i> , 2019; Blight and Fourie, 2003; Wei <i>et al.</i> , 2013; WISE, 2023; Bowker and Chambers, 2016; ICOLD, 2001).....	37
Table 2.2: Projected change in global mean surface temperature for the mid- and late 21st century, relative to the 1986–2005 period (IPCC, 2014; IPCC, 2022).....	55
Table 2.3: Comparison summary between the LE and GWR (adapted from Miyazaki <i>et al.</i> , 2012).	69
Table 3.1: Information on the statistically downscaled CMIP5 GCMs downscaled by the CSAG at the University of Cape Town to predict future climatic scenarios (rainfall and temperature) at station level at various locations within South Africa.	80
Table 3.2: Sample composition of silica dust and sand to replicate tailings material.	87
Table 3.3: Description of incremental addition of water to tall soil column. Rainfall depths based on station specific data (Smithers and Schulze, 2002).	91
Table 4.1: Present and estimated monthly A-Pan Equivalent Potential Evaporation (mm): Limpopo region (Schulze and Maharaj, 2007).	94
Table 4.2: Rainfall trends identified for each CMIP CGM.	98
Table 4.3: Summary of tailings characteristics (main table from MacRobert, 2013 and supplemented by other authors as indicated).	102
Table 4.4: P-values and indication of level of significance (Schmidt and Osebold, 2017; Ozili, 2023).	104
Table 4.5: Summary of the most significant observations that possibly contribute to transient pressure wave mechanisms contributing to the rapid mobilisation of groundwater.	113
Table 5.1: Soil parameters for different soils used to estimate soil hydraulic functions according to the formulation of van Genuchten (Salas-Garcia <i>et al.</i> , 2017).	133
Table 5.2: Water flow parameters used for the three SWCCs in Figure 5.18.	141
Table 6.1: Design rainfall data (mm) for Mokopane (Smithers and Schulze, 2002).....	149
Table 6.2: Adjusted future design rainfall data (mm) for Mokopane.	149

Table 6.3: Summary of factors considered to contribute to slope stability and transient pressure wave mechanisms in tailings porous medium..... 152

Table 6.4: Summary of individual physical responses per ponding event, interpretation and conclusions..... 158

Table 6.5: Risk Assessment Matrix of slope instability. 164



LIST OF FIGURES

Figure 1.1: Thesis lay-out and interrelationship between different sections.	31
Figure 2.1: Number and geographical distribution of historical tailings dam failures since 1960 (data from Kovacs <i>et al.</i> , 2020).....	33
Figure 2.2: CO ₂ Emissions, Temperature increases and global TSF failures over time (data from Lyu <i>et al.</i> , 2019; Azam and Li, 2010).	34
Figure 2.3: Corrego do Feijao Iron Ore Mine, Dam I (Google Earth 3D, Image Date July 7, 2018 as cited in Robertson <i>et al.</i> , 2019).....	39
Figure 2.4: Particle size distribution analysis for fine, coarse and average gradations for the Feijao Dam I (Robertson <i>et al.</i> , 2019).	41
Figure 2.5: Jagersfontein tailings disaster (modified from Planet Team, 2022).....	43
Figure 2.6: Particle size distribution analysis for fine, coarse and average gradations for Merriespruit Gold Tailings material (Papageorgiou <i>et al.</i> , 1999).....	44
Figure 2.7 (a) and (b): Plan and aerial view of Saaiplaas dam showing locations of failures 1, 2 and 3 (modified from Blight and Fourie, 2003; Fourie <i>et al.</i> , 2002).	45
Figure 2.8: Particle size distribution analysis for fine, coarse and average gradations for the Bafokeng tailings material (Blight <i>et al.</i> , 1981).....	46
Figure 2.9: Upstream tailings dam construction (modified from Wills and Finch, 2016).....	47
Figure 2.10: Downstream tailings dam construction (modified from Wills and Finch, 2016).	48
Figure 2.11: Centreline tailings dam construction (modified from Wills and Finch, 2016). ..	48
Figure 2.12: Current human induced global temperature trend (Allen <i>et al.</i> , 2018).	49
Figure 2.13 (a): Temperature increase based on SSP-scenarios (b): Risks associated with each Reason for Concern (RFC) at a global scale for increasing temperature scenarios (modified from IPCC, 2022).....	54
Figure 2.14: Antecedent and critical rainfall parameters (modified after Aleotti, 2004 in Waswa and Lorentz, 2016a).	57
Figure 2.15: Phreatic line and associated pore water pressure regime observed in a tailings pond built by the upstream method (Singh <i>et al.</i> , 2023).....	59
Figure 2.16: Schematic illustration of factors affecting hydraulic response and operational characteristics of a tailings dam (Pacheco, 2018).	62
Figure 2.17: Schematic depiction of GWR and the LE.	65

Figure 2.18: Moisture profiles under GWR: h_w - pore water pressure, θ_r - residual soil water content, θ_s - saturated soil water content (modified from Waswa, 2013 and Miyazaki <i>et al.</i> 2012).	66
Figure 2.19: The conditions of the Lisse effect occurrence. n : depth of infiltrated water following an intense rain; ΔH : water level rise in the observation well resulting from sharp wetting front during intense rain trapping air and increasing soil air pressure; h : distance from the ground surface to the upper boundary of the capillary fringe (modified from Miyazaki <i>et al.</i> , 2012; Weeks, 2005; Meyboom, 1967)....	70
Figure 2.20: (a) Effect of ponding depth of water level and air pressure; (b) Effect of air pressure in the unsaturated zone on water level (Guo <i>et al.</i> , 2008).	73
Figure 3.1: (a) Location of the mine and (b) tailings dam (modified from Alexander, 2018 and Temper <i>et al.</i> , 2015).	75
Figure 3.2: (a) Seismic activity in South Africa. (b) Major active faults in South Africa, with active faults marked in yellow (Manzunzu <i>et al.</i> , 2019).	76
Figure 3.3: Historical climate monthly averages (Polokwane) (constructed using data from CSAG, 2020 and Schulze and Maharaj, 2007).	78
Figure 3.4: Tailings Storage Facilities (SRK, 2011).	81
Figure 3.5: Schematic diagram of the column test apparatus and setup. θ_r = residual soil water content, θ_s = saturated soil water content.	83
Figure 3.6: Custom-made TDR used to measure volumetric water content.	84
Figure 3.7: Custom-made mini tensiometer.	85
Figure 3.8 (a) and (b): 1 Bar Honeywell differential pressure transducer (Honeywell, 2014).	85
Figure 3.9: Custom made pore air pressure probe (modified from Waswa, 2013).	86
Figure 3.10 (a) and (b): 0.1 Bar Differential pressure transducer (NXP, 2008).	87
Figure 3.11: Particle size distribution curve of sample (Lorentz <i>et al.</i> , 2019).	88
Figure 3.12: Tall soil column fitted with seven ports each consisting of a pore air pressure probe, mini tensiometer and a TDR probe.	89
Figure 4.1: The Köppen-Geiger climate classification at an unprecedented 1-km resolution for (a) the present-day (1980–2016) and (b) for the future (2071–2100) (Beck <i>et al.</i> , 2018).	92

Figure 4.2: Average maximum monthly temperatures 1960 -2099 based on projected future changes across 10 different statistically downscaled CMIP5 GCMs (RCP8.5). ..	93
Figure 4.3: Present and predicted monthly mean A-Pan Equivalent Potential Evaporation (mm): Limpopo.....	95
Figure 4.4: Present and predicted monthly maximum A-Pan Equivalent Potential Evaporation (mm): Limpopo.....	95
Figure 4.5: Present and predicted monthly minimum A-Pan Equivalent Potential Evaporation (mm): Limpopo.....	95
Figure 4.6: Mokopane average monthly rainfall, minimum and maximum temperature.	96
Figure 4.7: Malvern particle size distribution analysis.....	100
Figure 4.8: Tailings classification according to the United States Department of Agriculture.	101
Figure 4.9: Drying characteristics of tailings (modified from Lorentz <i>et al.</i> , 2019 and Blight <i>et al.</i> , 2012).	103
Figure 4.10: Pore air pressure observations immediately after ponding event 1.....	105
Figure 4.11: Volumetric water content a few days after ponding event 1.....	106
Figure 4.12: The total change in pressure directly proportional to the magnitude of compressed pore air pressure a few days after ponding event 1.....	107
Figure 4.13: Pore water pressure every 12 hours after application of ponding event 1.	107
Figure 4.14: Volumetric Water Content observation before, during and immediately after 1 st and 2 nd application of ponding event 2.	108
Figure 4.15: Instant response in pore air pressure immediately after ponding event 2.	109
Figure 4.16: Volumetric Water Content observation before, during and a few days after 1 st and 2 nd application of artificial rainfall event 2.....	110
Figure 4.17: Volumetric Water Content observation before, during and immediately after 1 st and 2 nd application of artificial rainfall event 3.	111
Figure 4.18: Volumetric Water Content observation before, during and a few days after 1 st and 2 nd application of artificial rainfall event 3.....	111
Figure 4.19: Volumetric Water Content observations over all three ponding events.....	112
Figure 5.1: Capillary tube simulating the void between soil particles (modified from Fredlund <i>et al.</i> , 2012).	119

Figure 5.2: Segment of the curved air-water interface showing the dependence of capillary pressure on the curvature R_1 and R_2 (modified from Fredlund <i>et al.</i> , 2012).....	120
Figure 5.3: High wettability $< 90^\circ$; transition angle at 90° ; low wettability $> 90^\circ$ (Yuan, 2013).	120
Figure 5.4: A convex-concave air-water interface at the contact of two spherical particles. The water lens has two radii of curvature for pendular ring R_1 and R_2 (Tuller and Or., 2004).	121
Figure 5.5: Water retention curves indicating the hysteretic relationship between the wetting and drying cycles (modified from Bear and Verruijt, 1987).....	124
Figure 5.6: Soil water characteristics curve: drying resulting in three desaturation zones. S1: Capillary zone; S2: Transition zone; S3: Residual zone (Fredlund <i>et al.</i> , 2012).	125
Figure 5.7: Factor of safety with respect to matric suction (ϕ^b) for the end-of-construction of earth dams (Fredlund <i>et al.</i> , 1994).	126
Figure 5.8: Influence of the water table on the safety factor in the case of static liquefaction and flow failure of the Stava tailings dam failure on July 19, 1985, Italy (Chandler and Tosatti, 1995).	129
Figure 5.9: (a) pdfs (solid lines) and cdfs (dotted lines) of s and FS when s affects (b) soil suction (ψ), (c) soil weight (W), and (d) both. Z_r - 90 cm, $\lambda = 0.22 \text{ d}^{-1}$, α - 1.5 cm, Δ - 0 cm, E_w - 0.01 cm d^{-1} , E_{\max} - 0.45 cm d^{-1} , ψ_s - 9 cm, b - 4.38, k_s - 100 cm d^{-1} , n - 0.42, β - 12.7, s_h - 0.08, $s_w=0.11$, $s^*=0.31$, s_{fc} - 0.52, c - 2 kPa, γ_d - 18 kN m^{-3} , γ_w - 10 kN m^{-3} , γ_t - 16 kN m^{-3} , θ - 50° , \emptyset - 15° , \emptyset_b - 10° (Muñoz, 2019).....	130
Figure 5.10: HYDRIS 1D Soil profile graphical editor: (a) Initial water content and (b) spacing of nodes.	134
Figure 5.11: (a) Profile information: water content over depth of the tall soil column; (b) Observation nodes: water content (HYDRUS 1D).	136
Figure 5.12: Observed Volumetric Water Content after event 1.	136
Figure 5.13: (a) Observed volumetric water content and (b) Theoretical volumetric water content after event 2.	137
Figure 5.14: (a) Observed volumetric water content and (b) Theoretical volumetric water content after event 3.	137
Figure 5.15: Observed Volumetric Water Content over all three rainfall events.	138
Figure 5.16: Theoretical Volumetric Water Content over all three ponding events.....	138

Figure 5.17: Theoretical and observed Soil Water Characteristic Curves (modified from Lorentz *et al.*, 2019)..... 140

Figure 5.18: SWCCs derived by HYDRUS 1D based on (i) the NNP and (ii) MacRobert (2013) compared with SWCC by Lorentz *et al.* (2019). 142

Figure 6.1: Comparison of intermediate future and more distant future scaling relationships to present climate scaling relationships for the study area, calculated from GCM rainfall output (Knoesen *et al.*, 2011). 146

Figure 6.2: Historical and adjusted future IDF curves derived from predicted design rainfall data: Mokopane..... 150



CHAPTER 1

1.1 Introduction

The global mining industry has seen an exponential rise in severe tailings dam failures since the 1960s. Similar to landslides on natural hillslopes, these disasters are often found to be directly related to rainfall parameters, duration and frequency and more importantly, intensity. Short duration high intensity rainfall events, often increasing under the force of climate change, have been found to provide additional energy in the tension saturation zone, thereby generating rapid physical processes that mobilise pre-event water (Guo *et al.*, 2008). This study builds on research previously presented by Lorentz *et al.* (2004) and Waswa and Lorentz (2016a) that investigated the rapid release and mobilisation of antecedent moisture through transient air pressure waves in natural hillslopes. Even though the contribution of pre-event water to streamflow by the rapid mobilization of groundwater has not previously been considered in the case of tailings dams, it could contribute significantly to understanding complex physical processes that contribute to a decrease in slope instability. Comprehension of the hydraulic mechanisms that control and transmit induced pore water pressure through transient pressure waves, would facilitate better long-term design and maintenance of tailings dams, thereby reducing geo-hydrological risks (Karim *et al.*, 2020). Some research has been conducted on these phenomena in natural hillslopes but have not been considered in the case of tailings dams.

It is further suggested that certain inherent features pertaining to tailings dams, makes these structures particularly vulnerable to the impact of climate change and the generation of transient pressure wave mechanisms. The low hydraulic conductivity of tailings material makes it more prone to saturated conditions when combined with pre-event water, and therefore also more susceptible to the formation of tension saturated or near-saturated conditions, enabling the transmission of an induced pressure head to a potential failure plane (Waswa and Lorentz, 2016b). Cloke *et al.* (2006) also argued that the fine nature of tailings media allows for a greater propensity for capillary fringe rise, thereby providing a continuous water phase necessary for GWR to occur. Capillary zone pre-event water is also supplemented by additional sources that exacerbate saturation rates. This includes the vast quantities of wet slurry that is discarded and stored together with tailings; rising consolidation water and the absence of phreatophytes (Blight *et al.*, 2012; Meyboom, 1967). These water sources, combined with the effects of climate change, may contribute significantly to the observed increase in the failure rate of tailings dams. The main focus of this study was to determine pressure propagation under certain rainfall intensities and how the wetting front affects the stresses in the porous medium

through pore water pressure by induced pneumatic pore air pressure pulses in the unsaturated and saturated capillary fringe zones. Data were collected and analysed to contribute to an understanding of the physical processes responsible for Ground Water Ridding (GWR) as well as the identification of indicators of the Lisse Effect (LE) and rapid water table response. The acquisition of information such as rainfall, the hydraulic, as well as geometric properties of soils, was also analysed. This was done by analysing climate change data, field observation data obtained from previous studies, laboratory experiments and numerical models.

1.1.1 Background to the Study

The collapse of mine tailings storage facilities (TSFs) has been demonstrating clear increasing trends in the last few decades. These disasters result in toxic mudflows that cause extensive damage, catastrophic environmental impacts, loss of life and severe socioeconomic disruptions. Statistical analysis of failure events, conducted by Azam and Li (2010), found the rate of failure of tailings dams to be two orders of magnitude higher than the failure rate of conventional water retention earth dams. This could be attributed to the fact that, unlike earth dams, the construction of TSFs is a dynamic process that is carried out over long periods of time. Since dam rises are constructed in parallel to tailings deposition, it has the potential for modifications leading to errors and long-term variability. South Africa's own mining industry, which is a major contributor to economic growth and development, has not been exempt from experiencing these disasters and saw two major failures in the last five decades. More recently, on the 11th of September 2022, the former Jagersfontein mine, previously referred to as the world's largest diamond mine, experienced a major failure in its TSF. Even though potential stability and environmental impacts had been a concern since the 1970's, maintenance efforts had been downscaled and vulnerable residents exposed to a high-risk hazard.

According to Roche *et al.* (2017) these disasters will intensify due to the increase in waste and rapid succession of dam rises brought about by growing mining activities. This study also recognises the effect that rainfall has had on all disasters researched and suggest that, due to climate change and intensifying extreme events, risk of slope instability increases exponentially. Gariano and Guzzetti (2016) stated that changing rainfall characteristics could make certain areas in southern Africa especially vulnerable to the possibility of landslide activity, which necessitates the re-evaluation of engineered slopes to determine dynamic conditions of slopes at risk. Research has shown that slope instability is caused by excessive stress in either foundation soils, embankments or insufficient control of water pressure, leading

to structural inadequacy and subsidence failure (Yaya *et al.*, 2017). Liu *et al.* (2018) suggested that approximately 30 – 40% of failures in TSFs are caused by seepage and a rise in the phreatic surface. Earlier research conducted by Johansson (2014), came to similar conclusions but extended this theory by stating that transient water flow affects pore air pressure conditions, water content, shear strength, and deformation behaviour of the soil. Chandler and Tosatti (1995) found that, under these conditions, the factor of safety in TSFs decreases considerably as the decant pond approaches the stability walls, thereby reducing freeboard and the width of the beach. This study challenged this particular view and suggested the possible contribution to slope instability through GWR and the LE by the propagation of pore air pressure on the porous medium.

1.2 General importance

Since the operational life span of a TSF, also referred to as life-of-mine (LoM), extends well into the future, the continuous heightening and expanding of TSFs, combined with climate change, increases risk and the vulnerability to failure (Temper *et al.*, 2015). The comprehension of hydraulic mechanisms in tailings porous medium is imperative to the efficient management of risks associated with slope instability and diminishing factors of safety. It is also important to recognise the impact of externalities brought about by climate change and the resulting increase in high intensity rainfall events.

1.3 Problem statement and research question

The occurrence of a tailings dam disaster initiates the investigation of possible causes, with subsequent conclusions normally pointing towards a combination of shear failure, liquefaction and piping. However, it is not known if, and to what degree, high intensity rainfall events contribute to physical and/or hydrological processes that cause slope instability. Therefore, this study will investigate an alternative failure mechanism resulting from high rainfall intensity events in partially saturated conditions. It was postulated that rainfall infiltration and an advancing wetting front may cause pore air propagation and transient pressure wave generation that eventually lead to a change in pore water suction. The change in pore water pressure, resulting from air pressure wave propagation, is known as GWR and the LE. Some research has been conducted on these phenomena in natural hillslopes, but the precise pore water pressure dynamics in tailings dams generated by feedback response and rapid transmission conditions are unknown. This study attempted to answer the following main research question: Do physical processes of pore water pressure dynamics, created by tension saturation

conditions, pore air pressure propagation and rainfall induced pressure head, generate transient pressure waves that contribute to slope instability in tailings dams? By answering this question, the hydrological mechanisms that regulate pore water pressure in tailings dams will be better understood, thereby facilitating better design and reducing the risk of failure.

1.4 Research objectives

The aim of this quantitative research study was to assess the stability of a tailings dam, by: (1) quantifying the extent of changing precipitation parameters, which includes intensity, duration and frequency through downscaled data from Regional Climate Models, to predict (to some degree) future precipitation trends and anticipated Intensity-Duration-Frequency (IDF) curves; (2) conducting extensive research into geological surveys to establish accurate water retention characteristics and hydraulic conductivities of the soil profile; (3) using expected future rainfall data and the hydraulic properties of tailings materials to describe and quantify physical processes of pore water pressure dynamics and slope instability criteria (4) performing laboratory experiments to determine feedback response and rapid transmission conditions of tailings dams when exposed to tension saturation conditions, induced pressure head and subsequent loading; (5) identifying the contribution of antecedent moisture conditions to the development of a potential failure plane; and (6) developing a suitable risk assessment tool to predict the probability of hazardous conditions.

1.5 Specific aim of study

During design of tailings beaches and side slopes, local hydrological conditions are considered to determine the most efficient management of water. This includes rainfall and flood frequency curves derived from existing meteorological data (Fayer and Hillel, 1986). However, changing rainfall characteristics brought about by climate change could have a significant impact on the typical geo-hydrological response of tailings dam materials. Seeing as precipitation intensity, frequency and duration contribute to subsurface conditions in the tailings in varying capacities, it is likely to also alter pore air pressure, water content and resistance to shear failure to such an extent that safety factors are reduced and the risk of slope failure increases. It should however be noted that slope failure is not always caused by the most extreme events. Although rainfall causes slope destabilisation, the challenge lies in determining precise triggering mechanisms leading to significant slope failures due to changes in pore air pressure throughout the impoundment (Bogaard and Greco, 2016).

1.6 Research hypotheses

First hypothesis:

Transient air pressure wave mechanisms create rapid water table responses after the introduction of additional energy in the capillary fringe. It was hypothesized that this energy is derived from high intensity rainfall events and gives rise to groundwater ridging.

Second hypothesis:

The second hypothesis described a similar situation whereby additional energy is derived from compressed pore air, resulting in the propagation of a descending pressure wave referred to as the LE. The downward pressure is brought about the wetting front, creating an impermeable lid that prevents the escape of pore air into the atmosphere. There is a direct relationship between confined pore air pressure in the unsaturated zone between the wetting front and the phreatic surface and the pressure head of water just below the water table. It was postulated and that an impermeable wetting front, brought about by a high intensity event, would result in a rise in water levels in observation wells that are disproportional to the amount of infiltrated rainwater.

Third hypothesis:

It was hypothesized that both the capillary zone and phreatic zone in tailings dams, respond rapidly to transient air pressure waves generated by high intensity rainfall events. These events introduce additional energy in the vadose zone, converting antecedent water held under tension in the capillary zone, to positive pore water pressure contained in the phreatic zone. The resulting GWR mechanism and rapid water table responses are thus inconsistent with the amount of infiltrated rainwater, seeing as it would include pre-event water held in tension in the capillary zone.

1.7 Overview of the methodologies

The methods used in this study consisted of a combination of different approaches to form a comprehensive conclusion to the research question. This included trend analysis of climatic conditions with special reference to increasing temperatures and rainfall intensities, investigation into existing field observations and geometric properties of tailings porous medium, laboratory experiments and numerical modelling using the HYDRUS software package.

1.8 Significance of the thesis

1.8.1 Contribution of this research to the State of Knowledge

This study attempted to assess risks associated with tailings material instabilities due to rainfall induced mechanisms in future climates. It included consideration of climatic factors, geohydrological characteristics and theories of slope failure and combines it with specific experimentation to demonstrate the likelihood of risks under future climatic conditions. The following contributions are subsequently also included:

- a) Determination of whether (and to what degree) high intensity rainfall events contribute to physical and/or hydrological processes that cause slope instability in tailings dams. This process was also investigated by considering the possibility of non-Darcian behaviour occurring in the saturated/unsaturated zones.
- b) A better understanding of the phreatic zone in TSFs. Tailings are not permanently saturated or waterlogged and may illustrate a recognisable response to transient pressure waves, contributing significantly to a change in the entire pore pressure regime and eventually contribute to slope instability.
- c) By better understanding pore air pressure propagation under certain rainfall intensities, it would be possible to anticipate the rate and mechanism for movement of water within the tailings dam, thereby reducing the risk of failure.
- d) A clear understanding of the hydraulic mechanisms that control and transmit induced pore air pressure, which contributes to slope instability in tailings dams through transient air pressure waves, would facilitate better long-term design and maintenance of tailings dams thereby reducing geo-hydrological risks (Karim *et al.*, 2020).
- e) This study has established the influence of rainfall intensity on pore air pressure propagation and the rapid transmission of pre-event water through transient pressure waves.
- f) This study demonstrated pore pressure response to an event. This includes capillary water held in tension being released to the saturated zone due to the application of a rainfall event of a particular intensity.

1.8.2 Contribution of this research to the broader scientific community, the mining industry and society as a whole

South Africa is among the 193 United Nation member states that have adopted a set of 17 Sustainable Development Goals (SDGs), highlighting a common agenda for development and global stewardship. Mining companies have the potential to become important allies in

achieving these goals and underpin the mining industry's contribution to development objectives. Even though the mining industry impacts on all 17 goals to a lesser or greater extent, it is the UN's description of the inherent need to manage risks and water-related disasters (SDG 11.5) that may be exacerbated in the face of climate change, that is most relevant to this study. The principal of sustainable development is based on social, economic and environmental concerns. By understanding how the failure of TSFs impacts each of these, it provides a holistic overview of the importance of reducing mining disasters and finding operational solutions for potential risks and hazards that contribute to slope instability.

1.9 Outline of the thesis

This is a traditional 'monologue style' thesis consisting of seven chapters. Figure 1.1 gives an overview of the lay-out and the interrelationship between different sections. Chapter 1 introduces the study and defines the background information for the problem to be studied. It also includes the research question, objectives of the study, as well as a broad overview of the methodologies used.

Chapter 2 includes an extensive literature review and an overview of published results pertaining to studies relating to the topic. It discusses the three main ideologies pertaining to this study, namely the main impacts of climate change, geotechnical properties of unsaturated tailings media and physical processes responsible for slope instability. Chapter 3 describes the research design and methodology in terms of climate data and hydrogeological analysis, sensor development, tall soil column set-up and procedures pertaining to laboratory experiments.

Chapter 4 presents data analysis and provides a summary of results. Outcomes of the soil column experiments, to verify the existence of transient pressure waves (in both air and water), are also reported. Theoretical development is discussed in Chapter 5 and includes a comparative analysis with numerical modelling using the HYDRUS software package. Chapter 6 provides an interpretation of results together with a comprehensive discussion and application of findings. It also includes analysis of climate change prediction models, development of future IDF curves and a proposed risk assessment tool. The study is concluded in Chapter 7 with an overall discussion, as it relates to the existing body of research. The literature cited in each chapter is contained in the list of References at the end of the thesis.

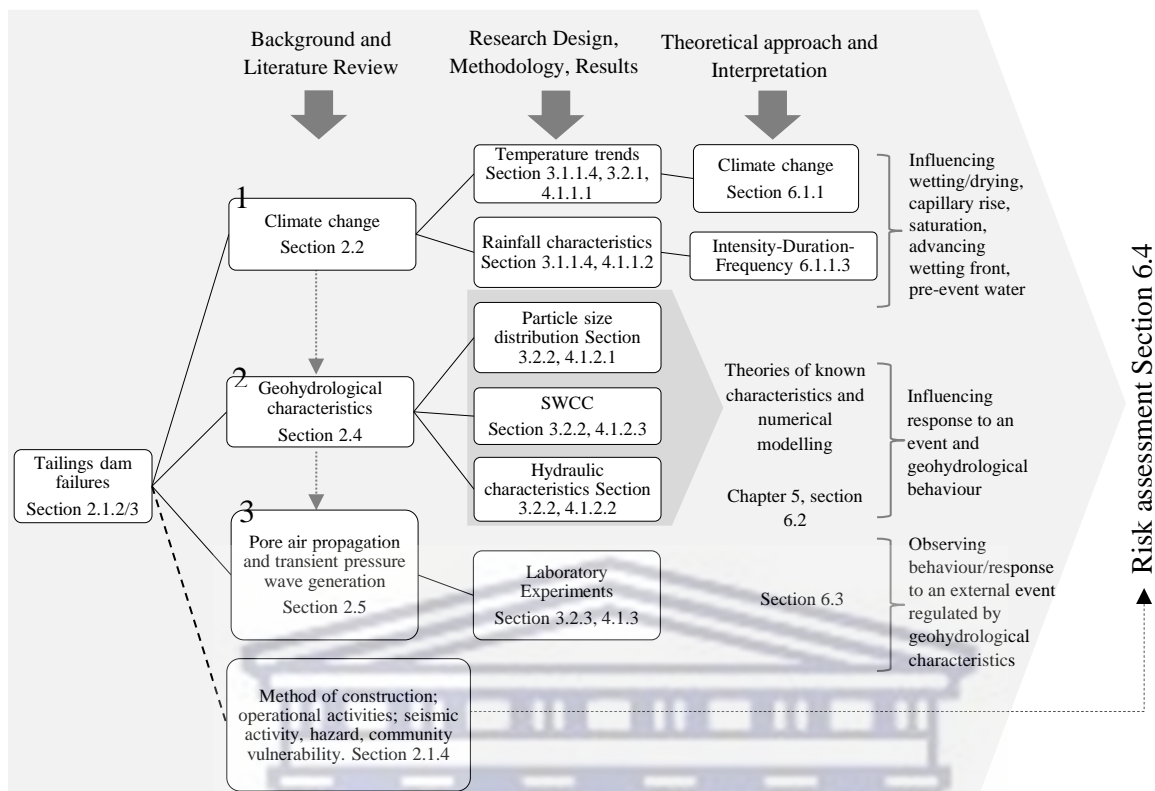


Figure 1.1: Thesis lay-out and interrelationship between different sections.

CHAPTER 2

2.1 Literature review

The literature review is structured into five distinctive parts, each tackling different aspects of this research. The first part provides the background of the study by offering an overview of historical TSFs failures and construction methods found to illustrate a higher vulnerability to instability. It also provides theories and/or concepts, which has been a foundational consideration in formulating research design. The second section gives an introduction to climate change, models used to predict future rainfall conditions and the effect of climatic factors on the physical processes involved with TSFs. Rainfall characteristics, found by previous studies, to exist during historical TSFs failures will be described. The third part evaluates fundamental porous medium characteristics that contribute to the formation of conditions conducive to GWR and the LE. The fourth section outlines the concept of rapid mobilisation of pre-event water through transient air pressure wave mechanisms, eventually giving rise to GWR and the LE. The final section provides an overview of the main points that provided the basis for the development of this study. Chapter 5 will further elaborate on the key concepts and theoretical approach of this study.

2.1.1 Background studies and problem statement

The occurrence of a tailings dam disaster initiates the investigation of possible causes, with subsequent conclusions normally pointing towards a combination of shear failure, liquefaction and piping. This study recognised that some physical/hydrological processes causing slope instability are still poorly understood, and has attempted to suggest an alternative failure mechanism resulting from high rainfall intensity events in partially saturated conditions. It was postulated that the occurrence of an advancing wetting front that infiltrates tailings after high rainfall intensities, will increase due to climate change and contribute to the generation of transient air pressure waves that rapidly increase the phreatic surface and change pore water suction. This rise in pore water pressure, resulting from air pressure wave propagation, is known as GWR and the LE. Some research studies have been conducted on these phenomena in natural hillslopes but have not been considered in the case of the unique porous tailings medium in TSFs.

2.1.2 Tailings dam failures

Blight *et al.* (2003) described TSFs as being some of the largest engineered structures responsible for the containment of mining waste. These dams consist of an external impounding dam wall that holds hydraulically deposited consolidating solids, supernatant water and stormwater. According to Karombo (2020) approximately 262 TSFs worldwide have been deemed to be of high risk of failure, while South Africa has the world's highest number of high risk facilities involving 52 active and 27 inactive tailings dams (Roche *et al.*, 2017). Lyu *et al.* (2019) found that, of the 3500 tailings dams worldwide, an average of three fail every year. This amounts to 31 major tailings dam failures between 2008 and 2018 (IGU, 2019). The geographical distribution of these failures that occurred since 1960 is illustrated in Figure 2.1.



Figure 2.1: Number and geographical distribution of historical tailings dam failures since 1960 (data from Kovacs *et al.*, 2020).

Figure 2.2 illustrates the annual number of TSF failures which clearly indicate a dramatic increase since the 1960's. Although the different trends shown are not necessarily interdependent, there seems to be some degree of correlation. Halabi *et al.* (2022) estimated a total of 356 failures have occurred in the last seventy years. Strachan and Van (2019) noted that construction of larger-capacity mills and the availability of large earthmoving equipment started at the same time, resulting in intensified mining activities and cumulative waste generation. Lyu *et al.* (2019) supported this notion and suggested that the increasing demand for mineral resources and rapid economic development results in the accelerated rising of dams

and consequently lower consolidation rates. It is further recognised that this timeframe was the start of rapid industrialisation, which also contributed to the increase in global temperatures brought about by climate change. By superimposing temperature trends with TSF failures, similar increasing patterns are identifiable.

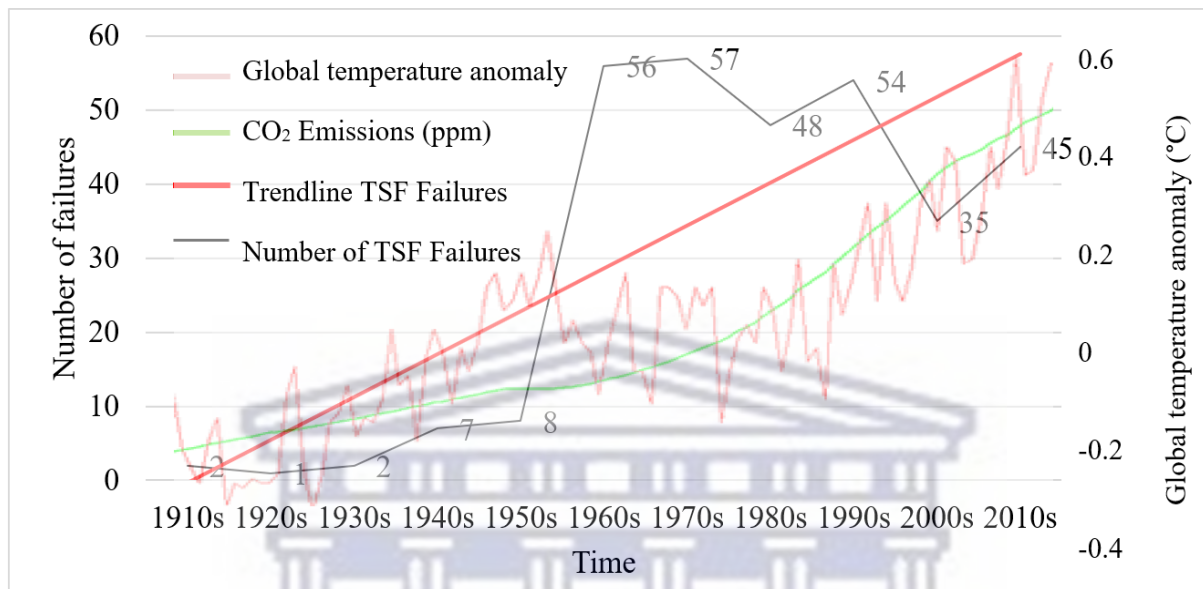


Figure 2.2: CO₂ Emissions, Temperature increases and global TSF failures over time (data from Lyu *et al.*, 2019; Azam and Li, 2010).

Fredlund *et al.* (2012) stated that the vast quantities of waste materials that are stored as a liquid or slurry in these low-level dams during mining and industrial activities, produce physical characteristics that increase the risk of failure. This includes the fact that (a) embankments are constructed by mined soil and coarse waste, which itself includes chemical reagents and process water used to extract minerals (Roche *et al.*, 2017); (ii) rapid multi-stage raising of the dam in order to facilitate high production and output rates (often preventing sufficient consolidation rates); (iii) poor remediation due to high rehabilitation costs; and (iv) poor design criteria combined with insufficient monitoring and control during operational phases (Rico *et al.*, 2008a). Bowker and Chambers (2016) stated that there are insufficient data on the severity that each of these elements contribute to a failure event. Even though various sources of literature e.g., Azam and Li (2010) and Roche *et al.* (2017) described the lack of management continuity, maintenance and monitoring as the most apparent reasons for failure, unpredictable triggering mechanisms such as extreme rainfall events and earthquakes often contribute significantly to the probability of such disasters. Lyu *et al.* (2019) also mentioned several other

possibilities contributing to exacerbated risks, including climatic conditions, inefficient monitoring of mining operations and the lack of reasonable regulations on design standards.

Rico *et al.* (2008a) reported that extreme rainfall events have been responsible for 25% of global and 35% of European tailings dam failures. Precipitation-triggered landslides on natural hillslopes have shown a similar increase over the last few decades. Jeong *et al.* (2017) found that when Seoul in South Korea experienced unusual high intensity rainfall events during two months in 2011, a record high of 150 landslides occurred in mountainous areas. The World Information Service on Energy (2020) stated a vast majority of the tailings dam failures documented since 1961, has occurred as a direct result of water action of the waste material but is exacerbated by additional water sources (Lyu *et al.*, 2019). Blight *et al.* (2012) mentioned that high saturation rates are continually augmented by water from sources other than slurry, including rising consolidation water, precipitation and the absence of phreatophytes that would normally be absorbing groundwater. This notion is supported by Fourie and Blight (2009) that found the presence of large quantities of stored water to be a significant contributing factor to most of the recent failures. Critical rainfall events have subsequently been identified as one of the most important factors triggering shallow landslides, and more specifically, tailings dam failures (Guang-jinx *et al.*, 2017; Muñoz, 2019).

Various researchers including Strachan and Van (2018), Fayer and Hillel (1986), Blight *et al.* (2012), Rico *et al.* (2008b), Halabi *et al.* (2022), DiSciullo *et al.* (2022), Fourie *et al.* (2022) and Azam and Li (2008) described tailings dam failures due to water loading as a result of one or a combination of the following conditions: (a) overtopping whereby higher intensity rainfall events generally lead to more run-off and floods which contribute to rising levels within the decant pond, thereby exceeding capacity of the impoundment. Unless sufficiently drained, freeboard could be reduced to such an extent that overtopping of the crest occurs. Due to retaining structures being constructed of permeable cohesionless materials, the friction caused by rapid flow over an unprotected embankment crest, may result in erosion and the loss of slimes is to be expected; (ii) rotational sliding and the reduction in shear resistance brought about by pore water pressure in saturated conditions cause instability problems in the form of circular arc slides. Other causes include changes in the water table, specific loading conditions or changes in hydraulic conductivity. The US National Committee on Large Dams categorizes rotational shear failure as the main driving force behind slope instability, which results in a flattening of the slope of the impoundment without a significant loss of tailings (Blight *et al.*,

2003); (iii) piping or internal erosion caused by a higher hydraulic gradient and material susceptibility leading to the formation of a low-pressure conduit allowing for concentrated flow. This is caused by the upward seepage force becoming equal to the submerged weight of the soil, resulting in particles being carried upward and deposited at the ground surface. Seeing as there exists no frictional resistance between particles, shear strength is lost, and liquefaction occurs. The resulting void space supports progressive erosion and the creation of a direct channel from the tailings pond to the dam face (Whitlow, 2001); (iv) erosion of surface material through gradual loss due to heavy rainfall and run-off; and (v) liquefaction whereby loose, saturated, fine-grained material is subjected to a rapid increase in pore water pressure which reduces shear strength and margin of safety. Seeing as tailings deposits largely consist of unconsolidated particles of uniform size, they are susceptible to temporary suspension in water, demonstrating the behaviour of a viscous fluid. Lyu *et al.* (2019) and Blight *et al.* (2012) suggested that some of the most severe tailings dam failures have resulted from liquefaction of unconsolidated fines brought about by a sudden increase in pore water pressure.

Pacheco (2018) and Lyu *et al.* (2019) further proposed that static liquefaction and eventual slope failure is caused by an imposed stress that exceeds maximum effective shear stress-shear strain of the saturated contractive granular tailings material. This is often the case in high productivity mining operations. As deposits into tailings dams increases, consolidation and a decrease in volume results in higher densities and increased shear strength. However, if loading stresses are applied to the soil mass under undrained conditions, it results in an increase in pore air pressure and pore water pressure and consequential decrease in shear strength in the unsaturated zone. Contractive and dilative states of saturated tailings are separated by the critical state line (CSL), also referred to as the steady-state line (SSL). It is regulated by initial void ratio (e) and confining effective stress (p'), thereby delimiting the behaviour of tailings materials. If the material is initially above the CSL in the compression plane, it will show contractive behaviour and if below the CSL, the behaviour will be dilative. Rodriguez *et al.* (2021) stated that after shear stress and deformation result in the tailings porous medium to contract, excessive pore pressure develops faster than what drainage systems can relieve. This study supports this notion, but also suggest that transient air pressure waves contribute significantly to variations in pore water pressure brought about by pre-event water. It was also recognised that the increase in height of wastewater as the height of the tailings dam increases, along with the associated physical mechanisms, add to instability of the slope (Hu *et al.*, 2017).

Do *et al.* (2021) found that excess pore water pressure increased with each raising phase and, although it would decrease after consolidation, it would not return to previous pressure rates. Each rise would therefore result in a continued build-up of porewater pressure. Additionally, if the rate of loading is too fast, excess pore water cannot dissipate fast enough, causing a reduction in shear strength and increased slope instability. The rate at which water is able to dissipate after loading depends on the hydraulic conductivity of the tailings material. Muñoz (2019) proposed that the rate of loading, hydraulic conductivity of the material and the provision of adequate drains, contribute to efficient water transfer which reduces pore pressure and increases shear strength. Fourie *et al.* (2022) mentioned the lack of human intervention and environmental failure modes as additional factors to consider when evaluating the stability of both proposed and existing TSFs.

2.1.3 Historical TSFs Disasters

From Figures 2.1 and 2.2 it is evident that the failure rate of TSFs have shown a significant increase over the last few decades. Table 2.1 provides a summary of some TSF disasters, method of construction and cause of failure (if available). Due to the recency of some of these events, the exact mechanism of failure has not yet been established, but nearly all were associated with heavy rainfall, and in some cases monsoon conditions. Fourie *et al.* (2022) also identified several triggering mechanisms that contribute to failure. These include high pond water levels, inhomogeneous tailings material, low density tailings mass, material of low hydraulic conductivity in the structural zone and heavy rainfall. Section 2.1.3.1 discusses some specific TSF failures and section 2.1.4 will explain the susceptibility to failure in relation to method of construction.

Table 2.1: Examples of global tailings dam failures (Lyu *et al.*, 2019; Blight and Fourie, 2003; Wei *et al.*, 2013; WISE, 2023; Bowker and Chambers, 2016; ICOLD, 2001).

Year	Location	Dam Type	Cause of failure
1928	Barahona (Chile)	Upstream	Earthquake
1937	Dos Estrellas (Mexico)	Upstream	Seepage
1948	Kimberley (Canada)	Upstream	Seepage
1958	Mailuu-Suu (Kyrgyzstan)	-	Earthquake (following heavy rainfall)
1960	La Luciana, Reocín (Santander)	-	-
1961	Jupille, Belgium	-	-
1962	Huogudu (China)	Upstream	Foundation failure
1963	Louisville, (USA)	-	-
1964	Kyrgyzstan	-	Earthquake
1964	Castano Viejo Mine (Argentina)	-	-
1965	El Cobre Old dam (Chile)	Upstream	Earthquake

1965	El Cobre New dam (Chile)		
1966	Aberfan (UK)	Water retention	Seepage
1966	Mirolubovka (Bulgaria)	Upstream	-
1970	Mufulira (Zambia)	Unknown	-
1972	Buffalo Creek (USA)	Upstream	Seepage
1974	Bafokeng (South Africa)	Upstream	Seepage
1974	GCOS (Canada)	Upstream	Seepage
1975	Mike Horse (USA)	Upstream	Overtopping
1976	Dashihe (China)	Upstream	Earthquake
1978	Syncrude (Canada)	Centerline	Foundation failure
1978	Mochikoshi (Japan)	Upstream	Earthquake
1978	Arcturus (Zimbabwe)	Upstream	Overtopping
1979	Union Carbide (USA)	Upstream	Seepage
1979	Church Rock (New Mexico)	Upstream	-
1985	Stava (Italy)	Upstream	Seepage
1985	Chenzhou (China)	Upstream	Overtopping
1985	Cerro Negro No. 4 (Chile)	Upstream	Earthquake
1986	Huangmeishan (China)	Upstream	Seepage
1988	Lixi (China)	Upstream	Overtopping
1991	Sullivan (Canada)	Upstream	Seepage
1993	Marsa (Peru)	Upstream	Overtopping
1993	Istanbul, (Turkey) LF	Unknown	Shear instability
1993	Saaiplaas (South Africa)	Upstream	High phreatic surface
1994	Longjiaoshan, Hubei, China	Upstream	-
1994	Tapo Canyon (USA)	Upstream	Earthquake
1994	Merriespruit (South Africa)	Upstream	Overtopping
1995	Omai (Guyana)	Unknown	Seepage
1995	Surigao (Philippines)	Upstream	Foundation failure
1996	Porco (Bolivia)	Upstream	Overtopping
1996	Sgurigrad (Bulgaria)	Upstream	Seepage
1998	Los Frailes (Spain)	Upstream	Foundation failure
1999	Surigao del Norte (Philippines)	Unknown	Slurry from burst pipe
2000	Inez, Kentucky (USA)	Unknown	Underground Collapse
2000	Baia Mare/Baia Borsa (Romania)	Downstream	Overtopping
2000	Dachang, Guangxi	Upstream	-
2002	San Marcelino Zambales (Philippines)	Unknown	Overtopping (UN)
2004	Pinchi Lake (Canada)	Unknown	-
2006	Zhenan mine, Shanxi	Upstream	-
2008	Xiangfen, Shanxi province	Upstream	-
2009	Karamken tailing plant (Russia)	Unknown	-
2010	Ajka (Hungary)	Downstream	Seepage
2011	Kayakari (Japan)	Unknown	Earthquake
2012	Sotkamo (Finland)	Unknown	-
2012	Padcal No. 3 (Philippines)	Upstream	Overtopping
2013	Ok Tedi (New Guinea)	Unknown	-
2014	Mount Polley (Canada)	Unknown	Foundation failure
2015	Fundão (Brazil)	Upstream	Seepage
2015	Samarco (Brazil)	Unknown	-
2015	Bento Rodrigues (Brazil)	Unknown	-
2019	Brumadinho (Brazil)	Upstream	Static liquefaction
2019	Rondônia, Brazil	Upstream	-
2019	Muri, Jharkhand, India	Unknown	-
2019	Hpakant, Kachin state, Myanmar	Upstream	Liquefaction
2019	Cobriza mine, Peru	Upstream	Overtopping
2019	La Rinconada, Ananea, Peru	Upstream	-
2020	Tieli, Yichun City, China	Unknown	-
2020	San José de Los Manzanos, Mexico	Unknown	-
2020	Hpakant, Kachin state, Myanmar	Unknown	Erosion, liquefaction
2021	Catoca mine, Saurimo, Angola	Unknown	-

2021	Yedikardes village, Turkey	Unknown	-
2021	San Antonio de María mine, Peru	Upstream	-
2021	Ulundi, South Africa	Unknown	-
2022	Pau Branco mine, Brazil	Upstream	Overtopping
2022	Banjhiberana village, India	Unknown	-
2022	Wenquan Township, China	Upstream	-
2022	Agua Dulce, Potosí, Bolivia	Upstream	-
2022	Jagersfontein (South Africa)	Upstream	-
2022	Mwadui Lohumbo, Tanzania	Upstream	-

Section 2.1.3.1 and 2.1.3.2 will elaborate on some of the above-mentioned disasters. The selection was based on severity, locality and time of failure.

2.1.3.1 Recent International Tailings Dam Failures

a) Brazil: Feijao Dam I: 2019

On the 25th of January 2019, the Corrego do Feijao Iron Ore Mine near Brumadinho, Brazil, collapsed. Reports suggested that the significant and rapid loss of strength resulted in liquefaction of tailings material which created a 30 m high mud wave, flowing rapidly downstream towards the Paraopeba River (Robertson *et al.*, 2019).

The dam illustrated in Figure 2.3 was constructed from 1976 to 2013 by the upstream method. By then, it had reached a height of 86 m and a length of 700 m. Each berm had upstream and downstream slopes of between 1.5H:1V and 2.5H:1V. A total of ten raises, each between 5 and 18 m, were constructed by the tailings on the beach close to the crest of the dam. This resulted in the instant flooding of excavations and created fragile areas which would later have to serve as the basis for future berms. Tailings deposition at Dam I stopped in mid-2016 (Robertson *et al.*, 2019).



Figure 2.3: Corrego do Feijao Iron Ore Mine, Dam I (Google Earth 3D, Image Date July 7, 2018 as cited in Robertson *et al.*, 2019).

Robertson *et al.* (2019) conducted a technical investigation into the cause of failure and subsequent liquefied flow slide. It was established that the stress state of the dam showed large sections to be under considerable loading conditions due to, amongst other reasons, high internal drainage. Despite tailings not being deposited since 2016, the water level within the dam did not show signs of significant drainage and remained reasonably constant. Similar results were obtained by Rotta *et al.* (2020) who applied the Soil Moisture Index (SMI) over the tailings dam to reconstruct ponding dynamics since 2011. Thereafter, a standard deviation map of SMI over time was generated to analyse the spatial variation patterns in moisture conditions over the dam. Rotta *et al.* (2020) found that the increase in moisture in different sections of the dam, implied that the fill material was becoming saturated until it collapsed. Evidence also pointed towards a high water table, possibly extending to the ground surface. Both these studies agree that saturated conditions, that allowed ponding close to the crest, were attributed to higher and more intense cumulative rainfall events measured since October 2019 up to failure in December 2019. The average rainfall over the preceding three-year period amounts to 1 400 mm. The analysis of rainfall data also provided a clear indication that the intensity of rainfall events increased in 2019. Robertson *et al.* (2019) generated a one-dimensional soil-atmosphere simulation consisting of climate data and surface hydraulic properties. This data were obtained from previous field and laboratory studies. The results showed a net infiltration capacity of 50% of rainfall. Computed water pressures from two-dimensional seepage models also indicated a high piezometric surface, particularly near the crest. According to Robertson *et al.* (2019) this would most likely have caused a loss in suction in the vadose zone coupled with a reduction in shear strength. High shear stresses and internal strains, which resulted in creep, combined with the brittle nature of the tailings material are recognised as major contributing factors to critical strength reduction and dam failure (Robertson *et al.*, 2019). Figure 2.4 illustrates gradation characteristics of the tailings at this mine, illustrating most of the material to fall within the fine silt fraction.

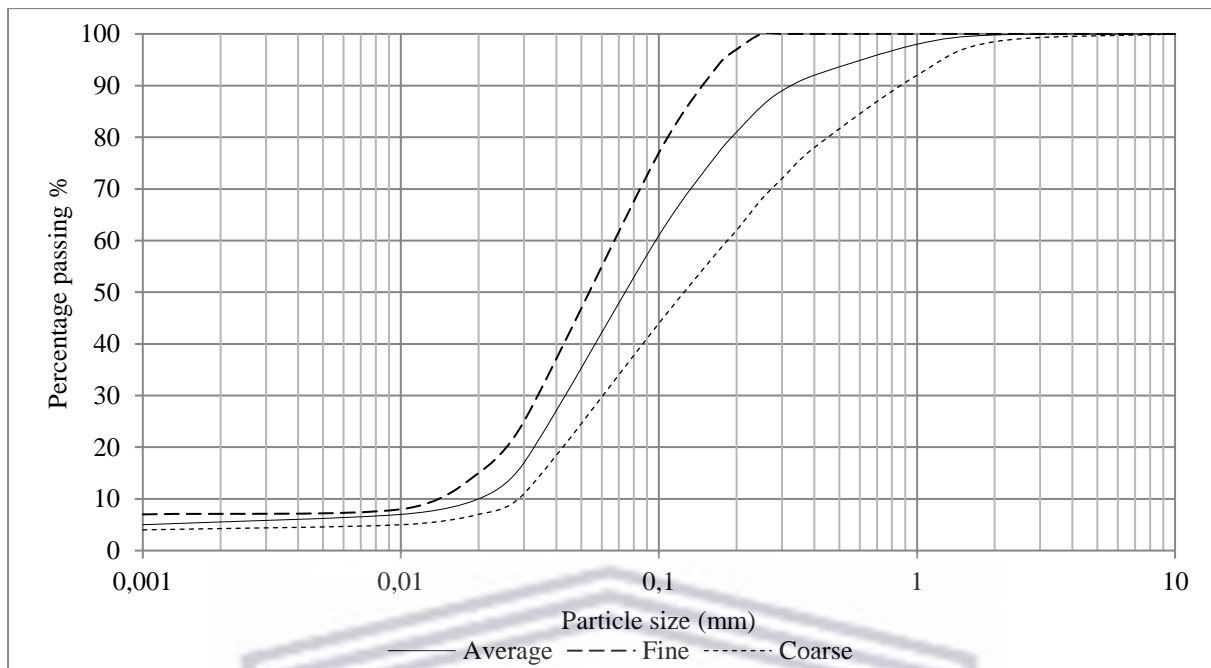


Figure 2.4: Particle size distribution analysis for fine, coarse and average gradations for the Feijao Dam I (Robertson *et al.*, 2019).

b) Canada: Mount Polley: 2014

The Canadian Mount Polley copper-gold mine carried out open pit and underground mining operations since 1997 (Roche *et al.*, 2017). After failure of the tailings dam in August 2014, it released an estimated 25 million m³ of waste into the basin. It has been recognised as one of the largest environmental disasters in Canada. The impact was exacerbated by the large quantities of metal contaminants including arsenic (84 831 kg), mercury (562 kg) and lead (38 218 kg) (IGU, 2019). Research conducted into the cause of this failure mentions, amongst other things, the lack of consideration given to extreme conditions such as floods. Chambers (2015) found that higher than expected precipitation resulted in overflow and high-water levels in the tailings pond (2.3 m below dam core). According to Lyu *et al.* (2019) failure had not been attributed to seepage or overtopping, but poor drainage in the finely graded tailings resulted in the load bearing capacity of the foundation to be exceeded. Both last mentioned authors agree that, even though the water level in the tailings pond was a major contributing factor to the damage associated with the dam failure, it could have been prevented with proper design, construction and monitoring activities.

c) Brazil, Fundão dam: 2015

Carmo *et al.* (2017) described the Fundão dam, located in south-eastern Brazil, as having been one of the megastructures of the Germano mining complex. It began operations in 2008 and was meant to have a lifespan of 25 years while ensuring a storage capacity of approximately 79.6 million m³ of fine tailings. Since operations commenced, the dam demonstrated various irregularities with regard to drainage, construction defects, upwelling and exceeded expected saturation rates. On the 5th of November 2015, the dam breached and released almost 43 million m³ [or 32 million m³ according to Fourie *et al.*, 2022] of tailings, killing 19 people and causing irreversible environmental damage (Carmo *et al.*, 2017). The high-density mudflow inundated the town of Bento Rodriguez, roughly 8 km from the dam site and advanced along the Rio Doce river for another 668 km. It eventually reached the Atlantic coast after 17 days (Roche *et al.*, 2017).

Technical reports concluded that the failure occurred due to liquefaction of the tailings. It was also found that structural damage to the starter dam had contributed to high levels of saturation and that the unexpected deposition of sludge in critical areas exacerbated the already unstable structure. Attempts to solve structural issues involved construction of a concrete gallery which caused the axis of the dam to retract, resulting in a significant reduction in the beach area and eventual exceedance of the critical limit (Carmo *et al.*, 2017).

2.1.3.2 South African Tailings Dam Failures

a) Jagersfontein tailings dam disaster: 2022

Slope failure of the tailings dam at the Jagersfontein mine occurred on the 11th of September 2022. Apart from being the world's oldest diamond mine of its kind, constructed using the upstream method, it is also the world's largest hand excavated pit spanning almost 20 hectares (Brown and van Wyk, 2022). Even though the de Beers mining group ceased operations in 1971, new owners sought to capitalize on improving technology to reprocess the tailings and extract diamonds that have been discarded. Operations were briefly interrupted in 2020 by exceedingly high-water levels, but these were resumed in 2021.

Several sources have reported the dam wall collapsed due to structural failure, releasing most of the tailings from the pond. The mud wave travelled approximately 8 500 m resulting in the inundation of farmland, including a nature reserve, and the loss of 500 animals and livestock. A further 154 residences were damaged, 76 people were injured and two were killed (Hansen,

2022). The plume spread over 1.5 km wide and entered several water sources, including water systems used for drinking water and agricultural activities (Petley, 2022). Figure 2.5 illustrates the location of the breach at the dam's southern side, releasing tailings waste to the nearby residential area and eventually also to receiving water bodies.



Figure 2.5: Jagersfontein tailings disaster (modified from Planet Team, 2022).

From satellite imagery taken before the breach, Petley (2022) was able to identify several sections of the dam wall that appear to have been severely eroded. Further mention is also made of the fact that, on both sides of the breach, fresh slimes were coating the walls of the tailings dam, illustrating the high mobility of the mine waste. Due to the recency of this disaster, official reports have not been yet been published and researchers are only speculating on possible contributing factors.

b) Merriespruit Disaster: 1994

On the 22nd of February 1994, the number four tailings dam, situated 320 m upslope of Merriespruit, collapsed. According to Rico *et al.* (2008b) the failure of the 31 m high northern wall of the gold tailings dam, caused detrimental impacts on the environment, the mining industry and resulted in 17 deaths. Davies *et al.* (2002) determined that, during this event, a 2.5 m high flood wave carried 600 000 m³ tailings material and 90 000 m³ wastewater over a distance of 2 km. Prior to failure, a high intensity rainfall event of 50 mm was received in a short span of 30 minutes. Although maintenance issues were found to be a contributing factor to the collapse, various studies found insufficient freeboard, poor pool control (leading to some

areas having high in situ void ratios) and static liquefaction as the most significant contributing factors.

Laboratory tests conducted by Papageorgiou *et al.* (1999) were able to define a series of steady state lines, which was found to be a good indication of liquefaction and susceptibility to liquefaction. This line represents the mean effective confining stress and corresponding void ratio at steady state conditions. It is influenced by tailings material properties such as particle size distribution, shape and fines content. For instance, an increase in fines content reduces hydraulic conductivity, resulting in an undrained response to loading conditions. Figure 2.6 illustrates the fine nature of soil porous medium at the Merriespruit tailings dam. From this analysis, it was found that approximately 79% of the fine limit of the liquefied material lies within the silt particle-size range, while 7% consists of fine sand and 14% clay-size particles. The course limit and samples containing up to 60% fines, illustrated a clay content of 5% and 8%, a silt fraction of 20% and 37% and a fine sand content of 75% and 55% respectively. Papageorgiou *et al.* (1999) also conducted a comparative analysis of in-situ void ratios from undisturbed samples, and determined that a large amount of these tailings plotted above the relevant steady state line and were likely in a metastable state. Fourie *et al.* (2009) identified overtopping, due to insufficient freeboard, slope erosion and progressive shear failure as causing the removal of confinement, exposing loose material and triggering static liquefaction under undrained loading conditions.

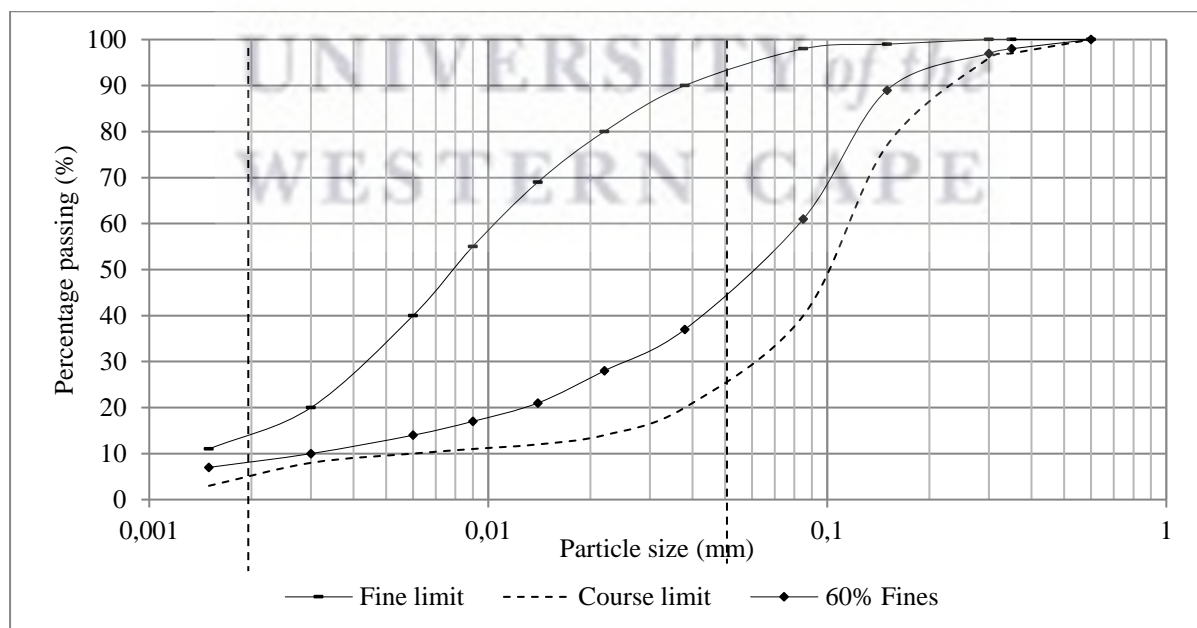


Figure 2.6: Particle size distribution analysis for fine, course and average gradations for Merriespruit Gold Tailings material (Papageorgiou *et al.*, 1999).

Less than a year before the Merriespruit disaster, the nearby Saaiplaas No. 5A tailings dam, experienced three separate flow failures, in three days. These are indicated in Figure 2.7 (a) and (b) below. Blight *et al.* (2003) describes the breach to be attributed to the high phreatic surface but according to Fourie *et al.* (2009) failure due to the high water table could possibly have been avoided if not for the reduction in unconsolidated effective stress. This may be attributed to the exponential rate of rise of 1,8 – 2,6 per annum to 2,8 per annum, resulting in the density of successive layers to be highly variable.

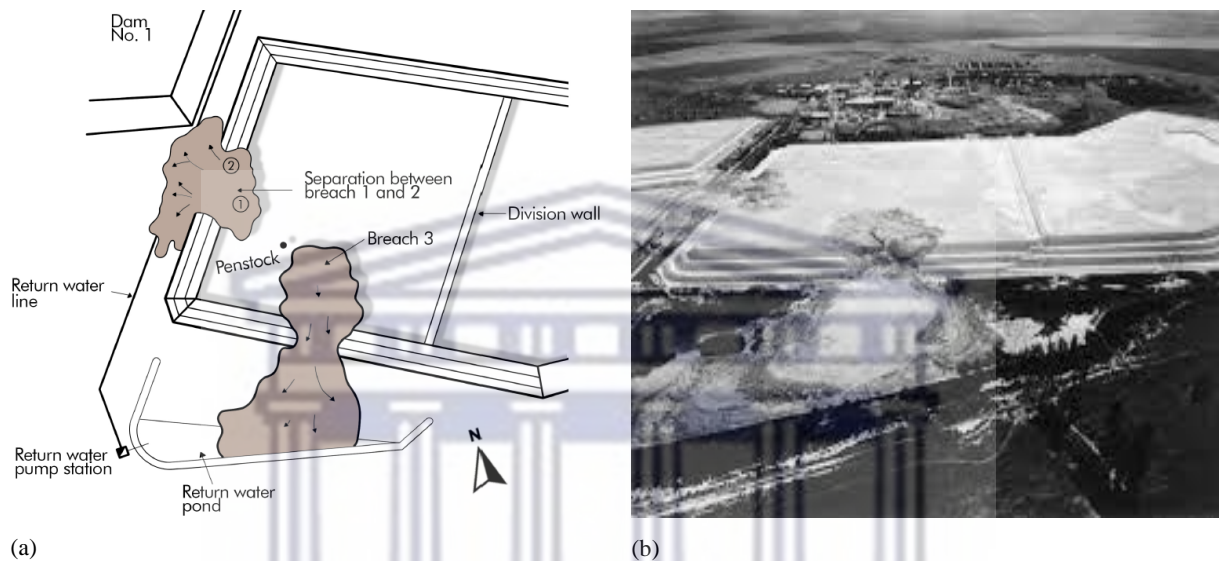


Figure 2.7 (a) and (b): Plan and aerial view of Saaiplaas dam showing locations of failures 1, 2 and 3 (modified from Blight and Fourie, 2003; Fourie *et al.*, 2002).

c) Bophuthatswana: Bafokeng South Mine: 1974

Similar to the above disasters, the Bafokeng platinum tailings mining disaster occurred after a high intensity rainfall event of an estimated 75 mm in the early hours of 11 of November 1974 (Lyu *et al.*, 2019). Blight *et al.* (2003) suggested that overtopping most likely led to breaching of the dam wall by erosion. After failure of the 20 m high dam wall, an estimated 3 million m³ liquefied tailings slurry were released over a distance of 42 km, demolishing surface structures, submerging an underground shaft and killing 13 people (Blight *et al.*, 1981; Rico *et al.*, 2008b). As all other TSFs in South Africa, this dam was constructed using the upstream method. Figure 2.8 below illustrates the particle-size distribution of tailings taken from the pool of the tailings dam. From this, it is evident that 87% of the liquefied materials lies within the silt particle-size range, while 1% consists of fine sand and 18% clay-size particles. As expected, Blight *et al.* (1981) found the material deposited around the walls of the dam to be considerably coarser. Jennings (1979) stated that even though gradation curves do not provide detailed information

on the cause of tailings dam failures, it does permit certain conclusions to be made. This includes a closer inspection of tailings characteristics that may contribute to unstable behaviour, especially during saturated conditions.

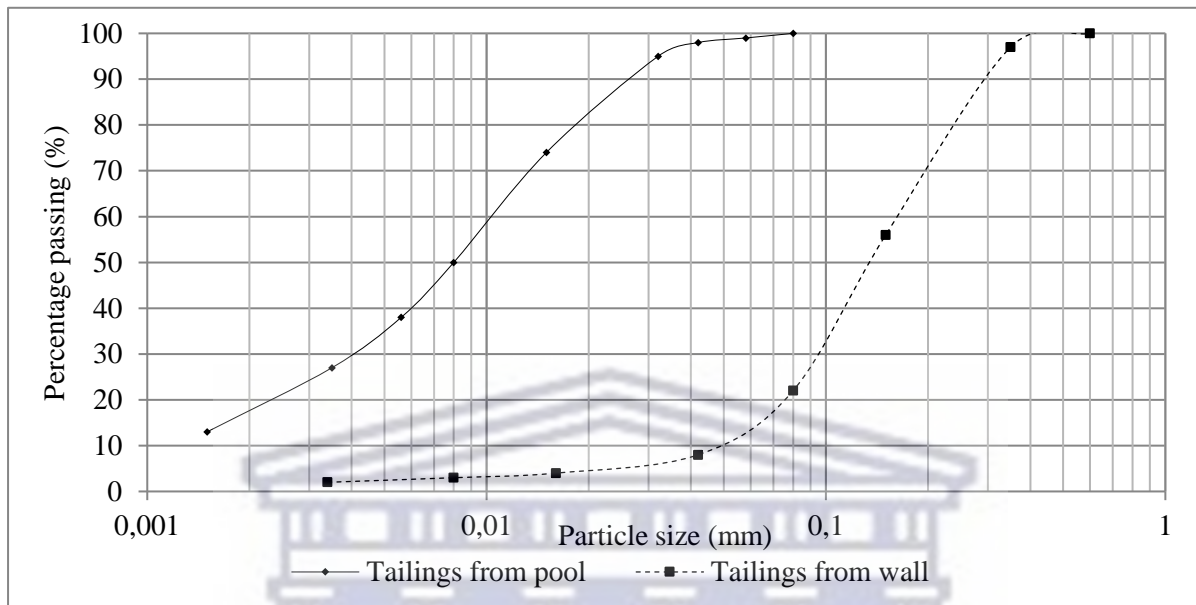


Figure 2.8: Particle size distribution analysis for fine, course and average gradations for the Bafokeng tailings material (Blight *et al.*, 1981).

2.1.4 Method of construction and relationship with failure

The stability of an engineered slope, as in the case of tailings dams, is largely dependent on the method of construction, which is simultaneously carried out during operational activities. It is affected by both internal and external factors such as local seismic activities, climate, topography, geology, extraction and deposition methods, hydrological conditions and economic considerations. Regardless of the construction method used, each layer is constructed with the coarse fraction of the tailings material, which are often susceptible to internal piping and liquefaction (EPA, 1994). Consideration of geotechnical properties is therefore a strong indicator of slope stability and deformation behaviour of the tailings porous medium.

Tailings dams, often built with steep slopes, are constructed by the successive raising of embankments by either one of the following three methods: Firstly, the upstream method, which has now been banned in many countries, is illustrated in Figure 2.9. It was developed in response to a need to operate at low economical costs by using the coarse fraction of the tailings as construction material. Even though this method has lower construction costs, it requires more monitoring, responds poorly to seismic activity, is not suitable for significant water

storage and restricts rapid height raising rates (Vick, 1990). Martin and McRoberts (1999) and Kossoff *et al.* (2014) considered upstream tailing dam models to be unstable, especially once operations cease. Carmo *et al.* (2017) and Rico *et al.* (2008b) agreed and stated that upstream dams are more susceptible to liquefaction and slope failures. It is estimated that ~ 90% of tailings dam failures that occur are constructed by the upstream method (Piciullo *et al.*, 2022; Lyu *et al.*, 2019). Strachan and Van (2018) conducted a comparison study into TSF failures based on the method of construction and found that the majority of failures are associated with dams constructed by the upstream method. However, Rodriguez *et al.* (2021) mentioned that since most tailings dams are constructed using this method, the high proportion of failures associated with this construction method may be misleading. Construction of an upstream dam commences with a small starter dam, where after the embankment is progressively raised on the upstream side (Wills and Finch, 2016). As the supernatant pond nears capacity due to discharge through, for example, cycloning or spigotting, the embankment is raised, and the process is repeated. The dam is therefore built on top of previously deposited unconsolidated slimes, which limits stability and wall height as well as being more prone to leakage (Martin and McRoberts, 1999; IGU, 2019). Bhanbhro (2014) suggested that under undrained conditions, an increase in pore water pressure and reduction in effective stresses could result in shear failure to occur. Do *et al.* (2021) also mentioned that the rate of filling of ponds increases porewater pressure, which decreases the stability of TSFs, especially with regard to upstream tailings dams.

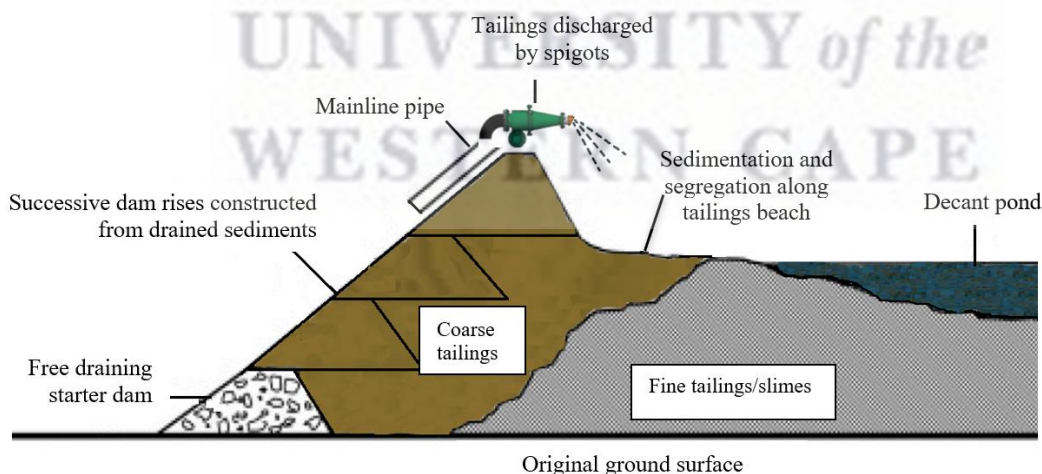


Figure 2. 9: Upstream tailings dam construction (modified from Wills and Finch, 2016).

The downstream construction method, illustrated in Figure 2.10, is the only method that achieves acceptable design and construction engineering standards (Wills and Finch, 2016). It involves successive construction of embankment walls on the downstream slope of the starter

dam. Wills and Finch (2016) described this method to provide more stability due to its ease of compaction, the incorporation of phreatic surface control measures and the fact that the dam raises are not structurally dependent upon the tailings deposits for foundation strength. According to Azizli *et al.* (1995) downstream dams are safer than dams constructed using the upstream method, under both static and seismic loading. It does however require increased fill volume to raise embankments and takes up large areas of land space, making it a challenging and a more expensive option.

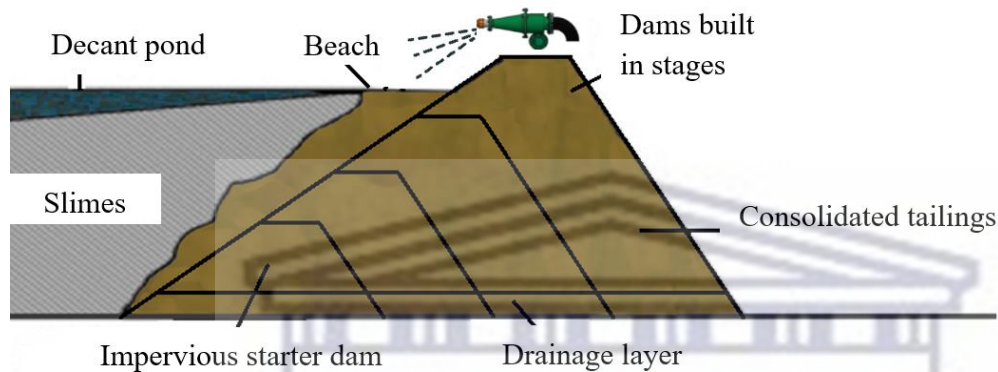


Figure 2.10: Downstream tailings dam construction (modified from Wills and Finch, 2016).

Figure 2.11 shows the lay-out of the centreline construction method that allows for the crest of the dam to remain in the same horizontal position as it is raised in succession. Construction therefore continues vertically on the crest of the existing dam. Sufficient decant facilities drain excess free water, thereby reducing the risk of failure (Wills and Finch, 2016). This method does not require a wide beach and dam raises may be added sooner than in the case of the other two methods. Even though this embankment type is not suitable as a permanent storage solution, short term storage of water due to heavy precipitation events will not affect the stability of the dam (EPA, 1994).

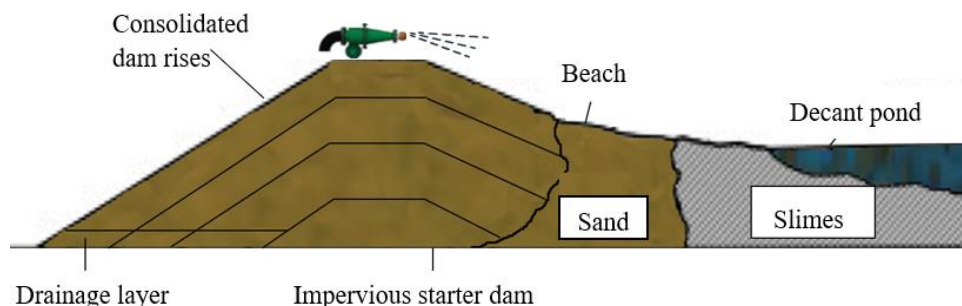


Figure 2.11: Centreline tailings dam construction (modified from Wills and Finch, 2016).

2.2 Climate Change

The Intergovernmental Panel on Climate Change (IPCC, 2014) defined climate change as a long-term increase in average surface air and sea surface temperatures, resulting in irreversible and permanent variability. Anthropogenic induced warming, through the emission of carbon dioxide, amounts to an average of 0.2°C per decade, which has resulted in an increase of 1°C (average) from pre-industrial levels to 2017. Figure 2.12 illustrates the warming trend since industrialisation, indicating a likely rise of 1.5°C (average) by 2040 (high confidence). Allen *et al.* (2018) found that most land regions already experience above average warming amounting to approximately 1.5°C (average). According to Gutiérrez *et al.* (2021) and Engelbrecht *et al.* (2015) mean annual temperature across different areas of southern Africa have already increased by between 1,04°C and 1,44°C (1961-2015) and 1,6°C and 1,8°C (1961-2010) respectively. Kruger and Nxumalo (2017) also found an increase in the number of hot days per year, as well as a decrease in the number of annual frost days. According to Lyakaremye *et al.* (2021) cold extremes are likely to decrease under all emission scenarios but would be most pronounced in the absence of mitigation measures.

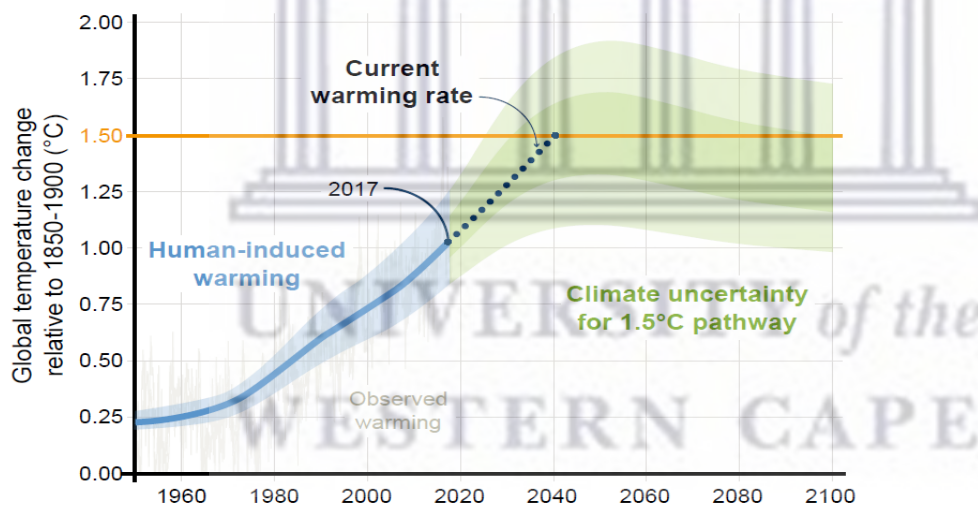


Figure 2.12: Current human induced global temperature trend (Allen *et al.*, 2018).

Based on this evidence, the IPCC's sixth assessment report (AR) (2022) predicted that mean annual temperatures in southern Africa will be 1,2°C, 2,3°C and 3,3°C higher than averages recorded between 1994 and 2005. It was further established that hot and very hot days are likely to increase while the annual number of heatwaves are likely to increase by between two and 12 days (Engelbrecht *et al.*, 2015; Weber *et al.*, 2018; Seneviratne *et al.*, 2021).

2.2.1 Climate Change and Rainfall

Several environmental consequences follow a rise in atmospheric temperatures. Higher temperatures cause an increase in evaporation, while a warmer atmosphere is able to hold more water vapour. This results in less frequent rainfall events, but of higher intensity and often of short duration. These changes in precipitation parameters, i.e. frequency, intensity and duration, are often observed and is expected to increase under all emission scenarios. Extreme events have already increased both in severity and frequency over the last century (Kruger and Nxumalo, 2017) while Mean Annual Precipitation (MAP) across large areas of southern Africa have increased between 128 and 256 mm during a period of 1980 to 2015 (IPCC, 2022). According to Kruger and Nxumalo (2017) long term station data in the southern parts of South Africa show significant trends in rainfall events that exceed 5 mm/hour over a period of 1921 to 2015. Although these trends seem to become more pronounced, various earlier studies already confirmed similar findings. Van Wageningen (2006) for instance established that precipitation trends in the Western Cape showed that even though there has been a noticeable decrease in rainfall frequency, yearly precipitation volumes seem to remain constant. This was attributed to individual rainfall events occurring at higher intensities. Arnell and Reynard (1996) explained that it was likely that small changes were taking place annually, while larger changes, i.e., extreme events, were expected to change known historical parameters of short-term hydrological features. Even earlier, Ruosteenoja *et al.* (2003) found the model-simulated temperature/precipitation change over the southern Africa area to be statistically significant. Although specific rainfall trends were weak, there was a tendency towards a significant decrease in the number of rain days in almost all hydrological zones. This suggested a propensity towards an increase in rainfall intensity and an increase in the duration of dry spells. This notion was supported by the Department of Environmental Affairs (2012), who recognised that the occurrence of annual extreme rainfall events in South Africa, indicate an increasing trend (DEA, 2012).

Not only has there been an increase in extreme events, but a decrease in frequency have also been evident, particularly during the dry season of different regions. While the frequency of droughts increased between 1961 and 2016, severity and prolonged dry spells have also occurred more regularly (IPCC, 2022; Seneviratne *et al.*, 2021). According to Spinoni *et al.* (2019) meteorological droughts have increased by up to three times per decade over the last

sixty years while multi-year drought over the southwestern part of South Africa increased by a factor of three (Otto *et al.*, 2018).

Precipitation characteristics vary widely from area to area and its inter-annual variability is often difficult to predict with precise certainty. Generally, variability, and particularly inter-annual variability, is modulated by large scale climate forcings and changes in temperature. Multi-model predictions indicate that large parts of southern Africa may become drier or experience significant changes in MAP. Under emission scenario RCP8.5, the area under study is projected to experience a decrease of between 10% and 20% in MAP, together with an increase in consecutive dry days (Engelbrecht *et al.*, 2015; Spinoni *et al.*, 2019). According to the IPCC (2022) higher temperatures in South Africa's summer rainfall regions will exacerbate high levels of evaporation and increase drought frequency as well as severity. Under RCP8.5 meteorological drought duration is expected to increase from two months (1950-2014) to about four months within thirty years (Ukkola *et al.*, 2020). High intensity rainfall and extreme events are projected to increase, across all warming scenarios, within the Limpopo region (Li *et al.*, 2021; Seneviratne *et al.*, 2021).

2.2.1.1 Possible impacts of climate change on Tailings Storage Facilities

Climatic factors impact directly on the hydrological behaviour of tailings material. This includes both wet and dry conditions that bring about the upward movement of water through capillary rise during dry periods and loss due to evaporation, and infiltration of water during rainfall events. From sections 2.1, it was shown that TSFs are susceptible to structural weakening by insufficient control of water pressure leading to erosion, seepage, slope instability, liquefaction, overtopping and subsidence failure (Yaya *et al.*, 2017). The loss in structural integrity brought about by variations in environmental and climatic factors is further described by Roche *et al.* (2017) as occurring through (i) amplified contraction-expansion cycles caused by more extreme wet-dry periods during floods and droughts; (ii) high intensity rainfall events contributing more significantly to erosion and consequent instability of slopes; and (iii) potential mass movement of dams, i.e. landslides, as a result of higher rainfall intensity/frequency/duration.

Seeing as rainfall events of high intensity leads to excessive infiltration with a subsequent rise in tension saturated or near saturated conditions, it would have a significant impact on the structural integrity of engineered slopes, potentially causing slope failure or volume

deformation. Changing rainfall characteristics brought about by climate change could make certain areas in southern Africa especially vulnerable to the possibility of landslide activity. As previously mentioned, this potential hazard necessitates the re-evaluation of engineered slopes to determine physical processes and identify slopes at risk (Gariano and Guzzetti, 2016). This notion was also put forward by Karim *et al.* (2020) who found that climate change would result in the Newbury research site in England to experience longer periods of saturation/near saturation conditions and higher suction magnitudes during dry periods. It is also suggested that the increased magnitude and decreased frequency of the wetting-drying cycles, would cause accelerated stiffness/strength degradation, leading to more rapid failure.

Antecedent moisture conditions are established by preceding rainfall events, evaporation rates, transpiration and winds (Muñoz, 2019). Hillel (1998) suggested that extreme wetting and drying cycles in natural soil profiles may lead to the formation of surface cracks or even eventual discrete, vertical columns allowing surface water to penetrate the subsurface. Infiltration into cracks concentrates water into ‘finger-like’ protrusions, preventing the uniform one-dimensional distribution of the wetting front until the soil reswells and these voids coalesce. This may become particularly prominent as temperature increases lead to more evaporation combined with extended dry periods under the force of climate change. Even though it is suggested that this magnitude of wetting and drying would not be relevant to tailings dams (since these facilities are wetted by sources other than precipitation only), climatic conditions have a significant impact on the movement of subsurface water and the establishment of a continuous porewater phase. Apart from physical changes in TSFs brought about by climate change, chemical changes (although not included in this study) are brought about irregular rainfall patterns and increased temperatures. This can cause a spike in the rate of oxidation of metal sulphides, resulting in higher levels of acid mine drainage (AMD). Seeing as AMD is a hazardous substance, concentrated levels may exacerbate the risk associated with failure (Roche *et al.*, 2017).

2.2.2 Determining future climates

2.2.2.1 General Circulation Models and Regional Climate Models

According to Rebetz *et al.* (1997) General Circulation Models, also known as Global Climate Models (GCMs), are useful application in determining large-scale projections over hundreds or even thousands of square kilometres. GCMs are based on estimated natural and anthropogenic emission scenarios, taking variables such as global population growth and the

socio-economic system into account. Schulze *et al.* (2011b) pointed out that, even though GCMs successfully simulate first order atmospheric processes, they are less capable in simulating the intensity, duration and frequencies of individual or extreme rainfall events. These inherent uncertainties result in (i) discontinuity between the output from GCMs at spatial scale as opposed to regional scale and (ii) intermodal disagreement. GCMs must therefore be downscaled from coarse to local spatial resolutions (Schulze *et al.*, 2011b). Confidence in future climatic conditions predicted by GCMs depends not only on the number of models used, but also which ones were used. In order to derive accurate future rainfall scenarios within South Africa, the Climate Systems Analysis Group (CSAG) of the University of Cape Town, has assembled data from ten different statistically downscaled CMIP5 (Coupled Model Intercomparison Project Phase 5) GCMs. Statistical downscaling involved empirical functions and has the advantage of computational efficiency. Anomalies were calculated relative to the historical period 1980 – 2000. Based on the premise that these relationships are likely to remain consistent in future, it provides an indication of future scenarios (CSAG, 2020).

By using downscaling techniques, inputs from GCMs are converted to project local climate at regional scale, resulting in Regional Climate Models (RCMs). According to Buma (1998) statistical/empirical downscaling involves establishment of a quantitative relationship between large scale variables (atmospheric surface pressure) and a local variable (e.g., wind speed at a particular site). This relationship is used to obtain local variables from the GCM output. After climate scenarios have been downscaled from global to regional scale, it could be linked to conceptual slope hydrology/stability models and be applied to single slopes, regional landslide studies, individual landslides and small catchment areas to predict the potential of rainfall induced landslides in a specific area (Buma, 1998). This study has analysed data derived by these GCMs to construct trend graphs that will be discussed in Chapter 3.

2.2.2.2 Concentration scenario: Intergovernmental Panel on Climate (IPCC)

The IPCC's Fifth and Sixth Assessment Reports described GCMs as being based on different greenhouse gas (GHG) concentration scenarios and pathways. These scenarios and pathways are in turn based on emissions driven by variables such as population size, economic activity, lifestyle, energy use, land use patterns, technology and climate policy (IPCC, 2014). Representative Concentration Pathways (RCPs) describe four different temperature scenarios depending on how much greenhouse gases are emitted. More recently though, the IPCC (2022) adopted a greenhouse gas concentration trajectory for its sixth Assessment Report (AR6)

consisting of both RCP and Shared Socio-economic Pathways (SSPs) scenarios. This gave rise to an updated set of climate model projections that predict more intense future climate change conditions. Since SSPs cover a wider range of GHG and air pollutant futures than RCPs, they are not directly comparable. However, in principle, RCPs relate to the core set of AR6 scenarios (IPCC, 2022). Figure 2.13 (a) illustrates temperature increases based on SSP-scenarios ranging from very low GHG emission scenarios (SSP1-1.9), low (SSP1-2.6 or RCP2.6), intermediate (SSP2-4.5 or RCP4.5, high (SSP3-7.0) and very high (SSP5-8.5 or RCP8.5) (IPCC, 2022). These increases are similar to projections relevant to each RCP scenario - shown in Table 2.2. Figure 2.13 (b) indicates the level of risk associated with each of the five ‘Reasons for Concern’ (RFC) associated with increasing temperature trends. RFCs include (i) unique and threatened systems, (ii) extreme weather events, (iii) distribution of impacts, (iv) global aggregate impacts and (vi) large-scale singular events (IPCC, 2022). Based on these projections, increasing temperature trends bring with it high risk extreme weather events and hazardous conditions.

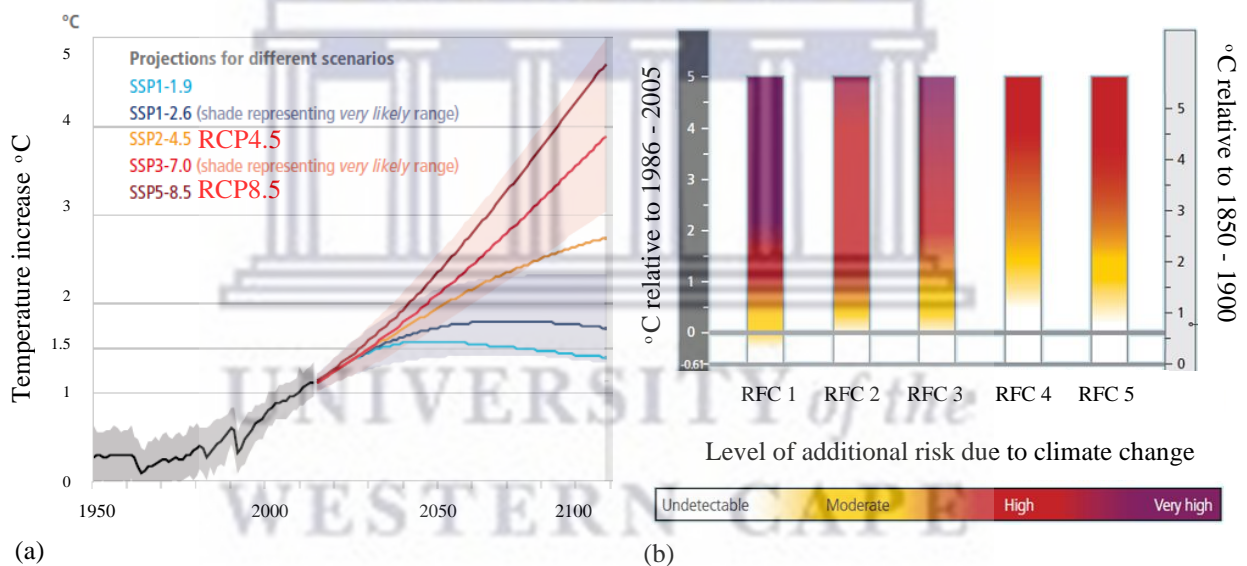


Figure 2.13 (a): Temperature increase based on SSP-scenarios (b): Risks associated with each Reason for Concern (RFC) at a global scale for increasing temperature scenarios (modified from IPCC, 2022).

Although emission scenario SSP5-8.5 (RCP8.5) is expected to result in an exacerbation of significant extreme events, all other possible future climate scenarios, also predict an increase in the frequency and severity of floods and droughts (IPCC, 2022). The likelihood of this scenario becoming a reality is probable seeing as global carbon emissions have risen to a new record level in 2018. The IPCC (2022) stated that this emission scenario would be distinct in

the southern Africa region, most likely resulting in significant temperature increases during the summer months and more intense and less frequent rainfall events. For the purpose of this study, and the availability of historical data, future climate change conditions for the study area has been analysed based on RCP8.5 and RCP4.5 projections. Further reasons for analysis of these scenarios are stated in Chapter 3.

Table 2.2: Projected change in global mean surface temperature for the mid- and late 21st century, relative to the 1986–2005 period (IPCC, 2014; IPCC, 2022).

Scenario	2046-2065		2081-2100			
	Mean	Likely range	Mean	Likely range		
Global Mean Surface Temperature change (°C)	RCP2.6	Stringent mitigation scenario	1.0	0.4 - 1.6	1.0	0.3 - 1.7
	RCP4.5	Intermediate scenarios	1.4	0.9 - 2.0	1.8	1.1 - 2.6
	RCP6.0	Intermediate scenarios	1.3	0.8 - 1.8	2.2	1.4 - 3.1
	RCP8.5	Very high GHG emissions	2.0	1.4 - 2.6	3.7	2.6 - 4.8

2.3 Characteristics of rainfall events during which failure occur

According to Sidle and Ochiai (2006) the most significant impact of climate change on landslides results from changes in regional annual and seasonal precipitation patterns. Another study conducted by Azam and Li (2010), suggested that even though the number of these failures were significantly higher in the 1960s, 70s and 80s, the number and frequency of recent disasters, caused by unusual weather, has increased. It was found that, globally, the failure of tailings dams due to unusual rain has increased from 25% pre-2000 to 40% after 2000 and accounts for the most detrimental factor leading to slope failure (Azam and Li, 2010). These findings were supported by Guang-jin *et al.* (2017) and Kristo *et al.* (2017) that identified extreme precipitation events to be one of the most important factors triggering tailings dam failures. Rico *et al.* (2008b) have also established that critical rainfall events have been the main cause of up to 3% of European tailings dam failures. Muñoz (2019) suggested that even though rainfall is not directly responsible for the occurrence of landslides, infiltration brings about changes in soil moisture dynamics, which lead to an increase in the driving forces acting on the sliding mass. Rodríguez *et al.* (2021) stated that the degree of saturation is the most significant factor controlling dam stability.

As previously mentioned, precipitation events are likely to become more unpredictable under the influence of climate change. This includes an increase in peak intensity leading to a greater proportion of the mean annual precipitation (MAP) being received in individual events. Pardeshi *et al.* (2013) listed the precipitation characteristics considered to evaluate slope stability to include: total rainfall volumes, peak intensity, event duration, cumulative rainfall and rainfall frequency. Even if MAP decreases, a distorted distribution of annual rainfall would result in flooding and significant changes to pore water pressure in slopes. Rainfall events of high intensity results in an increase in infiltration of wet mine waste with a subsequent rise in tension saturated or near saturated conditions. According to Abdul and Gillham (1984) rainfall intensity, along with surface slope and hydraulic conductivity, has a significant impact on the mobilisation of pre-event water, which could contribute to slope instability. This is supported by Rahardjo *et al.* (2016) who argue that rainfall infiltration causes slope instability by increasing porewater pressure which leads to a decrease in the shear strength of residual soils.

Further research studies found that high rainfall intensity events have a direct impact on the rate of GWR and the subsequent rise in the water table (Guo *et al.*, 2008). In contrast, Elsenbeer *et al.* (1995) made use of tracers at a streamflow and overland flow site and conducted sampling during two precipitation events of different intensities. It was found that during a rainfall event of extremely high intensity (177.7 mm), event water itself dominated the hydrograph. Pre-event subsurface sources were found to contribute to the rising limb of the storm hydrograph more significantly under lower intensity events (44.2 mm) of shorter duration. Khan *et al.* (2012) suggested the possibility that, even though extreme events trigger landslides, preceding rainfall conditions are responsible for establishing critical stability conditions in hillslope materials. A rainfall event of specific intensity and duration combined with particular antecedent moisture conditions is therefore necessary for failure to occur. The critical event is characterised by a spike in intensity that could eventually contribute to triggering slope instability (Figure 2.14). However, Ng and Shi (1998) warned against the use of a single threshold rainfall intensity as an indicator of landslide risk since slope stability would depend on not only rainfall intensity, but also initial pore pressure distribution.

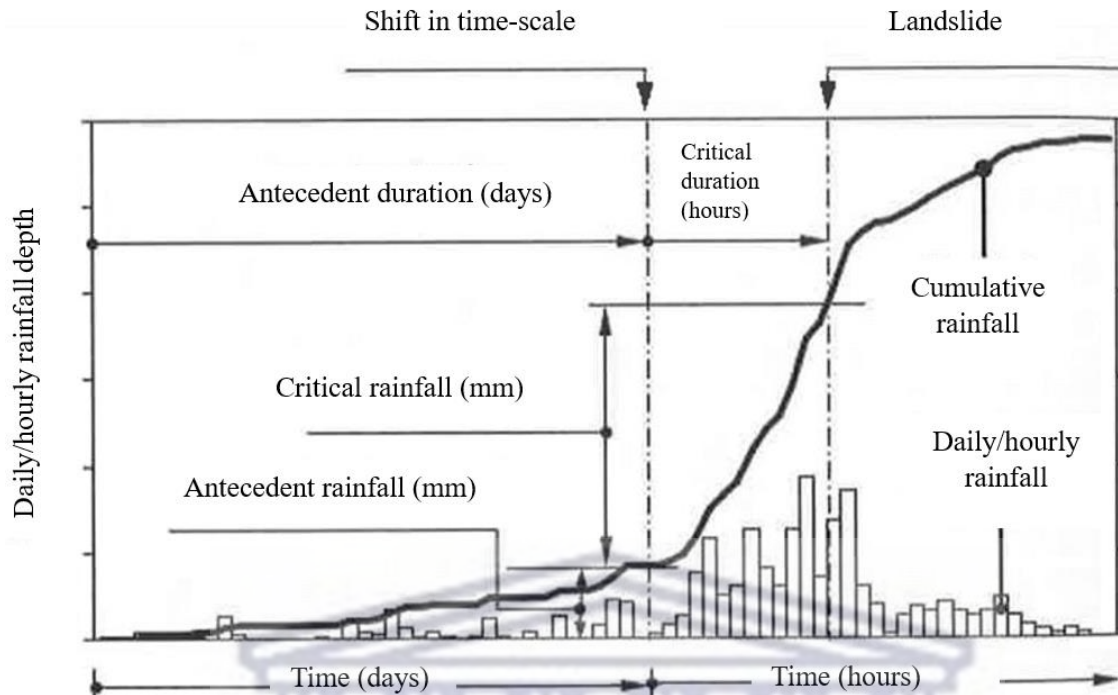


Figure 2.14: Antecedent and critical rainfall parameters (modified after Aleotti, 2004 in Waswa and Lorentz, 2016a).

Cloke *et al.* (2006) argued that rainfall intensity is only relevant when the capillary fringe does not extend to the ground surface and K_s is high enough to have rainfall-limited infiltration. Similarly, Zandarín *et al.* (2009) found that a high intensity rainfall event is not necessarily detrimental to dam safety, but rather lower intensity events that have a longer duration, resulting in more infiltration. Furthermore, events found to have a higher intensity towards the end of the event, than at the start, result in a far more destabilising effect than events with constant intensity. It is recognised that rainfall events associated with shallow landslides have been found to trigger these failures after a spike in intensity during the middle or towards the end of the critical event (Waswa and Lorentz, 2016a). Even though this study acknowledges that high intensity events are not necessarily the cause of landslides, it is suggested that it has an adverse effect on slope stability when combined with pre-event water.

The frequency of rainfall events impacts on antecedent moisture conditions which, in conjunction with a critical event, are known to trigger shallow landslides by the formation of a tension saturated or near-saturated porous medium (Aleotti, 2004). While freely drained soils reach near saturated conditions when exposed to extreme rainfall events, soils that exhibit characteristics such as low hydraulic conductivity, i.e. tailings, are more prone to saturated conditions when combined with significant antecedent rainfall (Rahardjo *et al.*, 2008). Soil

moisture, combined with a critical rainfall event of a particular intensity, could form a continuous pore water phase, thereby increasing pore water pressure and enabling the transmission of an induced pressure head (Marui *et al.*, 1993). The significance of pre-event water in slope stability is supported by a study conducted into the causes of twenty shallow landslides on the Nanyang Technological University Campus. An investigation into similar critical rainfall events, not leading to landslides, showed similar characteristics. However, the triggering rainfall event during which slope failure occurred, was found to be preceded by several non-critical rainfall events resulting in elevated levels of antecedent moisture conditions (Rahardjo *et al.*, 2001). Since rainfall events are becoming increasingly unpredictable under the force of climate change, it is likely to impact on rainfall frequency and potentially establish antecedent moisture conditions ideal for failure to occur.

According to Zandarín *et al.* (2009) infiltration of rainfall may cause an instant rise in the phreatic surface, but phreatic drawdown is delayed through the process of capillary action, particularly when combined with the low hydraulic conductivity of tailings. Blight *et al.* (2012) estimates the hydraulic conductivity of tailings porous medium between 2 – 3 m/a while López-Acosta (2016) found an average value of only 0,5 m/a. Low hydraulic conductivity therefore causes drainage from antecedent events to be delayed and the degree of saturation to stay high throughout the whole profile (Zandarín *et al.*, 2009). Supporting this concept is the model results of an extreme rainfall event measured at the Pedro Sotto Alba nickel mine, located in the southeast of Cuba. During this storm, 722 mm rainfall was measured in 48 hours, with a peak of 140 mm in 90 minutes (Zandarín *et al.*, 2009).

Figure 2.15 indicate the position of the phreatic surface and associated pore water pressure regime at different pond depths. It further illustrates widening and narrowing of the tailings beach, while still maintaining high levels of saturation. Additionally, phreatic water intersects the slope face of the dam at different heights above the base. Zandarín *et al.* (2009) established that the highest position of the phreatic surface occurs between the end of the preceding rainfall event and up to 11 days later. This point in time marks a critical condition for stability. Closely repeated rainfall events of lower intensities could therefore cause saturated or near saturated conditions of tailings and subsequent discharge of pre-event water. Zang *et al.* (2018) also reports that pre-event water, contained above the phreatic surface in the capillary fringe, plays an integral part in mobilising groundwater.

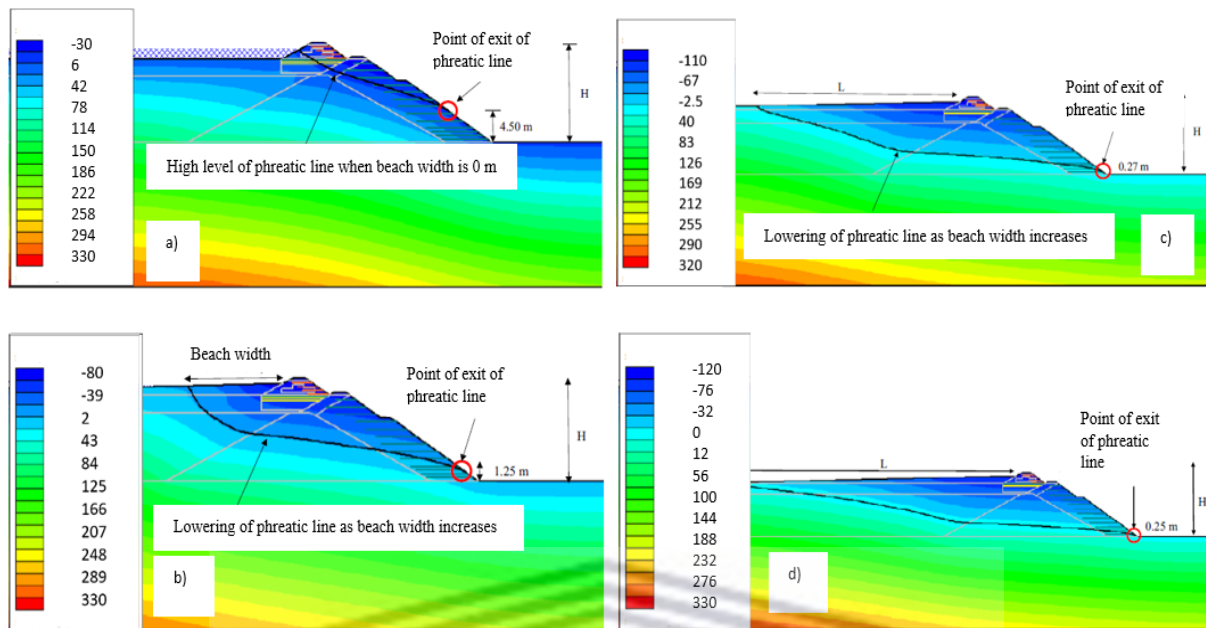


Figure 2.15: Phreatic line and associated pore water pressure regime observed in a tailings pond built by the upstream method (Singh *et al.*, 2023).

2.3.1 Pre-event water in the stream stormflow hydrograph

Kim *et al.* (2017) observed the presence of baseflow water in the stream stormflow hydrograph through hydrograph separation studies and the use of stable isotope tracers. Apart from rainwater, pre-event water in TSFs is supplemented by additional sources that contribute to saturation rates. This includes the vast quantities of wet slurry that is discarded and stored together with tailings; rising consolidation water and the absence of phreatophytes (Blight *et al.*, 2012; Meyboom, 1967). The low hydraulic conductivity of tailings also makes it more susceptible to the formation of tension saturated or near-saturated conditions when combined with pre-event water, thereby enabling the transmission of an induced pressure head to a potential failure plane (Katsura *et al.*, 2014). These pre-event conditions and tailings characteristics may contribute significantly to the rate of failure of tailings dams.

High rainfall intensity events lead to excessive infiltration while pre-event water present in the subsurface soil horizon during a critical event, is generated by infiltration of previous precipitation events, and augmented by rainfall frequency (Guo *et al.*, 2008; Rahardjo *et al.*, 2001). Studies conducted in natural hillslopes, found both these event characteristics to contribute significantly to tension saturated or near saturated conditions and have an impact on physical and hydrological processes that regulate structural integrity of earth embankments. Based on the concept of subsurface flow, Lorentz *et al.* (2004) found that water in natural

hillslopes contained within the near-surface macropore layers, contribute far more to the streamflow than groundwater.

Hallema *et al.* (2016) stated that surface response during a rainfall event is affected by hydrological processes brought about by climatic systems (e.g., precipitation, evaporation) that interact with soil conditions and characteristics (e.g. infiltration, runoff, porosity, hydraulic interconnectivity). Rainfall intensity is believed to impact on the rapid rise of the phreatic zone if (i) the capillary fringe extends to the ground surface, resulting in increased hydraulic gradients in the groundwater zone and eventual discharge to the stream or (ii) through the generation of free surface conditions at the ground surface, resulting in overland flow (Abdul and Gillham, 1984). According to Hallema *et al.* (2016) the soil surface divides rainfall water into an infiltration component, restricted by the soil's infiltration capacity, as well as a surface runoff component. The latter, also known as Hortonian overland flow (HOF), commences when the rainfall rate exceeds infiltration rate and the resulting infiltration excess flows off along the soil surface. During high intensity rainfall events, infiltration capacity controls overland flow while slope, interconnected pore spaces and channel network define structural hydraulic connectivity that determines how rapidly excess water is transferred. HOF is therefore surface controlled and occurs under unsaturated conditions, which are often the case during prolonged dry spells. However, a soil profile experiencing a critical event, and already saturated by pre-event water from a preceding low intensity rainfall event, will result in saturation overland flow (SOF). This would constitute soil/profile-controlled infiltration and would be dependent on water content and profile characteristics (Hallema *et al.*, 2016). Subsurface stormflow would have a slower response time than surface run-off seeing as the residence time of water at the surface is shorter than the residence time of water in the soil. Waswa (2013) confirmed that antecedent moisture conditions determine the dynamic interaction between rainfall intensity and saturated zones, contributing significantly to the stream stormflow hydrograph. In order to understand the presence of antecedent water in the hydrograph, it is necessary to comprehend the response of the phreatic water table during an event, which this study intends to investigate.

2.4 Fundamental principles related to porous medium conditions

Figure 2.16 illustrates various hydrological processes that have an impact on hydraulic boundary conditions in a typical TSF. These dams are constructed by the discharge of slurry, typically retaining a solid to liquid ratio of 1:3, which impacts significantly on the hydraulic

operation of the tailings dam. According to Zandarín *et al.* (2009) water segregates from the slurry after deposition, either infiltrating previously deposited tailings or running off to collect in the decant pond. The ratio between run-off and infiltration are impacted by several factors including rate and duration of discharge, antecedent moisture conditions, saturation rate and the location of the phreatic surface. Seeing as deposits are discharged through, for example, cycloning/spigotting from the perimeter of the tailings dam, a downward slope is formed towards the decant pond. Although this slope usually forms at less than 1%, it has little influence on the location of the phreatic surface. According to Bhanbhro (2014) this area, known as the tailings beach, facilitates the natural sorting of particle sizes. Heavier particles settle out shortly after discharge, which ensures higher hydraulic conductivity in the area near stability walls which helps reduce the water table level and thus pore water pressure (Zandarín *et al.*, 2009). Kossoff *et al.* (2014) referred to this as size-differentiated dispersal that helps preserve the integrity of the dam by placing the coarse, more porous material in the structure itself. The finest fraction is deposited near the decant pond where it settles under a water layer of variable depth (Rodríguez *et al.* 2021). According to Eriksson and Destouni (1997) in Fala *et al.* (2005), grain diameters of tailings can vary by over 6 orders of magnitude (between 1 µm and 1 m), depending on grinding specifications.

The geotechnical/geohydrological properties of tailings, that regulate physical behaviour, is greatly determined by flotation processes for metal extraction. Since target grinding specifications often include ultra-fine grinding technology to improve economic benefits, average values often range between 0.2 – 0.02 mm (Rodríguez *et al.*, 2021). According to Yang *et al.* (2015) these ultra-fine saturated soils of low hydraulic conductivity exhibit pore air pressure diffusion waves of slow velocities and short wavelengths. This study will however attempt to demonstrate that these could be much faster than ordinary unsaturated or saturated flow conditions.

Tailings are discharged at alternative points in order to control the location of the decant pond as well as the level of tailings. The high degree of saturation caused by the constant discharge of slurry water is further exacerbated by the infiltration of rainwater as well as soil suction and capillary rise during dry periods (Zandarín *et al.*, 2009). Guo *et al.* (2008) also suggested that fluctuations in the phreatic surface brings about the induction of sub-surface airflow, leading to groundwater movement. During rapid loading, as in the case of saturated soil conditions under high intensity events, drainage from soil pores becomes restricted, resulting in an

increase in pore water pressure. Continued soil saturation eventually reduces effective stresses, surface tension and shear resistance. Under these undrained conditions, shear failure is likely to occur due to frictional losses as well as the additional water weight being held in the soil slope. Figure 2.16 illustrates the hydrological processes impacting on hydraulic boundary conditions.

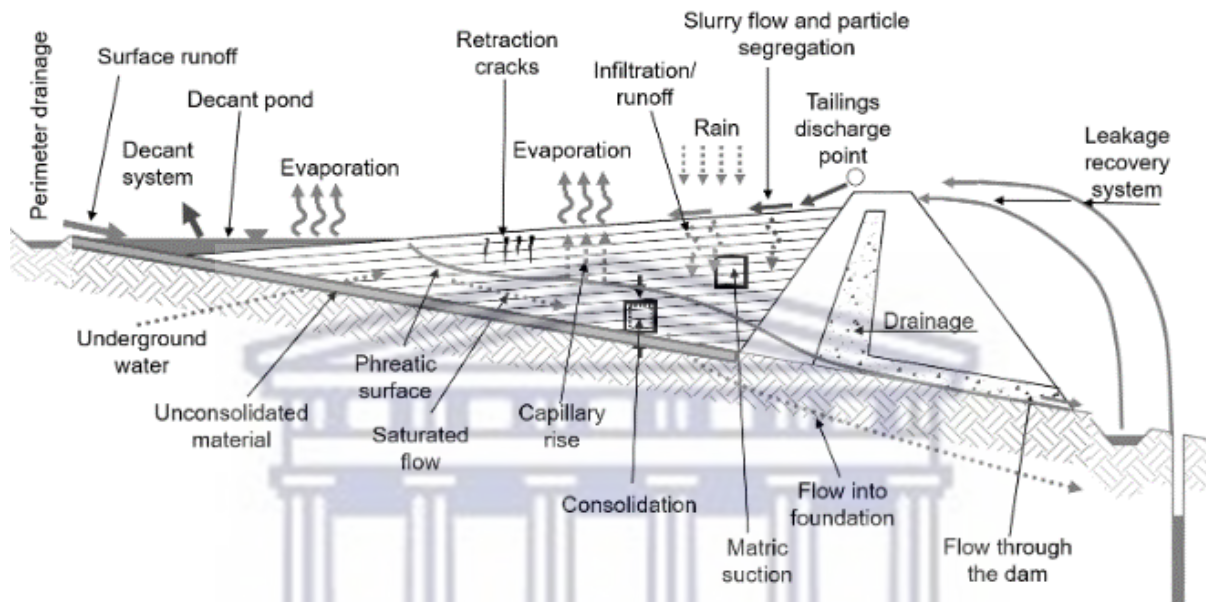


Figure 2.16: Schematic illustration of factors affecting hydraulic response and operational characteristics of a tailings dam (Pacheco, 2018).

Climatic conditions and environmental fluctuations have a significant impact on the moisture content of tailings. This interactive relationship is mainly controlled by rainfall as input and evaporation as output (Muñoz, 2019). The reduction of soil moisture during inter-storm periods is determined by considering historical wetting and drying processes (Muñoz, 2019). Zandarin *et al.* (2008) described these processes as infiltration-evaporation boundary conditions, which impacts on the hydraulic response of the deposit to extraordinary rainfall events. Through the process of constant infiltration and evaporation, soil is repeatedly subjected to wetting and drying cycles. The rate and amount of rainfall to infiltrate the tailings would depend on rainfall intensity, duration and frequency; surface conditions and unsaturated hydraulic conductivity. Another contributing factor would include the degree to which pre-event water is held in the profile. According to Zandarin *et al.* (2009), this is controlled by the height of the phreatic surface, capillary rise and rate of evaporation.

2.4.1 The geotechnical stability of tailings dams

In a study conducted by Muñoz (2019) rainfall parameters of up to forty days before a landslide on a natural hillslope were analysed. Other factors such as soil properties, vegetation and climate were also considered. It was concluded that a threshold factor of safety may be reached with varying precipitation characteristics. The factor of safety of tailings embankments are closely related to soil moisture and the location of the phreatic surface. According to Morton (2020) slope failure will most likely occur due to compression of water in the pores of the tailings porous medium, followed by compression and rearrangement of individual sediments. A further review of historical tailings dam failures indicated that most often, water has been the incipient factor that propagated failure. According to Liu *et al.* (2018) approximately 30-40% of failures in tailings dams are caused by two-dimensional seepage, leading to a rise in the phreatic surface. Flow consisting of both vertical and horizontal velocity components result in two sets of orthogonal curves consisting of equipotential (Φ) and flow lines (Ψ). The graphical construction of these curves forms a flow net, which may be used in the determination of seepage quantities and pressures by solving for Darcy's law (Whitlow, 2001). Johansson (2014) suggests that transient water flow affects pore-pressure conditions, strength, and deformation behaviour of soil.

It is believed that as the decant pond approaches the stability walls, the width of the beach as well as freeboard is reduced, leading to an increased probability of slope instability and shear failure. Pacheco (2018) found this occurrence to be particularly detrimental to the stability of upstream embankments. This study will attempt to challenge this particular view and investigate the possible contribution to slope instability through GWR and the LE by the propagation of pore air pressure on the porous medium.

2.5 Rapid mobilization of pre-event water

The movement of pre-event water within tailings could be brought about by the mechanism of induced pressure head. Waswa and Lorentz (2016a) argued that both a critical rainfall event and previous rainfall events contribute significantly to the establishment of the tension saturated continuous pore water phase, which enables rapid transmission of the induced pressure head to a potential failure plane. This study intends to demonstrate pressure diffusion mechanisms throughout the porous medium to accurately predict transient air pressure waves responsible for GWR and the LE which could have adverse impacts on the stability of the tailings dam structure.

2.5.1 Transient Pressure Wave Mechanisms

Whitham (1974) described a pressure wave as any clearly recognisable change within a pressurized system, resulting in a signal transfer within the specific medium. Even though the signal may become distorted, it is still recognised by a dynamic change in the magnitude and/or velocity of pressure. For the purpose of this study, reference to transient pressure waves include both air and water pressure, unless specified differently. This thesis also adopted the notion that pore air pressure waves descend downwards.

Waswa and Lorentz (2015) stated that transient pressure waves are responsible for the rapid release and mobilisation of previously stagnant antecedent moisture through the mechanisms of GWR and the LE. This enables groundwater levels, during storm events, to rise in disproportion with the amount of water infiltrating the soil profile and faster than predicted under Darcy's law. Cloke *et al.* (2006) suggested that the fine nature of tailings would contribute to exacerbated capillary fringe levels, establishing a continuous pore water phase and enhancing conditions facilitating the rapid mobilisation of pre-event water. Many researchers e.g., Rahardjo *et al.* (2004), Lins *et al.* (2009) and Salas-García *et al.* (2017) have investigated the occurrence of pore air propagation and transient pressure wave generation in unsaturated porous medium. These studies made use of tall soil columns fitted with instrumentation such as Time Domain Reflectometry (TDR), tensiometers and automatic data loggers, and were successful in demonstrating the water table response to a high intensity rainfall event. Waswa *et al.* (2013) also installed pore air pressure probes into a soil column and were able to observe differentiating pore air responses depending on the depth of the water table. It was also instrumental in identifying GWR to occur in a shallow water table, while the LE was observed in deeper groundwater sources. Rassam and Williams (2000) predicted SWCC in tailings with the use of a tall soil column fitted with two tensiometers and one TDR sensor, but only drainage cycle analysis had been carried out. Further soil columns studies were presented by Yang *et al.* (2004). The apparatus was equipped with TDR and tensiometer sensors placed at specific depths to measure water content and pore-water pressure. However, only water content and suction data were analysed. Findings of these studies will be discussed below.

2.5.1.1 Groundwater Ridging

The GWR hypothesis is described by Abdul and Gillham (1984) as a process occurring near the stream (and in this case near the tailings pond), that allows for the rapid rise of the water table to the surface. This rise occurs due to the conversion of capillary water held in tension in the unsaturated zone to phreatic water in the saturated zone.

The GWR mechanism consists of three main components consisting of rapid water table rise adjacent to the stream, rapid mobilization of pre-event water to the stream and eventual dominance of HOF. Figure 2.17 illustrates the mechanism of GWR, recognised by the rapid, uneven rise in the phreatic surface near the pond shortly after a high intensity event. According to Waswa and Lorentz (2015) the extension of the capillary fringe is a prerequisite for this mechanism to occur. This notion was supported by Zang *et al.* (2018) that found pre-event water, contained above the phreatic surface in the capillary fringe, to play an integral part in the GWR mechanism. It also allows for a continuous water phase, enabling rapid transmission to lower horizons (Waswa, 2013). This concept was reiterated by Turner and Nielsen (1997) after conducting GWR studies on beaches. Results found the rapid and exaggerated water table rise to be attributed to the upper extent of the capillary fringe to correspond with the sand surface. It was further determined that this rise was brought about by an insignificant amount of water applied to the surface (Abdul and Gillham, 1984).

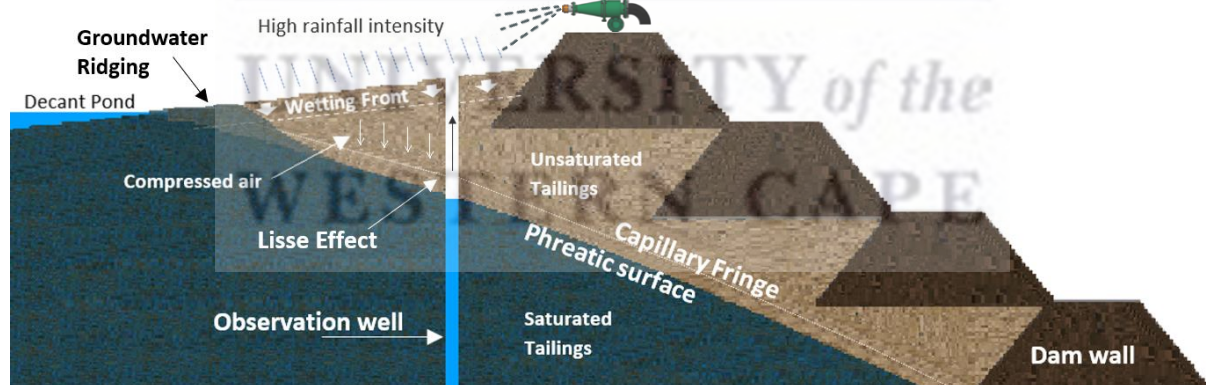


Figure 2.17: Schematic depiction of GWR and the LE.

Gilham (1984) and Abdul and Gillham (1984) argued that the rapid conversion of water held in the capillary zone occurs due to the fill-meniscus hypotheses, whereby the addition of small amounts of rainwater brings about a change in matric suction. This change relieves tension in the tension saturated capillary zone, resulting in vadose water converting to phreatic water with a subsequent rise in the water table. De Rooij (2010) postulated that a large change in potential

energy caused by the addition of small quantities of water is brought about by the volume of water experiencing the change in pressure potential and not so much by the amount of water added. More recently though, Waswa and Lorentz (2016a) proposed the energy hypothesis whereby the intensity of a rainfall event provides additional energy that transforms kinetic energy to potential energy, causing the conversion of vadose zone water to phreatic zone water. The extension of the capillary fringe provides the contact between the kinetic-energy-carrying intense raindrops and the potential-energy-deficient porewater. Moisture profiles involved with the process of GWR are illustrated in Figure 2.18.

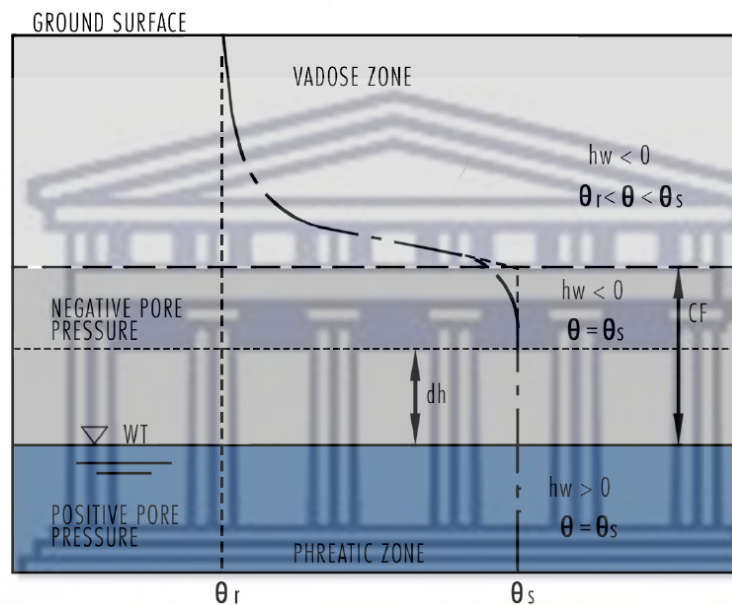


Figure 2.18: Moisture profiles under GWR: h_w - pore water pressure, θ_r - residual soil water content, θ_s - saturated soil water content (modified from Waswa, 2013 and Miyazaki *et al.* 2012).

Zang *et al.* (2018) also described the process of increasing pore air pressure below the wetting front, brought about by the unchangeable capillary pressure, which converts negative pore water pressure to positive pore water pressure. The addition of rainwater relieves the tension in the tension saturated capillary zone that converts vadose water to phreatic water and a rise in the water table. The only difference between the capillary fringe and phreatic zone would therefore be the energy content (Waswa and Lorentz, 2019). According to Zang *et al.* (2018) this increase is not dependent on the amount of rainwater infiltrating the soil during the high intensity event, but rather on the amount of pre-event water already held in the capillary zone. The rise in the water table is therefore disproportionate to the amount of infiltrated water. This

argument is supported by Cloke *et al.* (2006), who stated that even a small amount of infiltrated water can rapidly convert the negative capillary pressure head in the capillary fringe to a positive pressure head, thereby changing the water table gradient and forcing the pre-event water out.

Waswa and Lorentz (2016b) found that, seeing as an insignificant amount of rainfall is required to fill the capillary menisci in the capillary fringe, it would result in an almost immediate and excessive rise in the water table during an event. During this process, the steep hydraulic gradient is directed towards the stream and leads to the discharge of antecedent water into the stream (Zang *et al.*, 2018). It should however be mentioned that as rain intensity decreases, so does pore air pressure in the vadose zone with a subsequent reduction in induced air flow and groundwater ridging (Zang *et al.*, 2018). Abdul *et al.* (1984) suggested that seeing as capillary fringe GWR is entirely dependent on rainfall intensity, the surface slope and the hydraulic conductivity of the soil, it will not be responsible for pre-event water discharge in all environments. Previous studies note the complex interrelationship between riparian characteristics and GWR. Cloke *et al.* (2006) for instance found no evidence of ridge development in cases of low capillary rise and low water tables. The initial water table is therefore a strong indication of the zone of pre-event water proportions (PEZs) reached before the occurrence of a rainfall event. Rainfall intensity was found to control initial ridge development, especially if the capillary fringe did not reach the ground surface and hydraulic conductivity is high enough to allow for rainfall-limited infiltration (Waswa and Lorentz, 2019). However, according to Zang *et al.* (2018) the capillary fringe is only an influence factor, and not a controlling factor in the generation of GWR. The magnitude of GWR would be dependent on rainfall intensity, but it was further found that in order for rapid GWR to occur through antecedent moisture contribution from the capillary zone, a continuous water phase extending from the natural ground surface to the phreatic surface is required (Waswa and Lorentz, 2019). According to Cloke *et al.* (2006) the development of a positive ridge to also be dependent on soil type. Fine grained soils were found to encourage ridging by more readily allowing for the extension of the capillary zone to the ground surface while coarse grained soils allowed for increased infiltration capacities. Seeing as pore size, and inversely particle size of the soil media, will determine the height of the capillary fringe above the water table, the fine nature of tailings would contribute to higher rising water levels in the capillary zone. The rapid increase in the phreatic surface is met with an equally instant decline due to evaporation from

an emerging capillary fringe with a reduced curvature in menisci. This decrease is believed to continue until maximum negative capillary head has been established (Meyboom, 1967).

Previous soil column studies confirmed that a small amount of surface recharge could result in an instant disproportionate rise of the water table, simulating GWR responses. Khaled *et al.* (2011) carried out comparable tests on Toyoura sand and Chiba light clay soils that were packed homogeneously into two acrylic columns with 50 cm length and 7,5 cm ID. The initial Volumetric Water Content for the Toyoura sand was measured at 0,05 cm³.cm³ and the Chiba light clay at 0,4 cm³.cm³. After the addition of only 1 mm surface recharge, an instant fluctuation in the phreatic surface occurred, measuring a 50 mm rise within 10 seconds and a total rise of 120 mm. This upsurge was attributed to the rapid conversion of pressure head in the vadose zone. A similar field experiment, conducted by Gillham (1984), found a significant rise of 300 mm in a shallow water table, resulting from the addition of 30 mm of water. Results, confirmed by Waswa (2013), indicated a significant increase in pressure potential at the initial water table brought on by the advancing wetting front. It was further established that the rate of increase was directly related to the thickness of the capillary fringe and therefore proportional to, but less than, the magnitude of compressed pore air pressure. The rate of change in pressure potential also varied between grain size of soils. In fact, pressure potential in fine soils measured 15 cm-H₂O (1,471 kPa) less than in coarse soils within 10 minutes after application of a simulated rainfall event. The response in pressure potential also seems to be delayed in fine soils, such as tailing porous medium, which appears to be linked to the height of the capillary fringe (Cloke *et al.*, 2006).

2.5.1.2 Lisse Effect

Miyazaki *et al.* (2012) describes another mechanism of similar magnitude to GWR, but of different origin [a comparative summary listed in Table 2.3], that leads to the mobilisation of pre-event water through transient pressure waves. The LE, illustrated together with GWR in Figure 2.17, occurs due to the build-up of air pressure between the wetting front and the phreatic surface and is recognized by a disproportionate rise in a nearby observation well (Guo *et al.*, 2008). This effect is probable if pore air is present in the unsaturated vadose zone above the upper boundary of the capillary fringe and the phreatic surface is located at a sufficient depth below ground level.

Table 2.3: Comparison summary between the LE and GWR (adapted from Miyazaki *et al.*, 2012).

Lisse Effect	Groundwater Ridging
Depth to capillary fringe is less than to the water table.	The capillary fringe extends from the water table to almost to the natural ground surface.
Rapid rise in the well but slow recession.	Sharp rise in water table followed by correspondingly sharp decline.
Occurs during high intensity rainfall events.	Brought about by differentiating intensity rainfall events.
Water level in the observation well rises to compensate for the pressure increase in pore water below the water table caused by compressed pore air pressure above the water table.	Water table frequently rises to natural ground level.
Even though the actual water table level is not affected, the rise is significant in the well tapping the phreatic surface.	Affects both the water table level as well as the well tapping the phreatic surface.

Meyboom (1967) and Guo *et al.* (2008) described the downward moving wetting front, produced by the infiltration of a rainfall event, to act as a low permeability lid that restricts the outflow of air. Fayer and Hillel (1986) measured the quantity and persistence of encapsulated air in a field setting. After the application of artificial rainfall to the soil surface, soil moisture contents were monitored with a probe. Differences in porosity and the measured moisture contents were attributed to entrapped air pockets. Results indicated that encapsulated air was an important component in the occurrence of fluctuations in the shallow water table. The porous medium is expected to contain approximately 3 - 8% entrapped air according to Kutilek *et al.* (2007), while Fayer and Hillel (1986) found this value to be closer to 1.1 to 6.3% of the bulk soil volume, depending on the rate of sprinkling, soil depth, and initial soil moisture content. Fredlund *et al.* (2012) refuted this claim and argued that soil air content could be as much as 15% air by volume. Fayer and Hillel (1986) suggested that some entrapped air will escape vertically upwards and some will remain in the soil profile, reducing saturation moisture content. However, the momentary increase in saturated zone pressure may be sufficient to induce slope instabilities.

Weeks (2005) explained that, after application of rainfall to the ground surface, pressure is transmitted rapidly to the top of the capillary fringe and continues to build up until entrapped air pressure is higher than the pressure head of the infiltration profile above. Cloke *et al.* (2006) postulated that the increase in pore air pressure is accompanied by the induction of downward transient air pressure waves. In response, the increase in pore water pressure establishes a

continuous water phase in the capillary fringe, enabling the rapid transmission of antecedent water, and eventual rise of the water level in an observation well. Meyboom (1967) also found that the water level rise in an observation well (see Figure 2.17 for schematic description) to commence before actual recharge due to rainwater percolation. Instead, the water level increase was found to be driven by airflow induced by an advancing wetting front at approximately 0.6 - 1.0 m below ground surface. Figure 2.19 illustrates the LE whereby a rapid rise in water level in a well is observed during an event but holds little relationship to the water infiltrating the unsaturated soil profile (Bianchi and Haskell, 1966).

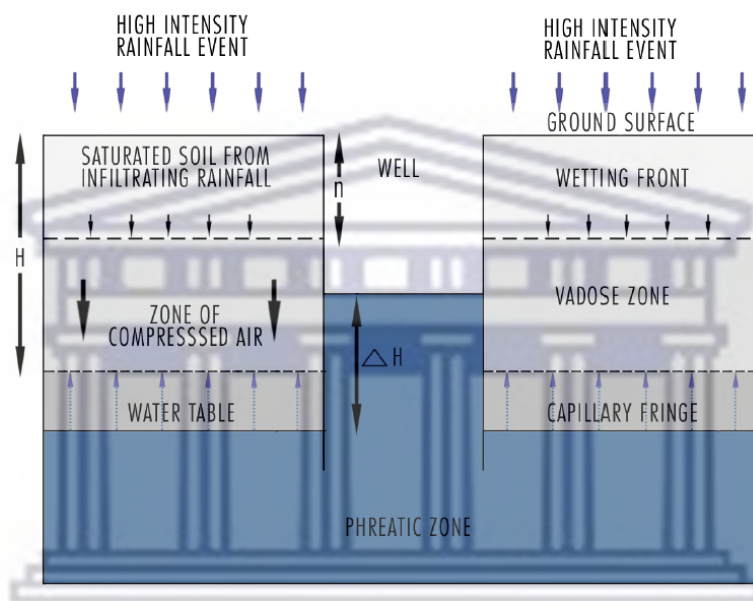


Figure 2.19: The conditions of the Lisse effect occurrence. n : depth of infiltrated water following an intense rain; ΔH : water level rise in the observation well resulting from sharp wetting front during intense rain trapping air and increasing soil air pressure; h : distance from the ground surface to the upper boundary of the capillary fringe (modified from Miyazaki *et al.*, 2012; Weeks, 2005; Meyboom, 1967).

It should be mentioned that Meyboom (1967) found the water level rise in the well to be delayed relative to the rise in air-pressure in the unsaturated zone. The ratio of rainfall to the rise in the water level was about 1:18. An earlier study by Hooghoudt (1947) found similar results and found a rainfall/rise ratio of 1:20 after solving for air pressure increase above the capillary fringe. Application of this calculation (equation [2.1]) presented a rise in the observation well of 533,4 mm after a rainfall event of 25,5 mm, infiltrating the soil profile to a depth of 25,5 mm and the capillary fringe at 508 mm below ground surface.

$$H_{\max} - H = \frac{n}{h - n} atm \quad [2.1]$$

Where $(H_{\max} - H)$ is the change in water level in the observation well, n is the depth of infiltrated water after a rainfall event and h distance from the ground surface to the upper boundary of the capillary fringe. Other researchers, e.g. Guo *et al.* (2008), found the maximum water level rise in the well would be less than the maximum air pressure induced by infiltration. This phenomena is described by equation [2.2] below (Weeks, 2005).

$$\Delta H = P_{WC} \left(\frac{m}{h - m} \right) \quad [2.2]$$

Where P_{WC} is atmospheric pressure in form of water column height, m is depth of rain penetration and h is the distance from the natural ground level. Seeing as the entrapped air causes a decrease in the magnitude of the vertical hydraulic gradient which restricts infiltration at ground surface, it will also contribute to higher levels of runoff. This explains why light rainfall events often demonstrate a disproportionate increase in run-off. Entrapped air may not only give the false impression of recharge, it may also reduce the amount of recharge that would be expected in its absence (Healy *et al.*, 2002).

Parametric studies suggest the likely response of the water level to: (i) geotechnical properties, including pore size distribution (λ) and hydraulic conductivity (k). Porous medium conditions demonstrate intrinsic hydraulic conductivity parameters that play a pivotal role in generating both GWR and the LE. Soil formations of low hydraulic conductivity inhibit the rate of infiltration, subsequently causing a delay in air-pressure response. In contrast, a soil with high hydraulic conductivity results in significant air pressure, but the response in the observation well will be diminished when compared to a less permeable soil profile. For instance, hydraulic conductivity of 400 mm/h (and permeability of $1 \times 10^{-11} \text{ m}^2$) demonstrated a maximum water level rise of 0,14 m compared to only 0,08 m for soil with a permeability of $1 \times 10^{-13} \text{ m}^2$ (Guo *et al.*, 2008). In contrast, higher levels of hydraulic conductivity do not guarantee maximum water levels in the observation well. This is due to high hydraulic conductivity that does not allow for ponding, resulting in the release of air from the ground surface. The magnitude of the LE is therefore insignificant in highly permeable soils and increases as hydraulic conductivity decreases. In short, an increase in hydraulic conductivity results in a more significant observation of the LE, however, if soil is highly permeable, the LE is eliminated seeing as air can freely escape through the descending wetting front (Guo *et al.*, 2008). Another soil property

impacting significantly on transient pressure waves is pore size distribution, which is directly related to soil uniformity. Seeing as high pore size distribution denotes a narrow range of particles and pore sizes, it would encourage higher levels of air pressure in the unsaturated zone and increasing water levels in the wells (Guo *et al.*, 2008); (ii) surface ponding depth. Results from simulation studies compiled by Guo *et al.* (2008), indicate that, during a high intensity rainfall event, the infiltration capacity of the tailings porous medium could be exceeded and cause ponding. Strachan and Van (2018) notes that the control of ponding and saturated conditions is necessary to reduce the risk of overtopping, seepage and piping. Their study did not consider ponding to cause increases in the water level of an observation well. Fredlund and Stianson (2011) observed an increasing ponding depth to inhibit the escape of air from the soil, which also contributes to higher compression values in the unsaturated zone, thereby intensifying the extent of the LE. Figure 2.20 (a) demonstrates the effect of a 2 cm, 6 cm and 10 cm ponding depth on the water level and air pressure (Guo *et al.*, 2008). Fayer and Hillel (1986) also noted the impact of ponding on encapsulated air contents within the soil profile after the application of artificial rainfall events in a field setup. After entrapped air persisted at 300 mm below surface for up to 28 days. The results indicate that encapsulated air is an important component of shallow water table fluctuations; (iii) air entry pressure h_b (bubbling pressure) of soil describes the pressure head (or suction value) at which air begins to enter the previously saturated soil and displaces the water contained in soil pores. It is also the pressure at which confined air would escape. In order for air to escape, air pressure must exceed air entry pressure (Guo *et al.*, 2008). Figure 2.20 (b) shows the significant effect of different air pressure values on the response magnitude of the water level in the observation well. A simulation study conducted by Guo *et al.* (2008) studied the sensitivity of the LE to the van Genuchten parameters which included air entry pressure. It was found that both the air entry value (AEV) and the depth of the capillary fringe, increased with an increase in air pressure; and (iv) rainfall intensity.

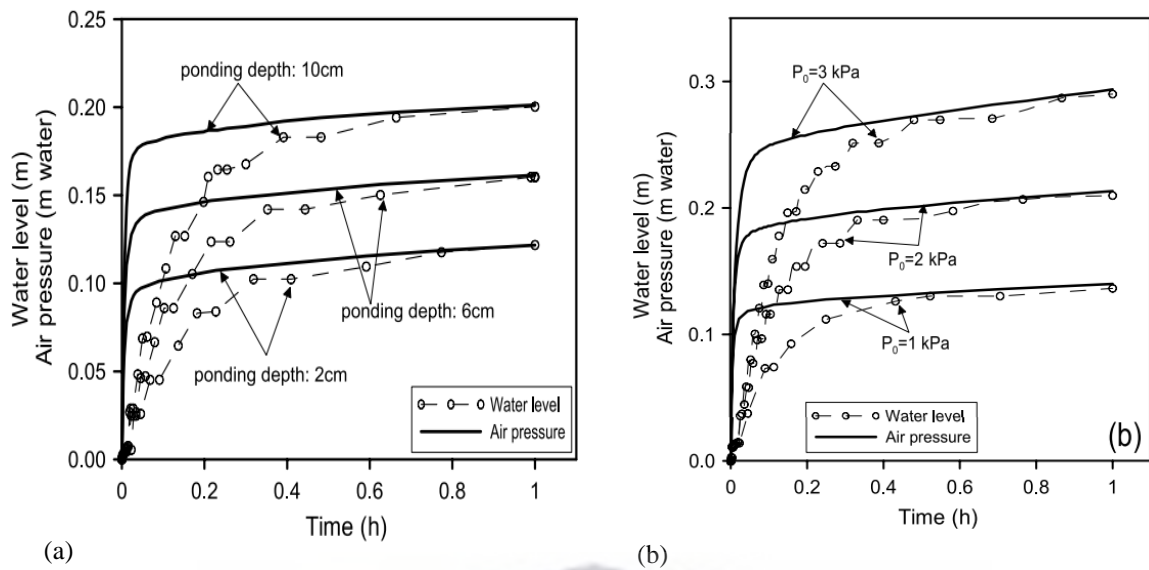


Figure 2.20: (a) Effect of ponding depth of water level and air pressure; (b) Effect of air pressure in the unsaturated zone on water level (Guo *et al.*, 2008).

2.6 Summary and Conclusions

The literature review provided strong background information with regard to known physical mechanisms contributing to slope instability in tailings dams. Additional theories and concepts that were considered to support the data analysis will further be discussed in Chapter 5.

Discussions pertaining to historical tailings dam failures and aggravating factors, such as the vulnerability of the upstream method of construction, further provided context to the severity of possible slope failures. Various research studies such as e.g., Lyu *et al.* (2019), Jennings (1979) and Blight *et al.* (1981) have identified seepage, overtopping, shear failure, piping and erosion as some of the most significant causes. Blight and Fourie (2003) also reported pore water pressure and a high phreatic surface to contribute to the generation of flow failure of mine waste dumps, tailings dams and municipal solid waste landfills. These concepts are further supported by Muñoz (2019) who described two mechanisms contributing to slope instability brought about by rainfall. These include, in line with Blight and Fourie (2003), an increase in pore water pressure due to precipitation recharging the water table and a decrease in soil suction brought about by the wetting front in the superficial layers of the soil. Although these studies have mentioned the significance of rainfall events, they failed to recognise the possibility that the rapid mobilisation of groundwater brought about by GWR and the LE, could be a principal mechanism causing slope instability in tailings dams.

Findings by various researchers such as Schulze and Bulcock (2011), established that higher atmospheric temperatures brought about by climate change, will most likely result in more regular occurrences of extreme events, higher rainfall intensities and irregular frequencies. According to Guo (2016) rainfall water infiltrates the tailings deposits or runs off to the decant pond where some evaporation occurs. Guo *et al.* (2008) suggested that the increase in water level in the tailings dam acts as a driving force for a rise in potential pressure head difference between the water-side and air-side of the dam. As water content increases due to infiltration into the unsaturated slope, the seepage line not only expands but also changes in movement regime. This is particularly relevant during extreme rainfall events and would contribute significantly to tension saturated or near saturated conditions. Rahardjo *et al.* (2001) supported this notion and found that high rainfall intensity events lead to excessive infiltration, while rainfall frequency impacts on antecedent moisture conditions and the generation of pre-event water. Water held under capillary tension is considered to be a source of antecedent moisture, which contributes to the rapid formation of near stream groundwater ridges. Unsaturated porous medium retains pre-event water above the phreatic surface through soil suction and capillary forces. It is also suggested that the capillary fringe closer to the pond, extends over a longer vertical distance than the capillary fringe closer to the dam wall, seeing as pore size decreases towards the point of final deposition.

These external environmental factors, combined with particular unsaturated porous medium characteristics, have an adverse impact on physical and hydrological processes that regulate structural integrity of engineered slopes and earth embankments. It is therefore possible to predict a continuation in the increasing trend in tailings dam failures. A review of previous literature found evidence of both GWR and the LE pertaining to unsaturated porous medium in natural hillslopes. This study will address the deficiency identified in terms of pore air propagation, transient pressure wave generation and rapid mobilisation of antecedent water in unsaturated tailings media. For this purpose, Chapter 3 will address the main facets pertaining to this study. This includes (i) determination of expected climatic changes in terms of temperature, rainfall and some other climatic features; (ii) determination of geotechnical characteristics of tailings porous material; (iii) laboratory experiments that include a tall soil column instrumented with seven ports, each consisting of a TDR, a mini tensiometer and a pore air pressure probe to determine hydraulic state variables and (iv) facilitate numerical modelling for unsaturated water flow modelling using HYDRUS-SLOPE.

CHAPTER 3

3.1 Research Design and Methodology

3.1.1 Site selection and study area

Although the consequences of potential structural failure will have detrimental impacts on ecological degradation, further risks pertaining to human life and economic development will ultimately also hamper South Africa's commitment to sustainable development. The active mining area situated in Mokopane in Limpopo was selected as the primary research area. Various mines have reported high production and deposition rates which could, combined with climate change, contribute to the potential risk of slope instability. Since the area has been identified as already showing significant signs of climate change, it was possible to identify specific impacts based on the analysis of relevant data, supplemented by finding of previous studies.

3.1.1.1 Location

The Limpopo Province is located to the north-eastern region of South Africa, bordering on Zimbabwe and Mozambique. The area contributes vast quantities of coal, copper, diamonds, gold, iron ore, nickel, platinum group metals, rare earth minerals and tin to South Africa's wealthy mineral industry. It is also home to the world's largest open pit platinum mine, located about 35 km to the north-west of Mokopane. See Figure 3.1.

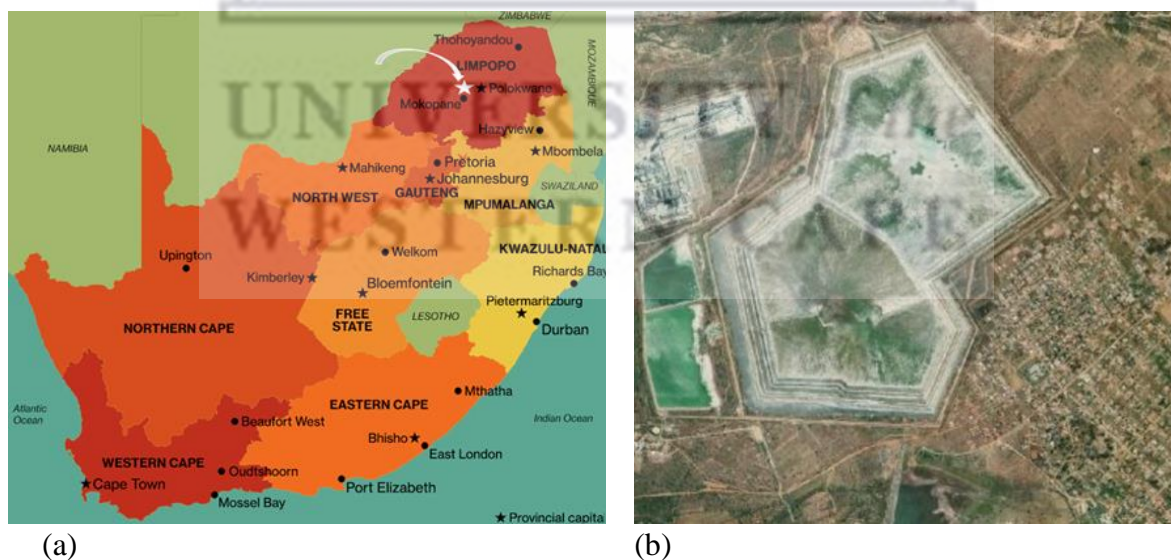


Figure 3.1: (a) Location of the mine and (b) tailings dam (modified from Alexander, 2018 and Temper *et al.*, 2015).

3.1.1.2 Local Geology

The mining area is situated on the strike of the Northern Limb of the Bushveld Complex (Anglo American Platinum Limited, 2014). TSFs are built on the Rustenburg Layered Suite, which is generally divided into five zones based on mineralogical and petrological variations (Manyeruke, 2007). The Rustenburg Layered Suite is underlain by a highly impervious black clay stratum, demonstrating a hydraulic conductivity of 0.03 m/a as opposed to the tailings' hydraulic conductivity of 2 - 3 m/a (Blight *et al.*, 2012). The area falls within the vicinity of a 30 – 100 m thick zone of mineralization known as the Platreef orebody that developed mostly at the base of the northern limb. According to Manzunzu *et al.* (2019) major subsidence within the Bushveld Basin during the Pliocene, caused the reactivation of major marginal faults resulting in most of depressed area of the Bushveld Basin to record high levels of seismic activity. Earthquake clusters and active faults in close proximity to the study area are illustrated in Figure 3.2 (a) and (b) below.

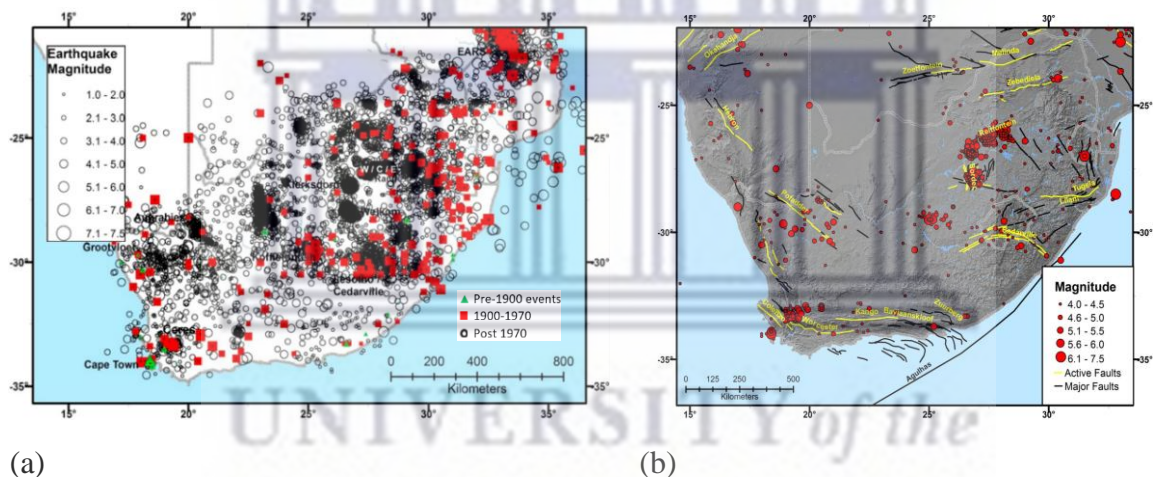


Figure 3.2: (a) Seismic activity in South Africa. (b) Major active faults in South Africa, with active faults marked in yellow (Manzunzu *et al.*, 2019).

3.1.1.3 Operational activities

Some operations started in 1991 and consists of large-scale open-cast mining techniques (Humphries *et al.*, 2006). The current infrastructure consists of four open pits, being the world's largest contributing source of primary platinum group metals (PGMs) (Temper *et al.*, 2015). Tailings dams, with a deposition area of 100 ha, were built to contain vast volumes of disposed mining waste, amounting to 70 million tons of rock and tailings waste annually (Temper *et al.*, 2015). Dam 1, serving the South Plant, has an annual tonnage rate of 3.5×10^6 Mt (dry basis). It was constructed by the upstream spigoted tailings construction method where tailings are

discharged in slurry form, facilitating a mean rise rate of 2,3 m per year (Blight *et al.*, 2012). Even though production rates increased by 48% between 2012 and 2016, settlement has been estimated between 1,0 and 0,1 mm per day, displaying a consolidation rate of 90% (Blight *et al.*, 2012). Dam 2 originally accommodated the production waste from the South concentrator. It was converted from a conventional upstream spigot deposition type dam to a waste rock impoundment dam with an annual tonnage rate on dry basis of 7.0×10^6 Mt (SRK, 2011). Seeing as approximately 75% of the walls of dam 2 were constructed of waste rock, the permeable structure allows seepage from tailings and poor water recovery rates. Storage volume was filled through a sequence of spigots, spaced three meters apart. The nominal rate of rise for this dam was higher than Dam 1 (4,6 m/a) which resulted in only 70% consolidation (Blight *et al.*, 2012). This modification was required to accommodate a higher rate of rise on the dam due to an increase in production rate after commissioning of the new North platinum concentrator (SRK, 2011). According to Rule (2011) Platreef ore processing consists of a multi-stage, mill-float-mill-float circuit system. Two different grinding technologies are employed, which includes mainstream inert grinding (MIG) that specifies target grinds at 80% - 45 μm and ultra fine grinding (UFG) that targets grind at 80% - 20 μm .

3.1.1.4 Climatic classification

The area falls within a summer rainfall region with a Mean Annual Precipitation (MAP) of 582 mm. The climate is predominantly dry and classified, according to the Köppen-Geiger climate classification system, as being a hot semi-arid region. Figure 3.3 illustrates historical average annual minimum and maximum temperature observations, which clearly demonstrate strong warming trends, particularly with regard to maximum temperature. Evaporation rates vary between 2 and 5 mm per day, but are at its highest during the summer rainfall season (LEDET, 2015). Seeing as Schulze (2012) predicts a 5% increase in evaporation for every 1°C increase in temperature, evaporation rates are expected to increase significantly due to climate change. The Limpopo region has a mean A-pan equivalent potential evaporation of 2 218 mm per year. Monthly values have been plotted in Figure 3.3 together with average minimum/maximum temperatures and average monthly rainfall (Schulze and Maharaj, 2007).

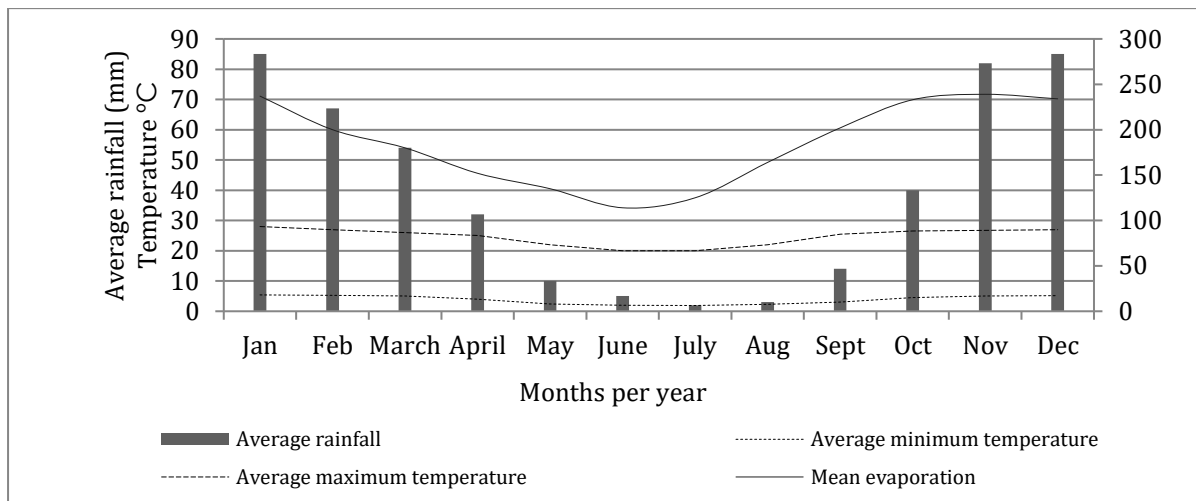


Figure 3.3: Historical climate monthly averages (Polokwane) (constructed using data from CSAG, 2020 and Schulze and Maharaj, 2007).

3.2 Data collection and analysis

This study identified how the wetting front affects stresses in the porous medium through pore water pressure by induced pneumatic pore air pressure pulses in the unsaturated and saturated (capillary fringe) zones. Since there are numerous variables that contribute to or influence the hydraulic behaviour of fine-grained soils such as tailings, there were three different data collection and analysis approaches followed. Data collected from these methods would therefore each contribute to a holistic understanding of the physical processes that generate and are responsible for the occurrence of GWR and/or the LE.

Firstly, a simple investigation into regional climate change was conducted to provide an overview of the extent of possible changing rainfall characteristics and justify the selection of design storms used during the simulation. This analysis was based on historical data combined with estimates of several prediction models. The results were also used to motivate the change to existing intensity-duration-frequency curves (see Chapter 6). Following the above-mentioned analysis, geotechnical properties of platinum tailings and its expected hydraulic behaviour were investigated and compared to the simulated sample, which were found to be virtually identical and sufficient for comparative analysis. Physical properties of tailings were supplemented by findings of various other studies to understand its hydrogeological behaviour and expected response to rainfall events. The third investigation focussed on the main objective of the study, which was to determine pore air pressure propagation under high rainfall intensities. For this reason, laboratory experiments were carried out to investigate the hydraulic

performance of the simulated tailings sample when exposed to different high intensity rainfall events. Sensor development, tall soil column set-up and methodology pertaining to these simulations are discussed in Section 3.2.3 below.

3.2.1 Climate change

To better understand future conditions relating to temperature variations, the CSAG of the University of Cape Town, combined temperature anomalies relative to the historical period 1980 to 2000 with projected future changes in temperature parameters. Data for the Polokwane region was downscaled from ten different CMIP5 GCMs and are described in Table 3.1. As previously mentioned under section 2.2.2.1, the CSAG carried out statistical downscaling by developing a statistical relationship between observed climate data and predictions by the climate model for the same historical period. Anomalies were calculated relative to the historical period 1980 – 2000. Based on the premise that these relationships are likely to remain consistent in future, it provides an indication of future scenarios. In order to derive accurate future rainfall scenarios within South Africa, the CSAG has assembled data from ten different statistically downscaled CMIP5 (Coupled Model Intercomparison Project Phase 5) GCMs. Although it is not specifically stated, the multi-model ensemble (MME) would have been based on the selection of the most appropriate GCMs to reduce the risk of uncertainties. For the purpose of the current study, these secondary data sets were analysed, together with projected future rainfall trends, and presented as a series of graphs (see Annexure C). Since data sets were based on the trend analysis of various temperature and rainfall parameters, it provided an assessment into trends relating to expected climatic changes in the study area. According to Pierce *et al.* (2018) the moderate representative concentration pathway RCP4.5, and the more extreme RCP8.5 should be used in less conservative approaches in analysing climate change impacts. For this reason, this study will only consider these two climate change scenarios. Trend analysis indicated an average increase of almost 2,6 – 4,8°C by the end of the century, which is consistent with predictions by the IPCC (2022) (see Table 2.2). These average temperature forecasts in terms of different emission scenarios clearly correspond with the emission scenario RCP4.5 and RCP8.5 temperature estimates put forward by the Climate System Analysis Group (UCT).

Table 3.1: Information on the statistically downscaled CMIP5 GCMs downscaled by the CSAG at the University of Cape Town to predict future climatic scenarios (rainfall and temperature) at station level at various locations within South Africa.

Global Model	Circulation	Description	Developed by:
1. MIROC-ESM		Model for Interdisciplinary Research on Climate - Earth system models	The University of Tokyo, NIES, and JAMSTEC (Watanabe <i>et al.</i> , 2011)
2. CNRM-CM5		Centre National de Recherches Météorologiques contributing to phase 5 of CMIP5	Centre National de Recherches Météorologiques—Groupe d'études de l'Atmosphère Météorologique (CNRM-GAME) and Centre Européen de Recherche et de Formation Avancée (Cerfacs) (Voltaire <i>et al.</i> , 2013).
3. CanESM2		Second generation Canadian Earth System Model	Canadian Centre for Climate Modelling and Analysis under the University of Victoria,
4. FGOALS-s2		Flexible Global Ocean-Atmosphere-Land System model, Spectral Version 2	Institute of Atmospheric Physics (IAP) and Laboratory of Numerical Modeling for Atmospheric Sciences and Geophysical Fluid Dynamics (LASG).
5. BNU-ESM		Beijing Normal University - Earth System Model	Beijing Normal University
6. MIROC5		Model for Interdisciplinary Research On Climate	The University of Tokyo Center for Climate System Research, National Institute for Environmental Studies, Japan, Japan Agency for Marine-Earth Science and Technology Frontier Research Center for Global Change
7. GFDL-ESM2G		Geophysical Fluid Dynamic Lab model - Earth System Model Version 2G	National Oceanic and Atmospheric Administration (NOAA)
8. MIROC-ESM-CHEM		Model for Interdisciplinary Research on Climate - Earth system models	Simulations of atmospheric chemistry in MIROC-ESM-CHEM are based on the chemistry model CHASER which has been developed mainly at Nagoya University in co-operation with the University of Tokyo, JAMSTEC, and NIES (Fig. 2). The CHASER model version used in MIROC-ESM-CHEM considers the detailed photochemistry in the troposphere and stratosphere by simulating tracer transport, wet and dry deposition, and emissions (Watanabe <i>et al.</i> , 2011).
9. GFDL-ESM2M		Geophysical Fluid Dynamics Laboratory model - Earth System Model Version 2M	National Oceanic and Atmospheric Administration (NOAA).
10. MRI-CGCM3		Coupled Global Circulation Model	The Meteorological Research Institute (MRI)

3.2.2 Tailings characteristics and geohydrological properties

Understanding the hydraulic properties of tailings material is essential for describing and predicting variables that may affect operational and slope stability. For practical problems, Fredlund and Xi (1994) described estimated soil properties as being adequate for analysis under

unsaturated conditions to base empirical predictions on. For instance, it would be acceptable practice to estimate unsaturated soil hydraulic conductivity using saturated hydraulic conductivity and the soil-water characteristic curve. This study depended on research conducted on the tailings dams shown in Figure 3.4. (Lorentz *et al.*, 2019; MacRobert, 2013; Blight *et al.*, 2012; Dacosta, 2017). An analysis into reported tailings characteristics was used as the basis for the prediction of hydrogeological responses and the behaviour of the porous medium. Some of the important parameters that were considered included particle size distribution, pore space distribution, hydraulic conductivity and water retention characteristics.



Figure 3.4: Tailings Storage Facilities (SRK, 2011).

3.2.3 Laboratory experiments

The experimental design involved infiltration experiments in a tall soil column under controlled boundary conditions while monitoring the physical response of hydraulic state variables to simulated rainfall events. Observations and results were used to determine phreatic surface dynamics, the soil moisture profile, pore water/air behaviour and physical processes under different rainfall intensities and varying antecedent moisture conditions. It also facilitated the analysis of flow of water throughout saturated tailings based on short-term, one-dimensional laboratory column flow.

It is further recognised that the complexity of physical processes occurring in the unsaturated zone, necessitated the need for automated data acquisition to accurately simulate infiltration

and predict transient pressure wave generation associated with unsaturated soil water flow. Automatic logging of the hydraulic state variables was therefore used to acquire data for the numerical assessment of hydraulic functions and parameterise the one-dimensional HYDRUS-SLOPE module for slope stability analysis. Due to ethical considerations and travelling restrictions during the Corona-virus lockdown, the tailings sample used in the laboratory was replicated to imitate the physical properties of tailings porous medium (see full discussion in section 3.2.3.3). These results generated data relevant to determination of feedback response and rapid transmission conditions of tailings when exposed to tension saturation conditions, induced pressure head and subsequent loading.

3.2.3.1 Laboratory apparatus

Laboratory experimentation included a large 2,85 m high leak-proof column (600 mm ID) filled up to 2,65 m with tailings replica at *in-situ* dry bulk density. The complex nature of physical and hydrological processes in the vadose zone, necessitated sensing devices and automated data acquisition techniques to accurately determine hydraulic properties of a homogeneous tailings medium and simulate the generation of transient pressure waves. For this reason, the PVC column was instrumented with seven data ports spaced 500, 600, 700, 800, 1100, 1400 and 1700 mm from the bottom of the pipe. Each port consisted of three probes including (i) a TDR to measure Volumetric Water Content (VWC), (ii) a 1 bar mini-tensiometer (MT) to measure soil pore water pressure and (iii) a 0.1 bar pore air pressure probe (PAPP) to measure pore air pressure. A drainage tube and piezometer were installed at a distance of 200 mm from the base of the pipe to discharge water and monitor the phreatic surface. The application of simulated rainfall events at different intensities was achieved by an artificial water supply system at the top of the column. Schematic details of the column apparatus and test setup are illustrated in Figure 3.5 and follows a similar design as the soil columns used by Waswa (2013) and Salas-García *et al.* (2017).

RAINWATER SIMULATOR - WATER SUPPLY TO
IMMULATE HIGH INTENSITY RAINFALL EVENT

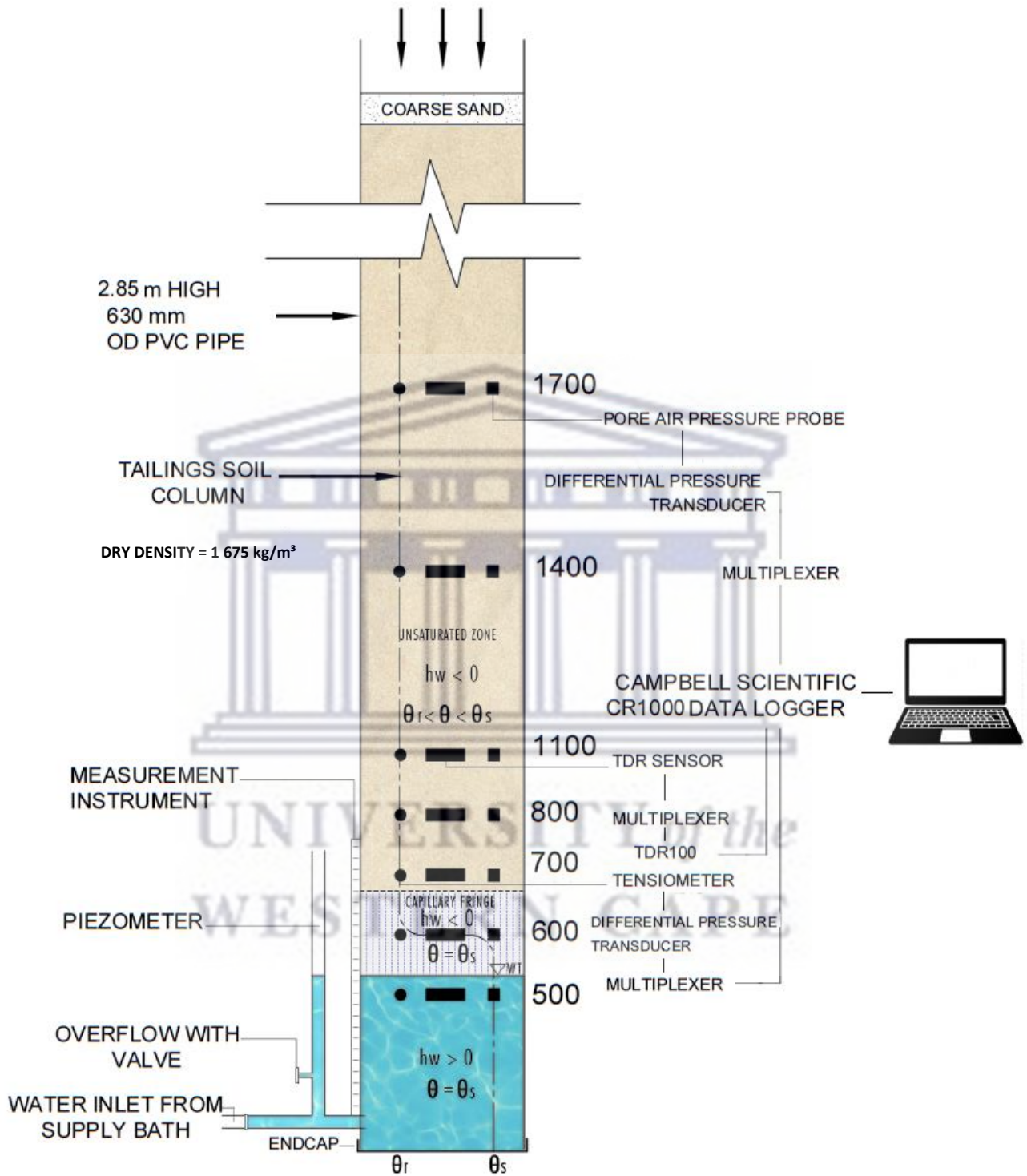


Figure 3.5: Schematic diagram of the column test apparatus and setup. θ_r = residual soil water content, θ_s = saturated soil water content.

3.2.3.2 Sensor development

a) Measurement of in situ water content was carried out by the TDR shown in Figure 3.6. The probes were custom-made to consist of three parallel stainless-steel rods with an exposed length of 200 mm, a diameter of 5 mm, blocked in resin and spaced at 50 mm apart. According to Fredlund *et al.* (2012) rods should be placed horizontally to measure water content at a specified depth. This device was connected to the TDR 100 wave excitation device through a coaxial cable. The soil water content data were recorded and temporarily stored on a CR1000 Campbell Scientific data logger via a SDMX50 Multiplexer and Campbell Scientific TDR100 wave generator.

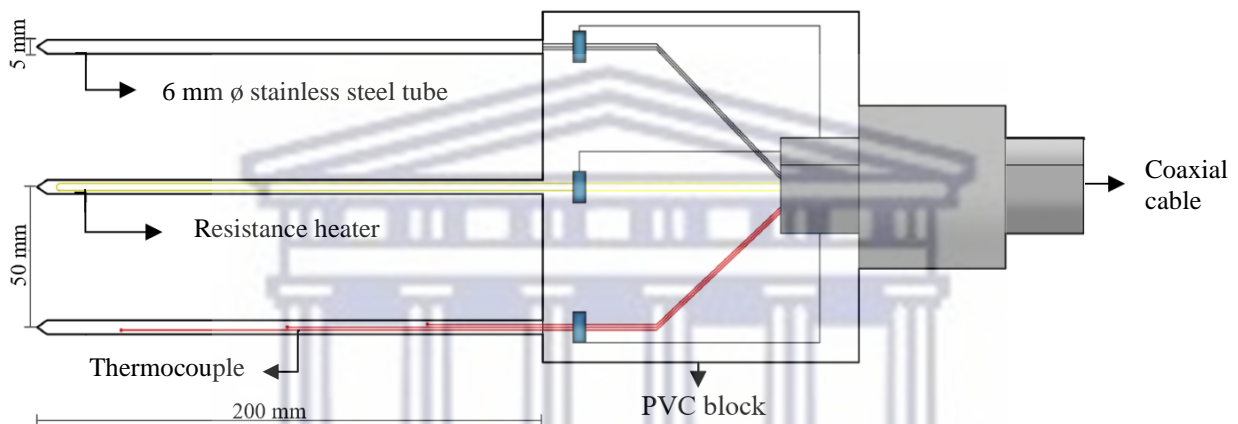


Figure 3.6: Custom-made TDR used to measure volumetric water content.

Matric suction is the difference between pore air and pore water pressure and has been measured using a direct method. This included measurement of negative pore water pressure by means of MT (Figure 3.7) able to measure matric suction up to almost 1 atm (Fredlund *et al.* 2012). MT were fitted with 25 mm-long porous ceramic-cups (15 mm exposed) with an outer diameter of 6 mm (SDEC 230). It comprised over the following characteristics:

Air entry value	-	1.5 Bar
Pore size	-	approx. 1.5 micron
Hydraulic conductivity	-	5.10 – 7 cm.s ⁻¹
Weight	-	1 gr.

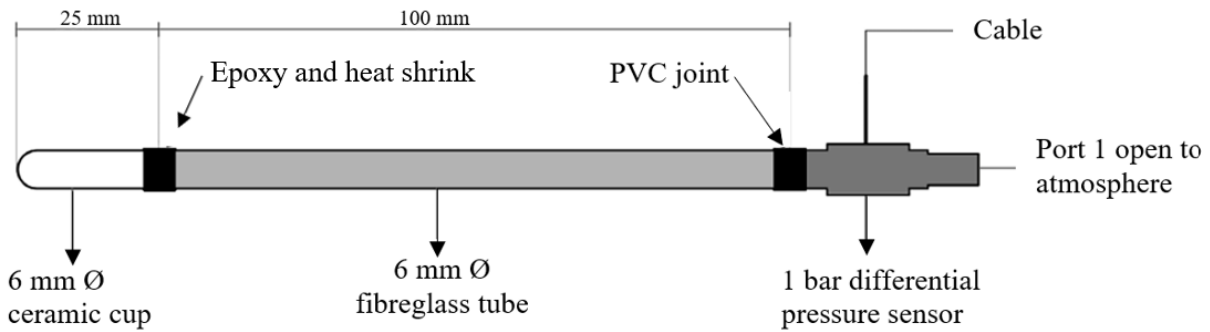


Figure 3.7: Custom-made mini tensiometer.

These porous cups were made of very thin, sensitive ceramics to act as the interface between the measuring system and negative pore water pressure in the tailings sample. The high-air-entry ceramic cup ensured a rapid response time. The open end of the ceramic cup was joined to one end of a 100 mm long rigid fibreglass tube of outside $\text{\O} - 6 \text{ mm}$ and inside $\text{\O} - 3 \text{ mm}$. This material has non-corrosive properties and low heat conductivity, while the small diameter and short length minimised the volume of water in the tensiometer tubing. The other end of the tube was connected through a PVC tube to a 1 bar Honeywell differential pressure transducer with a 0 to 100 kPa range for continuous measurement at each monitoring location. These are illustrated in Figure 3.8 (a) and (b) below. The 26PCCFA6D Honeywell differential pressure transducer [15 psi Max Pressure Reading (1 Bar)] had two ports, as indicated in the specifications illustrated below. Seeing as one port must have a higher pressure than the other (i.e. $P_1 > P_2$) the low pressure side, P2, was connected to the ceramic, since it recorded lower pressures than ambient, and P1 port was left open to atmosphere to discharge at ambient pressure.

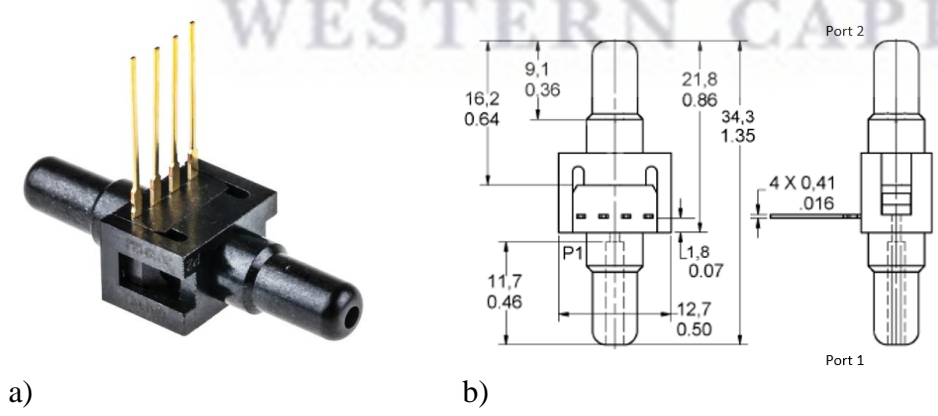


Figure 3.8 (a) and (b): 1 Bar Honeywell differential pressure transducer (Honeywell, 2014).

The tensiometers were completely filled with deaired water before insertion into the soil column to ensure equilibrium with the soil moisture content (Salas-Garcia *et al.*, 2017). The water in the MT was therefore also under negative pressure like the porewater in the soil, once equilibrium was reached (Fredlund *et al.*, 2012). The data of pore-water pressure and pore-air pressure were recorded and temporarily stored on a CR1000 Campbell Scientific data logger via differential pressure transducers of 1 bar Honeywell sensor and 0.1 bar Motorola MPX2010DP. The measurement of negative pore-water pressure was statistically equal to the matric suction when the pore-air pressure was atmospheric (Fredlund *et al.*, 2012).

b) For the measurement of pore air pressure, the pore air pressure probe in Figure 3.9 was constructed. The sharply pointed probe, similar to the probe developed by Waswa (2013), was constructed by making use of a solid 140 mm long PVC rod of 10 mm diameter. Five-millimeter transverse holes were drilled over 50 mm across the length of the PVC cylinder and orthogonally traversed by a 3 mm diameter hole in the longitudinal centre of the rod, penetrating the solid cylinder at the back end. The section of the probe, over which the transverse holes were made, was recessed and wrapped in a hydrophobic membrane, which allowed the flow of air at low pressure and the passage of water at very high pressure.

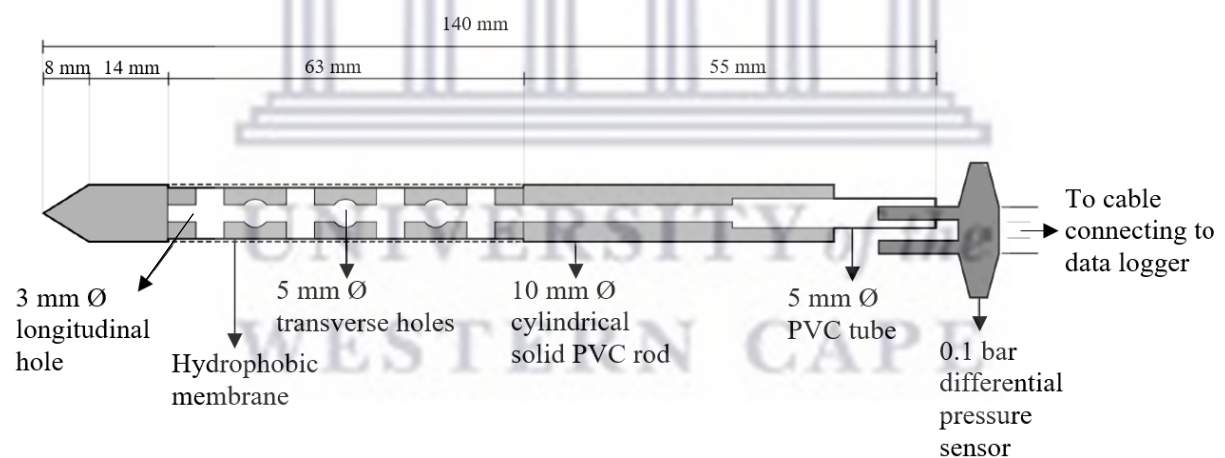


Figure 3.9: Custom made pore air pressure probe (modified from Waswa, 2013).

The PAPP was connected to a MPX2010DP, PCB Mount, differential pressure sensor [1.45 psi Max pressure reading (0.1 Bar)] by a 5 mm PVC tube. The transducer (shown in Figure 3.10 (a) and (b)) had two ports, as indicated in the specifications below. In this case, pore air pressure was anticipated higher than ambient, so the P1 port was connected to the air pressure sensor and the P2 port left open to ambient. Data pertaining to pore-air pressure responses were recorded and temporarily stored on a CR1000 Campbell Scientific Data Logger via differential pressure transducers of 0.1 bar Motorola MPX2010DP.

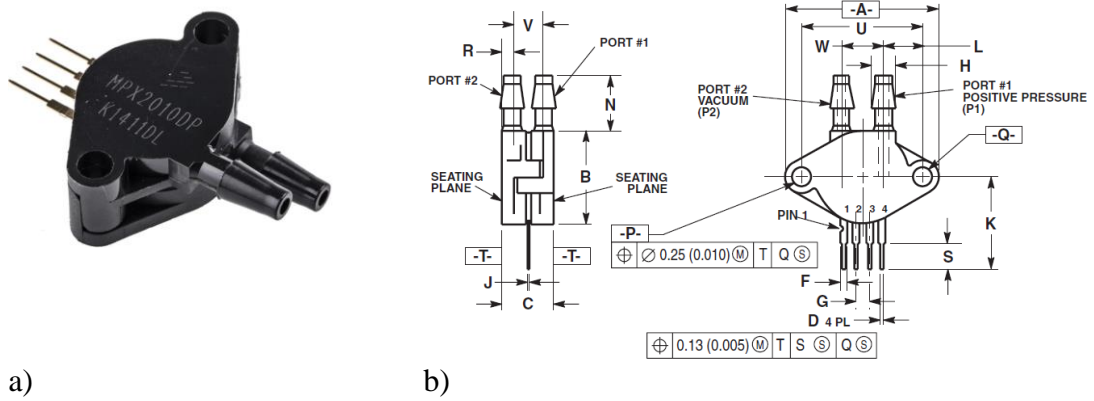


Figure 3.10 (a) and (b): 0.1 Bar Differential pressure transducer (NXP, 2008).

3.2.3.3 Material parameters

The tailings sample consisted of an artificial replica of similar physical characteristics. The experimental material was obtained from a commercial supplier and consisted of a concise mix of silica sand and silica dust. Materials were ordered and mixed in the laboratory (see Appendix A – Figure E) in ratios based on predetermined proportions (Table 3.2). The required volume calculations for the silica sand/dust mix ratio were based on the composite replicated by Lorentz *et al.* (2019) to produce a substitute material comparable to the particle size distribution of a platinum mine’s tailings sample. Figure 3.11 below shows similar particle size distribution curves between the original tailings sample and the replicated material. Since only physical characteristics were analysed, the substituted homogeneous sample was found to be sufficiently comparable to the original tailings sample. Individual grains of the soils were uniform shape, stable, clean and free of organic matter.

Table 3.2: Sample composition of silica dust and sand to replicate tailings material.

Component	Bulk density kg/m ³	Ratio of mix	Mass per 4 m ³ (kg)	Mass per 1 m ³ (kg)	Mass per 0.7 m ³ (kg)	Texture Class
Silica dust 325	1650	55%	3685	921,25	644,875	Silt-loam
Silica dust 150	1600	10%	670	167,5	117,25	Loam
AF45	1750	15%	1005	251,25	175,875	Sand
No. 2	1700	20%	1340	335	234,5	Sand
		100%		1675		

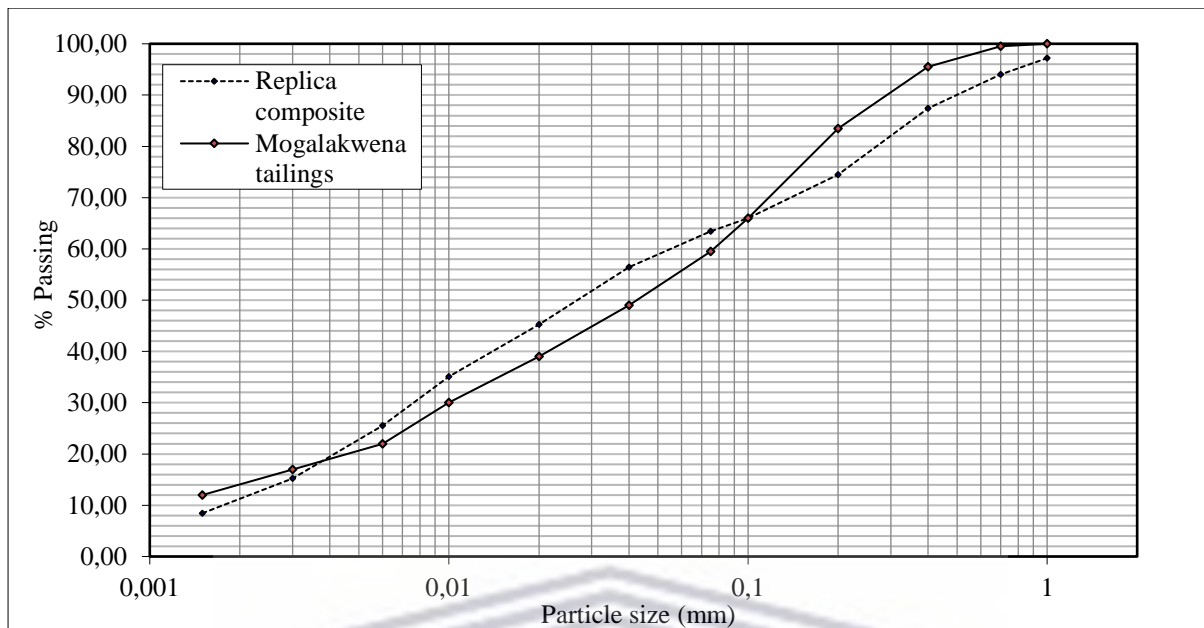


Figure 3.11: Particle size distribution curve of sample (Lorentz *et al.*, 2019).

3.2.3.4 Experimental Procedure

Similar to the procedure described by Waswa (2013), the PVC pipe was packed with dry tailings ($S = 20\%$) in 300 mm layers and administered the same number of blows after each deposit to ensure uniform bulk density of $1\,675\text{ kg/m}^3$. To avoid damage, instruments were installed into the wall of the PVC column after it had been filled and the soil sample had been compacted to the specified bulk density. The PAPP was connected to the 0.1 differential pressure sensor, which was connected to the CR1000 data logger. The TDR probes were connected to the CR1000 data logger via the SDMX50 Multiplexer and Campbell Scientific TDR100 wave generator. The MTs were connected to the 1 bar pressure transducer, which in turn was connected to a data logger in order to obtain measurements. These sensors connected to the CR1000 data logger via the multiplexer. Each instrument was pushed through the compression fitting into the soil and sealed to ensure a watertight connection. The complete set-up is illustrated in Figure 3.12 below. See Appendix B for the data program.

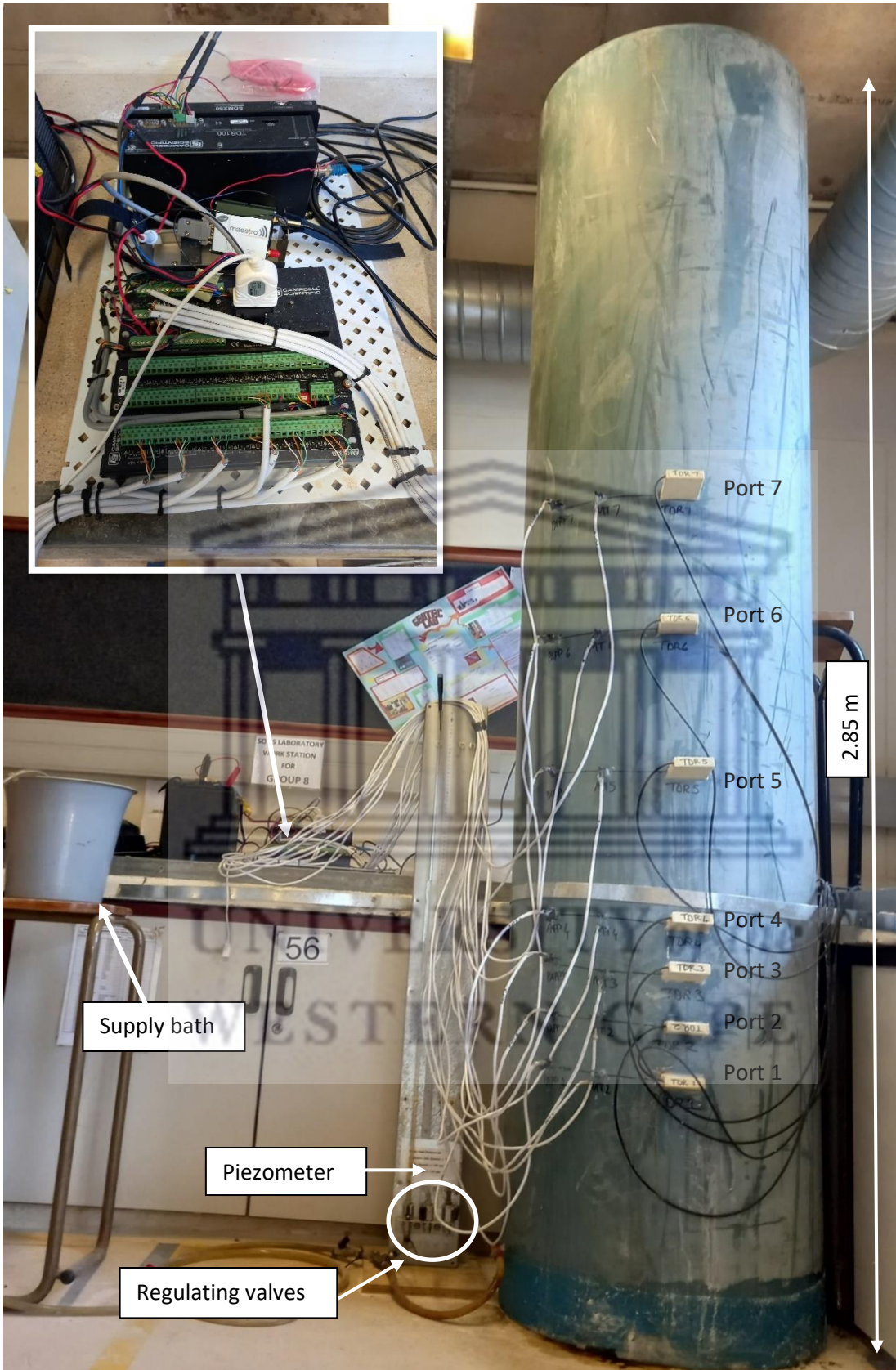


Figure 3.12: Tall soil column fitted with seven ports each consisting of a pore air pressure probe, mini tensiometer and a TDR probe.

After setup of the apparatus, deaired water was introduced from the bottom of the soil column to prevent the capture of pore air and eliminate resulting disproportionate water table responses (Waswa, 2016). Water was introduced from the supply bath through an inlet valve positioned 10 cm from the base of the column, thereby establishing a stable pre-simulation piezometric water level. The phreatic surface was positioned at approximately 400 mm from the base, just below port 1 (and visually confirmed by the piezometer). Initial TDR data indicated the saturated capillary fringe extended between port 4 and 5 (see Figure 4.11). After set-up, the installation was allowed to settle and water allowed to come to equilibrium. All sensors were monitored, by downloading data and plotting graphically, to ensure stability over at least four hours preceding the application of water at the surface boundary.

Proceeding with the experiment, the coarse-grained topsoil surface was subjected to the artificial application of rainfall at three different ponding depths, simulating surface recharge by means of a rainfall event. Design rainfall data for Mokopane were used to determine the magnitude of an event of particular return periods (Smithers and Schulze, 2002). Based on these estimations, storm events 1:200, 1:100 and 1:50 years were selected to represent high intensity rainfall events. Rainfall data analysis (Chapter 4) and estimations by Smithers and Schulze (2002) indicated that design storm data are projected to increase by 10% in short duration design rainfalls in the intermediate future (2046 - 2065) while some regions could reach long term increases of up to 40% by 2100. See Table 3.3 below. After the application of moderate (10%) increases, rainfall depth at each return period shifted to roughly the value of the next return period. Ultimately, this means that the frequency of design storms based on historical return periods will occur more often. For example, a 1:100-year design storm would have the same intensity as a historical 1:200 storm, but still have an annual occurrence probability of 1%. The three historical return periods selected, would therefore represent future high intensity rainfall events due to occur more often.

Table 3.3: Description of incremental addition of water to tall soil column. Rainfall depths based on station specific data (Smithers and Schulze, 2002).

Date	Start time	Event	Return period	Rainfall depth (mm): 15 min	Rainfall depth (mm): 1 hour	Volume (liter): 15 min	Volume (liter): 1 hour	Addition of water to tall soil column (liter)
29 Dec 2021	17h30	Test event 1	1:200 year	52.5	84.1	14.98	24	9 l over 30 min, 14 l over 15 min and 1 l over last 15 min
7 March 2022	15h20	Test event 2	1:100 year	46.7	74.9	13.288	21.2	8 l over 15 min and 13.2 l over 45 min
1 April 2022	16h04	Test event 3	1:50 year	41.3	66.1	11.734	18.7	7 l over 15 min and 11.7 l over 45 min.

Three infiltration tests were conducted to investigate the effect of different boundary conditions and the advancement of the wetting front. This also assisted in verifying the performance of the sensors installed in the ATC (Salas-Garcia *et al.*, 2017). Data from each experiment were recorded at 20 second intervals, downloaded and analysed to identify the rapid (and delayed) response of transient pressure waves when subjected to different rainfall intensities. After each application, the tall soil column was allowed to drain before the next experiment. By allowing continuous recording over five months, the response of each sensor was plotted in various time-series plots to identify increasing or decreasing responses to artificial rainfall. Transient profiles of water content and water flux obtained during the redistribution phases were also compared with simulated values (Hydrus-1D) (Salas-Garcia *et al.*, 2017). The results of numerical modelling are discussed in Chapter 5.

CHAPTER 4

4.1 Results

4.1.1 Climate change

4.1.1.1 Temperature trends

Increasing temperatures brought about by climate change impact on the geohydrological behaviour of tailings in two ways. Firstly, a warmer atmosphere changes historical rainfall characteristics, specifically rainfall intensity, which is particularly relevant to this study. Secondly, higher temperatures also result in higher levels of evaporation, thereby exacerbating the drying of tailings. These external factors have considerable impacts on the wetting-drying cycles of soils.

Existing climatic characteristics of the study area has been classified by the Köppen-Geiger climate system. According to this classification, the area is classified as a predominantly warm semi-arid (Bsh) region under present day conditions. Temperature anomalies predicted under the force of climate change impacts the surrounding area rather significantly under future conditions. This substantial difference is illustrated in Figure 4.1 (a) and (b).

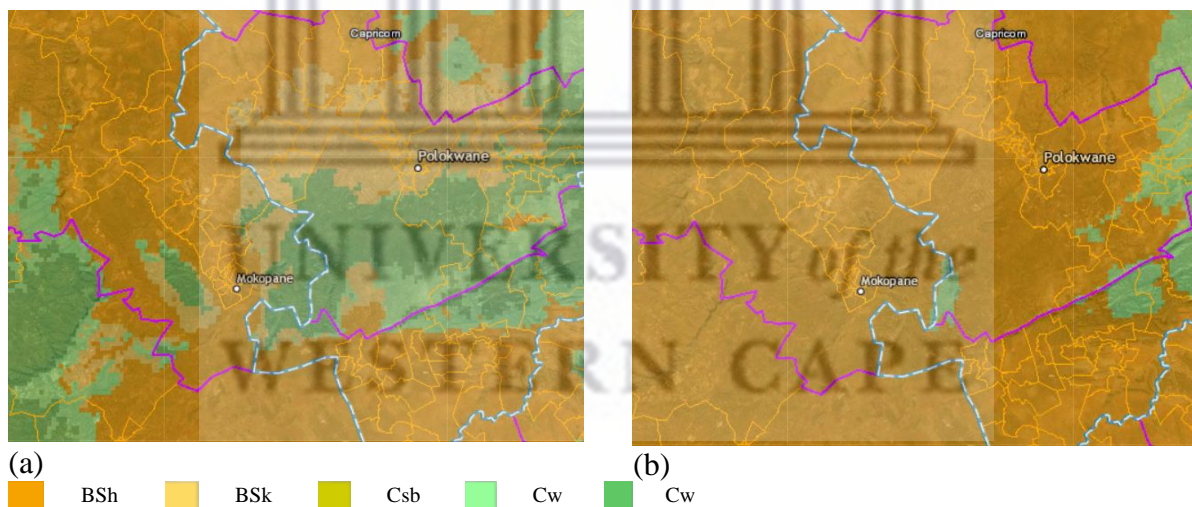


Figure 4.1: The Köppen-Geiger climate classification at an unprecedented 1-km resolution for (a) the present-day (1980–2016) and (b) for the future (2071–2100) (Beck *et al.*, 2018).

Figure 4.2 is based on data provided by the University of the Western Cape's CSAG and illustrate temperature trends and projected future forecasts. Anomalies were calculated relative to the historical period 1980 – 2000 (CSAG, 2020). All models show significant increase in average maximum temperature (t_{max}).

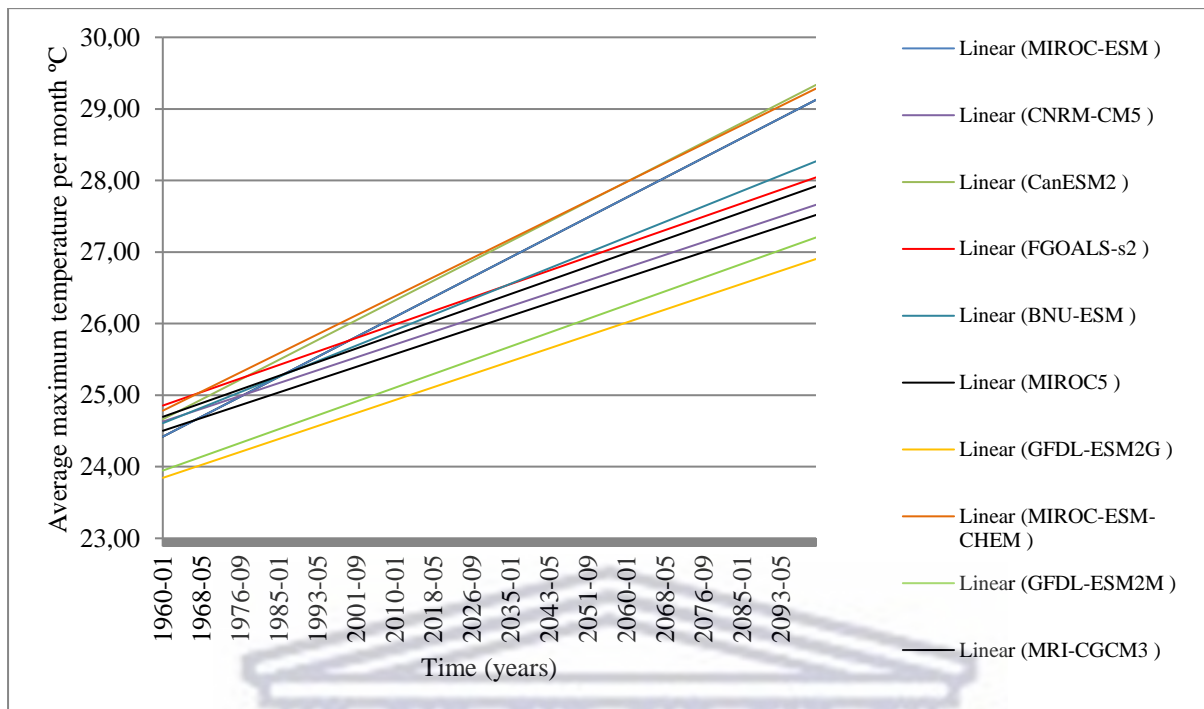


Figure 4.2: Average maximum monthly temperatures 1960 -2099 based on projected future changes across 10 different statistically downscaled CMIP5 GCMs (RCP8.5).

The same data have been studied further by analysing it on a monthly basis from January 1960 to December 2099 (not shown). These results showed strong warming trends in each month, while the strongest warming signal occurred in spring. Analysis of minimum temperatures (t_{min}) show strong warming in summer and winter. In addition to identifying strong warming trends, all models indicate an increase in the number of hot days exceeding 32°C and 36°C for both emission scenario RCP4.5 and RCP8.5. Days of which high temperatures exceed the ninety-fifth percentile of hot days (t_{max_95th}) also indicate a consistent increasing trend across all seasons. Although future emission scenarios under RCP4.5 imply less aggressive temperature increases, it would still likely result in a mean increase of approximately 3°C by 2100 as opposed to 6°C for emission scenario RCP8.5. These drastic temperature increases describe an anomaly well beyond the natural climatic variability of the area. These trends are confirmed by historical data obtained from the South African Weather Service (SAWS, 2020) whose historical temperature data from 1993 to 2020 have already shown clear signs of increasing trends in all four of Limpopo’s climatic zones.

According to Schulze *et al.* (2007) potential evaporation rates at a specific location displays relatively minor variations on an annual basis. This enabled the accurate estimation of monthly values using a minimum of only three years’ worth of temperature, rainfall and A-pan

evaporation data. Schulze *et al.* (2007) identified twelve relatively uniform evaporation response regions in South Africa. Temperature-based equations of A-pan equivalent evaporation for each region were developed, while recognising that forcing functions of reference potential evaporation vary between different areas and climatic conditions. Schulze *et al.* (2007) found the area under study as falling within a region that displays minimum and maximum yearly A-pan equivalent potential evaporation rates of between 1 896 mm and 2 592 mm, while daily evaporation rates vary between 2 and 5 mm (LEDET, 2015). It is predicted that for every 1°C increase in temperature, a 5% increase in evaporation could be expected (Schulze, 2011). The projected change in global mean surface temperature for the mid- and late 21st century, relative to the 1986 – 2005 period and under emission scenario RCP8.5, is 2,6°C to 4,8°C (IPCC, 2014). This increase in temperature would cause evaporation rates in the study area to increase between 13% and 24% by the turn of the century. Present and calculated predicted monthly potential evaporation values are stated in Table 4.1 and illustrated in Figures 4.3 – 4.5.

Table 4.1: Present and estimated monthly A-Pan Equivalent Potential Evaporation (mm): Limpopo region (Schulze and Maharaj, 2007).

Month	Annual Value %	Present Mean Value	Predicted Future Mean Value 13% Increase	Predicted Future Mean Value 24% Increase	Present Max Value	Predicted Future Max Value 13% Increase	Predicted Future Max Value 24% Increase	Present Min Value	Predicted Future Min Value 13% Increase	Predicted Future Min Value 24% Increase
January	10.5	237	267.81	293.88	292	329.96	362.08	168	189.84	208.32
February	9.2	193	218.09	239.32	238	268.94	295.12	146	164.98	181.04
March	8.9	191	215.83	236.84	222	250.86	275.28	159	179.67	197.16
April	7	152	171.76	188.48	165	186.45	204.6	132	149.16	163.68
May	6.1	135	152.55	167.4	152	171.76	188.48	120	135.6	148.8
June	5.2	114	128.82	141.36	128	144.64	158.72	101	114.13	125.24
July	5.7	125	141.25	155	136	153.68	168.64	112	126.56	138.88
August	7.3	164	185.32	203.36	181	204.53	224.44	142	160.46	176.08
September	8.9	202	228.26	250.48	239	270.07	296.36	166	187.58	205.84
October	10.2	233	263.29	288.92	294	332.22	364.56	187	211.31	231.88
November	10.2	239	270.07	296.36	287	324.31	355.88	179	202.27	221.96
December	10.7	234	264.42	290.16	288	325.44	357.12	175	197.75	217

The second column in Table 4.1 expresses monthly A-Pan equivalent potential evaporation as a percentage of annual rates. Since the highest temperatures are recorded during late spring and summer months, it is logical that these periods would also experience the highest evaporation

rates. Seeing as this is a summer rainfall region, observed monthly rainfall totals indicate the same months to receive the highest amount of rainfall.

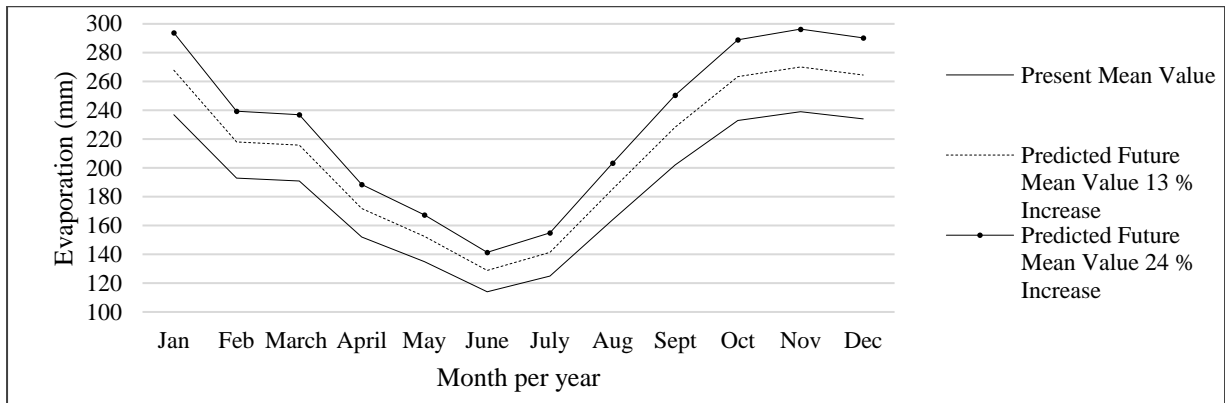


Figure 4.3: Present and predicted monthly mean A-Pan Equivalent Potential Evaporation (mm): Limpopo.

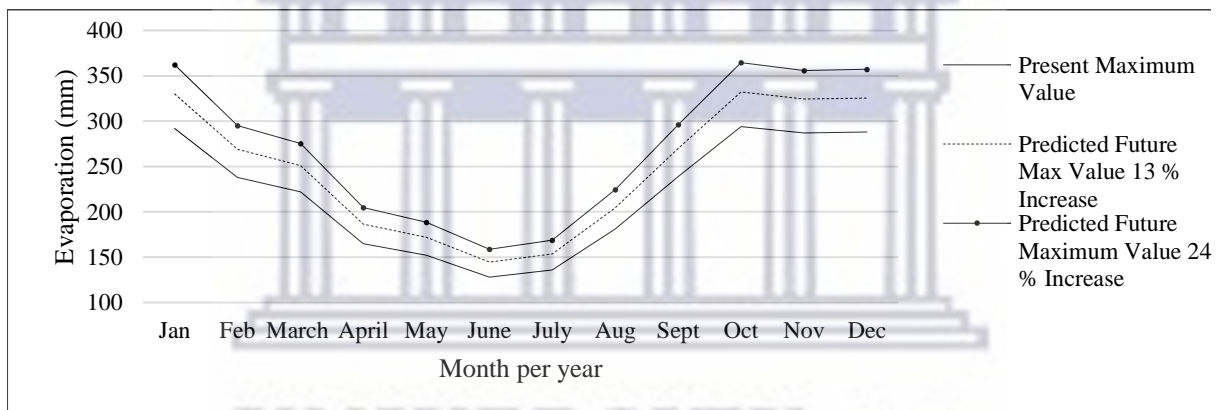


Figure 4.4: Present and predicted monthly maximum A-Pan Equivalent Potential Evaporation (mm): Limpopo.

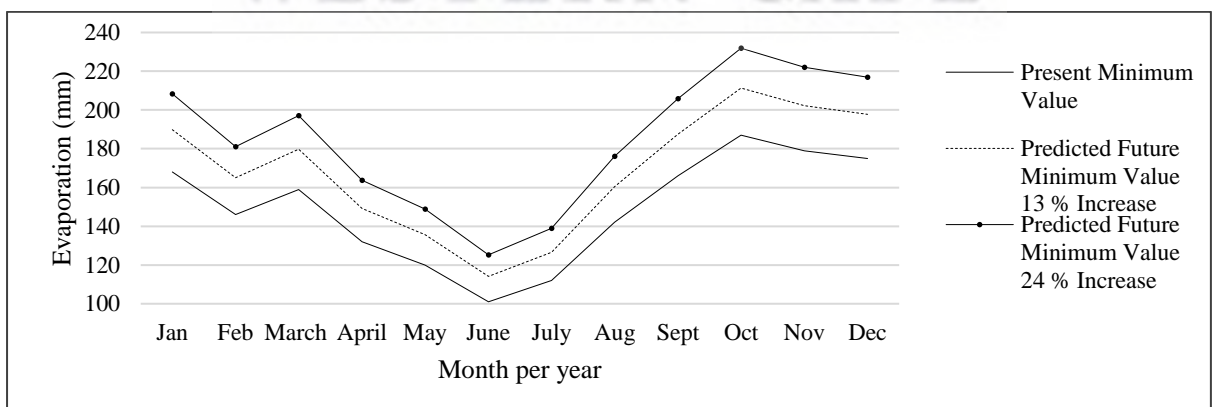


Figure 4.5: Present and predicted monthly minimum A-Pan Equivalent Potential Evaporation (mm): Limpopo.

4.1.1.2 Rainfall data

Several environmental consequences follow a rise in atmospheric temperatures. Schulze *et al.* (2011a) mentioned that climate change is likely to cause seasonal shifts resulting in an increase in extreme events and greater rainfall variability in terms of intensity, duration and frequency. A few studies have shown that, even though some areas will continue to receive its usual mean annual precipitation, individual rainfall parameters will most likely experience considerable changes (van Wageningen, 2006; Lawrence *et al.*, 2020). This would be particularly significant under emission scenario RCP8.5 which is likely to result in a rise in temperature of up to 6°C by 2100. Figure 4.6 is specific to the study area and illustrates historical temperature and rainfall patterns per month compared to future (2099) temperature and rainfall trends based on emission scenario RCP8.5.

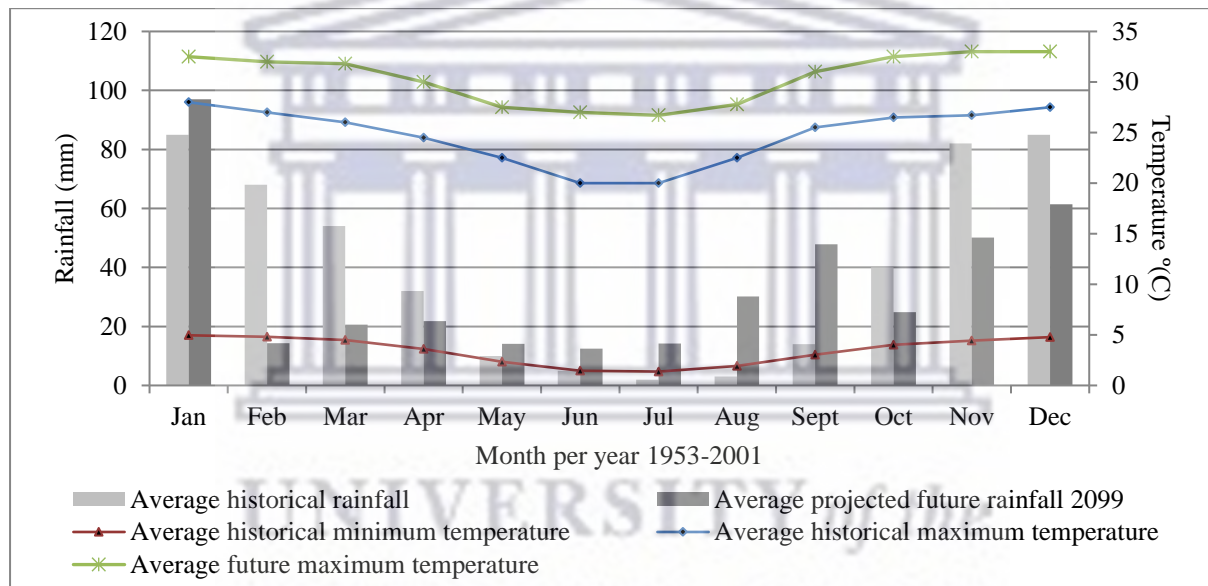


Figure 4.6: Mokopane average monthly rainfall, minimum and maximum temperature.

Different scales of changing rainfall characteristics are applicable to different areas, which required the analysis of rainfall data specific to the study area. Historical observations and predicted data were obtained through the Climate Information Portal presented by the CSAG. This data have been collated from the Computing Centre for Water Resources and the South African Weather Service and used to predict future scenarios through the application of the previously mentioned GCMs. The application of data to different global circulation models, based on different emission scenarios, enabled the prediction of possible rainfall characteristics in future. Appendix C consists of a series of graphs that are based on the analysis of various

rainfall parameters and provided a more in-depth assessment into trends relating to specific climatic conditions in the study area. Analysis of results will be discussed below.

4.1.1.2.1 Summary of rainfall trends

Figures C.1 – C.12 (Annexure C) shows the inconsistency in predictions made by statistically downscaled CMIP5 GCMs. Downscaled rainfall projections from CSAG (2020) in relation to changes in total monthly rainfall, maximum daily rainfall, count of wet days, mean dry spell duration and number of rain days above 5 mm, 10 mm and 20 mm, show large variations in forecasts up to 2099. Although the issue of intermodal disagreement has been described by Hewitson and Crane (2006) and Tarek *et al.* (2021) as being a result of their individual precipitation parameterization schemes, it illustrates the challenge of accurately predicting how rainfall is expected to change.

Figure C.1 and C.2 (Annexure C) shows total monthly rainfall trends. For both RCP4.5 and RCP8.5 all models (except FGOALS-s2, GFDL-ESM2M and MRI-CGCM3) indicate decreasing trends for total monthly rainfall. Even though there is a noticeable lack in consistency across future projections, the average trend between 1960 and 2099 points toward a decrease in total monthly rainfall. Figure C.3 (a) - (l) simplifies the same data into monthly representations to allow for analysis on a seasonal basis. The latter part of autumn (MAM) and the following three months of winter (JJA) exhibit a noticeable decreasing total monthly rainfall trend across all models (Figure C.3 (d), (e), (f), (h)). This supports findings made by Olivier *et al.* (2020) that the greater Limpopo area experienced above normal daytime temperatures combined with below-normal rainfall during the winter months of 2020. This trend has been particularly evident over the last decade as temperature and precipitation anomalies increase in terms of warming and dry conditions during the winter month of August.

The maximum daily rainfall per month for emission scenario RCP4.5 and RCP8.5 (Figure C.4 and C.5) indicate an annual decreasing trend across all models except GFDL-ESM2M. Analysis of monthly predictions does however contradict this approach and finds significantly less maximum daily rainfall during the winter season, but an increase in maximum daily rainfall, pointing towards the more frequent occurrence of extreme events during summer months. The frequency of rainfall events is illustrated by (i) number of wet days for both emission scenario RCP4.5 and RCP8.5 (Figure C.6 – C.7) and (ii) mean dry spell duration (Figure C.8 – C.9). This information would be relevant in suggesting possible antecedent

moisture conditions as well as the wetting-drying processes that regulate geo-hydrological behaviour. More comprehensive analysis of this data on a monthly basis shows significant monthly variations across different seasons, as well as different results among models.

Figure C.8 shows the duration of future monthly mean dry spells predicted by different GCMs. The same data were used to show trends in historical (measured) and future (predicted) monthly dry spell durations (see Figure C.9 a - 1). These trends are projected to increase, particularly during autumn (MAM) and winter (JJA). While the inconsistency between prediction models is particularly noticeable during summer, previous studies suggest that December and January are predicted to show the greatest changes in rainfall due to climate change (Dyson *et al.*, 2012). Figure C.10 – C.12 illustrates an existing average increasing trend, while the contrast in models predicting the number of wet days per month for both emission scenario RCP4.5 and RCP8.5 is significant. For the sake of simplicity, Table 4.2 summarises these results.

Table 4.2: Rainfall trends identified for each CMIP CGM.

CMIP5 GCM	RCP4.5	RCP8.5	RCP4.5	RCP8.5	RCP4.5	RCP8.5	RCP4.5	RCP8.5
	Total monthly rainfall 1960 – 2099		Maximum daily rainfall per month 1960 – 2099		Number of wet days per month 1960 – 2099		Mean dry spell duration per month 1960 – 2099	
MIROC-ESM	↓	↓	↓	↓	↑	↑	↓	↓
CNRM-CM5	↓	↓	↓	↓	↓	↓	↑	↑
CanESM2	↓	↓	↓	↓	↓	↓	↑	↑
FGOALS-s2	↑	No change	↓	↓	↑	↑	↑	↑
BNU-ESM	↓	↓	↓	↓	↓	↓	↑	↑
MIROC5	↓	↓	↓	↓	↑	↑	↑	↑
GFDL-ESM2G	↓	↓	↓	↓	↑	↑	↑	↑
MIROC-ESM-CHEM	↓	↓	↓	↓	↑	↑	↓	↓
GFDL-ESM2M	↑	↑	↑	No change	↑	↑	↑	↑
MRI-CGCM3	↑	↑	↓	No change	↑	↑	↓	↓

The IPCC (2007) suggested that the first indication of a possible change in rainfall intensities, could be obtained simply by dividing the annual rainfall by how many rain days there were. It was recognised that this approach was inadequate to estimate accurate intensity changes. The observed number of rainfall events between 1953 and 2001 exceeding 5 mm, 10 mm and 20 mm indicate an approximate 10% decade-on-decade increasing trend in the occurrence of events of higher intensities. This finding supports estimations made by Knoesen *et al.* (2011) that suggested that the area under study will most likely experience 0 - 10% changes in design rainfall parameters (i.e., intensity) during both intermediate (2046 - 2065) and future (2081 -

2100) timeframes. Motivation for rainfall intensities and extreme sequences adopted in this study to demonstrate future risks of tailings failure to rainfall induced mechanisms have been discussed in section 3.1.3.4.

4.1.2 Physical characteristics

4.1.2.1 Soil classification and particle size distribution

The analysis of particle density (ρ_p), porosity and particle size distribution of a particular soil is valuable in identifying certain fundamental physical properties that enable realistic estimations in terms of hydraulic behaviour (Skopp, 2011). Processing activities include ultra-fine grinding technology that aims to achieve the required grade of concentrates and recover metals from the host rock. This process results in a final fraction of 80% - 20 μm that is consequently deposited as tailings (Rule, 2011). Existing sieve analysis and particle size distribution curves from both Dam 1 and 2 were analysed to obtain information on the distribution of solid particles, the percentage of each particle size, classify the tailings sample and identify physical characteristics. No distinction was made between Dam 1 and 2 analyses, since only small negligible variations were found. This was supported by Blight *et al.* (2012) that confirmed the grading for Dam 1 to be slightly coarser than Dam 2 in the silt size range, but clay content was virtually identical. Previous studies conducted by Dacosta (2017), Blight *et al.* (2012) and MacRobert and Blight (2013) found the tailings porous medium to exhibit a uniquely fine nature in terms of particle size. Sample 1 (30 kg) particle size distribution analysis was obtained from Dacosta's (2017) study. The Malvern particle size analysis of this unconsolidated tailings sample (MPL/101), found 30% of the sample to be in the finest fraction. Subsequently, the results obtained from a particle size distribution analysis, showed finer particles at D_{0,9} (i.e. volume under 90 %) had a corresponding particle size of 197,39 μm and smaller (Dacosta, 2017). Sample 2 particle size distribution analysis was obtained from a study conducted by Blight *et al.* (2012). The combined particle size (0,002 m³) distribution curves are illustrated in Figure 4.7 and show similar curves representing the characteristics of a fine soil. From these studies, it is evident that, on average, approximately 10 - 15% of the unconsolidated tailings sample falls within the finest clay fraction and 58 – 70% in the fine to coarse silt fraction. The remaining 15 – 32% was found in the finest sand fraction (Dacosta, 2017; Blight *et al.*, 2012). Laboratory analysis by Lorentz *et al.* (2019), however, found Blinkwater Dam 1 and 2 to exhibit 12 – 15% clay, 36 – 39% silt and 46 – 52% sand fractions. An average of 75% of the tailings sample was therefore contained within the fine fractions of

silt and clay. Similar results were obtained by Jamiolkowski *et al.* (2010) after investigation into the Zelazny copper mine (Poland) that perform comparable grinding specifications. These fraction values were found to be characteristic of tailings and confirmed by various independent studies. This notion was also supported by Riquelme and Godoy (2017) after examining a collection of different tailings samples from TSFs located in the north of Chile. These values were indicative of the soil's water retention capacities and its predilection towards the establishment of a continuous water phase. Blight *et al.* (2012) also applied these results to the estimation of the SWCC of the tailings, which provided a reliable approximation of the bubbling pressure, desaturation rate and matric suction (see section 2.4.1.2). Presently hydraulic conductivity of the tailings varies between 2 – 3 m/a (Blight *et al.* 2012). These results support Kossoff *et al.*'s (2014) generalised classification of tailings particles sizes to fall in the range of 625 μm - 2 mm (sand) and 3.9 μm – 625 μm (silt). It does not contain a significant number of particles sizes > 2 mm (gravel) or < 3.9 μm (clay) (Dacosta, 2017).

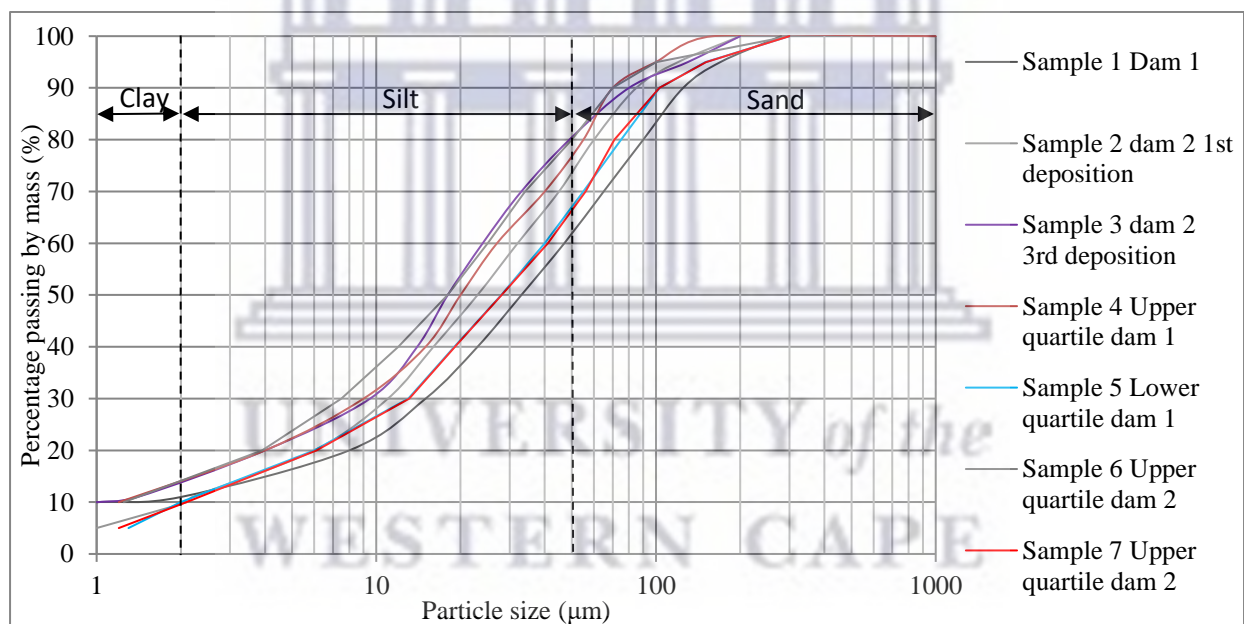


Figure 4.7: Malvern particle size distribution analysis.

4.1.2.2 Hydraulic characteristics

Results obtained from the above-mentioned analysis were indicative of the water content-soil suction relationship as illustrated by a SWCC to support the understanding of unsaturated soil behaviour. The distribution of solid particles was inversely linked to the distribution of void spaces and forms the basis for various estimation techniques (i.e. pedo-transfer functions (PTFs)) that have been proposed for assessing the SWCC (Chen, 2018). These values offer

information for further analysis into soil properties impacting on hydraulic behaviour and characteristics such as porosity (Skopp, 2011). Based on the particle size distribution analysis shown in Figure 4.7, the USDA soil textural classification system was used to classify the tailings. According to this classification system, the individual samples are classified as a loam (Lorentz *et al.*, 2019) to silty loam (Dacosta, 2017; MacRobert and Blight, 2013) which provides the first indication to expected soil hydraulic parameters and likely physical behaviour. This is shown in Figure 4.8.

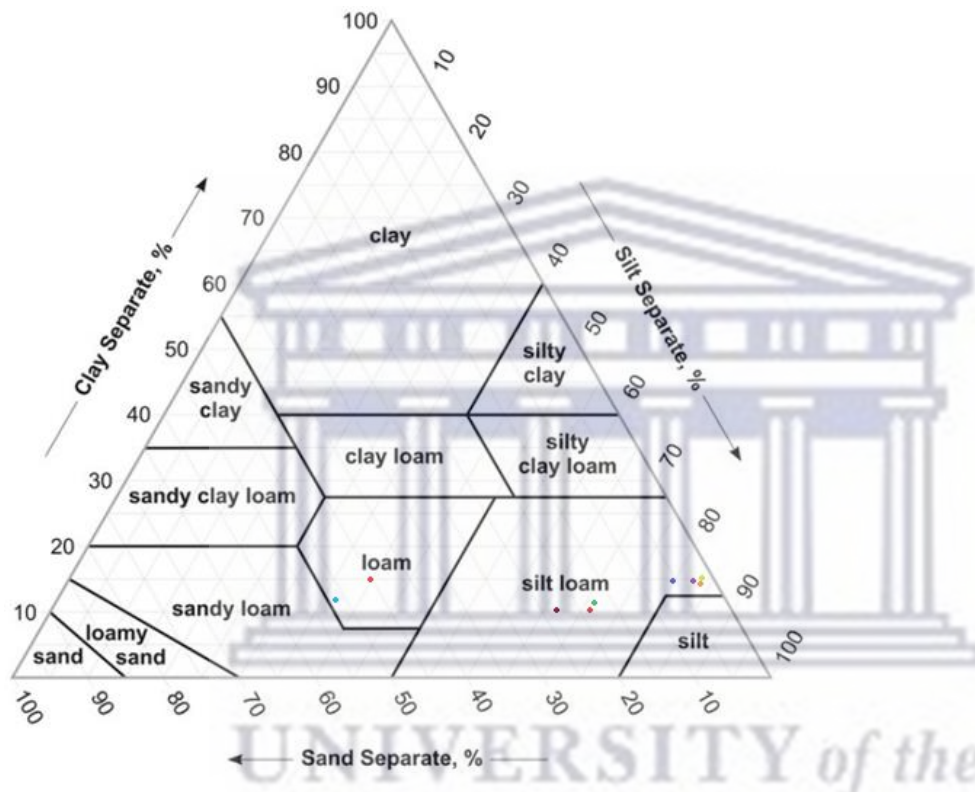


Figure 4.8: Tailings classification according to the United States Department of Agriculture.

Understanding the hydraulic properties of tailings material was essential for describing and predicting variables that may affect operational and slope stability. The most important parameters to consider were hydraulic conductivity i.e., how water moves; and water retention characteristics i.e., how water is retained. Particular properties of tailings material vary depending on their origin, mineral extraction processes, ore type and clay mineralogy (Hu *et al.*, 2017). This study considered the soil hydraulic parameters obtained from the Genuchten model (ROSETTA) as well as parameters found by MacRobert (2013) and Blight *et al.* (2012). The last two sources mentioned focussed specifically on hydraulic parameters and characteristics of tailings. These are presented in Table 4.3. Seeing as the TSFs originally consisted of two spigot deposition type dams (previously shown in Figure 3.4), material from

both dams have been considered. Dam 2 has been converted to a waste rock impoundment dam.

Table 4.3: Summary of tailings characteristics (main table from MacRobert, 2013 and supplemented by other authors as indicated).

Parameter		Value			Determination
Air Entry Value		2,549 kPa (Fig. 5.17)			Laboratory determined
Peak Dry Density (kg/m ³)		1 700 1 300 – 1 500 (Lorentz <i>et al.</i> 2019)			Volumetric Shrinkage Curves
Porosity		0,48 (0,6 - Blight <i>et al.</i> , 2012)			
RD after deposition		1,8 – 2,14 (Blight <i>et al.</i> , 2012)			Laboratory determined
Field Capacity, at 33 kPa		21% (4,3% standard deviation)			Laboratory determined Suction-Water Content Curves
Saturated Hydraulic Conductivity		7,5 × 10 ⁻⁸ m/s ⁻¹ (0,27 mm/h)			Triaxial tests on remoulded samples
Liquid Limit		Min	Max	Ave	Casagrande cup BS1377: Part 2 (1990)
		20	25	23	
Plastic Limit		Min	Max	Ave	BS1377: Part 2 (1990)
		18	21	19	
Particle Specific Gravity		3,10 (0,03 standard deviation) 3,0 – 3,6 (Fourie <i>et al.</i> , 2022)			Vacuum method BS1377: Part 2 (1990)
Grading Parameters (µm)		Min	Max	Ave	Particle size corresponding to 60% and 10% passing on the particle size distribution curves. Fala <i>et al.</i> (2005) report uniformity coefficient, CU (D60/D10), of at least 20.
	Dam 1, D ₆₀	20	60	31	
	Dam 1, D ₁₀	1	4	2	
	Dam 2, D ₆₀	21	30	26	
	Dam 2, D ₁₀	1	4	2	
Residual Volumetric Water Content θ _r (cm ³ .cm ⁻³)		0,044 0,1 (Lorentz <i>et al.</i> 2019)			Laboratory determined Suction-Water Content Curve
Saturated Volumetric Water Content θ _s (cm ³ .cm ⁻³)		0,46 0,55 (Lorentz <i>et al.</i> 2019)			Unspecified
Specific surface area		4,6 m ² /g			Generated from multipoint BET plot (Dacosta, 2017)
Field Capacity, Water Content at a Hydraulic Conductivity of 10 ⁻¹¹ m•s ⁻¹		Dam 1	22% (6% standard deviation)		Modified Kovács method on full range of grading parameters for each dam.
		Dam 2	23% (4% standard deviation)		
c' (kPa)		Silt with sand – fine		0	USCS classification (López-Acosta, 2016)
		Silty sand – coarse		0	
φ' (°)		Silt with sand – fine		25	USCS classification (López-Acosta, 2016)
		Silty sand – coarse		35	
Soil (tailings – silt) hydraulic functions according to the formulation of van Genuchten:					
α (cm ⁻¹)		n (-)		l (-)	K _s (mm.h ⁻¹)
0,001 0,014 (Lorentz <i>et al.</i> 2019)		1,581 2,1 (Lorentz <i>et al.</i> 2019)		0,5	0,27

4.1.2.3 Estimation of the Water Retention Curve

The SWCC for tailings porous medium, as established by Lorentz *et al.* (2019) (using the multi-step outflow method) and Blight *et al.* (2012) (discussed in section 5.3) are illustrated in Figure 4.9. The difference in cumulative water evaporation between the tailings and the water surface were attributed to the fact that hydraulic conductivity decreases as moisture content diminishes. From the graph it appeared that after rewetting of the drying tailings (at 300 kPa), it resulted in a steeper, almost completely reversible re-wetting branch. Blight *et al.* (2012) also mentioned slow drying may be attributed to high moisture profiles continuously being augmented by consolidation water and the addition of fine tailings (in the form of wet paste) to the surface. These findings were supported by Rodríguez *et al.* (2021) that further established that, even though sand, silt and clay tailings samples vary in particle size, they exhibit similar densities. It was also found that as particle sizes decrease, the air entry level increases. On the drying curve, a residual degree of saturation was noticed at approximately 15%. Based on these characteristics, the theoretical approach used by the current study to explain the expected hydraulic and physical behaviour of the tailings porous medium, is discussed in Chapter 5.

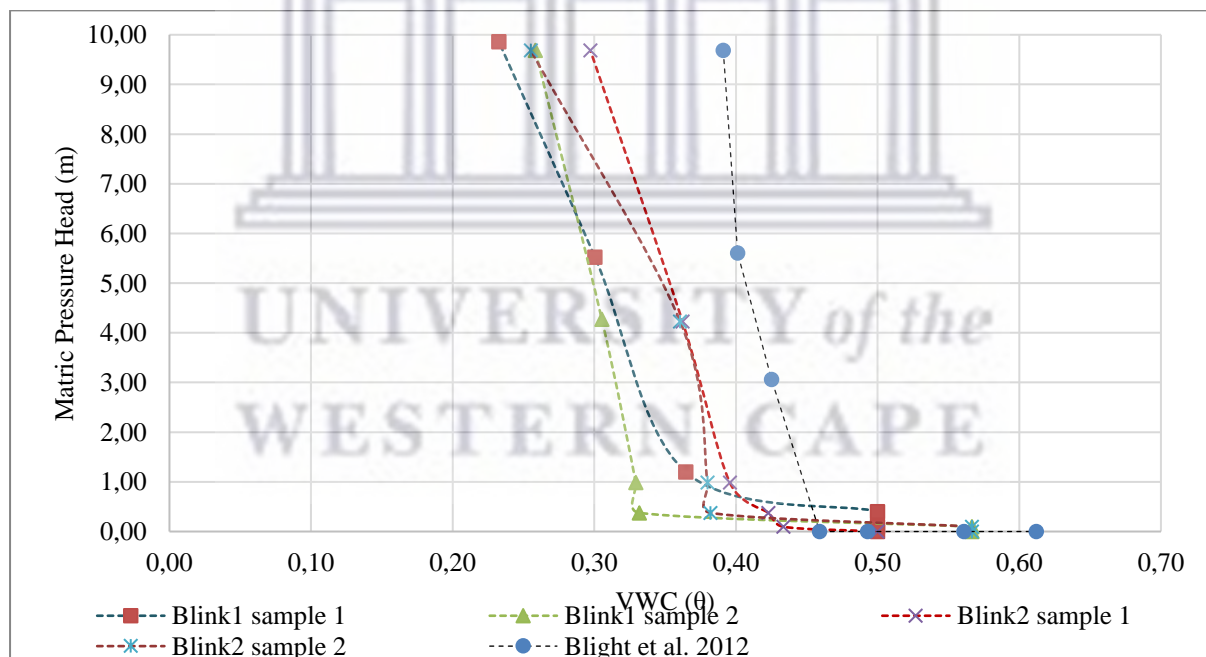


Figure 4.9: Drying characteristics of tailings (modified from Lorentz *et al.*, 2019 and Blight *et al.*, 2012).

4.1.3 Results from laboratory experiments

During the pre-simulation period, all sensors were monitored and found to be stable in the four hours preceding the application of water at the surface boundary. After application of simulated

rainfall events, there were several instant responses observed as soon as water was ponded onto the soil surface. There were also a number of delayed responses. Time-series analyses were conducted by plotting results over a period of one hour to illustrate rapid responses. Event 1 also recorded delayed responses and was subsequently also plotted across four days. For the sake of comparison, volumetric water content of event 2 and 3 were also shown over four days, though there were no delayed responses after the application of ponding events.

To further identify trends and develop valuable insights, data for each response was statistically analysed by simple analysis to determine probability (P-value) at a confidence level of 95% (or 0,05 significance level/alpha value). Probability calculations were based on hypothesis testing to determine the significance of results using the Anova: Single Factor method. P-value thresholds and corresponding levels of significance are indicated in Table 4.4 below.

Table 4.4: P-values and indication of level of significance (Schmidt and Osebold, 2017; Ozili, 2023).

Statistical measurement	Value	Interpretation	Meaning
p-value	> 0,05	Not significant	Deviation from the null hypothesis is not statistically significant, and the null hypothesis is not rejected.
	≤ 0,05	Significant	Null hypothesis rejected.
	≤ 0,01	Very significant	Strong evidence against the null hypothesis.
	≤ 0,001	Highly significant	Results unlikely to have occurred by chance alone.

It should also be mentioned that it was impossible to define an accurate phreatic surface, likely due to the soils' fineness and resulting high capillarity resulting in high matric suction (see Figure 4.9). Waswa (2013) owes this to the fact that the zero-pressure line may rise above the capillary fringe. The most significant responses are discussed below and summarised, together with interpretations, in Table 6.4.

Ponding event 1

Before application, the piezometric water level was measured manually with the use of the piezometer shown in Figure 3.5. It indicated the location of the water level just below Port 1. Assessing initial Volumetric Water Content at each probe, it is presumed that the four deep ports were located in the capillary fringe while the three shallow probes measured values close

to residual Volumetric Water Content. After application, ponding and low infiltration rates were visually observed, likely due to the soil sample's fine nature and low hydraulic conductivity. However, Figure 4.10 shows that an instant change (increasing at nearly the same rate and magnitude) in pore air pressure probes was observed at shallow ports 4 – 7, but appeared to dissipate towards deep PAPPs 1 – 3. The four deep tensiometers showed a slight response within 45 minutes after the start of the experiment (see Figure 4.12). This supports Boyle and Henry's laws that assume changes in pore water pressure – and subsequently also matric suction - were related to changes in pore air pressure ($\Delta u_a = \Delta u_w$) (Fredlund *et al.*, 1993). This observation indicated that tensiometric pore water pressure at MT1-4 in the vicinity of the capillary zone responded to compressed pore air pressure, before arrival of the wetting front. Fredlund and Rahardjo (1993) described these fluctuations in pore pressures to vary with depth and between each compacted layer, thereby demonstrating small variations (at each port) in hydrological response to external conditions.

As previously mentioned, data were statistically tested for probability with a confidence level of 95% using the Anova: Single Factor method, the p-value was 1,4E-302, rejecting the null hypothesis and proving results to be highly statistically significant.

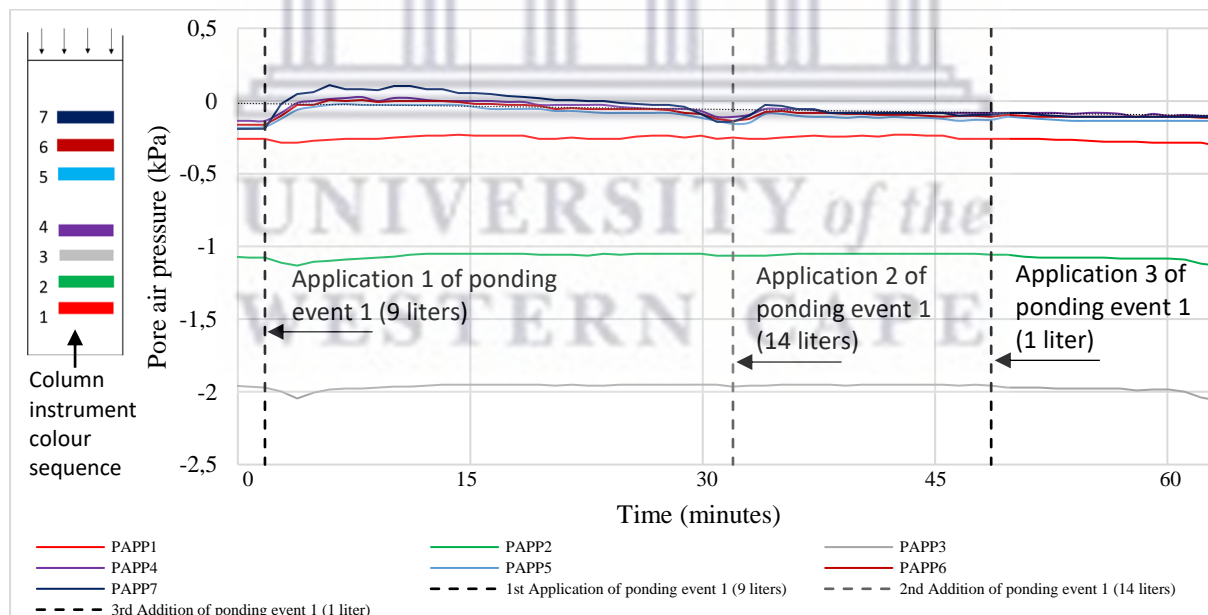


Figure 4.10: Pore air pressure observations immediately after ponding event 1.

Figure 4.11 illustrates the advancing wetting front that reached the three shallow TDRs 5-7 (0.95 m below surface) after approximately 73 hours. Although TDR1 recorded a steady, yet insignificant increase, the four deep TDRs remained fairly constant. The results of this data

analysis produced a p-value of 2,7E-123, rejecting the null hypothesis and proving results to be statistically significant.

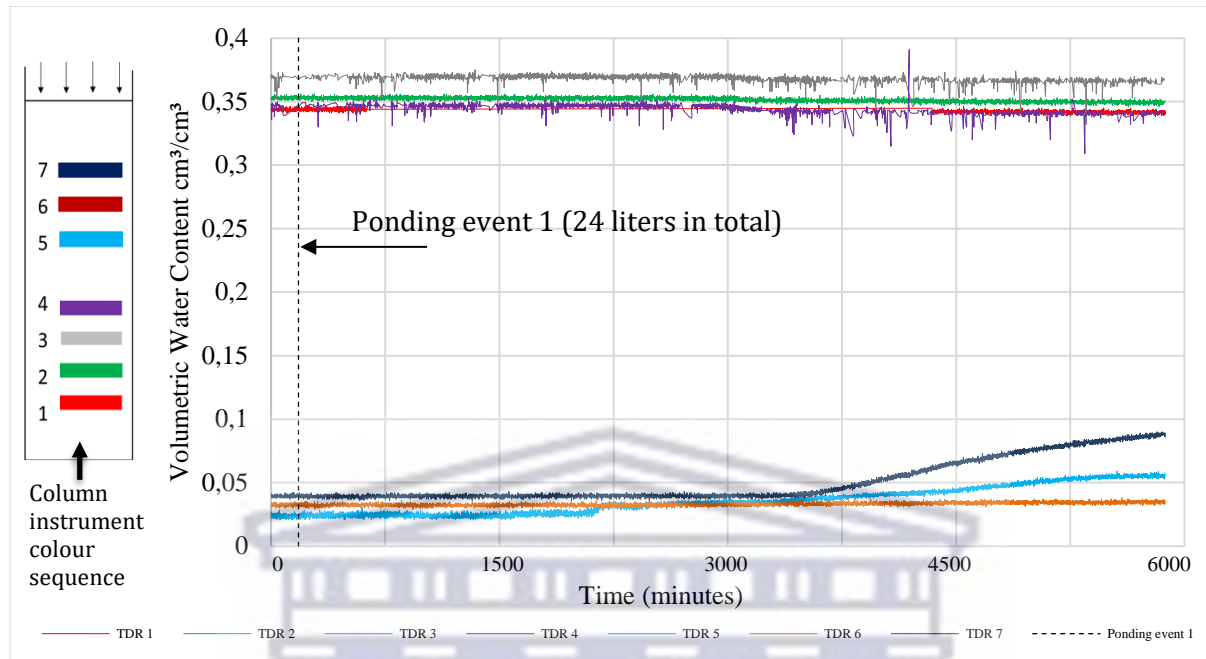


Figure 4.11: Volumetric water content a few days after ponding event 1.

The increase in pore air pressure in the vicinity of the capillary fringe, in response to the advancing wetting front, is shown in Figure 4.12. Imposed compressed pore air pressure also brought about corresponding responses of tensiometric pore water pressure at deep MTs 1-4 in the region of the capillary fringe. These results suggest that the magnitude of pore water pressure responses is directly related to the magnitude of compressed pore air pressure. Waswa (2013) observed a similar simultaneous response in tensiometric pore water pressure at different soil depths, after a rainfall event of 67,8 mm, that also consisted of a high peak 1-minute intensity of 228 mm/h. There was found to be a clear relationship between the total change in pressure potential in the vicinity of the water table and the amount of compressed pore air pressure imposed on the capillary fringe after an extended time. Similar to Torres *et al.* (1998), Waswa (2013) assumed this to be the result of compressed pore air ahead of the wetting front, pointing to signs of the LE. The proportional and corresponding change between pore air pressure and pore water pressure is therefore suggested to signal the presence of a pressure wave. All p-values were found to be highly significant [pore air pressure results p-value = 2,7E-230 and tensiometric pore water pressure results p-value = 1,6E-204].

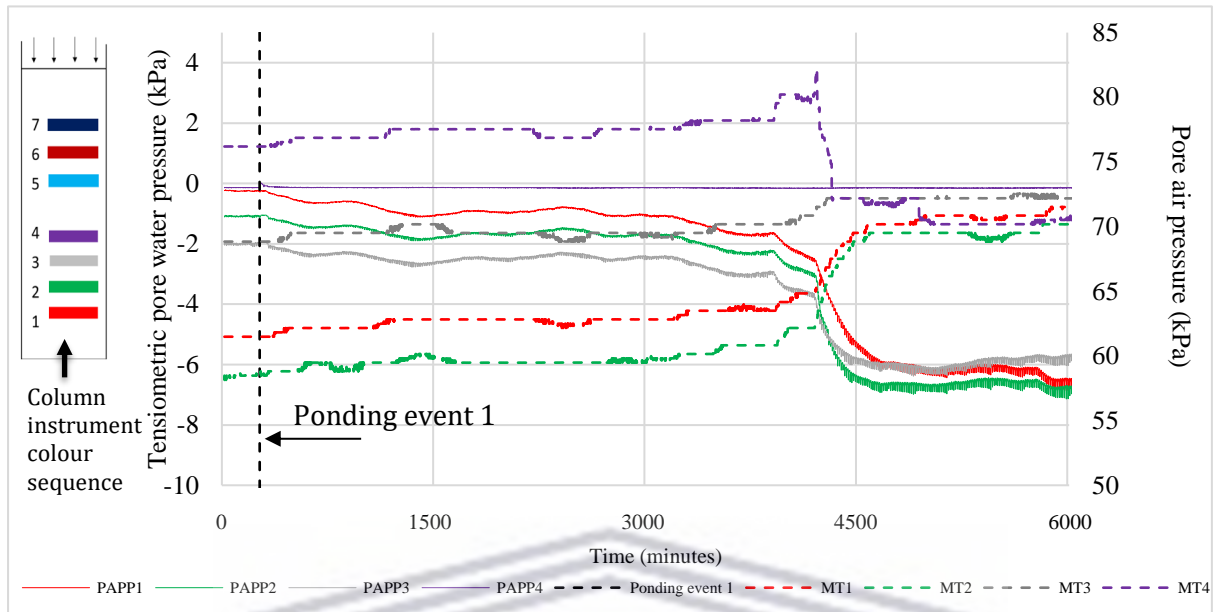


Figure 4.12: The total change in pressure directly proportional to the magnitude of compressed pore air pressure a few days after ponding event 1.

Additional analysis of pore water pressure responses after ponding event 1 is illustrated in Figure 4.13 and shows pressure conditions at 12 hourly increments across the entire column. From this illustration, it is clear that the greatest change in pressure was recorded at the 4 deep MTs, with little change recorded at the three shallow MTs. This is indicative of the wetting front not infiltrating deep enough to reach these sensors, but that recorded changes in the capillary fringe could be as a result of transient air pressure waves.

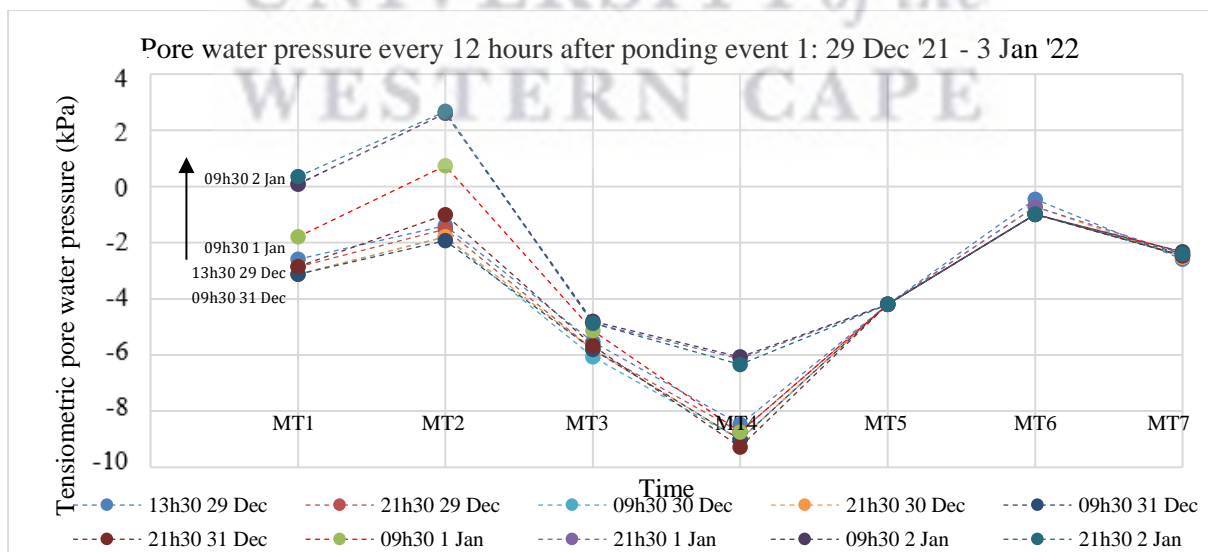


Figure 4.13: Pore water pressure every 12 hours after application of ponding event 1.

Ponding event 2

As mentioned in section 3.2.3.4 (experimental procedure), a second infiltration test was carried out in the tall soil column. Under the conditions described, it was possible to observe the effect of the advancing wetting front over time. Similar to event 1, the piezometric water level during the pre-simulation period of event 2 was observed at approximately 400 mm, meaning it was just below port 1. The four deep TDRs were again located in the capillary fringe, and it is presumed that TDR 4 was situated in the upper boundary of the capillary zone. After both applications of ponding event 2, volumetric water content at the three shallow probes immediately recorded changes, while the four deep probes increased shortly after (although at far less magnitude). This is shown in Figure 4.14. These results coincide with infiltration tests conducted by Salas-Garcia *et al.* (2017) that found a sharp increase in water content at the top of the column, eight minutes after ponding, which decreased shortly after ponded infiltration stopped. Comparable to the present study, water content measured by the deep instruments increased and decreased at a delayed time and at a slower rate as compared with those for the upper section. Similarly, Waswa (2013) observed volumetric water content at the shallowest sensor to respond after 44 minutes from the start of the experiment, before arrival of the wetting front. The p-value was 5,7E-193, rejecting the null hypothesis and proving results to be highly significant.

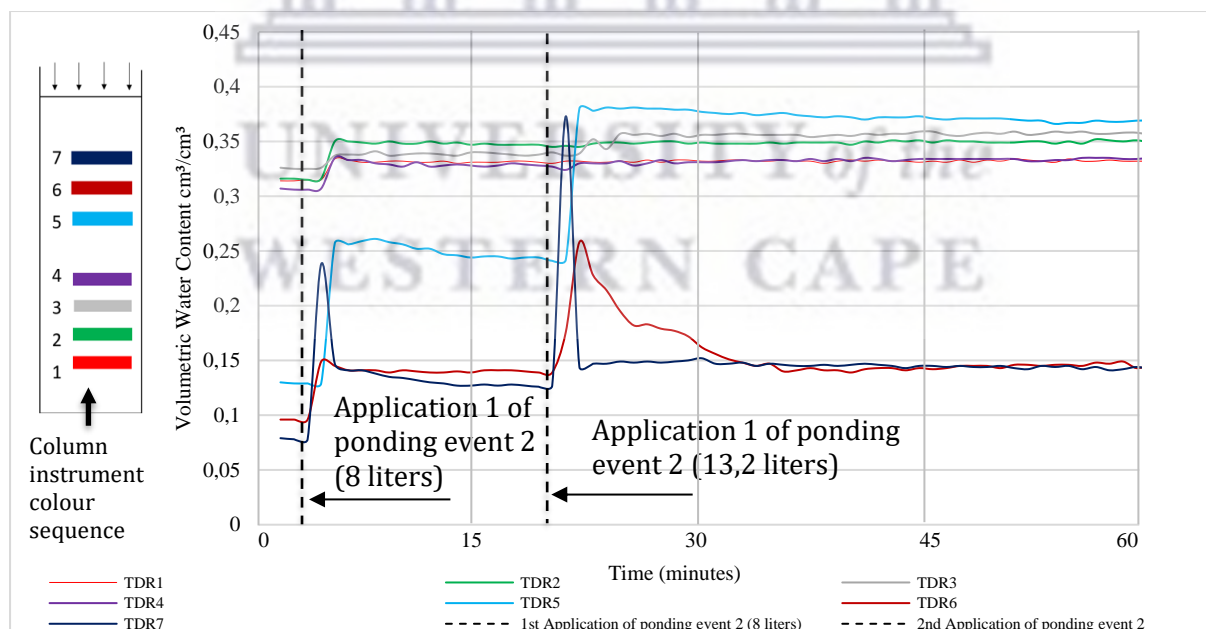


Figure 4.14: Volumetric Water Content observation before, during and immediately after 1st and 2nd application of ponding event 2.

Immediately following each application of ponding event 2, consisting of 8 and 13,2 liters respectively, pore air pressure ahead of the wetting front increased rapidly. The magnitude of increase between application 1 and 2 illustrates its sensitivity to ponding depth, which in turn is determined by rainfall intensity. Application 1 of event 2 resulted in less ponding and pore air pressure increases is at a maximum of 1,8 kPa. This is similar to Waswa's (2013) study that observed a 1,961 kPa change in pressure potential in fine soil within ten minutes of infiltration at the soil surface. The second application, of 13,2 liters, resulted in pore air pressure to increase instantly to a maximum of 10 kPa. Figure 4.15 shows the rate and magnitude of change in pressure at the lower boundary of the capillary fringe after ponding. In response, deep pore water pressure sensors recorded several rapid as well as gradual declines. MT1 for instance showed an inverted spike at application 2 resulting in a 0,5 kPa reduction in tensiometric water pressure. MT4 also decreased rapidly from 70 kPa to 60 kPa. Both MT2 and MT3 declined gradually between 10 – 50 kPa. The p-values were found to be highly significant at 9,83E-15.

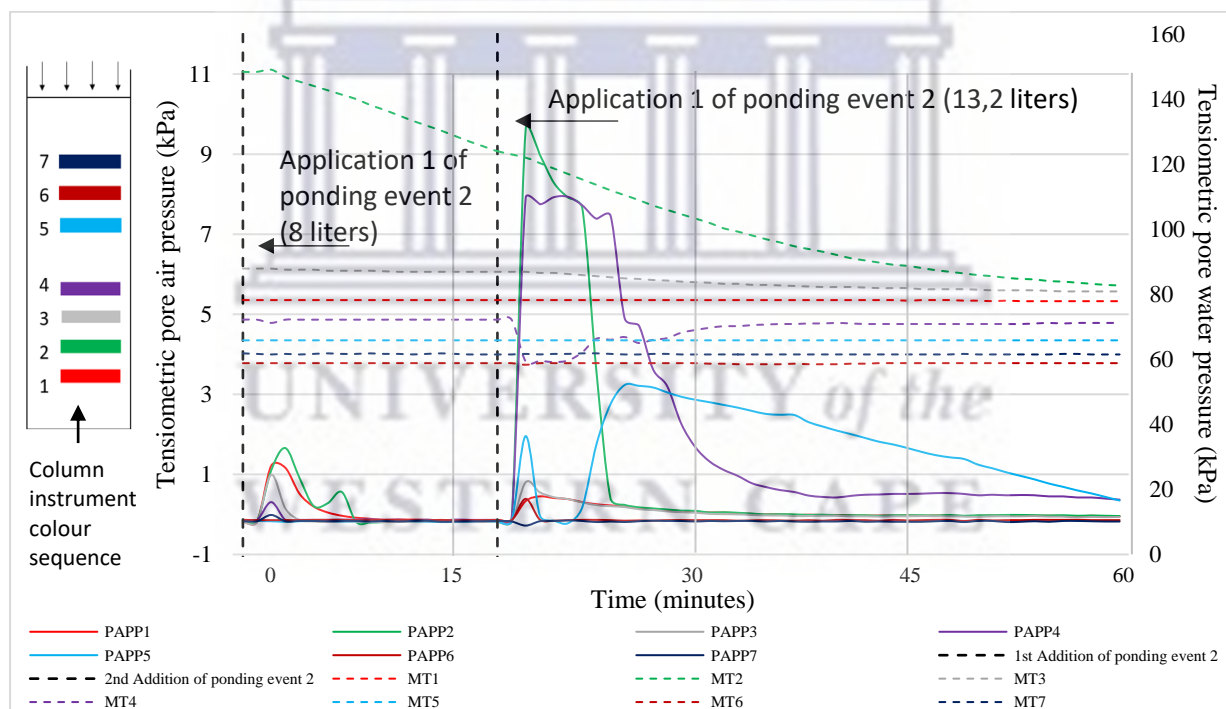


Figure 4.15: Instant response in pore air pressure immediately after ponding event 2.

For the sake of comparison, Figure 4.16 shows volumetric water content for ponding event 2 over four days, clearly illustrating no significant delayed responses. As discussed above, there were however significant rapid responses after the application of the ponding event.

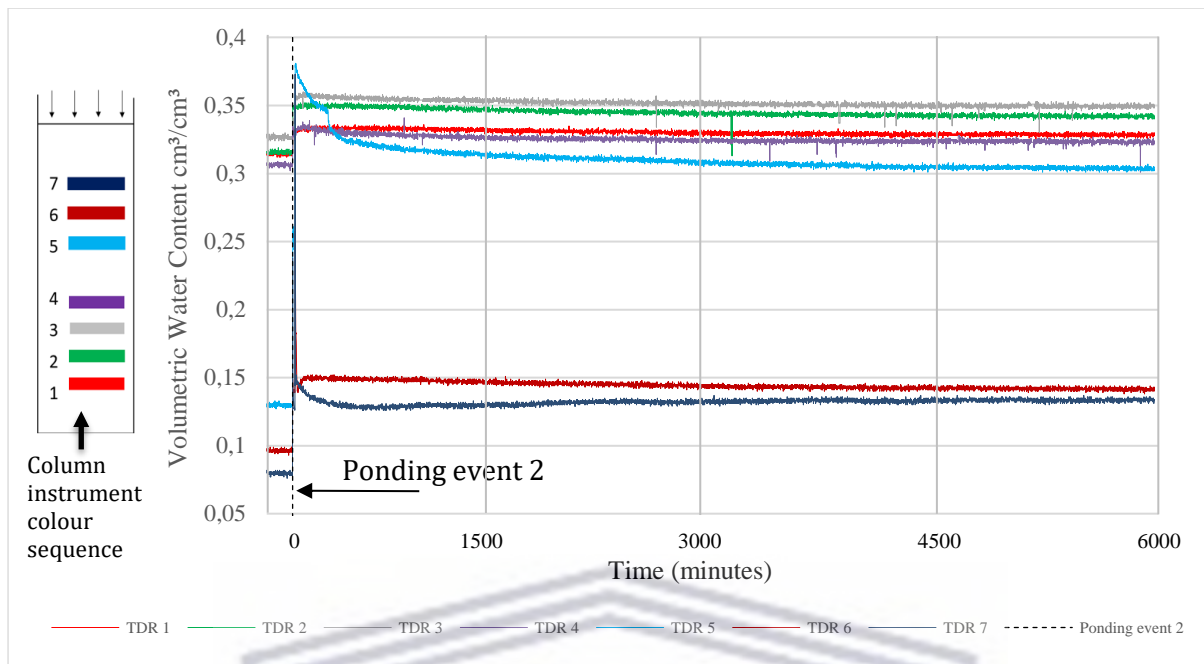


Figure 4.16: Volumetric Water Content observation before, during and a few days after 1st and 2nd application of artificial rainfall event 2.

Ponding event 3

Ponding event 3 consisted of the lowest simulated rainfall intensity. Even though there were no significant pressure changes observed in the unsaturated zone (therefore results not shown), the three shallow TDRs showed similar results to event 2. See Figure 4.17. Before application, TDR5 had a higher water content than the previous two events and resulted in a less spiked response than the other two deep TDR probes, while all deep TDRs recorded an instant increase in water content. The response at TDR5 was similar to that of TDRs 1-4 that also showed higher levels of initial water content. For the sake of comparison, Figure 4.18 shows volumetric water content for ponding event 3 over four days. The probability value was found to be highly significant at $2,3E-09$.

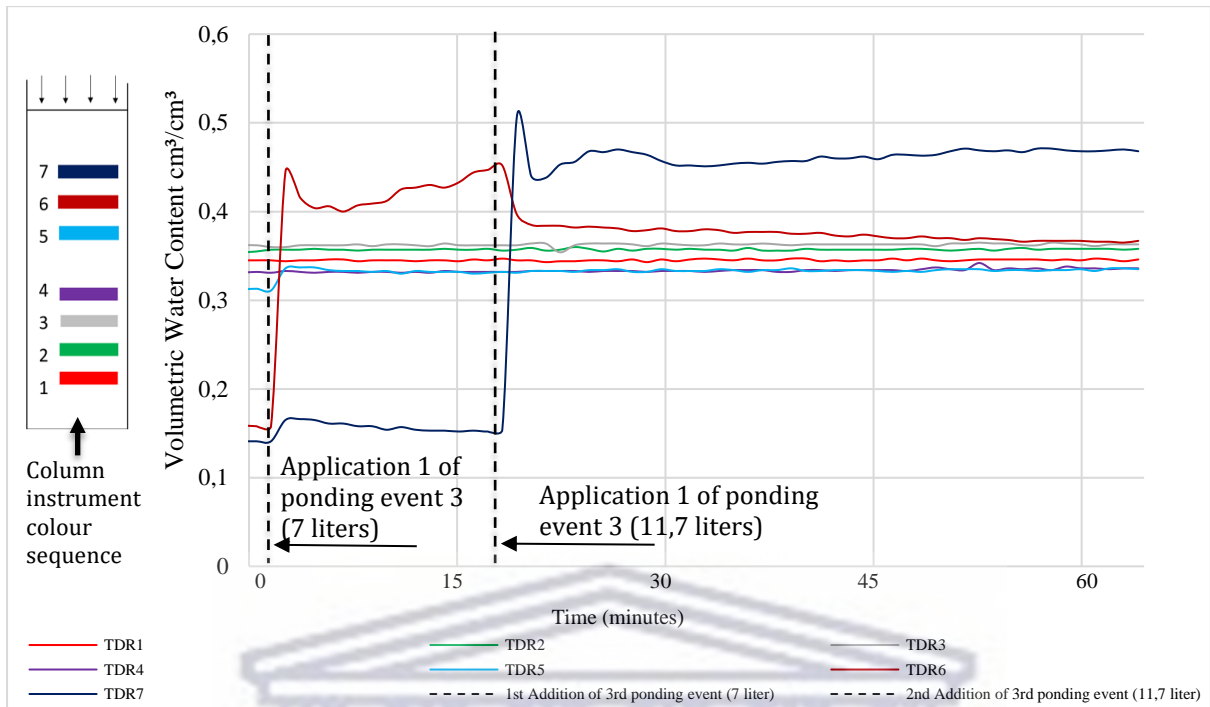


Figure 4.17: Volumetric Water Content observation before, during and immediately after 1st and 2nd application of artificial rainfall event 3.

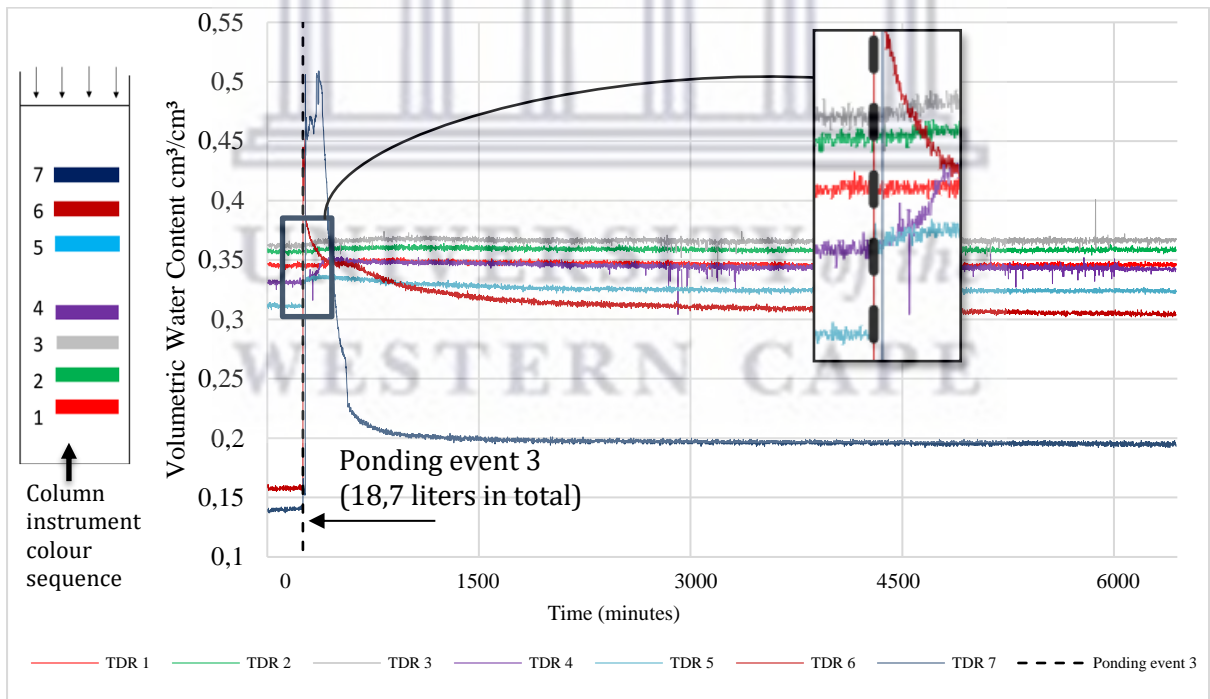


Figure 4.18: Volumetric Water Content observation before, during and a few days after 1st and 2nd application of artificial rainfall event 3.

Figure 4.19 shows volumetric water content at each port over the entire period of time. From these observation conditions, the results show that the water content, in the upper and mid-boundary increased sharply during each infiltration test (although increase after event 1 was delayed). It is further evident that the instant spike at ponding events 2 and 3 are followed with an asymptotical decrease back towards steady state values. Similar to results obtained by Salas-Garcia *et al.* (2017), the deepest sensors increased and decreased less rapidly and eventually declined to reach the same steady-state condition as compared with those of the upper portion.

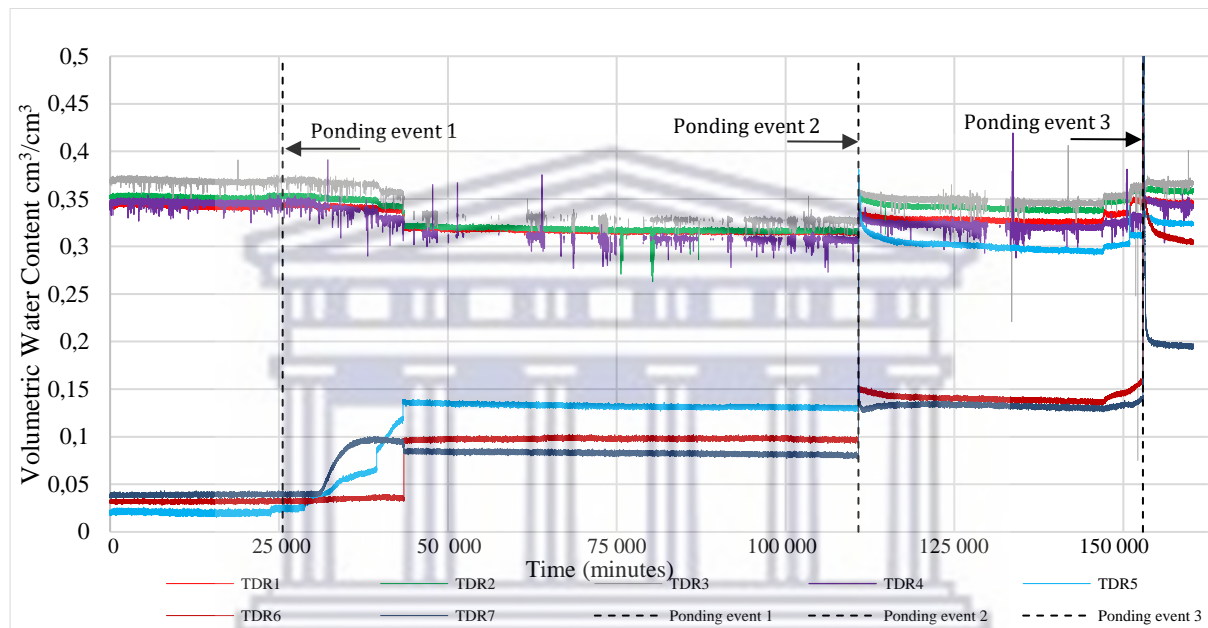


Figure 4.19: Volumetric Water Content observations over all three ponding events.

4.2 Conclusion

Climate change

Model projections and analysis of historical temperature trends indicated consistent increases across both minimum and maximum temperatures for the area under study. Even though GCMs are, to some degree, capable of simulating this first order atmospheric process, it is less capable of doing this while simulating second order atmospheric processes such as rainfall parameters (Knoesen *et al.*, 2011). Although some conclusions can be drawn from the analysis above, intermodal disagreement were evident in several categories. An interpretation of expected future rainfall conditions that could potentially contribute to slope instability, will be provided in Chapter 6.

Tailings characteristics and geohydrological properties

Based on parameters specific to the tailings material (Table 4.3), the particle size distribution analysis (Figure 4.7) and SWCC (Figure 4.9), it was possible to provide parametric projections to estimate probable physical- and hydrogeological behaviour after exposure to high rainfall intensity events. Interpretation of the hydraulic mechanisms that contribute to pore air propagation, transient pressure wave generation and rapid water table responses are discussed in Chapter 6. This discussion further highlights the relationship (and relevance) between high intensity rainfall events, the role/behaviour of tailings when exposed to these events and determination thereof through the use of laboratory experiments.

Laboratory experiments

Each high intensity rainfall event exceeded the soil's infiltration capacity, which resulted in ponding, preventing air from escaping. The advancing wetting front pushed air into the soil and since the soil surface was sealed off, air pressure increased due to compression. Most pore air pressure -, tensiometric pore water pressure -, and water content sensors responded as soon as or shortly after water was applied to the soil surface. The significant response of deep PAPPs were met with similar responses in pore water pressure. Observations indicate that tensiometric pore water pressure responded to the compressed pore air pressure, before the arrival of the wetting front. From Figure 4.12, it is also evident that the magnitude of pore water pressure responses in the vicinity of the capillary fringe are directly related to the magnitude of compressed pore air pressure. This finding suggests that pore air pressure ahead of the wetting front caused the propagation of pressure waves that mobilised pre-event water and reduced pore water suction. Table 4.5 provides somewhat of an overview of responses recorded in the tall soil column that indicate pore air propagation and transient pressure wave generation.

Table 4.5: Summary of the most significant observations that possibly contribute to transient pressure wave mechanisms contributing to the rapid mobilisation of groundwater.

Observation	Event/probe
Rapid u_a response proportional to ponding depth	Event 1,2 – all PAPPs
u_a response to advancing wetting front	Event 1 - deep probes 1 - 4
Proportional Δu_w to Δu_a	Event 1 - deep probes 1 - 4
Rapid VWC response to ponding event	Event 2,3 – all TDRs
*Delayed VWC response to ponding event	Event 1, shallow TDR 5 - 7

Matric suction and capillary pressure contribute to slope stability but observed results indicating an increase in pore water pressure has the opposite effect and contribute to a potential

decrease in the factor of safety. The rapid, non-linear response of groundwater also suggests the possibility of non-Darcian behaviour. It is further proposed that the number of irregular responses could potentially be attributed to entrapped air pockets (Fayer and Hillel, 1986). According to Cey *et al.* (2006) a variation in response could be the result of the flow system becoming increasingly distorted after repeated infiltration events resulting in soil moisture approaching saturation. All probability calculations were found to be statistically significant at a confidence level of 95%. Further analysis of observations and interpretation of responses are discussed in Chapter 6.



CHAPTER 5

5.1 Theoretical Approach

The following section will present various assumptions and theories that this study has considered and used to make predictions regarding the generation of transient pressure waves in tailings porous medium. The fundamental principles and physical behaviour related to specific soil characteristics will also be discussed, while recognising the unique engineering challenge presented by tailings dams that require analysis of both saturated and unsaturated flow under various boundary and soil conditions.

5.2 Assumptions

Although the current study followed certain conditions assumed by Waswa (2013), additional assumptions were also made. Herewith a combined list: (i) tailings porous medium is both homogeneous and isotropic; (ii) physical properties of the porous medium are constant in space and time; (iii) air is in a continuous phase above the capillary fringe and water is a continuous phase beneath the upper boundary of the capillary fringe; (iv) air and water viscosities are constant and homogeneous; (v) water is incompressible and air, as a gas, is compressible; (vi) an increase in pore air pressure increases effective stress/strength; (vii) hydraulic conductivity for an unsaturated soil is, among other things, determined by pore-size distribution, and can be estimated from the soil–water characteristic curve; (viii) climatic conditions cause matric suction to change with depth below surface; (ix) shear strength is reduced with an increase in pore water pressure; (x) evaporation (although not considered in this study) influences the SWCC and causes an upward seepage of groundwater thereby contributing to the establishment of a continuous water phase – particularly relevant to increasing atmospheric temperatures under the force of climate change; (xi) the fine nature of tailings contribute to capillary rise through soil suction; (xii) pre-event water exists permanently in the subsurface profile; (xiii) tailings are subjected to constant augmentation from sources other than rainfall – including consolidation water and moisture from sludge deposition; and (xiv) tailings dams require analysis of both saturated and unsaturated flow under various boundary and soil conditions.

5.3 Rainfall induced pore air pressure diffusion and transient pressure wave generation through porous soil media: Theories

Rainfall thresholds for landslides, particularly minimum intensity and/or duration of an event, are defined through a set of governing equations contained in empirical or physical models to

be used as an instrument for early warning systems (EWS). The challenge in predicting TSF failures should however consider the identification of complex soil processes and specific hydraulic behaviour of fluids in porous medium. It is suggested that these processes not only regulate mechanical behaviour of tailings, but also determine the physical response to events (over time and space). Following Corey (1986) this complex set of processes will depend on the following characteristics of tailings materials: (i) the ratio of specific surface area to total volume; (ii) pore size, which is related to grain size and particle size distribution; (iii) pore size distribution; (iv) mechanical stability of porous medium with regard to aforementioned characteristics; and (v) the ratio of interconnected pore volume to total volume (porosity) which is determined by structure, shape of grains, grain size distribution, packing and cementation.

Matric suction, together with the degree of saturation, influences the mechanical behaviour of unsaturated porous medium. It is determined by soil properties including particle size distribution and the geometry of the pores between the soil particles. The distribution of voids and the amount of water in voids are inversely linked to the size distribution of solid particles, therefore the fine nature of tailings makes it susceptible to the mechanism of soil suction, capillary forces and the retention of pre-event water and the perpetual establishment of a continuous water phase.

In a soil system that is in contact with the atmosphere, either the wetting phase or the non-wetting phase is at atmospheric pressure. Corey (1986) argues that if the soil is sufficiently partially saturated for an interconnected air phase to exist, the air is at atmospheric pressure while the wetting phase (i.e. soil water) is at less than atmospheric pressure (negative). To achieve a continuous air phase, an amount of approximately 15% air by volume is required (Fredlund *et al.*, 2012). Even though both the capillary zone and the phreatic zone could be saturated, they would be separated by an atmospheric pressure of zero while the capillary zone would exhibit negative pore water pressures as in the case of the vadose zone. Fredlund *et al.* (2012) states that it is the negative pore-water pressure relative to the internal or external air pressure that qualifies the soil as an unsaturated soil. Negative pore water pressure will tend to be hydrostatic and serve as the measure of soil suction exerted on the pore water by the soil (Whitlow, 2001). This was supported by Fredlund *et al.* (2012) who observed the depth of the water table and accompanying hydrostatic pore water pressure line, to point toward expected matric suction values. This line is an equilibrium pressure line that resembles either no net infiltration at ground surface or nearly equal inflow and outflow of moisture at the ground

surface. According to Corey (1986) water movement in soil depends on soil water potential which is a function of various forces acting on water, including matric and gravitational forces. It should be mentioned that this study attempted to prove that the saturated vadose zone (negative pressure) could be converted to positive pressure and be immersed by the phreatic surface through application of the energy hypothesis first presented by Waswa and Lorentz (2016a). This theory was previously discussed in section 2.5.1.1.

The degree of capillary pressure and soil suction is primarily regulated by environmental changes at ground surface and suction is only generated once water content falls below field capacity, thus creating partially saturated conditions (Blight *et al.*, 2012). Under extended dry periods, reduced rainfall frequency and more extreme maximum temperatures, evident under the force of climate change, tailings dehydrate and become unsaturated. As the tailings become unsaturated, matric suction develops, binding water more strongly in the smallest of pores at contact points between grains (Williams, 2015).

In contrast, a high intensity rainfall event resulting in excessive rates of infiltration will reduce matric suction and soil would become more saturated as more water is held by capillary forces (Fredlund *et al.*, 2012). According to Rodríguez *et al.* (2021) tailings saturate quickly but drain more than ten times slower due to high-suction capacities ranging between 2 and 300 MPa. To illustrate the impact of the above-mentioned characteristics and resulting physical behaviour of tailings porous medium, Blight *et al.* (2012) analysed a sample of 0,002 m³ that was collected along the wet beach of Dam 1 and tested it for soil suction characteristics by setting up a field experiment during the dry winter months. The experiment extended over a period of fourteen days and consisted of a bucket of tailings fitted with two calibrated gypsum block sensors, one centred 20 mm from the surface and the other at 100 mm below the surface. After the bucket of tailings was exposed for seven days, water content declined from 38,6% to 27%. During this time, suction steadily increased and reached 100 kPa. After another seven days water content had decreased to below 20% and suction was found to be close to 300 kPa. Blight *et al.* (2012) found negative pressure of this magnitude to be able to extract water up to the surface from a depth of 30 m. These findings illustrated the capillary forces and matric potential ψ_m of the porous soil medium as an important component of soil water potential ψ_s . In addition, Pelascini *et al.* (2022) suggested that, depending on the physical properties of the soil medium, rainfall induced pore air pressure changes has the potential to reach up to a few hundred kilopascals.

Various authors including Fredlund *et al.* (2012) and Waswa (2013) also found that fine grained soils release water at lower potentials, whereas coarser grained soils primarily include capillary binding and releases soil moisture at higher potentials. Porosity therefore plays a pivotal role in water holding capacity of soil. The complex geometry of the soil pore spaces around which water films are formed results in numerous air water and soil water contact angles. Matric potential is also responsible for lower potential energy of water, thereby binding it in the soil. Suction in tailings is therefore induced by the combined effect of interactive capillary and adhesive forces between the water and the soil matrix. Dippenaar *et al.* (2014) describes it as follows:

a) Negative capillary pressure in tailings is associated with matric suction. Fredlund *et al.* (2012) found the height of water rising in the capillary tube and the radius of curvature of the air-water interface, has a direct impact on the water content-matric suction relationship in soils. The fine nature of tailings and the radius of curvature of the air-water interface, contribute to the water content-matric suction relationship. Dippenaar *et al.* (2014) further explained that capillarity arises from surface tension between water and the contact angle with soil particles, causing water to wet the surface of the soil. The presence of the non-wetting air phase provides conditions for the formation of a curved liquid-gas (LG) interface, referred to as the menisci radii of curvature (R). The radius of this curvature has a significant influence on the height of capillary rise and the magnitude of the pressure difference between the two immiscible fluids, i.e. water and air (Fredlund *et al.*, 2012). The curved interface produces a surface tension force normal to the LG interface (contractile skin) creating a function of capillary pressure (P_c). This represents the pressure difference between the non-wetting phase (air pressure) and the wetting phase (water pressure) (Tuller and Or, 2004). It is referred to as the capillary pressure curve and is expressed by equation [5.1] (Bear and Verruijt, 1987):

$$P_c = P_a - P_w \quad [5.1]$$

Where P_c is capillary pressure, P_a is atmospheric pressure and P_w is water pressure. Figure 5.1 demonstrates conditions under which capillary rise takes place. Assuming the air in the void between soil particles is at atmospheric pressure ($P_a \approx 0$), the water in the void space would be at a lower pressure, $P_w < 0$. According to Bear and Verruijt (1987) the water just below the meniscus demonstrates negative capillary pressure while in unsaturated soil conditions, air pressure is higher than that of water. Farouk (2004) explained that this is due to

the tendency of soil particle surfaces to adsorb water more strongly than air, while air is compressed if it is completely covered in water. The contractile skin is therefore exposed to greater air pressure than water pressure. This difference in pressure denotes matric suction.

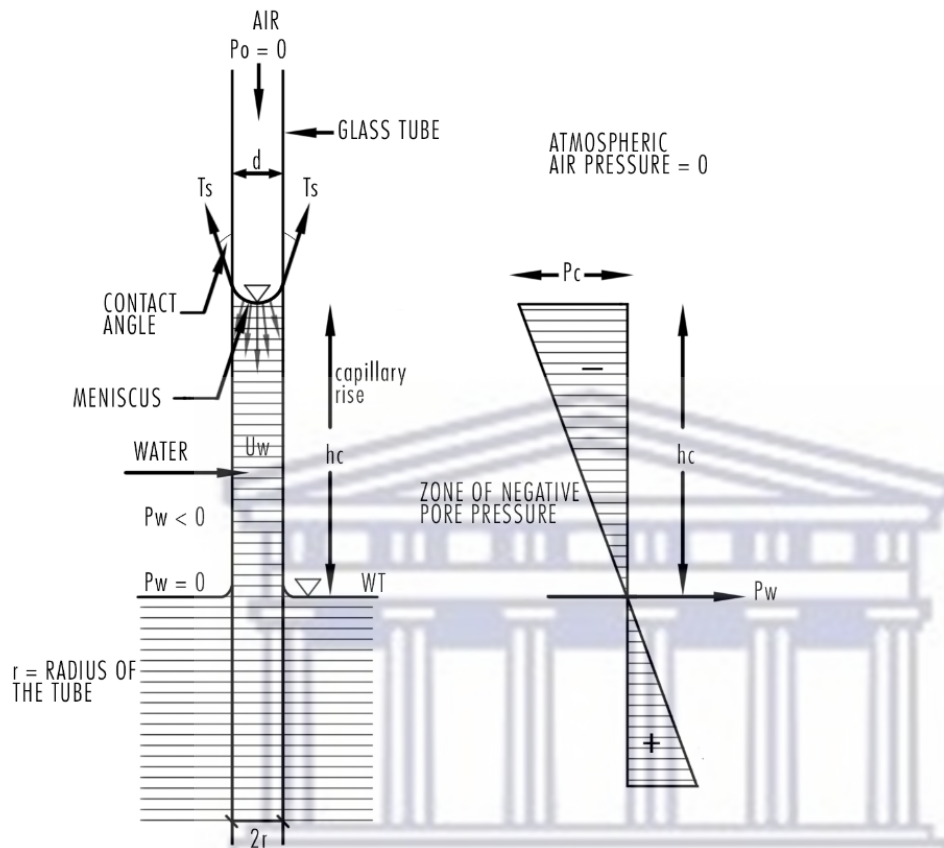


Figure 5.1: Capillary tube simulating the void between soil particles (modified from Fredlund *et al.*, 2012).

Figure 5.2 shows a minuscule portion of a curved air-water interface. Pressure is higher at the concave side of the LG interface and the pressure difference (capillary pressure) can be calculated using the Young-Laplace equation (Tuller and Or, 2004). From equation [5.2] it can be reasoned that as the radius of curvature decreases, matric suction increases, supporting the notion that suction decreases as water content rises (Farouk, 2004). Capillary pressure is therefore an indication of the inclination of the partially saturated porous medium to draw in water or to repel air (Bear and Verruijt, 1987).

$$P_o - P_c = \Delta P = \sigma \left[\frac{1}{R_1} + \frac{1}{R_2} \right] \quad [5.2]$$

Where ΔP is the pressure difference, P_0 is atmospheric pressure (external), P_C is capillary pressure (internal), σ is surface tension of the liquid-vapour interface and R is the radius of curvature of the surface along any two orthogonal tangents.

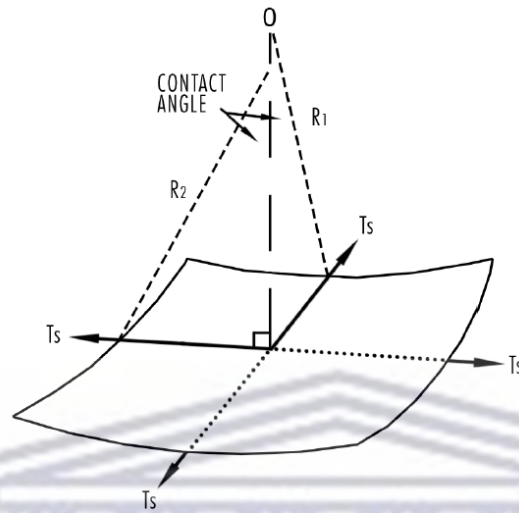


Figure 5.2: Segment of the curved air-water interface showing the dependence of capillary pressure on the curvature R_1 and R_2 (modified from Fredlund *et al.*, 2012).

According to Yuan (2013) wettability studies can quantify wetting characteristics of a solid material by determination of the solid surface tension. It involves the measurement of contact angles shown in Figure 5.3 and is defined as the angle formed by the intersection of the liquid-solid interface and the liquid-vapour interface. As the pressure difference between pore-air and pore-water approaches zero, the radius of curvature approaches infinity. The resulting flat air-water interface associated with zero matric suction, yields complete wetting at 0° , as in the case of a fully saturated soil (Farouk, 2004). Smaller contact angles correspond to high wettability, while large contact angles correspond to low wettability and compact droplets (Yuan, 2013). The angle of transition (θ) is 90° .

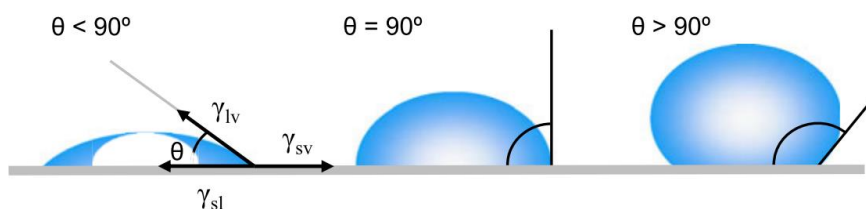


Figure 5.3: High wettability $< 90^\circ$; transition angle at 90° ; low wettability $> 90^\circ$ (Yuan, 2013).

Young's equation describes the relationship between the contact angle and the respective interfacial tensions by means of the following expression [5.3]:

$$\gamma_s = \gamma_L \cdot \cos \theta + \gamma_{sL} \quad [5.3]$$

Where γ_s is solid surface tension, γ_L is liquid surface tension and γ_{sL} is solid and liquid boundary tension.

Adsorptive forces result in the formation of hydration envelopes over particle surfaces. Hillel (1998) indicated that at low saturation rates, water forms isolated pendular rings around soil particle contact points (see Figure 5.4), demonstrating strong adhesion forces. Tuller and Or (2004) described these forces to be most prevalent in fine grained soils such as tailings. As rainfall infiltrates soil, saturation rates increase and these rings swell until a continuous water phase is formed that interrupts the continuous non-wetting air phase and reduces adsorptive forces thereby releasing water held in tension (Bear and Verruijt, 1987).

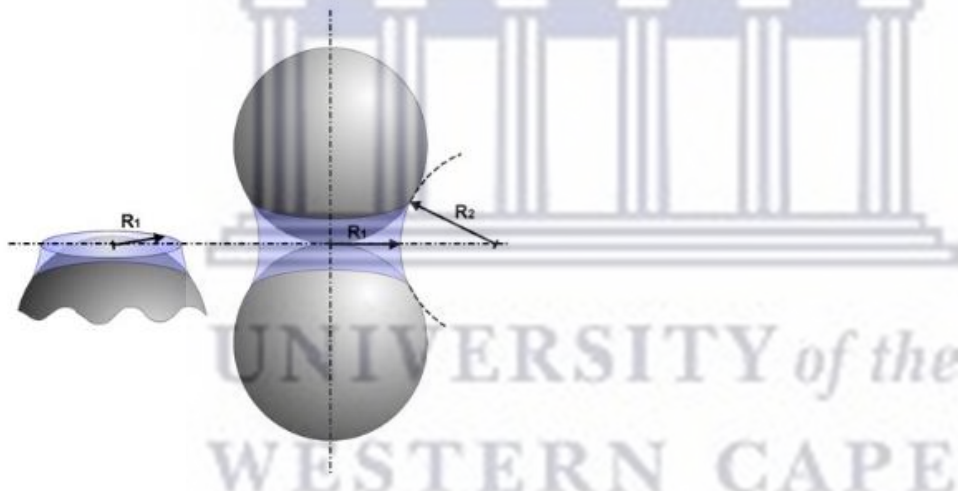


Figure 5.4: A convex-concave air-water interface at the contact of two spherical particles. The water lens has two radii of curvature for pendular ring R_1 and R_2 (Tuller and Or., 2004).

Particle size – and pore size distribution within tailings porous medium affects hydraulic properties, which determines flow parameters. Fala *et al.* (2005) described this relationship between physical and hydraulic properties as hydraulic conductivity and water retention characteristics. According to Darcy's Law, groundwater discharge is proportional to the hydraulic gradient and properties of the porous medium. Whitlow (2001) further states that groundwater discharge is regulated by hydraulic conductivity as well as the difference in soil water potential (ψ_s) between two points. Flow rate is therefore determined by the loss of head

and inversely proportional to the length of the flow path, allowing for the accumulation of water to the phreatic surface. Fluid velocity in a porous medium, as described by Darcy's law, is defined as the fluid flux through an elementary surface in the bulk volume, applied to small groundwater velocities to ensure laminar flow. Fluid flows through a complex system of geometrically irregular pore channels with different orientations and cross-sectional areas, resulting in both increased and decreased dispersion of flow velocities (Silin *et al.*, 2003). As the wetting front penetrates the soil profile, the average suction gradient decreases, while the constant gravitational force ensures further infiltration. In the unsaturated zone, pressure head is negative and expressed as suction head (ψ) (Hillel, 1998). Darcy's law for vertical flow is expressed as follows:

$$q = -K \frac{dH}{dz} = -K d(H_p - z)/dz \quad [5.4]$$

Where q is the quantity flowing in unit time (flux), K is hydraulic conductivity, H is the total hydraulic head (the sum of a pressure head H_p and a gravity head $H_z = -z$). Numerical experiments conducted by Cloke *et al.* (2006) confirmed that the greater the propensity for capillary fringe rise, the less likely it is that rapid Darcian flux of groundwater would occur. Richard's equation governs Darcian flow of groundwater in response to rainfall on a hillslope and may be written as (Bear and Verruijt, 1987; Iverson, 2000):

$$\frac{\partial \psi}{\partial t} \frac{d\theta}{d\psi} = \frac{\partial}{\partial x} \left[K_L(\psi) \left(\frac{\partial \psi}{\partial x} - \sin \alpha \right) \right] + \frac{\partial}{\partial y} \left[K_L(\psi) \left(\frac{\partial \psi}{\partial y} \right) \right] + \frac{\partial}{\partial z} \left[K_L(\psi) \left(\frac{\partial \psi}{\partial z} - \cos \alpha \right) \right] \quad [5.5]$$

Where ψ is groundwater pressure head, θ is Volumetric Water Content, t is time and α is the slope angle. Hydraulic conductivity is considered a key parameter, which may vary depending on groundwater pressure head or specific soil characteristics (Iverson, 2000).

5.3.1 Soil Water Characteristic Curves for Unsaturated Soils

The relationship between the physical and hydraulic properties of tailings porous medium is described by the water retention curve and hydraulic conductivity. These characteristics depend on particle size distribution as well as porosity of the soil sample. As particle size and porosity decrease, water retention capacities increase while hydraulic conductivity decreases (Fala *et al.*, 2005). Given the specific surface area of tailings particles (4,6 m²/g), these characteristics are particularly relevant (Dacosta, 2017).

The Soil Water Characteristic Curve (SWCC) was described by Tian *et al.* (2022) to reflect the relationship between water saturation and matric suction. Fredlund *et al.* (2012) highlighted its contribution to understanding the distribution of water in voids as well as the energy state of the water phase. Since matric suction is the difference between pore air pressure and pore water pressure, any change in either one of these parameters will cause a change in matric suction. The resulting change in the energy level will cause water to flow into the soil until new equilibrium conditions are reached (Rassam *et al.*, 2018). Demonstration of the energy state of the water phase plays a pivotal role in determining unsaturated soil property functions (USPFs) relevant to tailings. This includes properties such as hydraulic conductivity, water storage, shear strength and the volume-mass change functions (Fredlund *et al.*, 2012). Tuller and Or (2004) adds that it also provides an estimate of volumetric water content under a given matric potential. This implies a direct relationship between SWCC and hydraulic conductivity of the unsaturated porous medium. The soil structure would therefore regulate hydraulic properties and determine the characteristics of the SWCC. Experimental techniques used by Lins *et al.* (2009) found a constitutive relationship between soil suction and volumetric water content. The inverse simulation process further enabled accurate estimations of hydraulic properties and construction of the SWCC.

The shape of the soil water retention curve is defined by various models that consider volumetric water content or the degree of soil saturation as primary input. Amongst these is the van Genuchten model, which will also be used in this study. It is defined by equation [5.6] and allows for the characterisation of the relationship between hydraulic conductivity, saturation and pressure (Zhang *et al.*, 2022).

$$\theta(\psi) = \theta_r + \frac{\theta_s - \theta_r}{[1 + (\alpha|\psi|^n)]^{1-1/n}} \quad [5.6]$$

Where $\theta(\Psi)$ is the water retention curve, $|\psi|$ is suction pressure, θ_s is saturated water content, θ_r is residual water content, α is the inverse of the air entry suction and n is pore size distribution. The use of a SWCC to estimate soil suction is based on two points along the curve. This includes the air-entry value (or bubbling pressure at which a continuous non-wetting phase exists in a porous medium) and residual suction, with due consideration with regards to hysteresis created by the wetting and drying cycle (Fredlund *et al.*, 2012). Whether the air-

water interface is advancing or receding, different surface tension and wettability profiles exist (Bear and Verruijt, 1987). Variations in climatic conditions cause a continuous cycle of wetting and drying in tailings moisture content, resulting in continuous desorption and adsorption curves. This study suggests that the potential for these two extremes to increase in both frequency and magnitude is likely to occur under the force of climate change. The dynamic conditions created by hysteresis results in several possible observations from repeated cycles. Figure 5.5 illustrates typical behaviour between the wetting and drying curves of the SWCC.

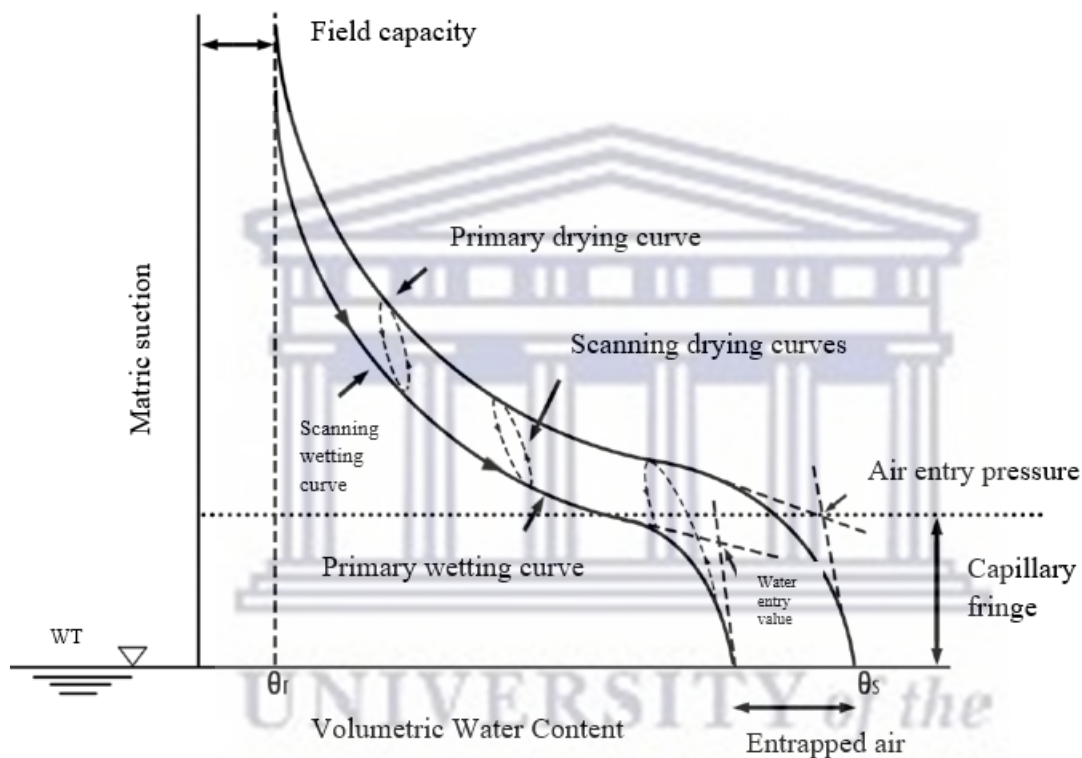


Figure 5.5: Water retention curves indicating the hysteretic relationship between the wetting and drying cycles (modified from Bear and Verruijt, 1987).

Fredlund and Pham (2006) further divided the SWCC into three distinctive zones or stages of desaturation, as illustrated in Figure 5.6. These areas are classified according to suction values and distinguished as follows:

- a) S_1 - low suction portion from a small suction value to the air entry suction (boundary effect stage);
- b) S_2 - intermediate suction from the air entry suction to residual suction (transition stage);
- c) S_3 - high suction from residual suction onwards (residual stage). This is also the point at which maximum shear strength due to suction occurs (Nishimura *et al.*, 2008). The SWCC,

together with saturated shear strength parameters (c' and ϕ') therefore provides an accurate prediction of the shear strength of unsaturated soils.

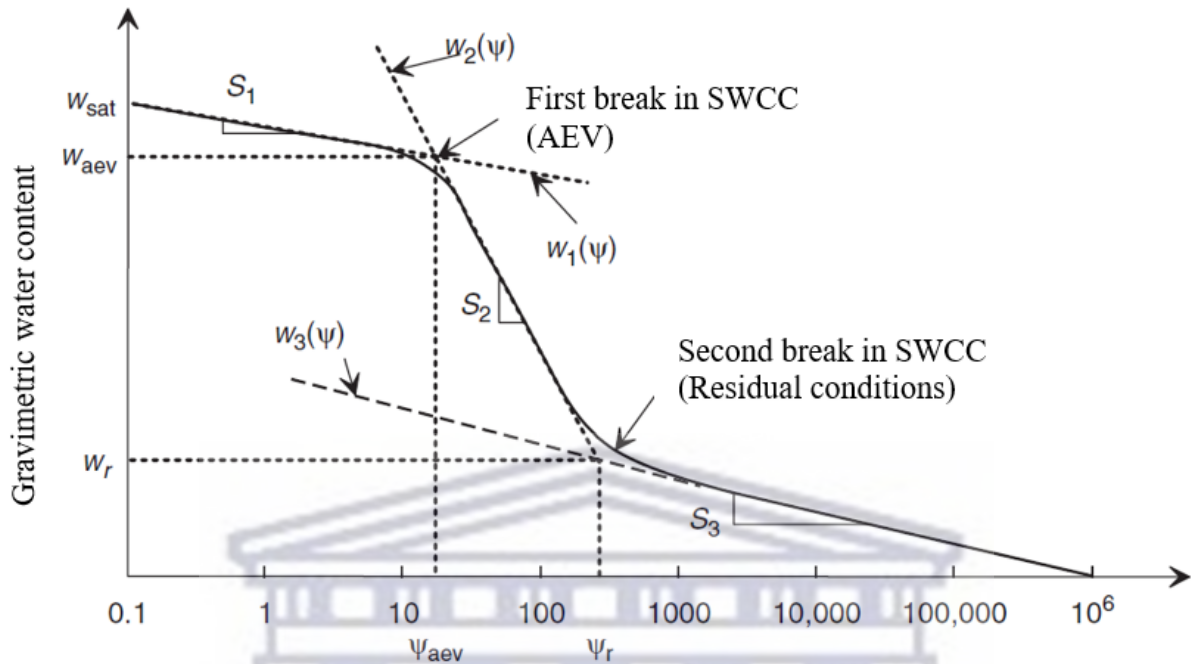


Figure 5.6: Soil water characteristics curve: drying resulting in three desaturation zones. S1: Capillary zone; S2: Transition zone; S3: Residual zone (Fredlund *et al.*, 2012).

5.3.2 Pore air pressure and slope stability of tailings dams

Pore water pressure and shear strength are considered some of the main factors when evaluating slope stability. However, the flow of groundwater is affected by pore air pressure that is triggered by infiltration after a rainfall event. Slope stability is therefore also impacted by the interaction of water and air (Tian *et al.*, 2022). Even though an increase in compressed pore air pressure reduces shear strength in the unsaturated zone and eventually contributes to slope destabilisation, it is not often considered in slope stability analysis methods (Tian *et al.*, 2022). In the case of fine-grained soils, such as tailings materials that exhibit low hydraulic conductivity, infiltration capacity is exceeded by high intensity rainfall events, thereby increasing run-off and ponding. The advancing wetting front causes an increase in pore air pressure (in the unsaturated zone) resulting in an increase in pore water pressure (in the saturated zone), higher water content and a decrease in capillary pressure (Muñoz, 2019). All of these conditions contribute to slope instability and a decrease in the factor of safety.

Sun *et al.* (2015) used numerical methods to investigate the characteristics of airflow induced by rainfall infiltration and the effects on unsaturated soil slope stability. It was found that, under these conditions, the safety factor for a given slip surface decreased during rainfall, and reached

the lowest value immediately after the event, whereafter it rose suddenly and increased until steady state conditions were reached. According to Sun *et al.* (2015) shifts in the safety factor is similar to that of the negative total air pressure acting on the slip surface. These findings were previously established by Fredlund *et al.* (1993) who demonstrated the destabilising effect of increased pore air pressure on earth dams. This was done by comparing the factor of safety at the end of construction, with and without regard for pore-air pressure. Findings pointed to lower safety factors if pore-air pressure was considered in the analysis (see Figure 5.7).

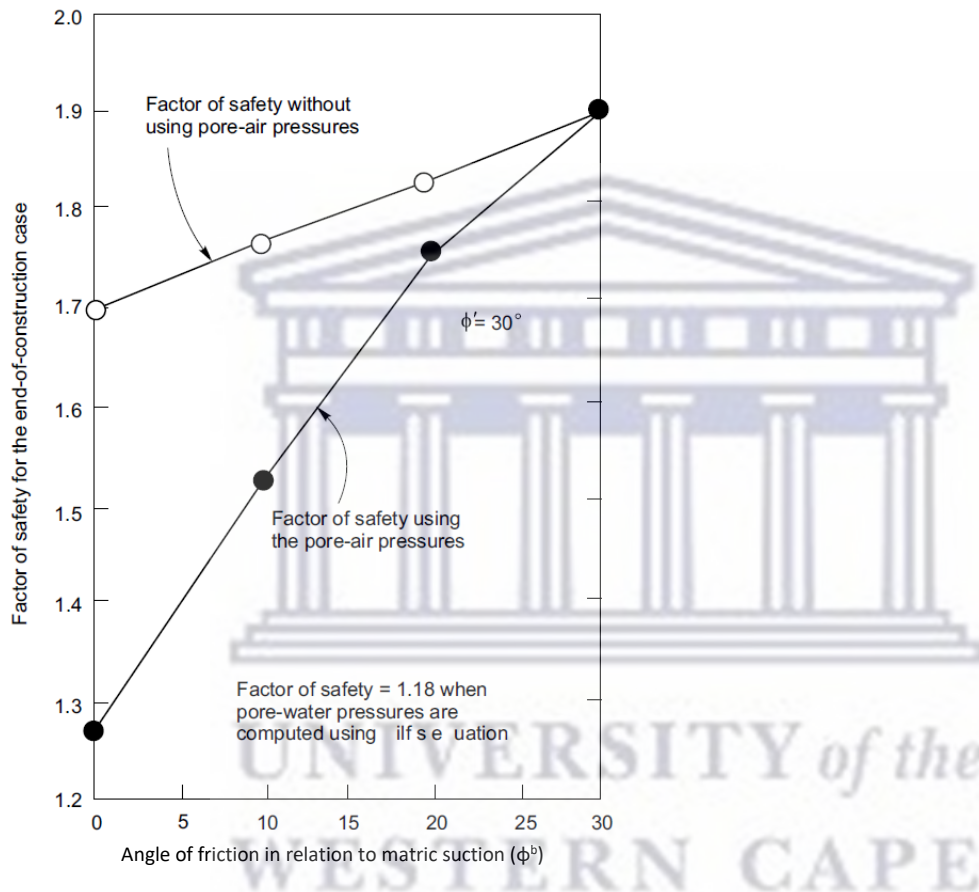


Figure 5.7: Factor of safety with respect to matric suction (ϕ^b) for the end-of-construction of earth dams (Fredlund *et al.*, 1994).

Additionally, negative pore water held in tension could be converted to positive pore water and also contribute to groundwater flow (Fredlund *et al.*, 2012). The addition of soil moisture through rainfall infiltration or the conversion of capillary water to phreatic water, could therefore be described as a dynamic element able to result in the loss of adsorptive forces and soil suction (ψ). The increase in soil weight (W) as it becomes increasingly saturated puts

further stress on shear strength and the factor of safety, which could trigger landslides. Fredlund *et al.* (1978) proposed equation [5.7] for interpreting the shear strength of unsaturated soils:

$$\tau_f = \tau_{sat} + \tau_{us} = [c' + (\sigma_n - u_a)\tan\phi'] + [(u_a - u_w)\tan\phi^b] \quad [5.7]$$

Where τ_f is shear strength of an unsaturated soil, τ_{sat} is shear strength under saturated conditions, τ_{us} is the contribution of suction towards shear strength, c' is effective cohesion, ϕ' is effective internal friction angle, $(\sigma_n - u_a)$ is net normal stress, $(u_a - u_w)$ is matric suction and ϕ^b is angle of shearing resistance due to the contribution of suction.

Pore air propagation brought about by a rainfall event, and the resulting variation in the phreatic surface, can be described by Iverson's (2000) diffusion model. This one-dimensional model is particularly relevant to the current study, since it is applicable to homogenous material where hydraulic properties do not change with depth. Similar to the HYDRUS software model, it considers the Richard's equation and assumes vertical diffusion as well as pre-event water. This model describes the pore water pressure front ψ_{rain} using the following 1D equation [5.8]:

$$\frac{\partial \Psi_{rain}}{\partial t} = D \cos^2 \alpha \frac{\partial^2 \psi_{rain}}{\partial z^2} \quad [5.8]$$

Where D is maximum hydraulic diffusivity, z is depth. The consequential development of excess pore air pressure, particularly in the unsaturated zone, results in a change in effective stress and consequent diminishment of the factor of safety.

Clifton *et al.* (1999) advised that, for unsaturated soils, the effect of pore air pressure on shear strength in the unsaturated zone must be interpreted in the context of the Mohr-coulomb strength equation. This was supported by Pelascini *et al.* (2022) who suggested that the equation [5.9] was able to accurately model a landslide on the slip surface if shear stress exceeds the Mohr-Coulomb criterion:

$$\tau_c = c + \sigma_{neff} \tan \phi \quad [5.9]$$

Where τ_c is the critical shear stress, c is cohesion (kPa), σ_{neff} is effective normal stress (kPa) and ϕ is the angle of internal friction ($^\circ$). Even though compressed pore air pressure reduces effective stress, it could also increase matric suction, further enhancing a continuous water phase. However, the addition of soil moisture through rainfall infiltration and gravitational

seepage could lead to a rise in pore water pressure, thereby changing the mechanism of soil suction (ψ) and further reducing the shear strength of the soil. Waswa and Lorentz (2016a) found another mechanism that contributes to the conversion of vadose water to phreatic water. They confirmed that, in natural hillslopes, pressure pulses generated by kinetic energy from a high intensity rainfall event, is introduced into the unsaturated zone, thereby converting capillary fringe water into phreatic water. This mechanism does however require the zone of tension saturation to extend to the ground surface. Pore air propagation and transient pressure waves thereby contribute to the mobilisation of pre-event water and change in pore water pressure, which in turn reduces shear strength of soil.

5.3.3 The phreatic surface and slope stability of tailings dams

The factor of safety of tailings embankments are closely related to soil moisture and the location of the phreatic surface. Since water content in TSFs are continually augmented by sources other than rainfall, a high groundwater table and continuous pore water phase is constantly present. In addition, TSFs could operate under undrained conditions, exacerbating pore water pressure during the application of compressive forces. The addition of soil moisture through rainfall infiltration or the conversion of vadose water to phreatic water, can change the mechanism of soil suction (ψ), thereby reducing effective stress.

Monitoring activities of tailings dams include the use of geotechnical instruments as well as open standpipe piezometers. Even though piezometers can provide large amounts of data, they are unable to measure negative pore water pressure, detect capillary water content or the matric suction potential of tailings. The resulting loss of margin of the safety factor can therefore occur without any peripheral warning (Pacheco, 2018). Chandler and Tosatti (1995) found the factor of safety in straight-line failure surfaces to reduce considerably with a rise in the water table, as illustrated in Figure 5.8. Muñoz (2019) argued that this assumption relates shear strength to soil moisture, which modifies soil suction (ψ) thereby causing the factor of safety to equation [5.10] below:

$$FS = FS_c + FS_{\psi_s}^{-b} \quad [5.10]$$

Where;

$$FS_c = \frac{c'}{\gamma_t Z \sin \theta \cos \theta'} \quad FS_{\psi} = \frac{\bar{\psi} \gamma_w \tan \phi^b}{\gamma_t Z \sin \theta \cos \theta'} \quad FS_{\phi} = \frac{\tan \phi'}{\tan \theta'}$$

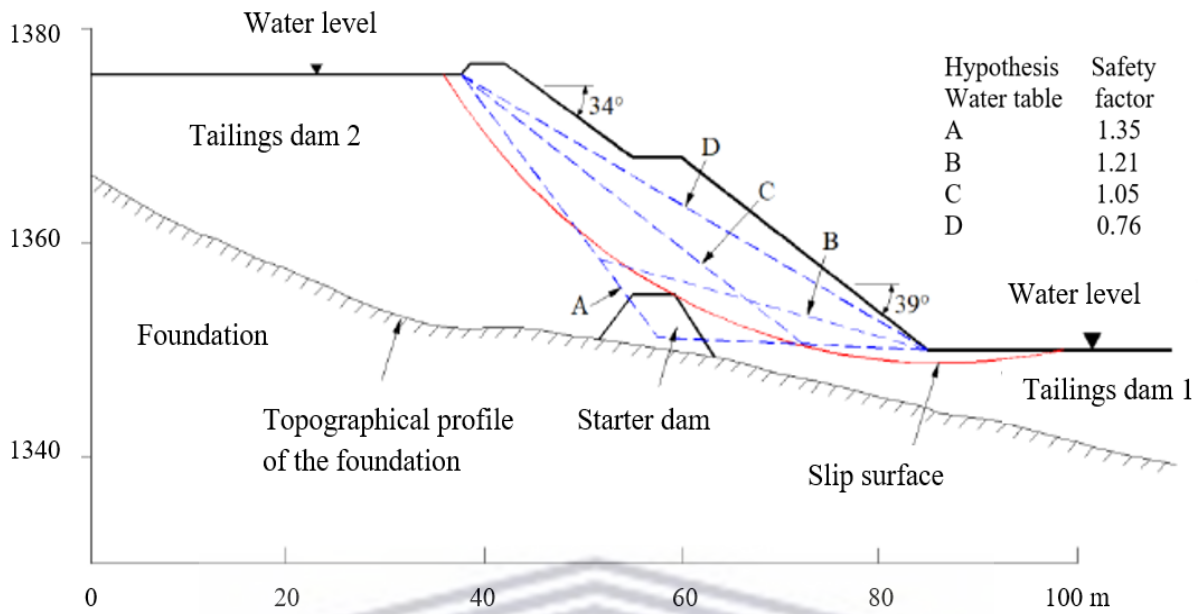


Figure 5.8: Influence of the water table on the safety factor in the case of static liquefaction and flow failure of the Stava tailings dam failure on July 19, 1985, Italy (Chandler and Tosatti, 1995).

Muñoz (2019) provided further insight into the relationship between the probability density function (pdf), cumulative distribution function (cdf) of a safety factor (FS) and constant conditions (a), soil moisture (that affects suction) (b), soil weight (c), or both (d). These results are plotted in Figure 5.9, which indicate soil moisture to play a significant role in FS when considering soil suction.

UNIVERSITY of the
WESTERN CAPE

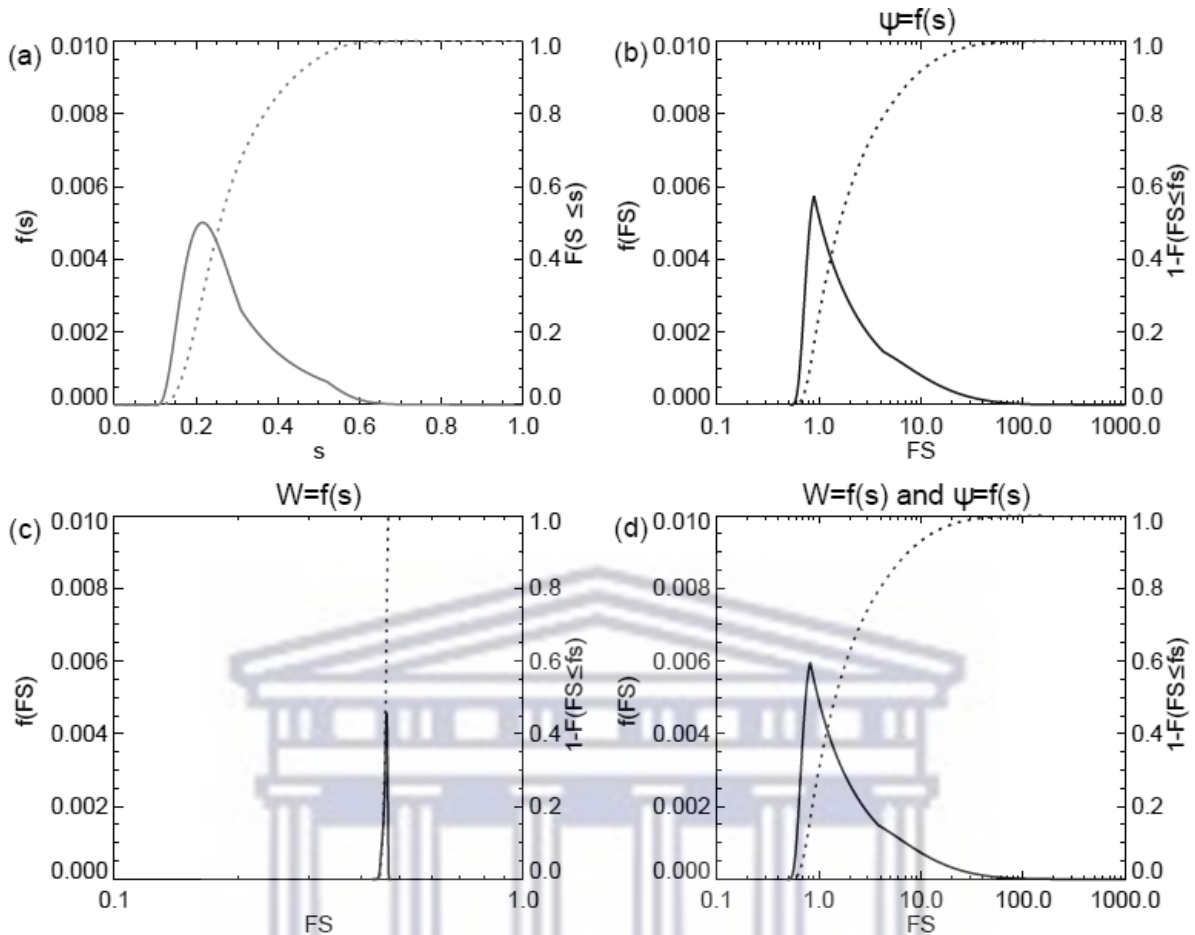


Figure 5.9: (a) pdfs (solid lines) and cdfs (dotted lines) of s and FS when s affects (b) soil suction (ψ), (c) soil weight (W), and (d) both. $Z_r - 90$ cm, $\lambda = 0.22$ d⁻¹, $\alpha - 1.5$ cm, $\Delta - 0$ cm, $E_w - 0.01$ cm d⁻¹, $E_{max} - 0.45$ cm d⁻¹, $\psi_s - 9$ cm, $b - 4.38$, $k_s - 100$ cm d⁻¹, $n - 0.42$, $\beta - 12.7$, $s_h - 0.08$, $s_w = 0.11$, $s^* = 0.31$, $s_{fc} - 0.52$, $c - 2$ kPa, $\gamma_d - 18$ kN m⁻³, $\gamma_w - 10$ kN m⁻³, $\gamma_t - 16$ kN m⁻³, $\theta - 50^\circ$, $\emptyset - 15^\circ$, $\emptyset_b - 10^\circ$ (Muñoz, 2019).

5.4 Numerical modelling for unsaturated water flow

Numerical simulation, such as finite element analysis, is often used to assess physical behavior and the stability and safety of tailings dams. These simulations require input parameters, which are typically obtained from laboratory testing. By using these input parameters, numerical simulations can provide a detailed understanding of the behavior of tailings dams under different conditions, including seepage, deformation, and seismic loading (Hu *et al.*, 2017). In order to facilitate the comparison of simulated (theoretical) and measured water pressure and content profiles, the same precipitation events as conducted in the laboratory were simulated by HYDRUS-1D. The measured groundwater level was used as input conditions, along with additional data from a combination of direct and indirect methods. This process enabled the

accurate estimation of physical and hydrological characteristics of the tailings porous medium to be used as input information into water flow simulations. The soil water movement simulated based on field data were analysed and compared with the laboratory simulation results.

Although various models have been employed in slope stability analysis, the majority of these have focussed on earth dams containing water and not for the estimation of a breach relating to tailings dams that include floods of high sedimentary content (Rico *et al.*, 2008a). The HYDRUS-1D model (version 4.17.0140) was selected, based on parameterisation data, to simulate water content, vertical flow and water distribution within the one-dimensional tall soil column. This numerical code facilitated the inversion of field monitoring data by using the van Genuchten model (Zhang *et al.*, 2022). Table 5.1 provides soil hydraulic parameters, according to the van Genuchten formulation, in order to facilitate input data and model these processes through saturated and unsaturated porous medium under steady-state or variable conditions (Salas-Garcia *et al.*, 2017). This research approach includes HYDRUS 1D numerical modelling that enabled the quantitative and qualitative description of pore air propagation in the tall soil column under different precipitation intensity and infiltration scenarios. The estimation of hydrodynamic parameters of unsaturated soils was also conducted. HYDRUS 1D uses a conceptual model to estimate physical behaviour by means of known inputs including hydraulic conductivity and water retention characteristics. It is also useful in verifying results obtained from measured data, in order to confirm results of quantitative assessment of soil hydraulic functions and water fluxes within the column. It should however be mentioned that the numerical approach assumes isothermal conditions and does not account for evaporation rates. The following section will provide background information and report on the formulation of responses by HYDRUS 1D.

5.4.1 HYDRUS 1D Numerical Model

HYDRUS-1D considers soil properties such as hydraulic conductivity, moisture content and bulk density. These parameters are defined in terms of averages and referred to as continuum properties of the porous medium (Tarboton, 2003). The mathematical model simulates soil moisture content and infiltration associated with unsaturated soil water flow profiles, by solving the modified form of the Richards equation for saturated and unsaturated flow (Salas-Garcia *et al.*, 2017). Richard's equation [5.11] is defined as follows:

$$\frac{\partial \theta(h)}{\partial t} = \frac{\partial}{\partial z} \left[K(h) \left(\frac{\partial h}{\partial z} + 1 \right) \right] \quad [5.11]$$

Where h is matric potential in cm, $K(h)$ is unsaturated hydraulic conductivity cm/d^{-1} , z is depth in cm, θ is volumetric water content in $\text{cm}^3 \cdot \text{cm}^{-3}$ and t is time in days. $K(h)$ and θ are solved according to van Genuchten as follows:

$$\theta(h) = \theta_r + \frac{\theta_s - \theta_r}{[1 + (\alpha h)^n]^m} \quad h < 0 \quad [5.12]$$

$$\theta(h) = \theta_s \quad h \geq 0 \quad [5.13]$$

$$K(\theta) = K_s S_e^1 \left(l - \left(l - \frac{1}{S_c^m} \right)^m \right)^2 \quad [5.14]$$

Where K_s is the saturated hydraulic conductivity in $\text{cm} \cdot \text{day}^{-1}$, $S_e = (\theta - \theta_r) / (\theta_s - \theta_r)$ is effective saturation (non-dimensional), and l is a factor of pore connectivity (non-dimensional); θ_s is saturated water content in $\text{cm}^3 \cdot \text{cm}^{-3}$; θ_r is the residual water content in $\text{cm}^3 \cdot \text{cm}^{-3}$; m , α , and n are empirical shape parameters, where $m = 1 - 1/n$. A high value of l corresponds to a low pore connectivity or a high pore tortuosity (Salas-Garcia *et al.*, 2017).

5.4.2 Variable parameters as input data for HYDRUS 1D

The one-dimensional finite element seepage model was developed using known hydraulic material properties (discussed in section 4.1.2), boundary - and initial conditions. It was run for a predefined time-step condition to predict the moisture and suction responses of the soil column. Each simulation was selected to run over the same time period as its observed counterpart to allow for accurate comparative analysis. Even though this study was interested in instant short-term flux and resulting changes in slope stability, long term water content was also analysed and compared to provide a comprehensive overview. This corresponds to some data analyses sheets illustrated in Chapter 4. The following section will explain the selection of variables made.

Water flow – Soil hydraulic property model:

The modified van Genuchten model illustrated some inconsistencies relating to the lack of second order continuity of the soil water retention function at saturation and the inability of the hydraulic conductivity function to account for microporosity. For this reason, Rassam *et al.* (2018) suggested that, for fine soils such as tailings, the van Genuchten-Mualem model with air-entry value of -2 cm should be used to improve the convergence of the numerical solution as well as the description of the hydraulic conductivity function. Selecting this option will also present a correction in the water retention function to force the slope of the retention function to become zero as saturation is approached. Although hysteresis was not included in the simulation, HYDRUS makes provision for it by using an empirical model that assumes that

drying scanning curves are scaled from the main drying curve, and wetting scanning curves from the main wetting curve.

Water flow – Soil hydraulic flow parameters:

Hydrus-1D requires the soil hydraulic parameters such as residual water content (θ_r , L3 L-3), saturated water content (θ_s , L3 L-3), saturated hydraulic conductivity (K_s , LT-1), inverse of the air entry value (α), pore size distribution index (n) and pore connectivity parameter (l) as input data (Patle *et al.*, 2017). Available soil hydraulic parameters were obtained from previous studies conducted by MacRobert (2013), Lorentz *et al.* (2019) and Blight *et al.* (2012) and supplemented with data from the Neural Network Prediction (NNP) option available in HYDRUS-1D. These parameters were determined using pedo-transfer function model (Rosetta) taken from Carsel and Parrish (1988) for the Genuchten model. The pore connectivity parameter (l) was entered as 0.5. These calibrated hydraulic parameters are shown in Table 5.1.

Table 5.1: Soil parameters for different soils used to estimate soil hydraulic functions according to the formulation of van Genuchten (Salas-Garcia *et al.*, 2017).

Soil	θ_r ($\text{cm}^3.\text{cm}^{-3}$)	θ_s ($\text{cm}^3.\text{cm}^{-3}$)	α (cm^{-1})	n (-)	m (-)	l (-)	K_s (cm.h^{-1})
Sand	0,045	0,430	0,145	2,680	0,627	0,5	29,70
Sandy loam	0,065	0,410	0,075	1,890	0,471	0,5	4,42
Loamy sand	0,057	0,410	0,124	2,280	0,561	0,5	14,59
ATC sand	0,055	0,420	0,130	1,900	0,474	0,5	21,00
The following parameters have been selected as inputs for this study:							
Tailings (silt)	0,044*	0,46*	0,0012	1,581	-	0,5	2,7

*MacRobert (2013)

Water flow - Initial Boundary conditions:

A homogeneous vertical soil profile of 2,65 m was considered as the flow domain to model recharge flux and allow for comparative analysis with lab observations. Apart from the hydraulic property functions, hydraulic boundaries were required to model the unsaturated soil behaviour. These were defined as follows:

- a) Upper boundary conditions were defined as an atmospheric boundary condition with surface run-off while bottom boundary conditions were set to variable pressure head seeing as the water table was at 2 150 mm below the soil surface. Rainfall was specified at upper

boundary as (i) event 1: 84,1 mm/h which corresponds to the 1:200 rainfall event in the area under study; (ii) event 2: 74,9 mm/h which corresponds to the 1:100 rainfall event in the area under study; (iii) event 3: 66,1 mm/h which corresponds to the 1:50 rainfall event in the area under study. As explained in section 3.2.3.4, these design storm calculations were based on data by Smithers and Schulze (2002).

b) Initial conditions were defined in terms of moisture contents in graphical mode in the soil profile. Since the water table was positioned at approximately 2 150 mm from the upper boundary surface, initial moisture content in the saturated zone was set as $0.46 \text{ cm}^3.\text{cm}^{-3}$ while the unsaturated profile was set as $0.044 \text{ cm}^3.\text{cm}^{-3}$. Volumetric water content in the capillary zone were estimated from recorded values obtained in the laboratory. Zones and spacing of nodes depicting the different initial water content levels are illustrated in HYDRUS 1 D's graphical mode, as depicted in Figure 5.10.

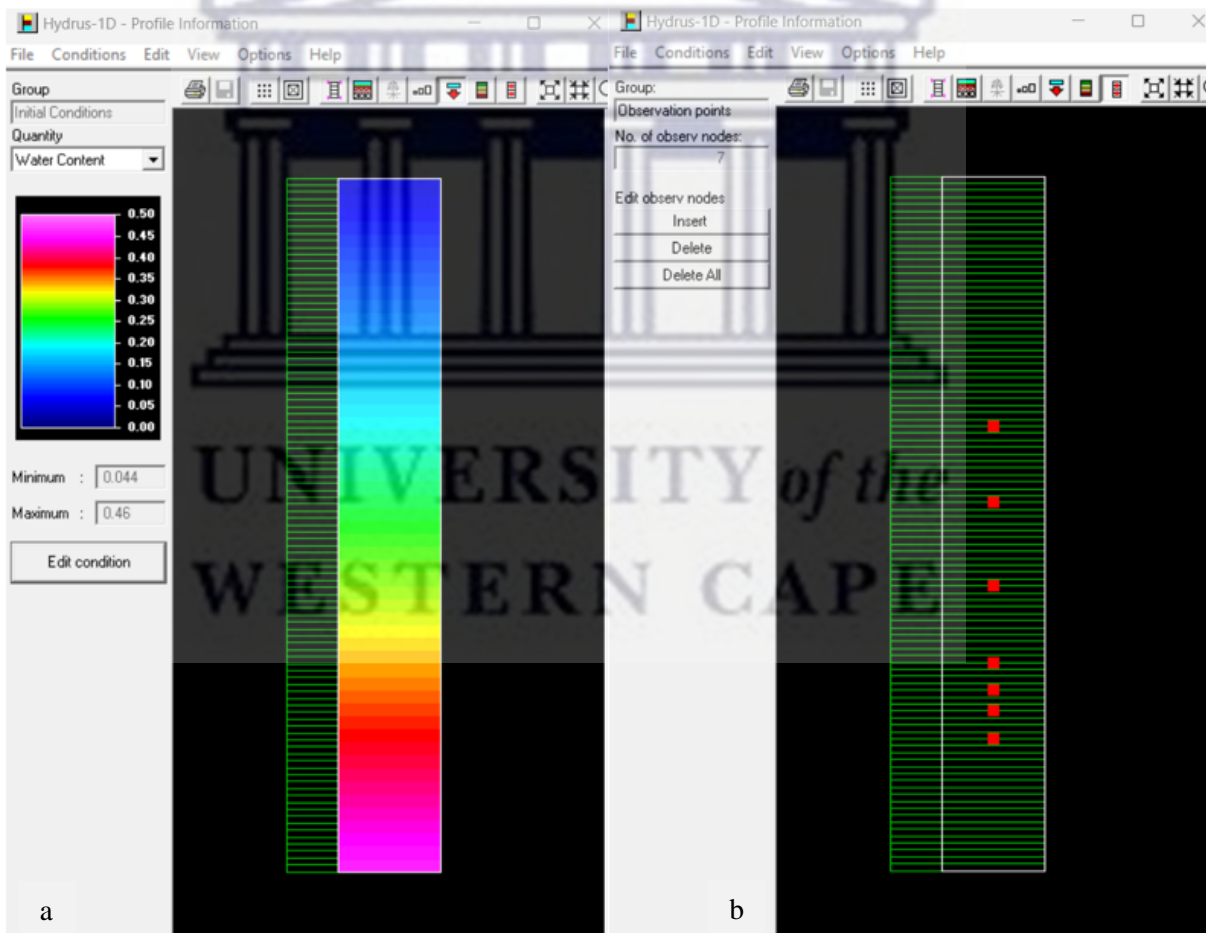


Figure 5.10: HYDRIS 1D Soil profile graphical editor: (a) Initial water content and (b) spacing of nodes.

- c) Time variable boundary conditions for event 1 – 3 were considered for precipitation rates [LT^1] for the first hour, with no events during the rest of the simulation. A fourth time variable boundary condition combining all three events were run in order to compare behaviour over the entire period of time with actual findings in the laboratory.
- d) Similar to Udukumburage *et al.* (2020), evaporation rates were not considered since individual simulations were over a short time period and protected conditions in the lab ensured negligible evaporation rates. This simplification allowed only the constant precipitation through ponding (flood conditions) to be considered.

5.4.3 Output results

Soil properties presented in Table 5.1 were used as input data to generate water pressure and water content simulations with the HYDRUS 1D model. It also provided modelled hydraulic properties such as the soil water retention curve for comparison with curves obtained by Lorentz *et al.* (2019). The following findings were observed:

The change in volumetric water content after ponding/rainfall event 1, simulated and observed, are shown in Figures 5.11 (b) and 5.12. These graphs illustrate contradictory responses over a 5-day period. Observed results indicated a delayed response and clear advancing wetting front from the boundary towards the lower probes. No significant responses were recorded at the four deep probes. Simulated responses show almost no change in the three shallow observation nodes. From Figure 5.11 (a) it is evident that infiltration only occurred up until 200 mm from the boundary, 700 mm above the top observation node. The four deeper observation nodes recorded slight increases in water content, but this is likely due to redistribution of initial conditions and water seeping to the lower part of the column under the force of gravity. It is further suggested that the uniform wetting front and redistribution of rainfall throughout the uniform soil profile, is likely a result of the homogeneity of soil properties.

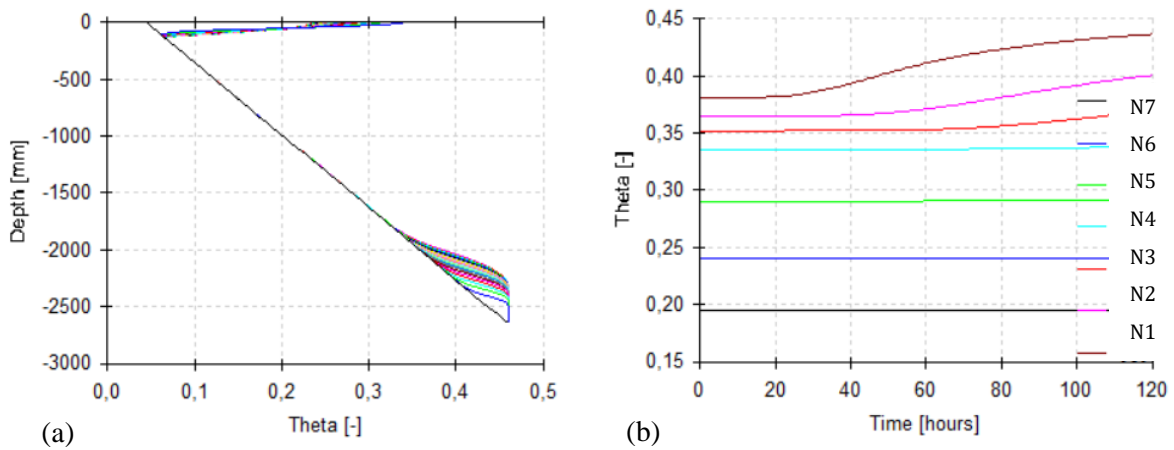


Figure 5.11: (a) Profile information: water content over depth of the tall soil column; (b) Observation nodes: water content (HYDRUS 1D).

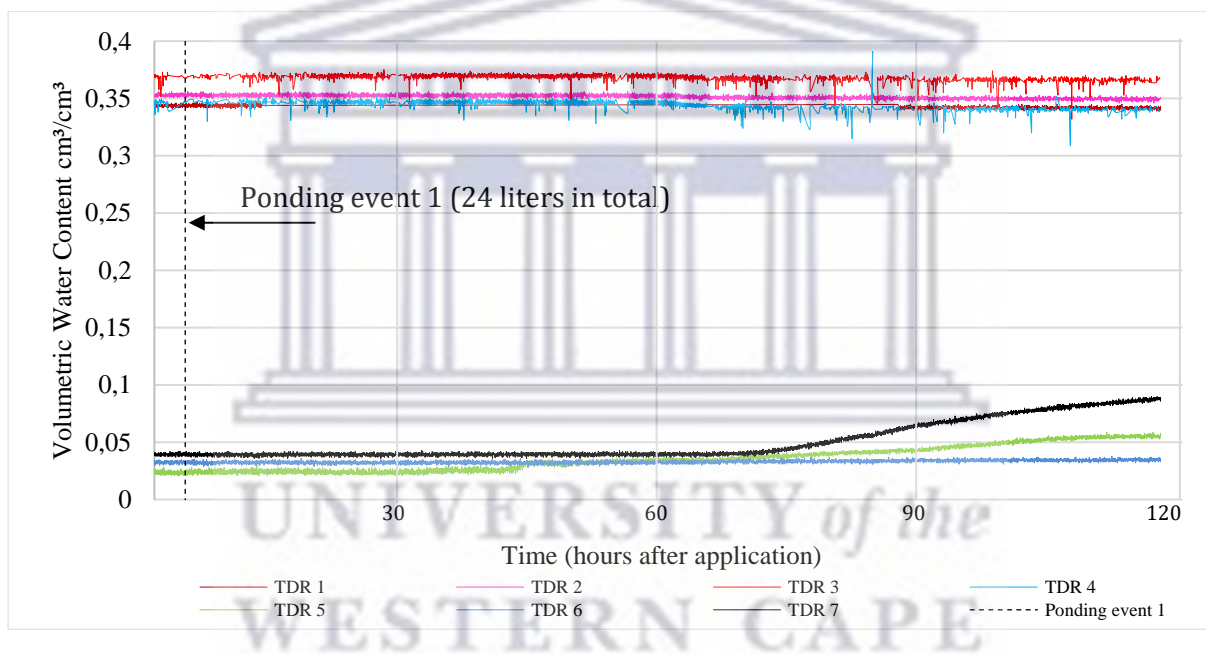
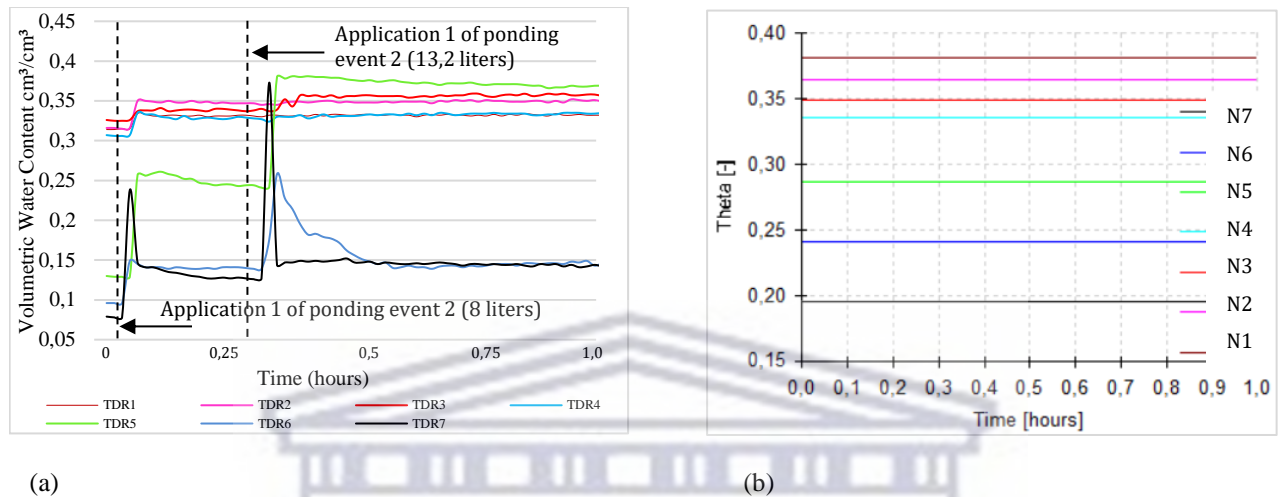


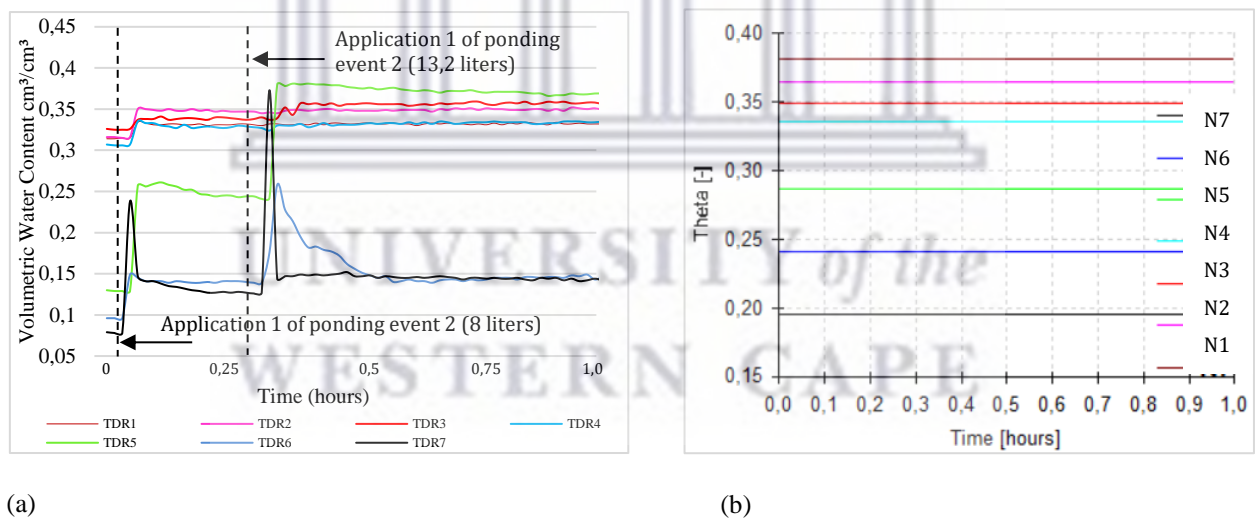
Figure 5.12: Observed Volumetric Water Content after event 1.

From Figure 5.13 (a) – previously discussed in Chapter 4 – the rapid increase in water content at the four deep probes are likely as a result of the increase in pore air pressure brought about by the advancing wetting front. The rapid and substantial increase in water content at the three shallow TDRs were likely due to preferential flow pathways created after infiltration of ponding event 1. The model’s illustration (Figure 5.13 (b)), similar to the simulation of event 1, did not register any substantial increase in water content at any of the shallow observation nodes. Even though there were some delayed increases registered at the deep observation nodes, the immediate response in observed reactions was not estimated by HYDRUS 1D. It

should however be mentioned that HYDRUS 1D will not model the pressure pulse that is the subject of this study. The model is therefore only used to illustrate that factors other than Darcian processes are involved. Similar results were obtained between observed and simulated water content levels after application/simulation of event 3 (see Figures 5.14 (a) and (b)).



(a) (b)
 Figure 5.13: (a) Observed volumetric water content and (b) Theoretical volumetric water content after event 2.



(a) (b)
 Figure 5.14: (a) Observed volumetric water content and (b) Theoretical volumetric water content after event 3.

Simulated (theoretical) and measured water content profiles over long term flux conditions were also compared. Under the observed conditions, shown in Figure 5.15, the results indicated that the water content, in the upper and mid-boundary increased sharply during each infiltration test. Observed volumetric water content results showed delayed responses only after event 1, whereafter θ_s was reached. From results discussed in Chapter 4, volumetric water content

observations recorded after ponding events 2 and 3 showed immediate changes, whereas, in the case of individual simulation events, only delayed responses were expected. Even though such responses could have been anticipated due to the low hydraulic conductivity of the soil, observed results – in contrast to HYDRUS 1D – demonstrate instant responses as illustrated in Figure 5.16.

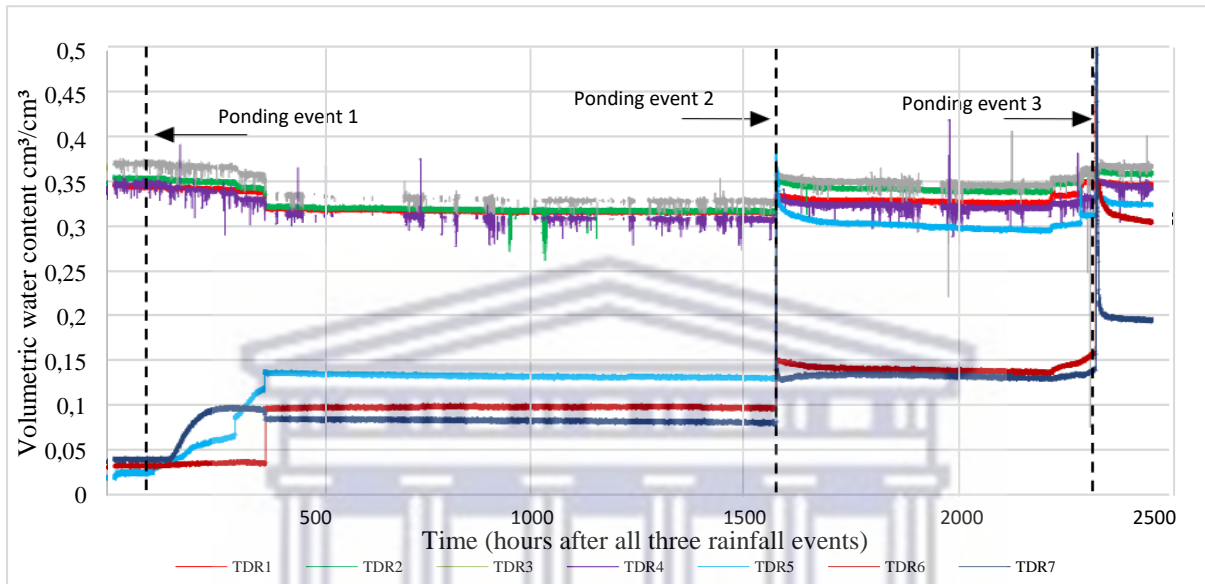


Figure 5.15: Observed Volumetric Water Content over all three rainfall events.

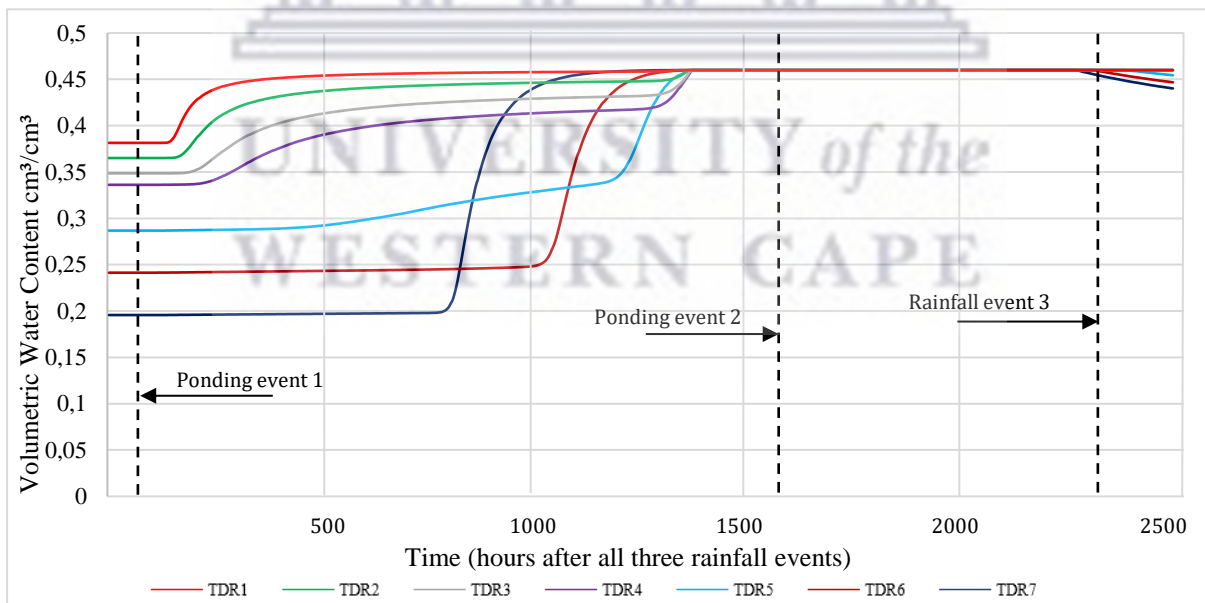


Figure 5.16: Theoretical Volumetric Water Content over all three ponding events.

Soil Water Characteristics Curve

SWCCs provide insight into the relationship between soil water content and pore water pressure. It is measured either through direct laboratory methods or indirect estimation techniques using numerical codes. From the comparative analysis between the SWCC model based on field observations and that of laboratory measurements, it is possible to identify, to some extent, the theoretical connection between soil water content and suction. Zhang *et al.* (2022) suggested that this method could enhance the understanding of hydrodynamic theory in unsaturated zones. However, both direct and indirect methods present certain challenges in terms of reliability.

Zhang *et al.* (2022) advised that laboratory methods often display limitations in terms of time, cost and accuracy. Since basic soil properties are established in the laboratory using disturbed soil samples, it often does not represent precise field conditions and therefore results may be potentially flawed. For these reasons, researchers sometimes rely on fractal theory to replace direct laboratory measurement. Indirect estimation techniques establish empirical relationships for physical soil parameters, such as bulk density and particle size distribution, and combine these with regression analysis, artificial neural network and supplementary mathematical methods to predict SWCC. However, indirect methods are only evaluated based on the statistical analysis of the measured data, and the predictions may also present inaccuracies (Zhang *et al.*, 2022).

For these reasons the SWCC produced through the theoretical simulation of soil water movement, was compared with a SWCC based on field data and laboratory analysis. Last mentioned water retention characteristics were derived by Lorentz *et al.* (2019) using the multi-step outflow method, and although these water flow parameters were replicated as input data into the numerical SWCC, results were not identical. These SWCCs are illustrated in Figure 5.17 below, with the theoretical HYDRUS 1D curve presenting residual suction at approximately 4100 mm-H₂O (40,2 kPa) and AEV at 376 mm-H₂O (3,68 kPa). The SWCC by Lorentz *et al.* (2019) displayed residual suction at approximately 1 900 mm-H₂O (18,631 kPa) and AEV at 260 mm-H₂O (2,549 kPa).

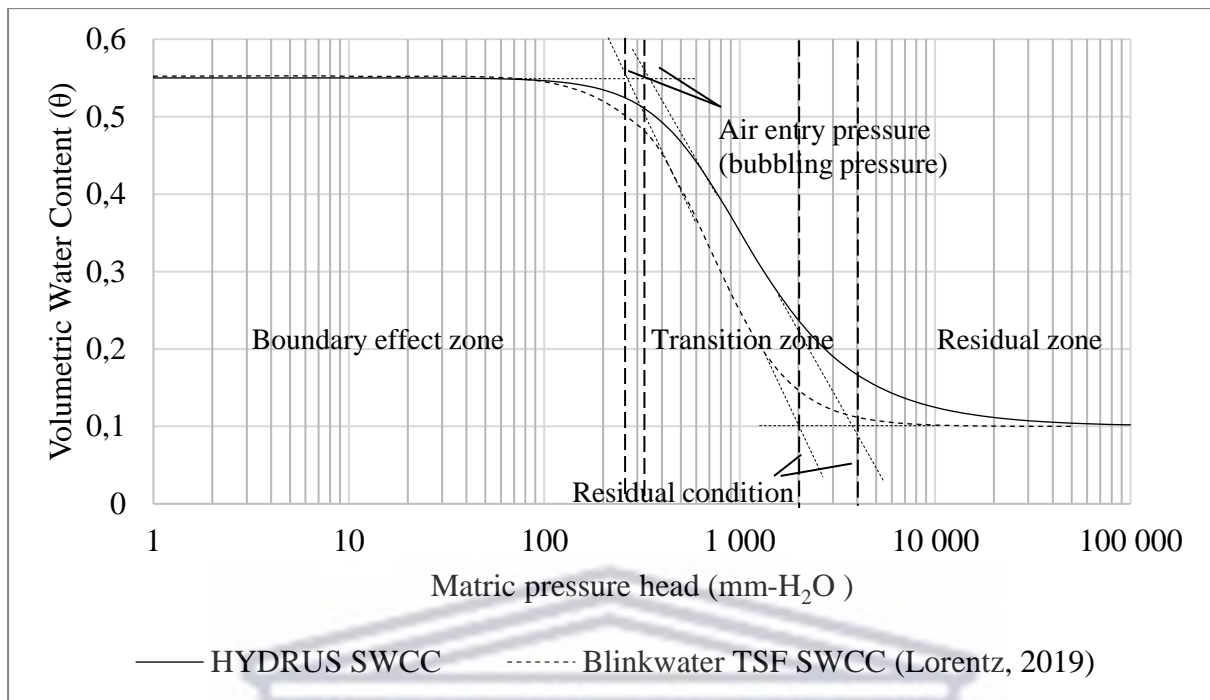


Figure 5.17: Theoretical and observed Soil Water Characteristic Curves (modified from Lorentz *et al.*, 2019).

Further analysis included a HYDRUS 1D SWCC derived from water flow parameters as suggested by MacRobert (2013) as well as relying on the NNP function of HYDRUS 1D. As previously mentioned, PTFs are used to predict van Genuchten (1980) water retention parameters and saturated hydraulic conductivity by using particle size distribution and bulk density as input data. This function enabled the inversion of field monitoring data and parameterisation of the model's parameters. These parameters were, in turn, used to simulate soil water movement throughout the tall soil column for the three simulated precipitation events. Water flow parameters used to illustrate each SWCC are listed in Table 5.2. It should also be noted that the tailings samples from Dacosta (2017) and MacRobert and Blight (2013) were classified as silty loam, while the sample obtained by Lorentz *et al.* (2019) appeared to fall within the coarser loam fraction. See the USDA soil textural classification system (Figure 4.8).

Table 5.2: Water flow parameters used for the three SWCCs in Figure 5.18.

Source	θ_s cm ³ .cm ⁻³	θ_r cm ³ .cm ⁻³	α	n	l	K_s mm/h	Method of determination
Lorentz <i>et al.</i> (2019)	0,55	0,1	0,014	2,1	0,5	0,36	Multi-step outflow method
HYDRUS 1D (MacRobert, 2013)	0,46	0,044	0,001	1,581	0,5	0,27	Laboratory determined Suction Water Content Curve
HYDRUS 1D (NNP)	0,393	0,052	0,001	1,491	0,5	10,07	Computed using the Neural Network Analysis based on PTFs (ROSETTA)

The same SWCC by Lorentz *et al.* (2019) is shown in Figure 5.18 below and compared with the two HYDRUS 1D curves detailed in Table 5.2 above. The less distinct curvature of both HYDRUS 1D SWCCs suggest an unreliable estimation of AEV of the soil sample (Fredlund and Houston, 2013) while the SWCC derived from direct measurement, illustrates a distinct break in curvature around 2 000 mm-H₂O (19,612 kPa), indicating residual suction. This curve also shows that there is a distinct air-entry at about 300 mm-H₂O (2,94 kPa). Since original soil samples analysed by the two independent studies mentioned above were also classified differently, it is expected to translate into dissimilar SWCCs. Variations are similar to results found by Rodríguez *et al.* (2021) while comparing SWCC of three tailings samples. Even though the samples had similar densities, their slight variation in size distribution, resulted in different SWCC. Although generally close agreement between moisture retention relationships were found, the finer soil sample exhibited a more gradual decrease in water content as matric suction increased. It should also be noted that similar bubbling pressures (AEV) were evident, but water entry pressures differed quite considerably. According to Islam *et al.* (2006) fine grained soils generally tend to exhibit higher saturated and residual volumetric water content, which contradicts values stated in Table 5.2.

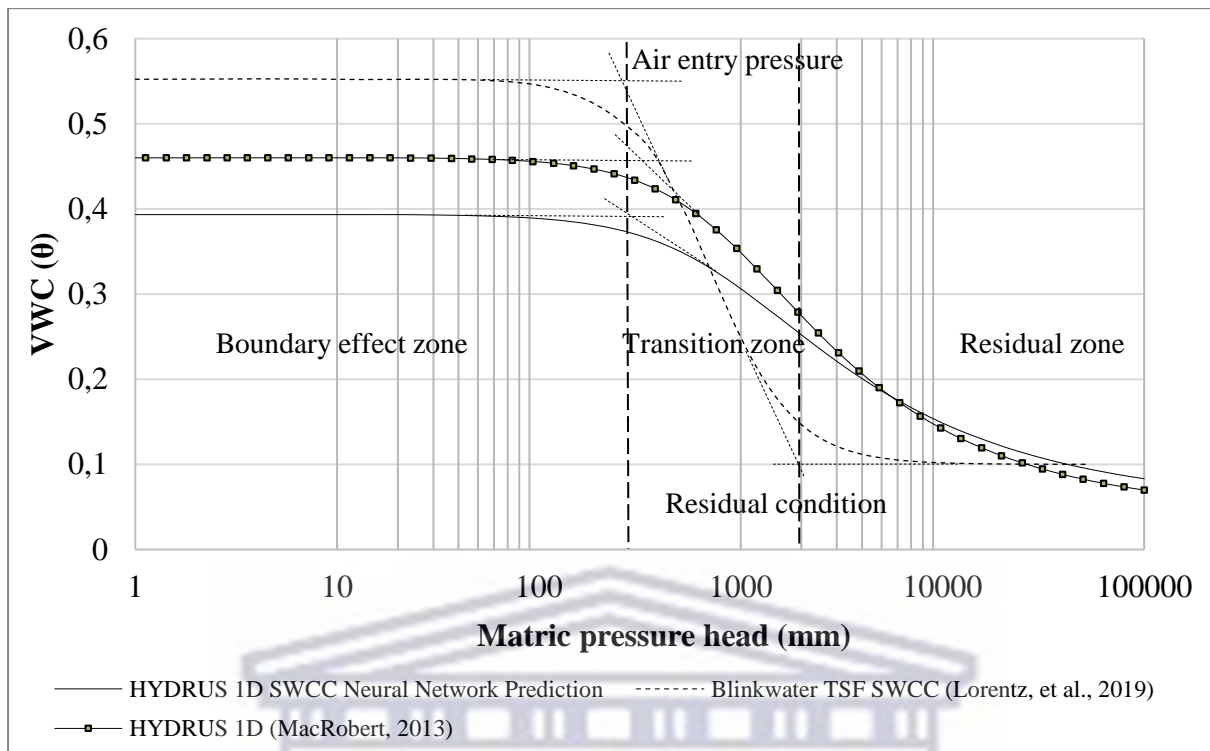


Figure 5.18: SWCCs derived by HYDRUS 1D based on (i) the NNP and (ii) MacRobert (2013) compared with SWCC by Lorentz *et al.* (2019).

5.5 Conclusion

The determination of a SWCC and other hydraulic soil characteristics was simplified through numerical studies. Even though, according to Fredlund *et al.* (2012), engineered slope designs are not readily influenced by the application of numerical modelling, it remains a useful tool to predict both long and short term geo-hydrological subsurface behaviour brought about by rainfall events. HYDRUS 1D is particularly valuable, as a numerical instrument, in establishing practices where the permanence of matric suction is part of the functionality of slopes. For this reason, the simulation presented in this study provides insight into the behaviour of unsaturated flow systems in tailings porous medium.

The comparative analysis above, does however highlight discrepancies between different approaches and HYDRUS 1D does not seem to capture all the relevant physics that are involved in simulating two-dimensional column flow. While numerical studies allow for a wide variety of factors to be considered during the design of a soil slope, its reliability is often questioned due to its limitation to consider site specific variations. The HYDRUS 1D predictions above, show saturated soils of low hydraulic conductivity to exhibit delayed

responses after a rainfall event. Even though, as discussed in Chapter 4, significant changes were delayed, modelled responses did not identify any rapid changes in pore water pressure. The simulations also suggest that water flow could be limited due to low hydraulic conductivity of the fine-grained layers. Although this would have been anticipated, some observed results (discussed in Chapter 4) demonstrated rapid response mechanisms, also at deep probes, indicating the presence of transient pressure waves, while modelled results predicted steady non-rapid responses. HYDRUS 1D does not model air pressure, which suggests that numerical modelling of unsaturated soil processes require further development.

One explanation could be the occurrence of preferential flow paths through macropores in the subsurface that has been evident in practical observations but not often included in models simulating hydrological responses (Hopp *et al.*, 2020). HYDRUS 1D, similar to various other numerical models, considers some form of the Darcy–Richards equation and requires specific estimated values of hydraulic properties as input. The accurate identification of soil hydraulic parameters for hydrological models may prove to be a challenge and the process may further be complicated by the parameterization of preferential flow in hydrological models (Hopp *et al.*, 2020). According to Hopp *et al.* (2020) this creates an inherent difference between the scale of measurements of physical soil characteristics and the scale of hydrological models that study flow at hillslope scale.

According to Sun *et al.* (2009) the use of numerical ‘desk-study’ results should be approached with caution since these are based solely on specific conditions and assumptions that may not represent actual geological and hydrological conditions. The differences in replications could, to some degree, also be attributed to field data errors caused by disturbed soil samples and/or simulated errors as a result of a selection of inaccurate hydraulic functions that can lead to a large discrepancy in water flow quantification. According to Salas-García *et al.* (2017) the differences between modelled and measured values may be caused by applied averaging data of atmospheric boundary conditions or by the possible existence of preferential flow paths in the soil. The magnitude of differences between approaches are similar to that found by Wu *et al.* (2019) while simulating soil water movement in the black soil area of Northeast China. In agreement with Zhang *et al.* (2022), it is suggested a purely theoretical approach should be supplemented with simulation based on field data to reproduce the soil water movement and change process more accurately. Zhang *et al.* (2022) also advised that the impact of hysteresis should not be ignored, so as to improve simulation accuracy and obtain a suitable SWCC. And

finally, it is proposed that the validity of different approaches should be verified and accurate parametrization should be performed to avoid errors in the prediction of hydrodynamic behaviour in fine grained soils such as tailings porous medium.



CHAPTER 6

6.1 Interpretation and discussion of results

6.1.1 Climate change

6.1.1.1 Temperature trends and predicted future temperature characteristics

The prediction of future climatic conditions in the study area was carried out based on the analysis of secondary data provided by CSAG (2020) and interpreted with reference to supporting literature. Parametric projections and analysis of historical temperature trends indicated consistent increases across both minimum and maximum temperatures. Although future emission scenarios under RCP4.5 imply less aggressive temperature increases, it would still likely result in a mean increase of approximately 3°C by 2100 as opposed to 6°C for emission scenario RCP8.5. These drastic temperature increases describe an anomaly well beyond the natural climatic variability of the study area. As a first order effect of climate change, increasing temperatures also result in an intensification of the water cycle, resulting in more intense rainfall but also more drought conditions. Since higher temperatures associated with climate change are also associated with increased levels of evaporation, it intensifies wetting-drying cycles of soils and are therefore critical in the analysis and modelling of soil moisture conditions (Muñoz, 2019). It is however suggested that the area directly under study is subjected to micro-climatic conditions, similar to that of heat islands generated in city centres, and would likely display higher temperatures. This may be caused by the absence of vegetation, topography, intense industrial activities and dust.

6.1.1.2 Interpretation of rainfall data and predicted future rainfall characteristics

Even though GCMs are reasonably capable of simulating first order atmospheric processes such as temperature, Knoesen *et al.* (2011) notes its inherent limitation in simulating second order atmospheric processes such as rainfall parameters. According to Tarek *et al.* (2021) it is generally accepted that GCMs are a major source of uncertainty in climate change impact studies. This study supports this view after finding a significant contrast in future rainfall trends from each of the GCMs analysed. Even though most projections point toward an overall change in rainfall characteristics, it is met with a high level of uncertainty due to the inconsistency in model predictions. The issue of intermodal disagreement again illustrates the challenge of accurately predicting how rainfall is expected to change. However, models pointing towards increasing rainfall intensity trends are consistent with forecasts made by Knoesen *et al.* (2011) and suggests that the area under study will most likely experience 0 - 10% changes in design

rainfall parameters (i.e., intensity) during both intermediate (2046 - 2065) and future (2081 - 2100) timeframes.

In an attempt to calculate short duration design rainfall (SDR) from GCMs, Knoesen *et al.* (2011) developed a technique which allowed for the processing of GCMs' daily rainfall records to obtain one-day mean annual maximum series (AMS) (L_{11} day) values. From these results, it was possible to calculate the SDR for the present climate. After application of this method to the study area, rainfall depth for each storm duration indicates increasing trends. This data are illustrated in Figure 6.1 below.

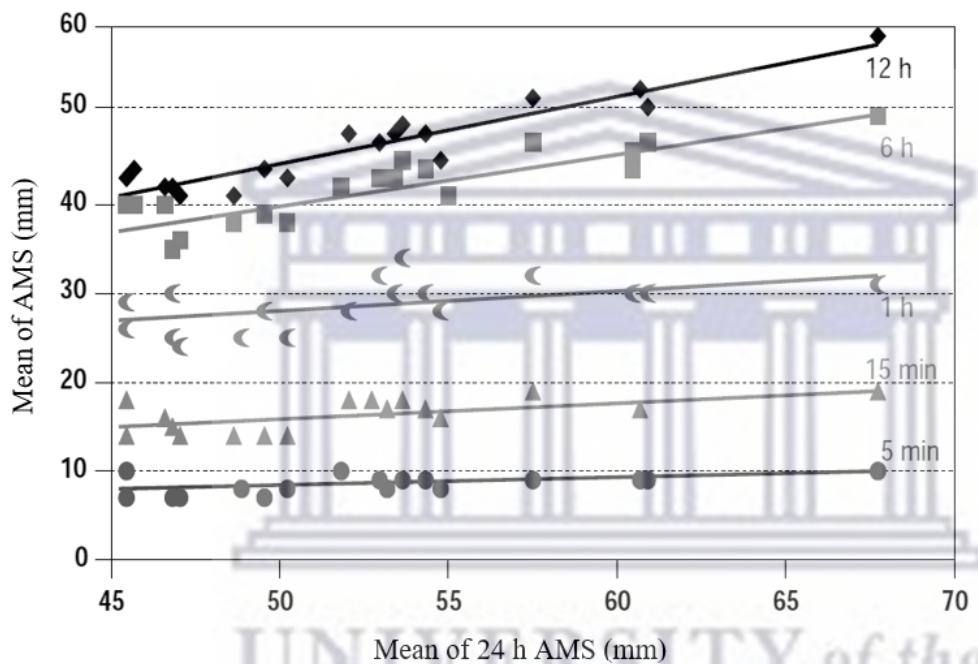


Figure 6.1: Comparison of intermediate future and more distant future scaling relationships to present climate scaling relationships for the study area, calculated from GCM rainfall output (Knoesen *et al.*, 2011).

Although there has been a significant increase in extreme rainfall events in the study area, it remains a challenge to establish consistent predictions of future events. Although intermodal disagreement contributes to this challenge, seasonal, monthly and interannual variability complicates an accurate assessment. However, based on historical data and the predictions of various academic sources (discussed below), it is expected that all seasons, but especially summer periods, would experience increased rainfall intensities. This is in line with findings by Burger (2012) that conducted a study on the effect of climate change on SDR at seven stations throughout South Africa, one of them being positioned in Limpopo. Data analyses

were divided into a study of the magnitude as well as the frequency of the SDR. Storm duration data generated from the combined autographic and AWS data were analysed for the generalised extreme value distribution (GEV) and the generalised Pareto distribution (GPD). All distributions indicated a likely increase in rainfall intensity in this region, particularly during the summer months (DJF) (Burger, 2012). According to Rapolaki (2020) the majority of two hundred extreme events in the greater Limpopo area (between 1981 and 2016) occurred during the late summer months. This prediction is supported by recent rainfall events within the study area that exceeded 50 mm/day. Over the last decade, the summer period of DJF also had two major events exceeding 100 mm/day, leading to flooding and large-scale damage to infrastructure (Munyai *et al.*, 2021). Extreme events have also been recorded earlier during the SON period, such as the event of 101 mm/h on the 21st of November 2016 (SAWS, 2020).

Models predicting higher rainfall projections with less wet days indicate that events, as well as the possibility of severe events, are likely to increase. This supports the idea that MAP values possibly only demonstrate small variations due to climate change, but intensity-duration-frequency parameters are likely to vary more significantly. Schulze *et al.* (2011a) found the average rate of change per decade of MAP in the study area to amount to less than 20 mm per decade for periods ranging from intermediate (2046 - 2065) to present (1971 - 1990), future (2081 - 2100) to present and future to intermediate. For the same timeframes, the median of changes to MAP are projected as 100-200 mm, 200-300 mm and less than 100 mm. These projections were based on averages using output from multiple GCMs. Cognisance was taken of the fact that the analysis of rainfall trends could be inherently inconsistent due to (i) intermodal disagreement and (ii) inaccurate prediction of second order atmospheric processes by GCMs. Confidence in future climatic conditions predicted by GCMs could further be flawed due to the discontinuity between the output from GCMs at spatial scale as opposed to local spatial resolutions. Even though the use of CMIP5 model rainfall data have been approached with caution due to uncertainty of reliability, intermodal disagreement and variance between seasons, the overall results of most models are consistent with predictions by various authors as discussed above.

6.1.1.3 Intensity-Duration-Frequency Curves

Based on the analysis of historical and projected future rainfall data, it was evident that existing rainfall design criteria should be updated to reflect expected climate change scenarios. IDF curves represents the probability of different intensity rainfall events occurring in relation to

the duration. This implies that each combination of rainfall intensity and duration, has a corresponding frequency or 'return period'. These relationships are illustrated as a contour plot, where the return period of each intensity is represented by a probability distribution (van der Zon, 2021). Seeing as intensity variability on sub-daily extreme precipitation is more sensitive to change, it is recognised that analysis of hourly and sub-hourly durations is of particular interest. Flood frequency analysis is required to ensure that the design of engineering structures provide sufficient stability to withstand the impact of peak floods brought about by extreme rainfall events. Seeing as climate change will exacerbate rainfall variability of both short and long duration events, historical observed data are often supplemented with rainfall-based methods of flood frequency estimations. This probabilistic approach includes the description of 'design rainfall' in terms of intensity (mm/h), frequency (return period) and duration (e.g., minutes, hours, or days) (Knoesen *et al.*, 2011). Current short duration design storm magnitudes (<24 hours), for the region under study, are summarised in Table 6.1 (Smithers and Schulze, 2002). This historical data were used to construct IDF curves that would have been relevant to the study area if climate change did not exist (see Figure 6.2).

Similar to predictions made by the IPCC (2022), Knoesen *et al.* (2011) suggested that South Africa is expected to experience an increase of up to 10% in short duration design rainfalls in the intermediate future (2046 - 2065) while some regions could reach long term increases of up to 40% by 2100. The study area has been identified as likely to experience 0 - 10% changes in design rainfall parameters during both intermediate (2046 - 2065) and another 10% during future (2081 - 2100) timeframes.

Table 6.1: Design rainfall data (mm) for Mokopane (Smithers and Schulze, 2002).

Duration	Return Period T						
	2	5	10	20	50	100	200
5 min	9.7	13.3	15.8	18.4	22	24.9	28
10 min	14.5	19.7	23.5	27.3	32.7	37	41.6
15 min	18.3	24.9	29.6	34.5	41.3	46.7	52.5
30 min	23.1	31.5	37.5	43.7	52.2	59.1	66.4
45 min	26.5	36.2	43.1	50.1	60	67.9	76.3
1 hr	29.3	39.9	47.5	55.3	66.1	74.9	84.1
1.5 hr	33.6	45.8	54.5	63.5	75.9	86	96.6
2 hr	37.1	50.5	60.2	70	83.8	94.8	106.5
4 hr	43.7	59.6	70.9	82.5	98.8	111.8	125.6
6 hr	48.1	65.6	78.1	90.9	108.7	123.1	138.3
8 hr	51.5	70.2	83.6	97.3	116.4	131.8	148.1
10 hr	54.4	74.1	88.2	102.6	122.8	139	156.1
12 hr	56.8	77.3	92.1	107.2	128.2	145.2	163.1
16 hr	60.8	82.8	98.6	114.7	137.3	155.4	174.6
20 hr	64.1	87.3	104	121	144.8	163.9	184.1
24 hr	66.9	91.2	108.6	126.4	151.2	171.2	192.3

In order to estimate the most extreme change in design storm characteristics brought about by climate change, existing design rainfall data in Table 6.2 have been amplified by 10% and used to construct future IDF curves, shown in Figure 6.2.

Table 6.2: Adjusted future design rainfall data (mm) for Mokopane.

Duration	Return period T						
	2	5	10	20	50	100	200
5 min	10.67	14.63	17.38	20.24	24.2	27.39	30.8
10 min	15.95	21.67	25.85	30.03	35.97	40.7	45.76
15 min	20.13	27.39	32.56	37.95	45.43	51.37	57.75
30 min	25.41	34.65	41.25	48.07	57.42	65.01	73.04
45 min	29.15	39.82	47.41	55.11	66	74.69	83.93
1 hr	32.23	43.89	52.25	60.83	72.71	82.39	92.51
1.5 hr	36.96	50.38	59.95	69.85	83.49	94.6	106.26
2 hr	40.81	55.55	66.22	77	92.18	104.28	117.15
4 hr	48.07	65.56	77.99	90.75	108.68	122.98	138.16
6 hr	52.91	72.16	85.91	99.99	119.57	135.41	152.13
8 hr	56.65	77.22	91.96	107.03	128.04	144.98	162.91
10 hr	59.84	81.51	97.02	112.86	135.08	152.9	171.71
12 hr	62.48	85.03	101.31	117.92	141.02	159.72	179.41
16 hr	66.88	91.08	108.46	126.17	151.03	170.94	192.06
20 hr	70.51	96.03	114.4	133.1	159.28	180.29	202.51
24 hr	73.59	100.32	119.46	139.04	166.32	188.32	211.53

Although increases seem to be relatively small, the cumulative effect of higher intensities, shorter duration and the increase/decrease in storm frequency may exacerbate the effect of extreme events and even cause a significant reduction in safety margins relating to slope stability. For example, at a storm duration of 5 minutes and a return period of 1:200 years, rainfall intensity could increase by 70 mm/h (for the intermediate period of 2046 to 2065) when compared with historical collected in 2012. Since rainfall parameters, and particularly higher intensity events discussed above, regulate infiltration and contribute to the energy hypothesis suggested by Waswa and Lorentz (2016a), it also affects pore air – and pore water pressure, both of which are important factors in the consideration of slope failures (Tian *et al.*, 2022).

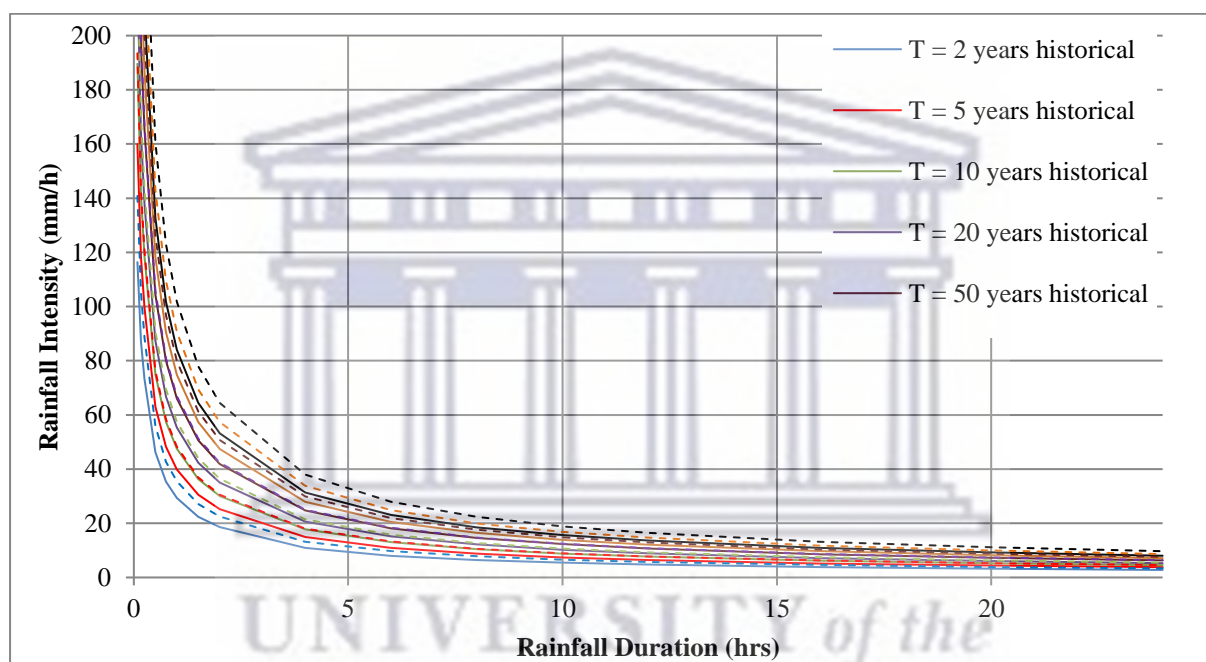


Figure 6.2: Historical and adjusted future IDF curves derived from predicted design rainfall data: Mokopane.

6.1.2 Climate change conclusions

The study has predicted climatic changes over the study area by analysing historical data and making use of existing prediction models that were downscaled to regional levels. All models indicated positive temperature changes of different magnitudes in the study area. Seeing as intermodal disagreement between circulation models were found to limit accurate second order atmospheric processes, i.e., rainfall parameters, one-day mean annual maximum series values, developed by Knoesen *et al.* (2011) were considered. These short SDR data, along with area specific climate change predictions, made it possible to determine the magnitude of increasing

rainfall intensities. Trend analysis of different historical rainfall data sets, including total monthly rainfall, observed monthly rainfall, maximum daily rainfall, number of wet days, mean dry spell duration, observed dry spell duration and rainfall events exceeding 5 mm, 10 mm and 20 mm were also conducted. It was concluded that the area under study is likely to become drier during dry seasons and experience more frequent high intensity events, particularly under RCP8.5. The projected increase in dry spell duration (and higher temperatures) combined with more extreme events, is expected to impact significantly on the wetting/drying cycles of tailings porous medium.

6.2 Interpretation of soil behavior based on characterisation

Chapter 4 provided an overview of the physical characteristics of fine-grained material relevant to this study. It includes secondary data to predict subsurface flow and geohydrological behaviour of tailings during and after rainfall events. Soil characteristics, and particularly hydraulic conductivity, has been mentioned by several authors as being a determining factor in the occurrence of both GWR and the LE. Since this study did not include experiments on material other than fine grained soils (replicating tailings porous medium), comparison with coarser material and propensity towards the rapid mobilisation of groundwater were derived from previous studies. These academic sources are listed in Table 6.3, together with a complete summary of factors that the present study has taken into consideration. These will be discussed in more detail in section 6.3.

UNIVERSITY *of the*
WESTERN CAPE

Table 6.3: Summary of factors considered to contribute to slope stability and transient pressure wave mechanisms in tailings porous medium.

Factor	Rational/relevance	Source
Soil characteristics e.g., hydraulic conductivity	Fine grained soils most likely to allow rapid mobilisation of groundwater due to holding pre-event water in tension, thereby establishing a large capillary fringe. > soil fineness = > soil water retention capacities and matric suction > hydraulic conductivity = > GW discharge	Abdul and Gilham (1989), Cloke <i>et al.</i> (2006), Guo <i>et al.</i> (2008), Zang <i>et al.</i> (2018), Gillham (1984).
Capillary Fringe	Establishment of a continuous pore water phase > CF height = > GWR	Abdul and Gilham (1984); Abdul and Gilham (1989); Cloke <i>et al.</i> (2006); Miyazaki <i>et al.</i> (2012); Zang <i>et al.</i> (2018)
Rainfall parameters e.g. intensity, duration and frequency and ponding depth.	Determines proportion of event – and pre-event water in stream. Only where the capillary fringe does not reach the ground surface and the Ks is high enough to have rainfall-limited infiltration. < rainfall intensity = < GWR > rainfall intensity = > pore air pressure	Waswa <i>et al.</i> (2013); Waswa and Lorentz (2016b); Gilham (1984), Meyboom (1967); Heliotis and Dewitt (1987); Guo <i>et al.</i> (2008); Zang <i>et al.</i> (2018)
Pore air pressure	Build-up of air pressure between the wetting front and water table contributes to the LE. Air pressure effects soil-water movement.	Guo <i>et al.</i> (2008); Waswa <i>et al.</i> (2013); Waswa and Lorentz (2016b); Zang <i>et al.</i> (2018); Tian <i>et al.</i> (2002); Sun <i>et al.</i> (2015)
Pre-event water and initial groundwater depth.	GWR, highly related to the depth of the phreatic surface and less dependent on the existence of the capillary fringe.	Waswa <i>et al.</i> (2013); Waswa and Lorentz (2016b); Cloke <i>et al.</i> (2006); Zang <i>et al.</i> (2018)
*Surface slope	< slope infiltration = > infiltration but also less storage	Abdul and Gilham (1984); Cloke <i>et al.</i> (2006)
**Vegetation	Reduce erosion, extract soil moisture	Sekhar <i>et al.</i> (1983)

*Cloke *et al.* (2006) also elaborates on sloping topographies and suggests that lower slopes encourage GWR since these riparian zones have less water storage capacity and lower overland flow velocity. The slope formed in the location of the tailings beach has been mentioned in section 2.4, and although it has not been considered in this study (together with the presence/absence of vegetation), it is recognised as a factor that is likely to influence the generation of the GWR mechanism. **Not considered due to the absence of vegetation on the tailings beach.

Based on parameters specific of tailings material (Table 4.3), the particle size distribution analysis (Figure 4.7) and SWCC (Figure 5.18), it is possible to estimate physical behaviour and hydraulic mechanisms that are likely to contribute to pore air propagation, transient pressure wave generation and rapid water table response. These expectations would for instance include the relationship between the physical and hydraulic properties of tailings porous medium that is described by the SWCC and known hydraulic conductivity. Firstly, from these observations

it was evident that small particle sizes combined with low porosity, exhibit higher water retention capacities and low hydraulic conductivity (Fala *et al.*, 2005). Given the fine nature of tailings soil particles, these characteristics are particularly relevant to this study. Secondly, findings reported by Gillham (1984) stated that rapid GWR and the LE are more likely to occur in coarse grained soils. However, in agreement with Cloke *et al.* (2006), it is suggested that fine grained soils actually have sufficient propensity to the rapid mobilisation of groundwater. This is based on its high-water retention capacities that enable a large capillary fringe, a continuous pore water phase and the storage of pre-event water. This study does however recognise that a coarse-grained soil is able to transmit more energy through the capillary fringe and in a more rapid manner compared to a fine textured soil. Additionally, the homogenous characteristics associated with this soil suggested the possibility of less dense particle packing and thus a more porous medium. Since the homogenous size, arrangement and interaction of soil particles determine its mechanical properties and physical behaviour, it is likely to impact on effective stress and shear strength parameters. Another concept to consider is that the movement of pore air within the soil medium is affected by soil characteristics and soil moisture content. Tian *et al.* (2022) also mentioned the air pressure gradient and the viscosity of the gas phase to contribute to this movement. Referring to the main drainage curve of Figure 5.18 (Lorentz *et al.*, 2019), the air entry value for the tailings porous medium is about 260 mm-H₂O and the residual water content is reached at a pressure head of approximately 380 1 900 mm-H₂O. From a hydrogeologic point of view, this would indicate that soil would remain saturated for a distance of about 26 cm above the phreatic surface, while the soil above 190 cm from the water table would be at the residual water content (Abdul, 1984). The particle surface area of the soil sample (4,6 m²/g) enables a high degree of adsorption and water movement under these conditions may deviate from the simple laws of capillarity and Darcian flow. Bound water retained in micropores is probably held more tightly due to larger surface area of soil particles and adsorptive forces. And lastly, the rapid movement of water observed after the application of artificial rainfall events, is likely due to transmissivity feedback and macropore flow (established after repeated applications and the development of preferential pathways), exacerbated capillary rise (due to high hydraulic conductivity) and less because of Darcian flux.

6.3 Interpretation of laboratory results

Following the analysis of laboratory results in section 4.1.3, various assumptions, interpretations and conclusions have been made to provide a description of physical mechanisms most likely taking place within the tall soil column, and presumably therefore also in TSFs. From the recorded observations, it is confirmed that pore air pressure propagation and transient air pressure wave generation are likely mechanisms in laboratory studies. These are discussed below and summarised in Table 6.4.

Although none of the ponding events resulted in the wetting front reaching the deep sensors, its approach (as recorded by the shallow probes) brought about pressurized pore air in the unsaturated zone, which in turn introduced additional energy into the capillary fringe and simultaneously changed pore water pressure. This study also recognised that the dynamic load applied to the soil surface could result in the tailings porous medium to contract, thereby enabling rapid responses evident by excess pore pressure values. This was particularly noticeable at ponding event 2 (see Figure 4.15). However, the delayed response of ponding event 1 (see Figures 4.11-12), demonstrated before arrival of the wetting front, suggests that transient air pressure waves contribute significantly to the generation of pore air propagation and a subsequent change in pore water pressure contributed by pre-event water. It was therefore postulated that the gradual rise in pore air pressure at the deep probes was an indication of entrapped air and, as the wetting front approached, it compressed. The corresponding change in tensiometric pore water pressure levels at MT1-3 in the vicinity of the capillary zone responded before arrival of the wetting front (on the 2nd of January at TDR 7) and suggests response due to compressed pore air pressure. These changes may suggest the formation of a distinct capillary fringe and rising phreatic surface, fed by groundwater and not due to infiltration. This was indicative of a downward air pressure wave that converts water held in tension in the capillary fringe, to positive pressure, thereby causing the phreatic surface to ascend upwards to the top of the capillary fringe. Fredlund and Rahardjo (1993) described these fluctuations in pore pressures to vary with depth and between each compacted layer, thereby demonstrating small variations (at each port) in hydrological response to external conditions. The results support the notion that downward air pressure propagation has an effect on the phreatic surface as well as the capillary fringe.

Ponding event 3, providing the lowest rainfall intensity, resulted in disparate, seemingly insignificant, fluctuations in the phreatic surface (and inadvertently also capillary fringe depth).

It is proposed that the response recorded by this event has indicated a degree of transient pore air pressure wave generation, but that ponding depth (i.e., rainfall intensity) did not reach thresholds high enough to establish a stable response. These results highlight the significance of both antecedent and critical rainfall in the formation of a continuous pore water phase and recognises pore water as the medium through which transient pressure waves are transmitted. It further suggests that lower intensity rainfall events may have less of an impact on the compression of pore air in the region of the capillary fringe, and thus less inclined to impose pressure that results in the diffusion of the injected energy through soil water.

The contradiction in responses between events could be associated with the second and third applications starting at a different initial water content distribution in the column (due to the first application distributed through the column). It should however also be mentioned, that a distortion in responses could also be attributed to the soil system becoming increasingly distorted after repeated infiltration events (Cey *et al.*, 2006). This notion also supports Hardie *et al.*'s (2013) claim that flow paths depend on the soil's wettability which changes with repeated application, changing the actual dynamics of soil water content. Salas-Garcia *et al.* (2017) attributes different responses to the use of capacitance-based soil moisture monitoring, which may be limited in soils in which macropore flow is enhanced at high antecedent soil moisture content. The last mentioned study further mentioned variations in water content monitoring, boundary conditions at the upper boundary, and porous medium features as possible contributing factors that contribute to inconsistent results. Comparable studies by Mustafa *et al.* (2015) whereby plots of the time series response of pore water pressure to climatic conditions were analysed, illustrate similar highly dynamic, nonlinear, and complex behavioural patterns.

Both theoretical and observed results indicate a delayed response after the first ponding/rainfall event. The difference in the rate and magnitude of change between ponding event 1, 2 and 3 observations may be explained by the fact that before ponding event 1, the soil had not previously been wetted or one may consider the contribution of pre-event water generated by event 1. It is further recognized that structured piles with horizontal fine-grained layers, similar to tall soil columns, could lead to vertical preferential flow paths, potentially changing flow patterns (Fala *et al.*, 2005). It is also possible that preferential flow paths developed in the tall soil column after each infiltration event. Responses observed during and shortly after ponding

events 2 and 3 are likely influenced by the cumulative effect of preceding events, which highlights the relevance of rainfall history, i.e. antecedent water, in assessing slope stability.

Additionally, it is proposed that the magnitude of responses in the vicinity of the phreatic surface is dependent on the amount of energy injected into the soil system, which in turn is determined by the intensity and duration of a rainfall event. This conclusion would support Waswa and Lorentz's (2016a) energy hypothesis, whereby the intensity of a rainfall event provides additional energy that transforms kinetic energy to potential energy. It is further recognised that these rainfall characteristics, combined with the soil's infiltration capacity, slope and general topography, would also regulate energy injected by ponding depth. Although the rapid (spiked) increase in pore air pressure after application 1 and 2 of event 2, alludes to the importance of rainfall intensity, it may very well have been brought about by the depth of rainfall resulting in ponding. The effect of ponding depth, which is essentially generated by rainfall intensity and duration, and the magnitude of pressurised pore air pressure, is clearly illustrated in Figure 4.15. The subsequent release of tension within the capillary fringe, brought about by this downward air pressure wave, causes the conversion of vadose zone water to phreatic zone water, resulting in volumetric water content values that are substantially above the residual value. This assumption was supported by the slight increase (4,5 mm) in water content at TDR 1 within hours after event 1 (not shown). This observation supports Cloke *et al.*'s (2006) study that found a rainfall event of medium intensity to allow for the mobilisation of pre-event water to contribute to GWR. In field conditions, this would mean that water level rise in an observation well would be delayed relative to the rise in air pressure in the unsaturated zone. These results indicate that the height of the initial water table, is a controlling factor in the formation of near-stream (or pond) ridges. capillary fringe

Results reported by Gillham (1984) and Waswa (2013) stated that rapid GWR and the LE is more likely to occur in coarse grained soils. This is supported by Yang *et al.* (2015) that assumes this theory likely due to the stability of macropores in fine grained soils, resulting in the rapid outflow of air ahead of a wetting front. However, even though this study only considered fine grained samples, results showed signs of rapid pore air pressure diffusion waves. Results interpreted here also suggested that fine grained soils, such as tailings porous medium, provides the ideal conditions for the entrapment of air, exhibit high (pre-event) water holding capacities and therefore potentially also provide ideal conditions for the establishment of a continuous pore water phase. It is further proposed that low hydraulic conductivity

associated with fine grained soils, enable the creation of an impermeable wetting front, preventing the escape of pore air and thus leading to higher levels of compression. The uniform nature of particle sizes found in TSFs, could also result in higher porosity, enabling the rapid movement of both air and water throughout the soil medium. It is however recognised that, due to the fine nature of tailings, the network of energy pathways is complex, thereby adding resistance to energy transference. Even though this causes higher energy losses and lower energy velocities, the results presented here show that the rate of response in the phreatic surface is rapid and possibly indicative of non-Darcian behaviour. In addition, the greater the propensity for capillary fringe rise, the less likely it is that rapid Darcian flux of groundwater would occur (Cloke *et al.*, 2006). These findings are supported by a study by Hogervorst *et al.* (2003) that found groundwater levels at 1 – 2 m in sandy soils without macropores, to rise within a few hours after a rainfall event. According to Miyazaki *et al.* (2012) this contradicts models that rely on the Richards equation, which could possibly explain the variation in observed and theoretical SWCCs illustrated in Figure 5.18. In agreement with Islam *et al.* (2006) fine grained soils generally tend to have higher saturated and residual volumetric water content but lower bubbling pressure, together with a gradual decrease in water content as matric suction increases. The shape of the SWCC is therefore very important.

Based on results mentioned in Chapter 4 and explanation of responses above (and summarised in Table 6.4), this study concluded that high intensity rainfall events cause the entrapment and compression of air in tailings porous medium, and results in an increase in water content and a decrease in soil suction. An increase in pore air pressure therefore serves as an indirect contributor to diminished shear strength and a reduction in the factor of safety.

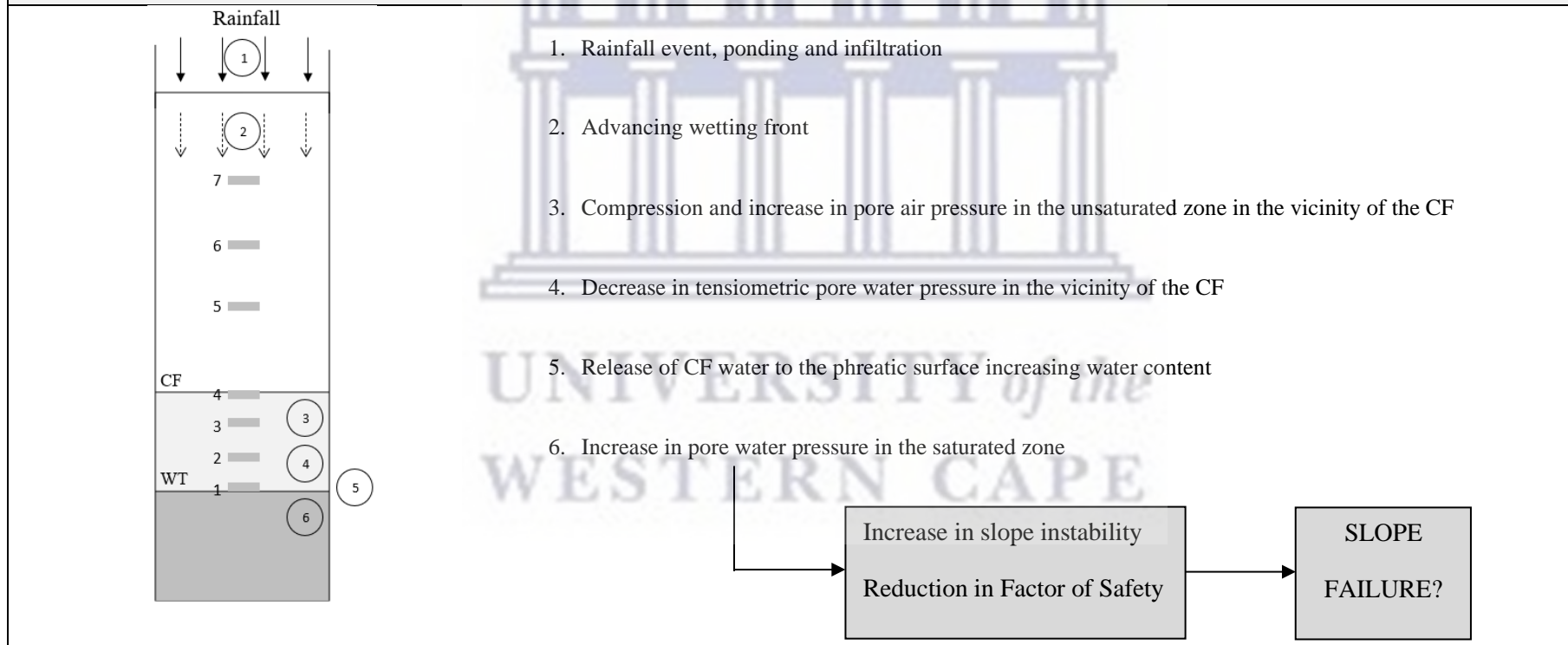
Table 6.4: Summary of individual physical responses per ponding event, interpretation and conclusions.

	Event 1	Event 2	Event 3
Initial conditions			
Position of the phreatic surface above base of the soil column	Approximately 400 mm from base* (Piezometer level was stable for 4 hours preceding each application).		
Height of the CF above phreatic surface.	Approximately 400 mm.	Approximately 400 mm.	> 400 mm
Initial VWC between the CF and the phreatic surface	0.34 – 0.355 cm ³ .cm ³ (Fig. 4.11)	0.31 – 0.33 cm ³ .cm ³ (Fig. 4.14)	0.31 – 0.36 cm ³ .cm ³ (Fig. 4.17)
Initial VWC between CF and top boundary (soil surface)	0.03 – 0.044 cm ³ .cm ³ (Fig. 4.11)	0.075 – 0.125 cm ³ .cm ³ (Fig. 4.14)	0.15 – 0.16 cm ³ .cm ³ (Fig. 4.17)
<p>$K_s = 0.27$ mm/h Dry bulk density = 1 675 kg/m³ * It was difficult to establish a stable water table. This may be caused by fine nature of the soil sample, together with its high capillarity, or due to the zero-pressure line that may rise above the CF (Waswa, 2013). <i>It is also this characteristic of fine soil and the great propensity for CF rise that makes rapid Darcian flux of groundwater unlikely</i> (Cloke <i>et al.</i>, 2006).</p>			
Experimental Procedure			
Return period and application	1:200 – 84.1 mm/h 9 liters over 30 minutes; 14 liters of 15 minutes; 1 liter over last 15 minutes.	1:100 – 74.9 mm/h 8 liters over 15 minutes; 13.2 liters of 45 minutes.	1:50 – 66.1 mm/h 7 liters 15 minutes; 11.7 liters of 45 minutes.
Note: After set-up, sensors were monitored, by downloading data and plotting graphically, to ensure stability over at least four hours preceding application. Individual responses are summarised below.			
Physical response			
Pore air pressure	Instant, yet small, increase at the 4 shallow probes (Fig. 4.10) after application 1 and 2 [≤ 0.5 kPa]. Application 3 (1 liter) did not register any response. Delayed response at deep PAPPs 1-4 recorded after 50 hours (Fig. 4.24). [≤ 10 kPa]	Instant increase at all PAPPs [≤ 1 kPa at shallow PAPP 5-7 and ≤ 10 kPa at deep PAPP 1-4]. Significant (rapid) increase in deep pore air pressure, more distinct in the 2 nd application resulting in deeper ponding depth (Fig. 4.15).	Disparate, yet insignificant fluctuations.

Pore water pressure	All MT excluding 5 and 7 recorded a small decrease in tension within 45 min. Significant change after 73 hours at deepest MT 1-4 (Fig. 4.12). [≤ 4 kPa]	Reduction in tensiometric pore water pressure responses recorded at MT 1 [≤ 0.5 kPa], MT 2-3 [10-50 kPa] and MT4 [≤ 70 kPa] (Fig. 4.15).	Disparate, yet insignificant fluctuations.
Volumetric Water Content	Shallow probes increase after approximately 73 hours illustrating infiltration by the advancing wetting front (Fig. 4.11). [≤ 0.05 cm ³ cm ³]	Rapid increase after application 1 and 2 [≤ 0.224 cm ³ cm ³ at shallow TDRs and ≤ 0.03 cm ³ cm ³ (0r 5%) at deep TDRs]. VWC at deep TDRs 1-4 responded 2 minutes after shallow probes (Fig. 4.14).	Spikes recorded at TDR 6 and 7 (Fig. 4.17/18) [≤ 0.4 cm ³ cm ³]. Before application TDR5 had a higher water content than the previous two events and resulted in a less spiked value (similar to TDRs 1-4). All deep TDRs indicated a small increase as soon as ponding started. [≤ 0.02 cm ³ cm ³].
Interpretation			
Pore air pressure	Instant PAPP responses likely generated by the energy of the high intensity event applied to the soil surface. Delayed increase in pore air pressure in the vicinity of the CF due to imposed compression rates induced by the advancing wetting front.	Higher magnitudes of ponding (i.e. rainfall intensity) result in increased pore air pressure rates. This is evident between application 1 and 2 and particularly relevant at deep PAPPs 1, 2 and 4.	Disparate, yet insignificant fluctuations likely due to the fact that ponding depth (i.e. rainfall intensity) did not reach thresholds high enough to establish a stable response. It is also suggested to wettability and the creation of preferential flow paths were influenced by previous ponding events.
Pore water pressure	Tensiometric pore water pressure decreased in response to compressed pore air pressure, before the arrival of the wetting front.	Substantial changes in pore water pressure coincide with PAPPs recording the most significant responses. Specifically MT's 2, 3 and 4	As above.
Volumetric Water Content	The wetting front advanced but infiltration only reached the shallow TDRs 5-7 after approximately 73 hours. The delay may be ascribed to a number of reasons, e.g. that this was the first application and wettability and flow dynamics were not yet established.	Instant increases in VWC at deep TDRs 1-4 likely caused by the reduction of tension in the CF, thereby releasing water to the phreatic surface.	Instant increases in VWC at deep TDRs 1-4 (5) likely caused by the reduction of tension in the CF, thereby releasing water to the phreatic surface.
NOTE: The contradiction in responses between events could be associated with the second and third applications starting at a different initial water content distribution in the column (due to the first application distributed through the column).			
Conclusions			
	Pressurized pore air in the unsaturated zone, which in turn introduced additional energy into the CF resulted in a simultaneous decrease in tensiometric pore water pressure.	The magnitude of pore air pressure responses is directly proportional to ponding depth (i.e. rainfall intensity). Pore water responses at deep probes indicate an upward water pressure	Some degree of transient pressure wave generation caused responses at the deep probes, but ponding depth was insufficient to trigger stable responses. Lower intensity

	<p>The magnitude of pore air pressure is dependent on the magnitude of the advancing wetting front while the magnitude of pore water pressure is influenced by the magnitude of pore air pressure. In other words, the magnitude of pore air pressure is dependent on ponding depth (i.e. rainfall intensity). Pore air pressure ahead of the wetting front caused the propagation of pressure waves that mobilised pre-event water and reduced pore water suction.</p>	<p>wave causing the water table to rise in response to a downward air pressure wave brought about by the descending wetting front.</p>	<p>rainfall events have less of an impact on the compression of pore air in the region of the CF, and thus less inclined to impose pressure that results the diffusion of the injected energy through soil water.</p>
--	---	--	---

A step-by-step description of the processes most prevalent from the above observations:



6.4 Risk assessment

As mentioned in Chapter 2, South Africa possesses just over 200 TSFs, of which 79 are classified as having a high risk of failure (Roche *et al.*, 2017). In order to provide an indication of risk associated with the TSFs, a basic risk assessment tool was developed. Previous risk assessments conducted by van den Berghe *et al.* (2011), Nišić (2021) and Zheng *et al.* (2011) were used as guidelines. This tool is presented in the form of risk assessment matrix (Table 6.5) and considers different hazardous conditions that contribute to slope instability. It takes into account a range of factors that each have been deemed, through expert judgement, data analysis and laboratory testing, to have an impact on slope stability. Probability and level of impact/severity have been carefully considered and assigned a score representing different levels of probability and severity. Comparison and alignment with risk assessments from studies mentioned above allowed for a reasonable indication of the risk associated with each hazard. Even though this approach may be considered highly subjective, it may provide the first indication to possible risk ratings relevant to a particular facility, thereby contributing to the prioritisation of high-risk scenarios.

The assessment also included analysis of physical and geological characteristics of the tailings material, earthquakes, the design and construction of the TSF, operational/production activities, rainfall intensity, the presence of pre-event water, capillary rise and slope. Kovacs *et al.* (2020) stated that the vulnerability of the surrounding area should also be considered in terms of the distance to waterbodies and human settlements downstream, including the landscape of the downstream territory. These factors would be exacerbated by political complications if potential failure would release waste and toxins into transboundary river basin systems. By evaluating these variables and establishing a clear relationship between them, the assessment tool provides the first step to an indication of the overall risk associated with the TSF. According to Kovacs *et al.* (2020) these assessments provide a *preliminary generalized semi-quantitative overview* and takes cognisance of different risks. It also enables the prioritization of different risks for further analysis. This information can be used to inform decision-making, prioritize risk mitigation measures, and improve the management of TSFs to minimize the risk of failure. It is important to note that the accuracy and reliability of this type of tool will depend on the quality and completeness of the data used to support it, as well as the methodology and assumptions used in its development. It is therefore important to regularly

review and update the tool to ensure it remains relevant and reliable over time. Motivation for selection of variables to be included in the risk analysis is discussed below:


- a) Various authors have indicated the inherent stability flaws associated with the construction of TSFs using the upstream method, which accounts for 90% of historical failures (Martin and McRoberts (1999); Kossoff *et al.* (2014); Carmo *et al.* (2017); Rico *et al.* (2008b); Lyu *et al.* (2019)). Since most TSF are constructed using the upstream method (although dam 2 was converted to a waste rock impoundment facility), it was considered as part of this risk analysis.
- b) After analysing both future IDF curves and responses recorded during laboratory experiments under differing ponding depths, high rainfall intensity events have the potential to trigger pore air propagation and transient pressure wave generation in the vicinity of the capillary fringe. For example, from Figure 6.2 it is evident that the 1:10 year storm will be replaced by the 1:2 year while the historical 1:200 storm event is exceeded by the future 1:100 year. In other words, the occurrence of extreme events is predicted to become more frequent. In order to predict the occurrence of events that are likely to contribute to slope instability, this study has considered design storms of equal and higher value than ponding event 2 since ponding event 3 did not illustrate any significant/immediate changes in recorded parameters. Even though low intensity events also exceeded the soil sample's (tailings replica) infiltration capacity, it is suggested that this evaluation include a rainfall intensity above ≈ 66 mm/h to consider extreme events that are presently increasing in frequency. Based on this assumption, future short duration high intensity events are likely to add to higher risk of GWR and the LE, which could contribute to slope instability. Since the area under study has already shown visible signs of future predictions, such as the event of 101 mm/h on the 21st of November 2016 (SAWS, 2020), it is suggested these conditions will be realised far sooner than previously estimated. The relevance of rainfall history plays a key role when assessing slope stability and will undoubtedly also influence the water content of the soil, the height of the water table and the capillary fringe, thereby establishing the presence of pre-event water. Additional moisture generated by the deposition of wet mining waste will further increase the weight of the soil, thereby adding to stress and reducing shear strength, making it more prone to sliding and collapsing.
- c) Production activities and specific grinding technology would impact on the fineness of the tailings material and consequently also on hydraulic properties and physical behavior. Although this would depend on the geology in the area as well, it is a well-known fact that

ultra-fine grinding technology improves economic benefits, often resulting in fractions as small as 80% - 20 μm . The level of grinding technology employed during the mine's production and operational activities have therefore been considered.

- d) Earthquake clusters and active faults in close proximity to the study area were previously illustrated in Figure 3.2 (a) and (b). According to Manzunzu *et al.* (2019) mining activities in the area induce seismic activity and trigger earthquakes at a rate much higher than observed in the tectonic regions of South Africa. Over the last two years there have been ten seismic activities between 10,5 to 64,2 km from the study area. These events registered between ML 3,3 and 4,2 while the largest event in this region occurred in 2014 and registered a magnitude of ML 5,5 (Manzunzu *et al.*, 2019). Even though there is no evidence of TSFs failing due to earthquakes in South Africa, the Global Industry Standard on Tailings Management recommends the inclusion of seismic criteria during design (Fourie *et al.*, 2022) and it has therefore also been included in the risk analysis.
- e) Severity of occurrence in terms of social, economic and environmental impacts has also been taken into account. Apart from the 'worst case scenario' of a TSF failing, daily operational activities also have adverse long term social and environmental consequences. This includes the generation of dust, uncontrolled seepage polluting water sources and noise.

In order to validate the matrix, this study has examined its predictions and compared it to the three TSF disasters in South Africa (see section 2.1.3.2). These scores were all above 200 (out of 225) indicating an extremely high risk of slope failure. Findings have therefore corroborated to a certain degree of reliability.

Table 6.5: Risk Assessment Matrix of slope instability.

Risk rating key: 			Impact/Severity					
			Insignificant 1	Minor 2	Significant 3	Major 4	Severe 5	
Implications of rainfall	Hazard	Probability						
	Rainfall intensity > hydraulic conductivity	Almost certain 5	Yellow	Orange	Red	Dark Red	25	
		Likely 4	Yellow	Orange	Red	Dark Red		
		Moderate 3	Green	Yellow	Orange	Red		
		Unlikely 2	Green	Yellow	Orange	Red		
		Rare 1	Light Green	Green	Yellow	Orange		
	25/25							
	Probability of preceding rainfall contributing to prevent water (high water table)	Almost certain 5	Yellow	Orange	Red	Dark Red	25	
		Likely 4	Yellow	Orange	Red	Dark Red		
		Moderate 3	Green	Yellow	Orange	Red		
Unlikely 2		Green	Yellow	Orange	Red			
Rare 1		Light Green	Green	Yellow	Orange			
25/25								
Soil characteristics	High capillary fringe	Almost certain 5	Yellow	Orange	Red	Dark Red	12	
		Likely 4	Yellow	Orange	Red	Dark Red		
		Moderate 3	Green	Yellow	Orange	Red		
		Unlikely 2	Green	Yellow	Orange	Red		
		Rare 1	Light Green	Green	Yellow	Orange		
	12/25							
	Low hydraulic conductivity (soil fineness)	Almost certain 5	Yellow	Orange	Red	Dark Red	16	
		Likely 4	Yellow	Orange	Red	Dark Red		
		Moderate 3	Green	Yellow	Orange	Red		
		Unlikely 2	Green	Yellow	Orange	Red		
Rare 1		Light Green	Green	Yellow	Orange			
16/25								
Ultra fine grinding technology/geology (soil fineness)	Almost certain 5	Yellow	Orange	Red	Dark Red	25		
	Likely 4	Yellow	Orange	Red	Dark Red			
	Moderate 3	Green	Yellow	Orange	Red			
	Unlikely 2	Green	Yellow	Orange	Red			
	Rare 1	Light Green	Green	Yellow	Orange			
25/25								
Engineering factors	High volume and/or highly hazardous waste substances	Almost certain 5	Yellow	Orange	Red	Dark Red	20	
		Likely 4	Yellow	Orange	Red	Dark Red		
		Moderate 3	Green	Yellow	Orange	Red		
		Unlikely 2	Green	Yellow	Orange	Red		
		Rare 1	Light Green	Green	Yellow	Orange		
	20/25							
	Upstream method of construction	Almost certain 5	Yellow	Orange	Red	Dark Red	20	
		Likely 4	Yellow	Orange	Red	Dark Red		
		Moderate 3	Green	Yellow	Orange	Red		
		Unlikely 2	Green	Yellow	Orange	Red		
Rare 1		Light Green	Green	Yellow	Orange			
20/25								
Short beach length, steep starter dam slope, high dam height, limited drainage facilities	Almost certain 5	Yellow	Orange	Red	Dark Red	16		
	Likely 4	Yellow	Orange	Red	Dark Red			
	Moderate 3	Green	Yellow	Orange	Red			
	Unlikely 2	Green	Yellow	Orange	Red			
	Rare 1	Light Green	Green	Yellow	Orange			
16/25								

Other impacts	Seismic activity	Almost certain 5					
		Likely 4			12		
		Moderate 3					
		Unlikely 2					
		Rare 1					
	12/25						
	Impact of TSF failures on sustainable development, thereby increasing risk:						
	Social, economic, environmental impact e.g. inhabited areas and/or nearby water sources	Almost certain 5				20	
		Likely 4					
		Moderate 3					
		Unlikely 2					
		Rare 1					
	20/25						
	Total: 191/250 ≈ 19,1 Risk rating: Very High						

Even though this tool may be useful as a first order assessment of risk, particularly when considering future climatic risks, there are however certain limitations. First of all, it did not consider the extent of safety measures such as regular inspections, maintenance and mitigation strategies implemented as part of remedial or preventative action. Furthermore, although this study did not find the extension of the capillary fringe to the ground surface a requirement for the rapid mobilisation of groundwater to occur, its presence was acknowledged as being a contributing factor and not a controlling factor. Due to the fine nature of tailings porous medium, the capillary fringe is likely to extend to the ground surface, particularly due to the constant addition of wet mining waste, contributing to infiltration rates and a high-water table. These conditions, combined with high intensity rainfall events, provide the ideal environment for the generation of transient pressure waves and the rapid mobilisation of pre-event water.

6.5 Conclusion

This study confirmed that high intensity rainfall events, combined with pre-event water, contribute to the creation of an induced pressure head and the rapid, and in some cases delayed, mobilisation of groundwater. In contrast to expected Darcian behaviour (as shown by the HYDRUS 1D predictions), observations suggest alternative flow and related physical mechanisms. As expected, because of the fine nature of soil and its great propensity for capillary fringe rise, this implies the presence non-Darcian responses, similar to those found by Waswa *et al.* (2013). Even though Waswa *et al.* (2013) suggests GWR and the LE are more likely to occur in coarse grained soils – due to its higher porosity allowing for the rapid transmission of an induced pressure head - conclusions based on the hydraulic behaviour of tailings after ponding events, indicate a possibility for the rapid mobilisation of groundwater to occur in fine grained soils. This study did however recognise the slow progression of the first wetting front and suggests this to be exacerbated by the fineness of the soil. This is

supported by Waswa (2013) that found pore water responses in fine-grained soil to lag in response to compressed pore air in comparison with coarse-grained soils. Although some research studies have also suggested that soils of low hydraulic conductivity exhibit pore air pressure diffusion waves of slow velocities and short wavelengths (Yang *et al.*, 2015), the responses observed after each ponding events 2 and 3, suggest that these could be much faster than ordinary unsaturated or saturated flow conditions. This response therefore refutes the theory suggested by Pelascini *et al.* (2022) that even though infiltration induces pore air pressure changes, its effects are delayed as a result of flow and diffusion. Results further indicated that deep pressure responses are sensitive to ponding depth and ensuing loading conditions.

The significant response of deep MTs suggested that pore air pressure ahead of the wetting front caused the propagation of pressure waves that mobilised pre-event water and reduced pore water suction. Due to the fine nature of the soil and slow infiltration rates, this change is likely to be brought about by loading conditions, compressed air pressure and the subsequent generation of transient pressure waves. The magnitude of change in pore water pressure was found to be less than the magnitude of induced air pressure, which implies that the extent of water level rise would be less than the magnitude of induced air pressure. Although the 10 kPa increase in pore air pressure mentioned in Table 6.4 would result in the phreatic surface rising by only 1 m (under hydrostatic conditions), it may contribute significantly to reducing slope stability. Since the factor of safety of tailings embankments are closely related to soil moisture and the location of the phreatic surface, a seemingly insignificant rise in the phreatic surface may approach threshold conditions. As previously mentioned, the factor of safety in straight-line failure surfaces reduce considerably with a rise in the water table (see Figure 5.8) (Chandler and Tosatti, 1995). Muñoz (2019) also provided insight into the relationship between the safety factor and the influence of the water table in combination with other factors such as soil suction, soil weight or both (see Figure 5.9).

It is further recognised that, although airflow, caused by an advancing wetting front, may induce movement in the phreatic surface, fluctuation in the water table may also further induce sub-surface air flow. It was also established that the rise of the phreatic surface is regulated by time-dependent flux boundary conditions and that the magnitude of water table response is regulated by the magnitude of compressed pore air pressure. This is similar to the observed results interpreted by Waswa (2013), whereby the increase in pore air pressure was associated

with a reduction in pore water tension (see section 4.1.3). This indicated that pore air pressure has transferred to the water phase across the meniscus. Even though a relaxation of pore water tension could be caused by the arrival of the wetting front, it would have arrived as a rapid response and changes to pore water suction would be attributed to the rapid air phase pressure pulse.

The disparate fluctuations in the phreatic surface could possibly be attributed to the rapid response of groundwater to surface recharge, brought about by pore air propagation and the generation of transient pressure waves. These pressure diffusion mechanisms cause an exacerbated increase in the water table that changes matric suction ($u_a - u_w$) and reduces slope stability in partially saturated conditions. In agreement with results obtained by Waswa *et al.* (2013), this change was found to vary between 2 and 50 kPa. It is suggested that the magnitude of change is determined by, amongst other things, antecedent rainfall events, rainfall intensity and soil characteristics. Results further indicate the presence of transient pressure waves in saturated and partially saturated tailings material, signalling rapid water table response and air pressure induced groundwater fluxes. In agreement with Iverson (2000), it is proposed that these mechanisms contribute to slope instability and that landslide responses to rainfall involve transient processes with different intrinsic timescales.



CHAPTER 7

7.1 Conclusion

Conditions in the study area, predicted under the force of climate change, include temperature increases across both minimum/maximum values and seasonal variations. These atmospheric changes result in a shift in rainfall parameters. It is suggested that the magnitude of future climatic conditions is likely to have a significant impact on the soil's physical behaviour, and therefore also on the stability of TSFs. Firstly, the more intense magnitude and possibly accelerated frequency of wetting-drying cycles could cause enhanced stiffness/strength degradation that could contribute to more rapid progressive failure. It was also recognised that not only rainfall conditions, but also higher temperatures and intense dry periods or drought conditions could result in the tailings material to exhibit higher suction magnitudes. This study further suggests that historical IDF curves are no longer an accurate estimation for design criteria and should be adjusted (see Figure 6.2) to compensate for future climatic conditions.

The overall effect of climate change on TSFs also relates to its response to external mechanisms. Since physical behaviour and transmissivity feedback depends largely on the unique geohydrological features of tailings, proper characterisation enabled the prediction of pore air propagation in tailings in response to external factors. This notion is supported by various authors, who suggest a strong interrelationship between soil characteristics and the rapid mobilisation of groundwater. Even though Cloke *et al.* (2006) argues that the relationship between capillary fringe height and hydraulic conductivity is overestimated, it is suggested that a greater propensity for capillary fringe rise (particularly in fine grained soils) makes the rapid Darcian flux of groundwater less likely. It is also suggested that higher water retention capacities and low hydraulic conductivity make this soil medium particularly susceptible to retention of pre-event water. This study is of the opinion that the intrinsic geo-hydrological characteristics of tailings make it vulnerable to mechanisms of transient pressure wave generation that could eventually be evident through the occurrence of both Ground Water Ridging and the Lisse Effect. Results indicate the presence of groundwater movement before arrival of the wetting front.

The most interesting interpretation to emerge from the analysis is the change in pore water pressure above the water table, not due to infiltration, but rather due to a change in tension, thereby indicating the release of water from the tension saturated zone to the phreatic surface. This may not necessarily result in the physical flow of pre-event water, but merely an

adjustment in pressure as the porous soil medium is fully saturated in the capillary fringe and below water. It further appears that the laboratory experiments conducted in this study demonstrate the rapid mobilisation of groundwater before arrival of the wetting front. It is therefore confirmed that, as rain water infiltrates into soils, the downward wetting front compresses the pore air and increases pressure between the wetting front and the capillary fringe. This finding is consistent with previous studies, which have shown that these responses can appear as either Ground Water Ridging or the Lisse Effect depending on water table depth (Waswa, 2013).

According to Waswa (2013) Ground Water Ridging is more likely to occur due to the energy of the rainfall event, whereas the Lisse Effect is more likely to occur due to compressed pore air. Another important finding was that the magnitude of groundwater level responses was directly related to the magnitude of the compressed pore air pressure. In turn, it was found that the extent of pore air propagation was determined by ponding depth (i.e. rainfall intensity) and points to the significance of energy injected into the tension saturation zone just above the phreatic surface as the downward air pressure wave propagates towards the water table. As it reached the water table, groundwater started to ascend as an upward water pressure wave. In contrast to Waswa (2013), and since the laboratory set up did not allow for the extension of the capillary fringe throughout the tall soil column, a continuous pore water phase was not found to be a prerequisite for Ground Water Ridging to occur. This finding was also reported by Zang *et al.* (2017).

This study enumerates the rainfall induced movement of air and water in tailings to illustrate its possible contribution to an alternative mechanism and loading conditions that lead to slope instability (Smith and Connell, 1973). The change in pore air pressure influences normal stress, matric suction and shear strength while pore water pressure, generated by pre-event water, contribute to stresses that reduce shear strength, and thus a lower factor of safety. This assumption is made on the premise that the energy content above the water table changes from negative pore water pressure to positive pore water pressure. Morton (2020) stated that a change in effective stress causes the rearrangement of particles (or volume deformation) that, under undrained conditions, lead to compression of water in soil voids. This results in higher pore water pressure and further changes in effective stress. As described by Morton *et al.* (2008), the stress state for any point in a slope is governed by the principal stresses and the acting water pressure. From these observations, it can be concluded that both surface water

and groundwater play significant roles in the failure of tailings dams. Based on the above, it is suggested that transient air pressure waves are generated by the intensity of a rainfall event as well as by the advancement of a wetting front. These pressure diffusion mechanisms cause an increase in the water table that changes groundwater pressure heads and matric suction, thereby reducing slope stability in partially saturated conditions.

Due to the physical characteristics and high suction capacity of tailings porous medium, it saturates quickly but drains up to ten times slower, providing for a constant high-water table and large volumes of pre-event water sources (Zang *et al.*, 2018). It is also these same characteristics of tailings (fineness) that causes higher energy losses and lower energy velocities. However, the results presented here show that the rate of response in the phreatic surface could be rapid and indicative of non-Darcian behaviour. Based on this work, the probability of tailings dam slope failure by rain induced instabilities in future climates is more likely than under historical conditions.

7.2 Recommendations for policy and engineering design

Based on observations by Rodriguez *et al.* (2021) it is evident that the failure of tailings dams does not occur based on one factor only. The contribution of weather, climate, operational/production activities, maintenance effort, design and construction, closure and post-closure, governance and accountability, risk assessment and management and stakeholder engagement/communication should all be considered.

Due to the inherent vulnerability of these structures, planning of tailings dams will have to factor in this uncertainty and address the associated risks. Climate change mitigation and adaptation measures put in place by the mining industry would reduce risks associated with extreme events and ensure a more robust system. The development of such plans would require reliable data coupled with good planning and a zero-risk approach (Roche *et al.*, 2017). The risk assessment tool mentioned in Chapter 6 considers technical, operational, environmental, social and economic factors that influence the likelihood and associated risk of a potential failure. It also provides the first step in determining relevant factors and associated risks that are appropriate to a specific site and its distinct characteristics. It would also ensure the calculation of the safety factor has taken all on-site variables into consideration. This finding broadly supports the work of other studies (Robertson *et al.*, 2017; Rodriguez *et al.*, 2021) and suggests that the formulation of engineering design protocols and practices should be more

purposefully integrated with the outcomes of theoretical, field and laboratory studies to develop the most cost-effective and safe systems. The current study supports Rodriguez *et al.*'s (2021) belief that triggering mechanisms that eventually result in static liquefaction and flow failure are permanent and gravitational. Risk reduction should be regarded from the perspective of both mitigation and adaptation strategies. It should therefore be standard practice that each TSF have a comprehensive risk assessment plan that includes preventative measures as well as a comprehensive emergency plan in the event of a breach. These plans should be updated regularly in response to variables such as tailings volume, increase in vulnerability or any other changes that could increase risk and/or hazards. Risk assessments would also be useful in scenario planning designed to assist decision-makers in identifying potential outcomes and impacts, assess responses, implement suitable adaptation and resilience strategies and/or adjust existing policy requirements. Policy and decision-makers should facilitate the establishment of such strategies through systematic, transformative and integrative approaches.

The design and construction of TSF should be supported by extensive desk-studies and comprehensive investigations into site conditions such as topography, surface and groundwater sources and geology to determine long term engineering stability and drainage patterns. From a practical viewpoint, mitigation measures should include additional pre-construction design measures, such as sufficient consideration of compressed pore air pressure in design calculations and methods of slope stability analysis. Drainage systems and seepage control measures that are designed to limit groundwater levels more aggressively, would also contribute to the efficient reduction of pore water pressure. Since tailings dams are continually supplemented with sludge and wet mining waste, additional water sources such as rainfall adds to loading conditions that further increases pressure. For these reasons, it is suggested that supplementary drainage systems be incorporated near the face of the tailings dam (Rodriguez *et al.*, 2021). Since initial indications and risk assessment point towards a high probability of slope instability, assessment of vulnerable TSFs should be supplemented by a comprehensive analysis of hydraulic and geotechnical parameters.

Prerequisites regarding siting should also be reviewed. It is recognised that the establishment of mining facilities, residential areas and informal settlements nearby are unavoidable. It is however recommended that the placement of these areas is planned in accordance with high-risk protocol to prevent loss of life and damage to property in the event of dam failure. Since the siting of mines rely on geology, it's positioning is rather fixed. However, the siting of waste

containment facilities such as TSFs should be as far away as possible from waterways, and on stable geology. It is also advised that if the natural topography slopes towards ecologically sensitive areas, barriers such as berms should form the first line of defence to minimise damage. These structures could add additional advantages such as the reduction of dust during mining operations as well as visual deterrence of industrial activities.

Operational plans should also include the particulars and regulated enforcement of regular inspections and scheduled maintenance efforts. Apart from visual inspections, it is suggested that continuous automated monitoring equipment be installed and reviewed to identify anomalies as soon as they appear. The importance of regular compulsory monitoring practices, together with an appropriate risk response plan, cannot be overemphasised. Meyer and Hrubec (1998) described the purpose of instrumentation monitoring is to provide real-time information, but also to verify the validity of assumptions made during the design process. Even though visual inspections should be conducted regularly, it is likely to only identify movement after it has already occurred and failure is imminent. Morton (2019) advises a strategy that identifies the cause of movement before it occurs, thereby activating an early warning system. Morton (2019) also recommends the monitoring of rainfall, pond levels, up- and downstream surface and groundwater flows (and pressures), as well as active monitoring of pore water pressure within the slopes of the TSF. To add to these, it is advised that the measurement of pore water pressure be monitored at strategic points along the tailings dam to identify any significant rise in water content before it saturates the constructed dam walls. This may include measurements in the unsaturated zone, the capillary fringe or below the phreatic surface. Different monitoring networks and multiple points that deliver real time information would provide a reliable indication of developing risks. The identification of high-risk conditions triggers intervention early on to prevent failure. The intensity of monitoring activities is likely to depend on the method of construction, the level of risk/hazard and its potential impact on social, economic and environmental factors.

Planning, design, construction, operation, maintenance and close-out of a TSF should be assigned a framework of relevant laws and regulations. This includes the National Environmental Management Act 107 of 1998 (NEMA). It is the most important environmental piece of legislation in South Africa, regulating various aspects pertaining to socio-economic and environmental protection. This act also includes listing notices to *identify activities that would require an environmental authorisation prior to the commencement of that activity and*

to identify competent authorities in terms of sections 24(2) and 24D of this Act. Since the construction of TSFs are included in these notices, the planning, design, operation and eventual close-out of these engineering facilities are subjected to various requirements and stringent obligations. This includes closure, post-closure and rehabilitation plans to ensure long term stability and reduce additional social, economic and environmental risks. Although NEMA requires engagement between stakeholders, communication is often influenced by external barriers that hamper equitable engagement. Effective stakeholder involvement should therefore be established during the planning phase and maintained throughout operational and close-out phases to assist in identifying concerns, potential solutions and include local knowledge in decision-making processes, thereby minimising negative socio-economic and environmental impacts.

NEMA is further divided into several sub-laws of the following are relevant to the mining industry: the National Environmental Management: Waste Act, No. 59 of 2008 (NEMWA); the National Environmental Management: Biodiversity Act, No. 10 of 2004; the National Environmental Management: National Forests Act, No 84 of 1998; the National Environmental Management: Protected Areas Act, No. 57 of 2003; the National Heritage Resources Act, No. 25 of 1999; and the National Environmental Management Air Quality Act, No. 39 of 2004. Mine owners are legally responsible to comply with all the above-mentioned regulations, laws and legislation pertaining to TSFs. Non-compliance in this regard will in future be addressed by the National Environmental Management Laws Amendment Act No. 2 of 2022 (NEMLAA 4). Even though this act is not yet in effect, it will affect changes to the above-mentioned environmental legislation pertaining to the mining industry. This includes stricter regulation of TSF and enforcement of fines and administrative penalties for non-compliance with environmental laws. In addition to NEMA, TSFs are required to comply with the provisions of the Mine Health and Safety Act, No. 29 of 1996, as well as the Dam Safety Regulations, published under the National Water Act, No. 36 of 1998.

7.3 Limitations

Since this study only considered a particular TSF and parameters concerned with its specific tailings porous medium, simulations were limited to one fine grained soil sample. Even though particular attention was paid to Ground Water Ridging and the Lisse Effect in TSFs, different mining operations and grinding technology results in material of varying physical

characteristics. It would therefore not be possible to draw a comparative analysis and apply the same conclusions on all TSFs. As previously mentioned, the sample had been made up artificially to replicate the tailings porous medium to produce a similar particle size distribution curve. However, since there is no universally accepted method for measuring particle shape, establishment of these features was restricted. The physical effect of this particular characteristic was therefore not considered. Furthermore, the role of evaporation was briefly discussed, but this study did not take it into account as a major contributing factor in the movement of soil moisture or its contribution to the establishment of a capillary fringe. The effect of extreme future temperature changes was also not considered but its effect, particularly on the clay fraction of tailings, is acknowledged as causing exacerbated wetting-drying cycles, and therefore impacting on hysteresis in the SWCC (Kristo *et al.*, 2019). These conditions influence soil structure and changes its hydraulic conductivity and reduce peak strength. It should also be mentioned that, because of the limited scale and artificial conditions under which laboratory tests were conducted, it is not precise what the practical significance of the results will be. And lastly, in contrast to Cloke *et al.* (2006), this study did not consider the effect of the surface slope normally found on tailings beaches. Even though lower slopes reduce instability, it is recognised that it also facilitates less run-off, higher infiltration rates and ponding that results in extended loading conditions, preventing the escape of pore air.

7.4 Future Perspectives and Recommendation for Further Research

Further research is required to address the limitations discussed above. It is also suggested that, in order to produce a generalised approach that would be applicable to a wider variety of climatic conditions, different soil hydraulic functions and TSFs in general, additional studies may be required. For instance, whether or not humid conditions prevent the capillary fringe of being responsible for rapid mobilisation of pre-event water, as indicated by Cloke *et al.* (2006). The role of evaporation and slope morphology was large ignored in this study. Since the top surface of the tailings beach is exposed to atmospheric boundary conditions that allow for water infiltration as well as extraction by evaporation, additional consideration should be given to the role of evaporation, particularly with regards to wetting-drying cycles and the hysteretic nature of tailings porous medium. It should also be mentioned that this study did not investigate future rainfall events in detail and, similar to du Plessis and Burger (2015), this was partly due to the limited amount of reliable digitised autographic data available in South Africa. Future studies

may therefore be useful in determining a more accurate estimation of the magnitude and frequency of future rainfall events.



REFERENCES

- Abdul, A. S., and Gillham, R. W. (1984). Laboratory Studies of the Effects of the Capillary Fringe on Streamflow Generation. *Water Resources Research*, 20(6), 691–698.
- Abdul, A. S., and Gillham, R. W. (1989). Field Studies of the effects of the capillary fringe. *Journal of Hydrology*, 112, 1–18.
- Aleotti, P. (2004). A warning system for rainfall-induced shallow failures. *Engineering Geology* 73:247-265.
- Alexander, M. (2018). The nine provinces of South Africa. South Africa Gateway.
<https://southafrica-info.com/>
- Allen, M.R., O.P. Dube, W. Solecki, F. Aragón-Durand, W. Cramer, S. Humphreys, M. Kainuma, J. Kala, N. Mahowald, Y. Mulugetta, R. Perez, M. Wairiu, and K. Zickfeld, (2018). Framing and Context Supplementary Material. In: *Global Warming of 1.5°C. An IPCC Special Report on the impacts of global warming of 1.5°C above pre-industrial levels and related global greenhouse gas emission pathways, in the context of strengthening the global response to the threat of climate change, sustainable development, and efforts to eradicate poverty* [Masson-Delmotte, V., P. Zhai, H.-O. Pörtner, D. Roberts, J. Skea, P.R. Shukla, A. Pirani, W. Moufouma-Okia, C. Péan, R. Pidcock, S. Connors, J.B.R. Matthews, Y. Chen, X. Zhou, M.I. Gomis, E. Lonnoy, T. Maycock, M. Tignor, and T. Waterfield (eds.)]. www.ipcc.ch/sr15
- Anglo American Platinum (2021). Ore Reserves and Mineral Resources report 2021.
<https://www.angloamericanplatinum.com/~media/Files/A/Anglo-American-Group/Platinum/report-archive/2021/ore-reserves-mineral-resources-report>
- Anglo American Platinum Limited. (2014). Anglo American Platinum Mogalakwena Mine.
<https://www.angloamericanplatinum.com/~media/Files/A/Anglo-American-Group/Platinum/presentation-and-speeches/2014/site-visit-mogalakwena-presentation-021014>
- Arnell, N. W. and Reynard, N.S. (1996). The effects of climate change due to global warming on river flows in Great Britain. *Journal of Hydrology*, 183, 397–424.
- Azam, S., and Li, Q. (2010). Tailings dams failures: A review of the last 100 years. *Geotechnical News*, 28(4), 50–53. <http://ksmproject.com/wp-content/uploads/2017/08/Tailings-Dam-Failures-Last-100-years-Azam2010.pdf>

- Azizli, K.M, Chee Yau, T., and Birrel, J. (1995). Technical note design of the Lohan Tailings Dam, Mamut Copper Mining SDN. BHD., Malaysia. In Mamut Copper Mining Sdn. Bhd, 8 (95).Ba-Te, B. (2005). Flow of air-phase in soils and its application in emergent stabilization of soil slopes. M.Phil thesis, Department of Civil Engineering, Hong Kong University of Science and Technology.
- Bear, J., and Verruijt, A. (1987). Modeling Groundwater Flow and Pollution. (First Edit). D. Reidel Publishing Company.
- Beck, H. E., Zimmermann, N. E., McVicar, T. R., Vergopolan, N., Berg, A., and Wood, E. F. (2018). Present and future Köppen-Geiger climate classification maps at 1-km resolution. *Nature Scientific Data*, 180214, 1-12. <https://doi.org/10.1038/sdata.2018.214>
- Bhanbhro, R. (2014). Mechanical properties of tailings: basic description of a tailings material from Sweden. PhD thesis, Luleå tekniska universitet.
- Bianchi, W. C., and Haskell, E. E. (1966). Air in the vadose zone as it affects water movements beneath a recharge basin. *Water Resources Research*, 2(2), 315–322.
- Blight, G., Copeland, A., Jardine, P., and MacRobert, C. (2012). Measurements on freshly-deposited surfaces of two platinum tailings dams. *Journal of the Southern African Institute of Mining and Metallurgy*, 112(11), 911–917. https://doi.org/10.36487/acg_rep/1263_02_blight
- Blight, G. E., and Fourie, A. (2003). a Review of Catastrophic Flow Failures of Deposits of Mine Waste and Municipal Refuse. *Associazione Geotecnica Italiana*, July, 1–17.
- Blight, G. E., Robinson, M. J., and Diering, J. A. C. (1981). The flow of slurry from a breached tailings dam. *Journal of the South African Institute of Mining and Metallurgy*, 81(1), 1–8.
- Bogaard, T. A. and Greco, R. (2016). Landslide hydrology: from hydrology to pore pressure. *WIREs Water*, 3, 439–459. <https://doi.org/10.1002/wat2.1126>
- Bowker, L. N. and Chambers, D. (2016). Root Causes of Tailings Dam Overtopping: The Economics of Risk and Consequence. 2nd International Seminar on Dam Protection Against Overtopping. Colorado, USA, 7-9 September 2016 <https://www.researchgate.net/publication/348372037>
- Brown, M., and van Wyk, D. (2022). Report on the Jagersfontein Tailings Disaster, 11, 1-36. <https://www.bench-marks.org.za/wp-content/uploads/2022/10/Jagersfontein-report.pdf>

- Buma, J. (1998). Finding the most suitable slope stability model for the assessment of the impact of climate change on a landslide in southeast France. *Earth Surface Processes and Landforms*, 25, 565–582.
- Burger, G. J. (2012). The Influence of Climate Change on Short Duration Rainfall in the Western Cape. Master of Engineering, Department of Civil Engineering, Stellenbosch University.
- Carmo, F. F. D., Kamino, L. H. Y., Junior, R. T., Campos, I. C. de, Carmo, F. F. do, Silvino, G., Castro, K. J. da S. X. de, Mauro, M. L., Rodrigues, N. U. A., Miranda, M. P. de S., and Pinto, C. E. F. (2017). Fundão tailings dam failures: the environment tragedy of the largest technological disaster of Brazilian mining in global context. *Perspectives in Ecology and Conservation*, 15(3), 145–151. <https://doi.org/10.1016/j.pecon.2017.06.002>
- Carsel, R., and Parrish, R. (1988). Developing joint probability distributions of soil water retention characteristics. *Water Resources Research*, 24(5). 755-769.
- Cey, E., Rudolph, D., and Therrien, R. (2006). Simulation of groundwater recharge dynamics in partially saturated fractured soils incorporating spatially variable fracture apertures. *Water Resources Research*, 42(9). <https://doi.org/10.1029/2005WR004589>
- Chambers, D. M. (2015). A Review of the Report on Mount Polley Tailings Storage Facility Breach, Independent Expert Engineering Investigation and Review Panel. Center for Science in Public Participation. Bozeman, MT. 1-12
- Chandler, R. J. and Tosatti, G. (1995). The Stava dams failure, Italy, July, 1985. *Geotechnical Engineering*, 113(2), 67–79.
- Chen, Y. (2018). Soil–Water Retention Curves Derived as a Function of Soil Dry Density. *GeoHazards*, 1(1), 3–19. <https://doi.org/10.3390/geohazards1010002>
- Clifton, A. W., Wilson, G. W., and Barbour, S. L. (Editors) (1999). *The Emergence of Unsaturated Soil Mechanics: Fredlund Volume*. NRC Research Press. 466-495.
- Climate Systems Analysis Group (CSAG) (2020). The Climate Information Portal. University of Cape Town. <http://cip.csag.uct.ac.za/webclient2/app/>
- Cloke, H. L., Anderson, M. G., McDonnell, J. J., and Renaud, J. P. (2006). Using numerical modelling to evaluate the capillary fringe groundwater ridging hypothesis of streamflow generation. *Journal of Hydrology*, 316(1–4), 141–162. <https://doi.org/10.1016/j.jhydrol.2005.04.017>
- Corey, A.T. (1986) *Mechanics of Immiscible Fluids in Porous Media*. 2nd Edition, Water Resources Publications, Littleton, CO.

- Dacosta, M. A. (2017). Mineralogical characterization of South African mine tailings with aim of evaluating their potential for the purposes of Mineral Carbonation. Master of Science Thesis, Department of Geological Sciences, University of Cape Town.
- Davies, M., McRoberts, E., and Martin, T. E. (2002). Static liquefaction of tailings: fundamentals and case histories. Tailing Dams 2002: Association of State Dam Safety Officials, U.S. Society on Dams, April 29-May 1, 2002, Las Vegas, Nevada.
- Davis, C. (2010). A climate change handbook for the North-Eastern South Africa, Pretoria: Climate Change Research Group. Council for Scientific and Industrial Research (CSIR).
- Department of Environmental Affairs (2012). 2nd South Africa Environment Outlook. A report on the state of the environment. Executive Summary. Department of Environmental Affairs, Pretoria. 60.
- de Rooij, G. H. (2010). Menisci, pressures, and potentials Big and small: menisci in soil pores affect water pressures, dynamics of groundwater levels, and catchment-scale average matric potentials Menisci, pressures, and potentials. *Hydrol. Earth Syst. Sci. Discuss*, 7, 6491–6523. <https://doi.org/10.5194/hessd-7-6491-2010>
- Dippenaar, M. A., van Rooy, J. L., Breedts, N., Huisamen, A., Muravha, S. E., Mahlangu, S., and Mulders, J. A. (2014). *Vadose Zone Hydrology: Concepts and Techniques*. 1-194. Water Research Commission. https://www.researchgate.net/publication/361209137_Testing_of_hydromechanical_properties_of_the_variably_saturated_residual_dolomite_wad
- Do, T. M., Laue, J., Mattsson, H., and Jia, Q. (2021). Numerical analysis of an upstream tailings dam subjected to pond filling rates. *Applied Sciences*, 11, 6044. <https://doi.org/10.3390/app11136044>
- du Plessis, J. A., and Burger, G. J. (2015). Investigation into increasing short-duration rainfall intensities in South Africa. *Water SA*, 41(3), 416–424. <https://doi.org/10.4314/wsa.v41i3.14>
- Dyson, L. L., Engelbrecht, C. J., Turner, K., Landman, S. (2012). Water Research Commission. (n.d.). A short-term heavy rainfall forecasting system for South Africa with first implementation over the Gauteng Province. South African Water Research Commission Report No. 1906/1/12, 124. https://www.researchgate.net/publication/260532020_A_baseline_climatology_of_sounding-derived_parameters_associated_with_heavy_rainfall_over_Gauteng_South_Africa

- Elsenbeer, H., Lorieri, D., and Bonell, M. (1995). Mixing-model approaches to estimate stormflow sources in an overland flow dominated rainforest catchment. *Water Resources Research*, 31(9), 2267–2278. <https://www.researchgate.net/publication/364115156>
- Engelbrecht, F., Adegoke, J., Bopape, M., Naidoo, M., Garland, R., Thatcher, M., McGregor, J. Katzfey, J., Werner, M. and Ichoku, C. 2015: Projections of rapidly rising surface temperatures over Africa under low mitigation. *Environmental Research Letters*, 10(8), 085004, doi:10.1088/1748-9326/10/8/085004
- Fala, O., Molson, J., Aubertin, M., and Bussi re, B. (2005). Numerical modelling of flow and capillary barrier effects in unsaturated waste rock piles. *Mine Water and the Environment*, 24(4), 172–185. <https://doi.org/10.1007/s10230-005-0093-z>
- Farouk, A., Lamboj, L., and Kos, J. (2004). A Numerical Model to Predict Matric Suction Inside Unsaturated Soils. 44(4).
- Fayer, M. J., and Hillel, D. (1986). Air encapsulation: I. Measurement in a field soil. *Soil Sci. Soc. Am.*, 50(3), 568–572.
- Fourie, A. B., and Blight, G. E. (2009). Preventing catastrophic failures and mitigating environmental impacts of tailings storage facilities. *Procedia Earth and Planetary Science*, 1(1), 1067–1071.
- Fourie, A. B., Blight, G. E., and Papageorgiou, G. (2002). Static liquefaction as a possible explanation for the Merriespruit tailings dam failure: Reply. *Canadian Geotechnical Journal*, 39(6), 1441–1442.
- Fourie A, Verdugo R, Bjelkevik A, Torres LA, Znidarcic D (2022) 20ICSMGE State of the Art - Tailings. In Md. M. Rahman and M. Jaksa (Eds.), 20th International Conference on Soil Mechanics and Geotechnical Engineering - State of the Art and Invited Lectures (pp. 121–183).
- Fredlund, D. G., and Houston, S. L. (2013). Interpretation of soil-water characteristic curves when volume change occurs as soil suction is change. In: *Advances in unsaturated soils: proceedings of the first Pan-American Conference on Unsaturated Soils, Cartagena de Indias, Colombia, 20-22 February 2013*. CRC Press/Balkema. 15-31.
- Fredlund, D.G., Morgenstern, N.R., and Widger, R. A. (1978). The shear strength of Unsaturated Soils. *Canadian Geotechnical Journal*, 15(3), 313–321.
- Fredlund, D. G., and Pham, H. Q. (2006). A volume-mass constitutive model for unsaturated soils in terms of two independent stress state variables. *Proceedings of the Fourth International Conference on Unsaturated Soils, ASCE*, 1, 105–134.

- Fredlund, D. G., and Rahardjo, H. (1993). Soil mechanics for unsaturated soils. John Wiley and Sons Inc., New York. <https://doi.org/10.1002/9780470172759>
- Fredlund, D. G., Rahardjo, H., and Fredlund, M. D. (2012). Unsaturated Soil Mechanics in Engineering Practice. John Wiley and Sons Inc., New York. <https://doi.org/10.1002/9781118280492>
- Fredlund, D. G., Rahardjo, H., and Ng, T. (1993). Effect of pore-air and negative pore-water pressures on stability at the end-of-construction. Proceedings of the International Conference on Dam Engineering, 12-13 January 1993. Johor Bahru, Malaysia. 43-51.
- Fredlund, D. G., and Stianson, J. (2011). Quantification of moisture flux boundary conditions from climatic datasets. Proceedings of the NSAT 2011 Symposium on Unsaturated Soils., September 19-21, 2011.
- Fredlund, D. G., Xing, A., and Huang, S. (1994). Predicting the permeability function for unsaturated soils using the soil– water characteristic curve. Canadian Geotechnical Journal, 31, 533–546.
- Fredlund, M. D., and Xi, A. (1994). Equations for the soil-water characteristic curve. Canadian Geotechnical Journal, 31(3), 521–532.
- Freescale Semiconductor Literature Distribution Centre (NXP). (2008). Freescale Semiconductor: + 10 kPa On-Chip Temperature Compensated and Calibrated Silicon Pressure Sensors. <https://www.nxp.com/docs/en/data-sheet/MPX2100.pdf>
- Gariano, S. L., and Guzzetti, F. (2016). Landslides in a changing climate. Earth Science Reviews, 162(2016), 227–252.
- Gillham, R. W. (1984). The capillary fringe and its effect on water-table response. Journal of Hydrology, 67(1–4), 307–324. doi: 10.1016/0022-1694(84)90248-8
- Guang-jin, W., Jing-wen, K., Chao, D., Yong-jun, T., and Xiang-yun, K. (2017). Study on tailings dam over-topping failure model test and break mechanism under the rainfall condition. Tehnicki Vjesnik - Technical Gazette, 24(6), 1897–1904. <https://doi.org/10.17559/tv-20170619031221>
- Guo, H., Jiao, J. J., and Weeks, E. P. (2008). Rain-induced subsurface airflow and Lisse effect. Water Resources Research, 44(7), 1–9. <https://doi.org/10.1029/2007WR006294>
- Guo, J. (2016). Stability Analysis of the Earth Dams and Dikes under the Influence of Precipitation and Vegetation, Doctor of Engineering, Faculty of Environmental Sciences, Technische Universität Dresden.

- Gutiérrez, J.M., Jones, R.G. and Narisma, G.T., 2021. IPCC interactive Atlas. In Climate change 2021: The physical science basis. contribution of working group I to the sixth assessment report of the intergovernmental panel on climate change. Cambridge University Press Cambridge.
- Halabi, A. L. M., Siacara, A. T., Sakano, V. K., Pileggi, G., and Futai, M. M. (2022). Tailings Dam Failures: A Historical Analysis of the Risk. *J Fail. Anal. and Preven*, 22, 464–477. <https://doi.org/10.1007/s11668>
- Hallema, D. W., Moussa, R., Sun, G., and McNulty, S. G. (2016). Surface storm flow prediction on hillslopes based on topography and hydrologic connectivity. *Ecological Processes*, 5(1), 1–13. <https://doi.org/10.1186/s13717-016-0057-1>
- Hansen, K. (2022). Jagersfontein Covered in Mining Waste. Earth Observatory. <https://doi.org/https://earthobservatory.nasa.gov/images/150497/jagersfontein-covered-in-mining-waste>
- Hardie, M., Lisson, S., Doyle, R., and Cotching, W. (2013). Determining the frequency, depth and velocity of preferential flow by high frequency soil moisture monitoring. *Journal of Contaminant Hydrology*, 144, 66–77.
- Healy, R. W., and Cook, P. G. (2002). Using groundwater levels to estimate recharge. *Hydrogeology Journal*, 10, 91–109. <https://doi.org/10.1007/s10040-001-0178-0>
- Heliotis, F.D., and DeWitt, C. B. (1987). Rapid water table responses to rainfall in a northern peatland ecosystem. *Water Resource Bulletin*, 23(6), 1011–1016.
- Hewitson, B., and Crane, R. (2006). Consensus between GCM climate change projections with empirical downscaling: Precipitation downscaling over South Africa. *International Journal of Climatology*, 26, 1315–1337.
- Hillel, D. (1998). *Environmental Soil Physics*. Amsterdam: Elsevier Academic Press.
- Hogervorst, F. A. N., de Rooij, G. H., and Bierkens, M. F. P. (2003). Rapid rise after rainfall of a shallow groundwater table in a sandy soil: comparing simulations to observations. *Geophysical Research Abstracts*. European Geophysical Society.
- Honeywell. (2014). TruStability Board Mount Pressure Sensors. <https://sps.honeywell.com/us/en/products/advanced-sensing-technologies/healthcare-sensing/board-mount-pressure-sensors/trustability-hsc-series>
- Hopp, L., Glaser, B., Klaus, J., & Schramm, T. (2020). The relevance of preferential flow in catchment scale simulations: Calibrating a 3D dual-permeability model using DREAM. *Hydrological Processes*, 34(5), 1237–1254. <https://doi.org/10.1002/hyp.13672>

- Hooghoudt, S. B. (1947). Observations of groundwater levels for agriculture. TNO Hydrological Research Committee, Reports Technical Meetings, 1–6, 94–110.
- Hu, L., Wu, H., Zhang, L., Zhang, P., and Wen, Q. (2017). Geotechnical properties of mine tailings. *Journal of Materials in Civil Engineering*, 29(2), 1–10. [https://doi.org/10.1061/\(ASCE\)MT.1943-5533.0001736](https://doi.org/10.1061/(ASCE)MT.1943-5533.0001736)
- Humphries, G., Rule, C., and Wolmarans, E. (2006). The development of a process flowsheet for the new Anglo Platinum, PPRust north concentrator, incorporation HPGR technology. International Platinum Conference ‘Platinum Surges Ahead’, The Southern African Institute of Mining and Metallurgy. 129–136.
- ICOLD (2001) Tailings Dams—Risk of Dangerous Occurrences, Lessons Learnt from Practical Experiences. Bulletin 121. United Nations Environmental Programme (UNEP), Division of Technology, Industry and Economics (DTIE) and International Commission on Large Dams (ICOLD), Paris.
- IPCC. (2014). Climate Change 2014: Synthesis Report. Contribution of Working Groups I, II and III to the Fifth Assessment Report of the Intergovernmental Panel on Climate Change. [Core Writing Team; R.K. Pachauri and L.A. Meyer (eds.)]. IPCC, Geneva, Switzerland, 151.
- IPCC. (2022): Climate Change 2022: Impacts, Adaptation, and Vulnerability. Contribution of Working Group II to the Sixth Assessment Report of the Intergovernmental Panel on Climate Change [H.-O. Pörtner, D.C. Roberts, M. Tignor, E.S. Poloczanska, K. Mintenbeck, A. Alegría, M. Craig, S. Langsdorf, S. Löschke, V. Möller, A. Okem, B. Rama (eds.)]. Cambridge University Press. Cambridge University Press, Cambridge, UK and New York, NY, USA, 3056 pp., doi:10.1017/9781009325844.
- Islam, N., Wallender, W. W., Mitchell, S., Wicks, S., and Howitt, R. E. (2006). Performance evaluation of methods for the estimation of soil hydraulic parameters and their suitability in a hydrologic model. *Geoderma*, 134(1–2), 135–151.
- Iverson, R. M. (2000). Landslide triggering by rain infiltration. *Water Resources Research*, 36(7), 1897–1910. <https://doi.org/10.1029/2000WR900090>
- Jamiolkowski, M., Carrier, W.D., Chandler, Richard, Hoeg, K., Swierczynski, W., and Wolski, W. (2010). The Geotechnical Problems of The Second World Largest Copper Tailings Pond at Zelazny Most, Poland. *Geotechnical Engineering*, 41(1), 1–15.
- Jennings, J. E. (1979). The failure of a slimes dam at Bafokeng: Mechanisms of failure and associated design considerations. *Die Siviele Ingenieur in Suid Afrika*, 21(6), 135–143.

- Jeong, S., Lee, K., Kim, J., and Kim, Y. (2017). Analysis of rainfall-induced landslide on unsaturated soil slopes. *Sustainability (Switzerland)*, 9(7), 1–20. <https://doi.org/10.3390/su9071280>
- Johansson, J. (2014). Impact of Water-Level Variations on Slope Stability. PhD thesis, Luleå University of Technology.
- Karim, R., Hughes, D., Kelly, R., and Lynch, K. (2020). A rational approach for modelling the meteorologically induced pore water pressure in infrastructure slopes. *European Journal of Environmental and Civil Engineering*, 24(14), 2361–2382. <https://doi.org/10.1080/19648189.2018.1506824>
- Karombo, T. (2020). South Africa has the world's highest number of environmentally dangerous tailing dams. *Quartz Africa*. <https://qz.com/africa/1786297/south-africa-has-most-environmentally-dangerous-tailing-dams/>
- Katsura, S., Kosugi, K., Yamakawa, Y., and Mizuyama, T. (2014). Field evidence of groundwater ridging in a slope of a granite watershed without the capillary fringe effect. *Journal of Hydrology*, 511, 703–718.
- Khaled, I. M., Tsuyoshi, M., Kohei, N., Taku, N., and Hiromi, I. (2011). Experimental and Modelling Investigation of Shallow Water Table Fluctuations in Relation to Reverse Wieringermeer Effect. *Open Journal of Soil Science*, 01(02), 17–24. <https://doi.org/10.4236/ojss.2011.12003>
- Khan, Y. A., Lateh, H., Baten, M. A., and Kamil, A. A. (2012). Critical antecedent rainfall conditions for shallow landslides in Chittagong City of Bangladesh. *Environmental Earth Sciences*, 67(1), 97–106. <https://doi.org/10.1007/s12665-011-1483-0>
- Kim, H., Cho, S., Lee, D., Jung, Y. Y., Kim, Y. H., Koh, D. C., and Lee, J. (2017). Influence of pre-event water on streamflow in a granitic watershed using hydrograph separation. *Environmental Earth Sciences*, 76(82), 1–10. <https://doi.org/10.1007/s12665-017-6402>
- Knoesen, D. M., Schulze, R. E., and Smithers, J. C. (2011). Climate Change and Short duration Day Design Rainfall: A 2011 Perspective. In R.E. Schulze. 2011. A 2011 Perspective on Climate Change and the South African Water Sector (199–205). Water Research Commission, Pretoria, RSA, WRC Report TT 518/12, Chapter 7.1, 199-205.
- Koseki, J., Kimhor, H., Nakajima, S., Mulmi, S., Watanabe, K., and Tateyama, M. (2010). Negative pore air pressure generation in backfill of retaining walls during earthquakes and its effect on seismic earth pressure. *Soils and Foundations*, 50(5), 747–755.

- Kossoff, D., Dubbin, W. E., Alfredsson, M., Edwards, S. J., Macklin, M. G., and Hudson-Edwards, K. A. (2014). Mine tailings dams: Characteristics, failure, environmental impacts, and remediation. *Applied Geochemistry*, 51, 229–245. <https://doi.org/10.1016/j.apgeochem.2014.09.010>
- Kovacs, A., Lohunova, O., Winkelmann-Oei, G., Mádai, F., and Török, Z. (2020). Safety of the Tailings Management Facilities in the Danube River Basin: Technical report. German Environmental Agency, Project No. 118221 FB000473/ENG Reference number: Z6 - 90 213-51/79. <https://unece.org/sites/default/files/2022-07/Safety%20of%20the%20Tailing>
- Kristo, C., Rahardjo, H., and Satyanaga, A. (2017). Effect of variations in rainfall intensity on slope stability in Singapore. *International Soil and Water Conservation Research*, 5(4), 258–264. <https://doi.org/10.1016/j.iswcr.2017.07.001>
- Kristo, C., Rahardjo, H., and Satyanaga, A. (2019). Effect of hysteresis on the stability of residual soil slope. *International Soil and Water Conservation Research*, 7(3), 226–238. <https://doi.org/10.1016/j.iswcr.2019.05.003>
- Kruger, A. C. and M. Nxumalo (2017). Surface temperature trends from homogenized time series in South Africa: 1931–2015. *International Journal of Climatology*, 37(5), 2364–2377, doi:10.1002/joc.4851.
- Lawrence, J., Blackett, P., and Cradock-Henry, N. A. (2020). Cascading climate change impacts and implications. *Climate Risk Management*, 29. <https://doi.org/10.1016/j.crm.2020.100234>
- Li, C., Zwiers, F., Zhang, X., Li, G., Sun, Y. and Wehner, M. (2021). Changes in Annual Extremes of Daily Temperature and Precipitation in CMIP6 Models. *Journal of Climate*, 34(9), 3441–3460, doi:10.1175/JCLI-D-19-1013.1.
- Limpopo Economic Development Environment and Tourism (LEDET). (2015). Limpopo Environmental Outlook Report: Climate Change for the Limpopo Province, South Africa.
- Lins, Y., Schanz, T., and Fredlund, D. G. (2009). Modified pressure plate apparatus and column testing device for measuring SWCC of sand. *Geotechnical Testing Journal*, 32(5). <https://doi.org/10.1520/GTJ101318>
- Liu, C., Shen, Z., Gan, L., Xu, L., Zhang, K., and Jin, T. (2018). The Seepage and Stability Performance Assessment of a New Drainage System to Increase the Height of a Tailings Dam. *Applied Sciences*, 8(1840). <https://doi.org/10.3390/app8101840>

- López-Acosta, N. P., and Menoza, J. A. (2016). Study of Unsaturated Soils by Coupled Numerical Analyses of Water Flow-Slope Stability. In *Groundwater - Contaminant and Resource Management* (163-191). <https://doi.org/10.5772/63903>
- Lorentz, S.A., Thornton-Dibb, S., Pretorius, C., and Goba, P. (2004). Hydrological Systems Modelling Research Programme: Hydrological Processes Phase II Quantification of Hillslope, Riparian and Wetland Processes. WRC Report No 1320/1/08. Water Research Commission, Pretoria
- Lorentz, S.A., Terrell, C. and Ngubane, S. (2019). Laboratory determination of selected tailings and silica sand materials. University of KwaZulu-Natal.
- Lyu, Z., Chai, J., Xu, Z., Qin, Y., and Cao, J. (2019). A Comprehensive Review on Reasons for Tailings Dam Failures Based on Case History. *Advances in Civil Engineering*. 1-18. <https://doi.org/10.1155/2019/4159306>
- MacRobert, C. J., and Blight, G. E. (2013). A field study of the in-situ moisture regime during active hydraulic tailings deposition. *Journal of the South African Institution of Civil Engineering*, 55(3), 57–68.
- MacRobert, C. (2013). Field capacity and moisture loss during active deposition on Tailings Dams. 18th International Conference on Soil Mechanics and Geotechnical Engineering: Challenges and Innovations in Geotechnics, ICSMGE 2013, 2, 1143–1146.
- Manyeruke, T.D. (2007) Geochemical variations of the Platreef in the Northern Limb of the Bushveld Complex: Implications for the origin of the PGE mineralisation, PhD Thesis, University of Pretoria, 206. https://www.researchgate.net/publication/324484206_Platinum-group_minerals_of_the_F_and_T_zones_Waterberg_Project_Far_Northern_Bushveld_Complex_implication_for_the_formation_of_the_PGE_mineralisation
- Manzunzu, B., Midzi, V., Mulabisana, T. F., Zulu, B., Pule, T., Myendeki, S., and Rathod, G. W. (2019). Seismotectonics of South Africa. *Journal of African Earth Sciences*, 149, 271–279. <https://doi.org/10.1016/j.jafrearsci.2018.08.012>
- Martin, T. E., and McRoberts, E. C. (1999). Some considerations in the stability analysis of upstream. *Proceedings of the Conference in Tailings and Mine Waste*, December, 287–302. https://www.tib.eu/en/search/id/BLCP%3ACN028387622/Some-considerations-in-the-stability-analysis-f/?tx_tibsearch_search%5Bsearchspace%5D=tn#documentinfo
- Marui, A., Yasuhara, M., Kuroda, K., and Takayama, S. (1993). Subsurface water movement and transmission of rainwater pressure through a clay layer. *IAHS Publ*, 216, 463–470.

- Meyer, T., and Hrubec, D. (1998). Geotechnical instrumentation and monitoring for pit slope stabilization and remediation. International Conference; 5th, Tailings and Mine Waste, 27–34. https://tailingsandminewaste.com/wp-content/uploads/TMW2014_proceedings.pdf
- Meyboom, P. (1967). Groundwater Studies in the Assiniboine River Drainage Basin: Hydraulic Characteristics of Phreatophytic vegetation in the south-central Saskatchewan. Geological Survey Bulletin, 139.
- Miyazaki, T., Ibrahim, M. K., and Nishimura, T. (2012). Shallow Groundwater Dynamics Controlled by Lisse and Reverse Wieringermeer Effects. *Journal of Sustainable Watershed Science and Management*, 1(2), 36–45. <https://doi.org/10.5147/jsWSM.2012.0065>
- Morton, K.L., Muresan, M.C. and Ramsden, F. (2008). Importance of pore pressure monitoring in high walls. SA IMM conference on surface mining August 2008. SA ISSN 0038-223X/3.00 Jnl of the South African Institute of Mining and Metallurgy Volume 108 November 2008. https://www.researchgate.net/publication/348279170_The_Use_of_Accurate_Pore_Pressure_Monitoring_for_Risk_Reduction_in_Tailings_Dams
- Morton, K. L. (2019). Accurate pore pressure monitoring reduces tailings dam risk. *Mining Review Africa*, 12, 12–14. <https://www.miningreview.com/health-and-safety/accurate-pore-pressure-monitoring-reduces-tailings-dam-risk/>
- Morton, K. L. (2020). Tailings dam risk reduction using accurate pore pressure monitoring. South African Institute of Mining and Metallurgy, Tailings Storage Conference 10-13th February 2020 Johannesburg South Africa, 37–47. <http://www.gardguide.com>
- Muñoz, E. (2019). Soil moisture dynamics in water- and energy-limited ecosystems. Application to slope stability. <http://bdigital.unal.edu.co/73824/6/1128281996.2019.pdf>
- Munyai, R. B., Chikoore, H., Musyoki, A., Chakwizira, J., Muofhe, T. P., Xulu, N. G., & Manyanya, T. C. (2021). Vulnerability and adaptation to flood hazards in rural settlements of Limpopo province, South Africa. *Water (Switzerland)*, 13(24). <https://doi.org/10.3390/w13243490>
- Mustafa, M. R., Rezaei, R. B., Rahardjo, H., Isa, M. H., and Arif, A. (2015). Artificial neural network modelling for spatial and temporal variations of pore-water pressure responses to rainfall. *Advances in Meteorology*, Article ID 273730, 1–12.
- Ng, C. W. W., and Shi, Q. (1998). Influence of rainfall intensity and duration on slope stability in unsaturated soils. *Quarterly Journal of Engineering Geology*, 31(2), 105–113. <https://doi.org/10.1144/GSL.QJEG.1998.031.P2.04>

- Nishimura, T., Toyota, H., Vanapalli, S. K., and Oh, W. T. (2008). The shear strength behavior of a silty soil in the residual zone of unsaturation. *12th International Conference on Computer Methods and Advances in Geomechanics*, 3, 2213–2221.
- Nišić, D. (2021). Preliminary risk assessment of dam failure at the location of the cukaru peki deposit, bor (Serbia). *Minerals*, 11(10).
- Olivier, C., Engelbrecht, C., Bopape, M., and Botai, J. (2020). Status of climate in South Africa and predictions for the 2020-2021 summer season. *Advisory Panel on Weather and Climate*, October 2020, 1–15.
- Ozili, P. K. (2023). The acceptable R-square in empirical modelling for social science research. <https://mpira.uib.uni-muenchen.de/115769/>
- Otto, F. E. L., Wolski, P., Lehner, F., Tebaldi, C., van Oldenborgh, G. J., Hogesteeger, S., Singh, R., Holden, P., Fučkar, N. S., Odoulami, R. C., & New, M. (2018). Anthropogenic influence on the drivers of the Western Cape drought 2015-2017. *Environmental Research Letters*, 13(12). <https://doi.org/10.1088/1748-9326/aae9f9>
- Pacheco, R. L. R. (2018). Static liquefaction in tailings dam and flow failure. *Geotechnical Risks Seminar*. Complutense University of Madrid (UCM). Madrid, Spain. 1-11.
- Papageorgiou, G; Fourie, A.B. and Blight, G. E. (1999). Static Liquefaction of Merriespruit Gold Tailings. *Geotechnics for Developing Africa*, 61–72.
- Pardeshi, S. D., Autade, S. E., and Pardeshi, S. S. (2013). Landslide hazard assessment: Recent trends and techniques. *SpringerPlus*, 2(1). <https://doi.org/10.1186/2193-1801-2-523>
- Patle, G. T., Singh, D. K., Sarangi, A., and Sahoo, R. N. (2017). Modelling of groundwater recharge potential from irrigated paddy field under changing climate. *Paddy and Water Environment*, 15(2), 413–423. <https://doi.org/10.1007/s10333-016-0559-6>
- Pelascini, L., Steer, P., Mouyen, M., and Longuevergne, L. (2022). Finite-hillslope analysis of landslides triggered by excess pore water pressure: the roles of atmospheric pressure and rainfall infiltration during typhoons. *Natural Hazards and Earth System Sciences*, 22(10), 3125–3141. <https://doi.org/10.5194/nhess-22-3125-2022>
- Petley, D. (2022). Analysing the aerial and satellite imagery of the Jagersfontein tailings dam disaster. *The Landslide Blog*. <https://doi.org/https://blogs.agu.org/landslideblog/2022/09/13/jagersfontein-tailings-dam-2/>
- Planet Team. (2022). Planet Application Program Interface. In *Space for Life on Earth*. <https://doi.org/https://www.planet.com/>

- Piciullo, L., Storrøsten, E. B., Liu, Z., Nadim, F., and Lacasse, S. (2022). A new look at the statistics of tailings dam failures. *Engineering Geology*, 303:106657. <https://doi.org/10.1016/j.enggeo.2022.106657>
- Pierce, D. W., J. F. Kalansky, and D. R. Cayan, (Scripps Institution of Oceanography). 2018. Climate, Drought, and Sea Level Rise Scenarios for the Fourth California Climate Assessment. California's Fourth Climate Change Assessment, California Energy Commission. Publication Number: CNRA-CEC-2018-006.
- Rahardjo, H., Choon, L. E., and Tami, D. (2004). Capillary Barrier for Slope Stabilisation. *Geotechnics*, 17(January), 70–72.
- Rahardjo, H., Leong, E.C. and Rezaur, R. B. (2008). Effect of antecedent rainfall on pore-water pressure distribution characteristics in residual soil slopes under tropical rainfall. *Hydrological Processes*, 22(4), 506–523.
- Rahardjo, H., Li, X. W., Toll, D. G., and Leong, E. C. (2001). The effect of antecedent rainfall on slope stability. *Geotechnical and Geological Engineering*, 19(3–4), 371–399. <https://doi.org/10.1023/A:1013129725263>
- Rahardjo, H., Satyanaga, A., and Leong, E. C. (2016). Effects of Rainfall Characteristics on the Stability of Tropical Residual Soil Slope. *E3S Web of Conferences*, 9, 1–6. <https://doi.org/10.1051/e3sconf/20160915004>
- Rapolaki, R. S. (2020). An analysis of heavy rainfall events over the Limpopo River Basin in southern Africa, their moisture sources and pathways. PhD thesis. Department of Oceanography. University of Cape Town.
- Rassam, D. W., and Williams, D. J. (2000). A Dynamic Model for Determining the Soil Water Characteristic for Coarse Grained Soils. *Geotechnical Testing Journal*, 23(1), 67–71.
- Rassam, D., Šimůnek, J., Mallants, D., and van Genuchten, M. Th. (2018). The HYDRUS-1D software package for simulating the movement of water, heat, and multiple solutes in variably-saturated media: Tutorial, version 1.00. In CSIRO Land and Water, Australia (Issue July).
- Rebetez, M., Lugon, R. and Baeriswyl, P. (1997). Climate change and debris flows in high mountain regions: the case study of the Ritigraben torrent (Swiss Alps). *Clim. Chang.* 371–389.
- Rico, M., Benito, G., and Díez-Herrero, A. (2008a). Floods from tailings dam failures. *Journal of Hazardous Materials*, 154(1–3), 79–87. <https://doi.org/10.1016/j.jhazmat.2007.09.110>

- Rico, M. B., Diez-Herrero, A., and Pereira, H. G. (2008b). Reported tailings dam failures: a review of the European incidents in the worldwide context. *Journal of Hazardous Materials*, 152, 846–852.
- Riquelme, J., and Godoy, C. (2017). SWCC: Experimental results of copper tailings and spent ore. In: *Proceedings of the Tailings and Mine Waste Conference*. November 2017. 9
- Robertson, P. K., de Melo, L., Williams, D. J., and Wilson, G. W. (2019). Report of the Expert Panel on the Technical Causes of the Failure of Feijão Dam I. 81.
- Roche, C., Thygesen, K., Baker, E. (Eds.) (2017). *Mine Tailings Storage: Safety Is No Accident. A UNEP Rapid Response Assessment*. United Nations Environment Programme and GRID-Arendal, Nairobi and Arendal. https://gridarendal-website-live.s3.amazonaws.com/production/documents/s_document/371/original/RRA_MineTailings_lores.pdf?1510660693
- Rodríguez, R., Muñoz-Moreno, A., Vanessa Caparrós, A., García-García, C., Brime-Barrios, Á., César Arranz-González, J., Rodríguez-Gómez, V., Javier Fernández-Naranjo, F., and Alcolea, A. (2021). How to Prevent Flow Failures in Tailings Dams. *Mine Water and the Environment*, 40(1), 83–112. <https://doi.org/10.1007/s10230-021-00752-8>
- Rotta, L. H. S., Alcântara, E., Park, E., Negri, R. G., Lin, Y. N., Bernardo, N., Mendes, T. S. G., and Souza Filho, C. R. (2020). The 2019 Brumadinho tailings dam collapse: Possible cause and impacts of the worst human and environmental disaster in Brazil. *International Journal of Applied Earth Observation and Geoinformation*. 90, 102-119. <https://doi.org/10.1016/j.jag.2020.102119>
- Rule, C. M. (2011). Stirred milling-new comminution technology in the PGM industry. *The Journal of The Southern African Institute of Mining and Metallurgy*, 111, 101–107.
- Ruostenoja, K., Carter, T. R., and Tuomenvirta, H. (2003). *Future climate in world regions: an intercomparison of model-based projections for the new IPCC emissions scenarios*. Finnish Meteorological Institute, Finland.
- Salas-García, J., Garfias, J., Martel, R., and Bibiano-Cruz, L. (2017). A Low-Cost Automated Test Column to Estimate Soil Hydraulic Characteristics in Unsaturated Porous medium. *Geofluids*, 2017, 1–13. <https://doi.org/doi.org/10.1155/2017/6942736>
- Schulze, R. E. (2012). *A 2011 Perspective on Climate Change and the South African Water Sector*. Water Research Commission, Pretoria, RSA, WRC Report 1843/2/11.

- Schulze, R. E., and Bulcock, L. M. (2011). Climate Change and Thresholds of Daily Rainfall Amounts Exceeded: A 2011 Perspective. In Schulze, R.E. (Ed) 2011. A 2011 Perspective on Climate Change and the South African Water Sector (103–106).
- Schulze, R. E., Hewitson, B. C., Barichievy, K. R., Tadross, M. A., Kunz, R. P., Horan, M. J. C., and Lumsden, T. G. (2011a). Methodological approaches to assessing eco-hydrological responses to climate change in South Africa. Water Research Commission, Pretoria.
- Schulze, R. E., Knoesen, D. M., Kunz, R. P., and Lumsden, T. G. (2011b). General Circulation Models and Downscaling for South African Climate Change Impact Studies: A 2011 Perspective. In A 2011 Perspective on Climate Change and the South African Water Sector (21–30).
- Schulze, R. E., and Maharaj, M. (2007). A-Pan Equivalent Reference Potential Evaporation. In R. E. Schulze (Ed.), South African Atlas of Climatology and Agrohydrology. Water Resource Commission, Pretoria, RSA, WRC Report 1489/1/06, Section 13.2.
- Schmidt, J. S., & Osebold, R. (2017). Environmental management systems as a driver for sustainability: state of implementation, benefits and barriers in German construction companies. *Journal of Civil Engineering and Management*, 23(1), 150–162. <https://doi.org/10.3846/13923730.2014.946441>
- Sekhar, D. M. R. and, and Jakhu, M. R. (1983). Primary vegetative growth on an old tailings dam, Zawar mines. *Minerals and the Environment*, 5(4), 128–132. <https://doi.org/10.1007/BF02093334>
- Seneviratne, S. I., Zhang, X., Adnan, M., Badi, W., Dereczynski, C., Luca, A. D., Ghosh, S., Iskandar, I., Kossin, J., Lewis, S., Otto, F., Pinto, I., Satoh, M., Vicente-Serrano, S. M., Wehner, M., Zhou, B. and Allan, R. (2021) Weather and climate extreme events in a changing climate. In: Masson-Delmotte, V. P., Zhai, A., Pirani, S. L. and Connors, C. (eds.) *Climate Change 2021: The Physical Science Basis: Working Group I contribution to the Sixth Assessment Report of the Intergovernmental Panel on Climate Change*. Cambridge University Press, Cambridge, UK, pp. 1513-1766.
- Sidle, R.C., Ochiai, H. (2006). Landslides: processes, prediction, and land use. American Geophysical Union.
- Silin, D., Korneev, V., and Goloshubin, G. (2003). Pressure diffusion waves in porous media In: SEG Technical Program Expanded Abstracts 2003. Soc. Explor. Geophys., Tulsa, OK. 2323–2326. doi:10.1190/1.1817821

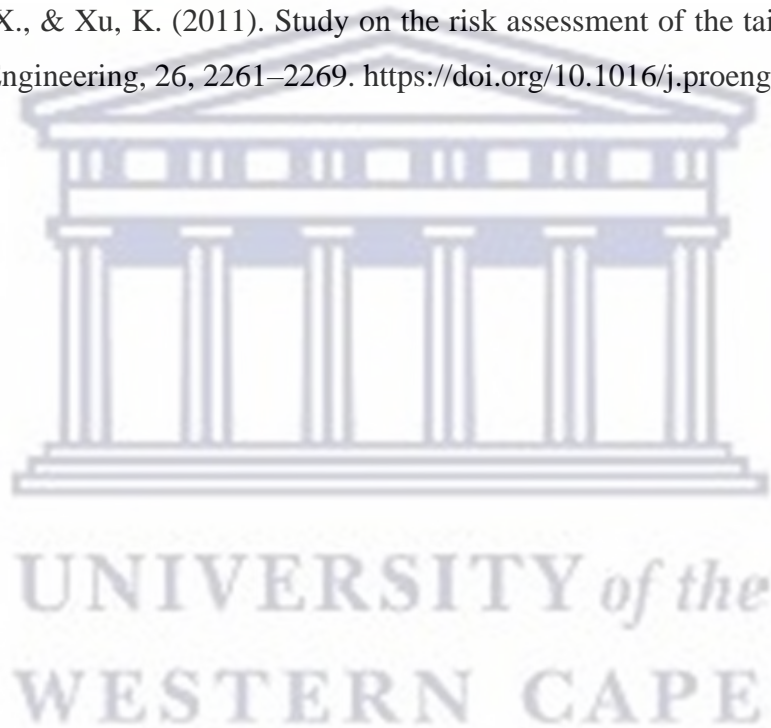
- Singh, S., Kumar, A., and Sitharam, T. G. (2023). Stability investigation of embankments of a tailings pond for its dry closure: an Indian case study. *Sādhanā Indian Academy of Sciences*, 48(29), 1–22.
- Skopp, J. M. (2011). Physical Properties of Primary Particles. In P. M. Huang, Y. Li, and M. E. Sumner (Eds.), *Handbook of Soil Sciences: Properties and Processes* (Second Edition, 1–9). CRC Press.
- Smith, E., and Connell, D. (1973). The Role of Water in the Failure of Tailings Dams. In *Tailings and Waste Disposal: Seepage, Contamination, Regulations and Control*. Miller Freeman Publications. 627–650.
- Smithers, J. C., and Schulze, R. E. (2002). Design Rainfall and Flood Estimation in South Africa. December, 1–180. Water Resource Commission, Pretoria, RSA, WRC Project No: K5/1060.
- South African Weather Service (SAWS) (2020). Mokopane Historical Weather Data.
- Spinoni, J., Barbosa, P., De Jager, A., McCormick, N., Naumann, G., Vogt, J.V., Magni, D., Masante, D. and Mazzeschi, M. A new global database of meteorological drought events from 1951 to 2016. *Journal of Hydrology: Regional Studies*, 22, 100593, doi:10.1016/j.ejrh.2019.100593.
- SRK (2011). Anglo Platinum, Mogalakwena: Tailings, Heap Leach and Waste Focus. <http://www.srk.com/files/File/newsletters/SRKnews-44-Tailings-letter-LR.pdf>
- Strachan, C., and Van, B. (2018). Conclusions from evaluation of tailings dam incidents. Fort Collins, Colorado: Stantec.
- Sun, J., Liu, Q., Li, J., and An, Y. (2009). Effects of rainfall infiltration on deep slope failure. *Science in China, Series G: Physics, Mechanics and Astronomy*, 52(1), 108–114. <https://doi.org/10.1007/s11433-009-0004-6>
- Sun, D., Zang, Y. and Semprich, S. (2015). Effects of Airflow Induced by Rainfall Infiltration on Unsaturated Soil Slope Stability. *Transport in Porous Media*, 107(3), 821–841. <https://doi.org/10.1007/s11242-015-0469-x>
- Tarboton, D.G. (2003) Rainfall-runoff processes. Utah State University, Logan. 1-30
- Tarek, M., Brissette, F., and Arsenault, R. (2021). Uncertainty of gridded precipitation and temperature reference datasets in climate change impact studies. *Hydrology and Earth System Sciences*, 25(6), 3331–3350. <https://doi.org/10.5194/hess-25-3331-2021>
- Temper, L., del Bene, D., and Martinez-Alier, J. (2015). Mapping the frontiers and front lines of global environmental justice: the EJAtlas. *Journal of Political Ecology*, 22, 255–278.

- Tian, W., Peiffer, H., Malengier, B., Xue, S., and Chen, Z. (2022). Slope Stability Analysis Method of Unsaturated Soil Slopes Considering Pore Gas Pressure Caused by Rainfall Infiltration. *Applied Sciences* (Switzerland), 12(21). <https://doi.org/10.3390/app122111060>.
- Torres, R. D., Montgomery, W. E., Anderson, S. P., and Loague, K. (1998). Unsaturated zone processes and the hydrologic response of a steep, unchanneled catchment. *Water Resource Res.*, 34(8), 1865–1879.
- Tuller, M., and Or, D. (2004). Retention of water in soil and the soil water characteristic curve. *Encyclopedia of Soils in the Environment*, 4, 278–289. http://www.engr.uconn.edu/environ/envphys/pdf/vadose_pdf/SWC_revised01.pdf
- Turner, I. L., and Nielsen, P. (1997). Rapid water table fluctuations within the beach face: Implications for swash zone sediment mobility. *Coastal Engineering*, 32, 45–59.
- Udukumbura, R. S., Gallage, C., Dawes, L., and Gui, Y. (2020). Determination of the hydraulic conductivity function of grey Vertisol with soil column test. *Heliyon*, 6(11), e05399. <https://doi.org/10.1016/j.heliyon.2020.e05399>
- Ukkola, A. M., De Kauwe, M. G., Roderick, M. L., Abramowitz, G., and Pitman, A. J. (2020). Robust future changes in meteorological drought in CMIP6 projections despite uncertainty in precipitation. *Geophysical Research Letters*, 46. <https://doi.org/10.1029/2020GL087820>.
- United Nations Office for Disaster Risk Reduction (UNDRR). (2020). The human cost of disasters: an overview of the last 20 years (2000-2019). <https://www.undrr.org/media/48008/download>
- van den Berghe, J.F., Ballard, J.C., Pirson, M and Reh, U. (2011). Risks of Tailings Dams Failure. Proceedings of the 3rd International Symposium on Geotechnical Safety and Risk, Munich, Germany, June 2-3, 2011. Bundesanstalt für Wasserbau, Karlsruhe, Germany.
- van der Zon, J. M. G. (2021). The return period of rainfall-induced static liquefaction of tailings dams: A modelling study. MSc thesis, Delft University of Technology.
- van Wageningen, A. (2006). The Impact of Climate Change on Hydrological Predictions with Specific Reference to 24-hour Rainfall Intensities in the Western Cape. MSc thesis, Department of Civil Engineering, Stellenbosch University.
- Vick, S. G. (1990). Planning, Design and Analysis of Tailings Dams. BiTech Publishers Ltd., Richmond.

- Voldoire, A., Sanchez-Gomez, E. and Salas Mélia, D. (2013). The CNRM-CM5.1 global climate model: description and basic evaluation. *Climate Dynamics*, 40, 2091–2121. <https://doi.org/10.1007/s00382-011-1259-y>
- von Storch, H., and Zwiers, F. W. (1988). Recurrence Analysis of Climate Sensitivity Experiments. *Journal of Climatology*, 1, 157–171.
- Waswa, G. W. (2013). Transient pressure waves in hillslopes. PhD thesis. Department of Civil Engineering. University of Kwa-Zulu Natal.
- Waswa, G. W., and Lorentz, S. A. (2015). Energy considerations in groundwater-ridging mechanism of streamflow generation. *Hydrological Processes*, 29, 4932–4946.
- Waswa, G. W., and Lorentz, S. A. (2016a). Energy consideration in intense-rainfall triggered shallow landslides. *South African Geotechnical Conference*, 327–333.
- Waswa, G. W., and Lorentz, S. A. (2016b). Transmission of pressure head through the zone of tension saturation in the Lisse effect phenomenon. *Hydrological Sciences Journal*, 61(10), 1770–1777. <https://doi.org/10.1080/02626667.2014.943230>
- Waswa, G.W., Lorentz, S.A. (2019). Dynamics of groundwater flow and upwelling pressure heads at a wetland zone in a headwater catchment. *SN Appl. Sci.* 1, 1069. <https://doi.org/10.1007/s42452-019-1052-9>
- Waswa, G. W., Clulow, A. D., Freese, C., le Roux, P. A. L., & Lorentz, S. A. (2013). Transient Pressure Waves in the Vadose Zone and the Rapid Water Table Response. *Vadose Zone Journal*, 12(1), vzj2012.0054. <https://doi.org/10.2136/vzj2012.0054>
- Watanabe, S., Hajima, T., Sudo, K., Nagashima, T., Takemura, T., Okajima, H., Nozawa, T., Kawase, H., Abe, M., Yokohata, T., Ise, T., Sato, H., Kato, E., Takata, K., Emori, S., and Kawamiya, M. (2011). MIROC-ESM 2010: Model description and basic results of CMIP5-20c3m experiments. *Geoscientific Model Development*, 4(4), 845–872. <https://doi.org/10.5194/gmd-4-845-2011>
- Weber, T., Haensler, A., Rechid, D., Pfeifer, S., Eggert, B., & Jacob, D. (2018). Analyzing Regional Climate Change in Africa in a 1.5, 2, and 3°C Global Warming World. *Earth's Future*, 6(4), 643–655. <https://doi.org/10.1002/2017EF000714>
- Weeks, E.P. (2005). The Lisse effect revisited. *Ground Water*, 40(6), 652–656. <https://doi.org/10.1111/j.1745-6584.2002.tb02552.x>
- Wei, Z., Yin, G., Wang, J. G., Wan, L., and Li, G. (2013). Design, construction and management of tailings storage facilities for surface disposal in China: Case studies of

- failures. In *Waste Management and Research*. 31(1), 106–112.
<https://doi.org/10.1177/0734242X12462281>
- Whitham, GB. 1974. *Linear and nonlinear waves*. Wiley-interscience
- Whitlow, R. (2001). *Basic Soil Mechanics (Fourth Edi)*. Pearson Education Ltd.
- Williams, D. J. (2015). Placing Soil Covers on Soft Mine Tailings. In *Ground Improvement Case Studies: Compaction, Grouting and Geosynthetics*. Geotechnical Engineering Centre, The University of Queensland, Australia. 51–81.
- Wills, B. A., and Finch, J. A. (2016). Tailings Disposal. *Wills' Mineral Processing Technology*, 439–448. <https://doi.org/10.1016/b978-0-08-097053-0.00016-9>
- WISE. (2023). Chronology of major tailings dam failures. World Information Service on Energy Uranium Project. <https://www.wise-uranium.org/mdaf.html>
- Wu, Y., Yang, A., Zhao, Y., and Liu, Z. (2019). Simulation of soil water movement under biochar application based on the hydrus-1D in the black soil region of China. *Applied Ecology and Environmental Research*, 17(2), 4183–4192.
- Yang, D., Lang, Q., and Zhang, L. (2015). Propagation of pore pressure diffusion waves in saturated porous medium. *Journal of Applied Sciences*, 134902(117).
<https://doi.org/10.1063/1.4916805>
- Yang, H., Rahardjo, H., Wibawa, B., and Leong, E. C. (2004). A Soil Column Apparatus for Laboratory Infiltration Study. *Geotechnical Testing Journal*, 27(4), 347–355.
- Yaya, C., Tikou, B., and Lizhen, C. (2017). International Journal of Mining Science and Technology Numerical analysis and geophysical monitoring for stability assessment of the Northwest tailings dam at Westwood Mine. *International Journal of Mining Science and Technology*, 27(4), 701–710. <https://doi.org/10.1016/j.ijmst.2017.05.012>
- Yuan, Y. and Lee, T.R. (2013). Contact angle and wetting properties. In: Bracco G, Holst B, eds. *Surface Science Techniques Springer Series, Surface Sciences*. Vol. 51. Berlin: Springer, 3–34. <https://doi.org/10.1007/978-3-642-34243-1>
- Zandarín, M. T., Oldecop, L. A., Rodríguez, R., and Zabala, F. (2009). The role of capillary water in the stability of tailing dams. *Engineering Geology*, 105(1–2), 108–118.
- Zandarín, M. T., Oldecop, L., and Pacheco, R. R. (2008). Stability of a tailings dam considering the hydro-mechanical behaviour of tailings and climate factors. *Unsaturated Soils: Advances in Geo-Engineering - Proceedings of the 1st European Conference on Unsaturated Soils, E-UNSAT 2008, August 2014*, 925–931.
<https://doi.org/10.1201/9780203884430.ch128>

- Zang, Y. G., Sun, D. M., Feng, P., and Semprich, S. (2017). Effects of Airflow Induced by Rainfall on Shallow Groundwater Table Fluctuations. *Groundwater*, 55(3), 375–386. <https://doi.org/10.1111/gwat.12486>
- Zang, G., Sun, D. M., Feng, P., and Semprich, S. (2018). Numerical Analysis of Groundwater Ridging Processes Considering Water-Air Flow in a Hillslope. *Groundwater*, 56(4), 5. <https://doi.org/10.1111/gwat.12602>
- Zhang, P., Chen, G., Wu, J., Wang, C., Zheng, S., Yu, Y., Li, Y., and Li, X. (2022). The Application and Improvement of Soil–Water Characteristic Curves through In Situ Monitoring Data in the Plains. *Water (Switzerland)*, 14(24). <https://doi.org/10.3390/w14244012>
- Zheng, X., Xu, X., & Xu, K. (2011). Study on the risk assessment of the tailings dam break. *Procedia Engineering*, 26, 2261–2269. <https://doi.org/10.1016/j.proeng.2011.11.2433>



APPENDIX A

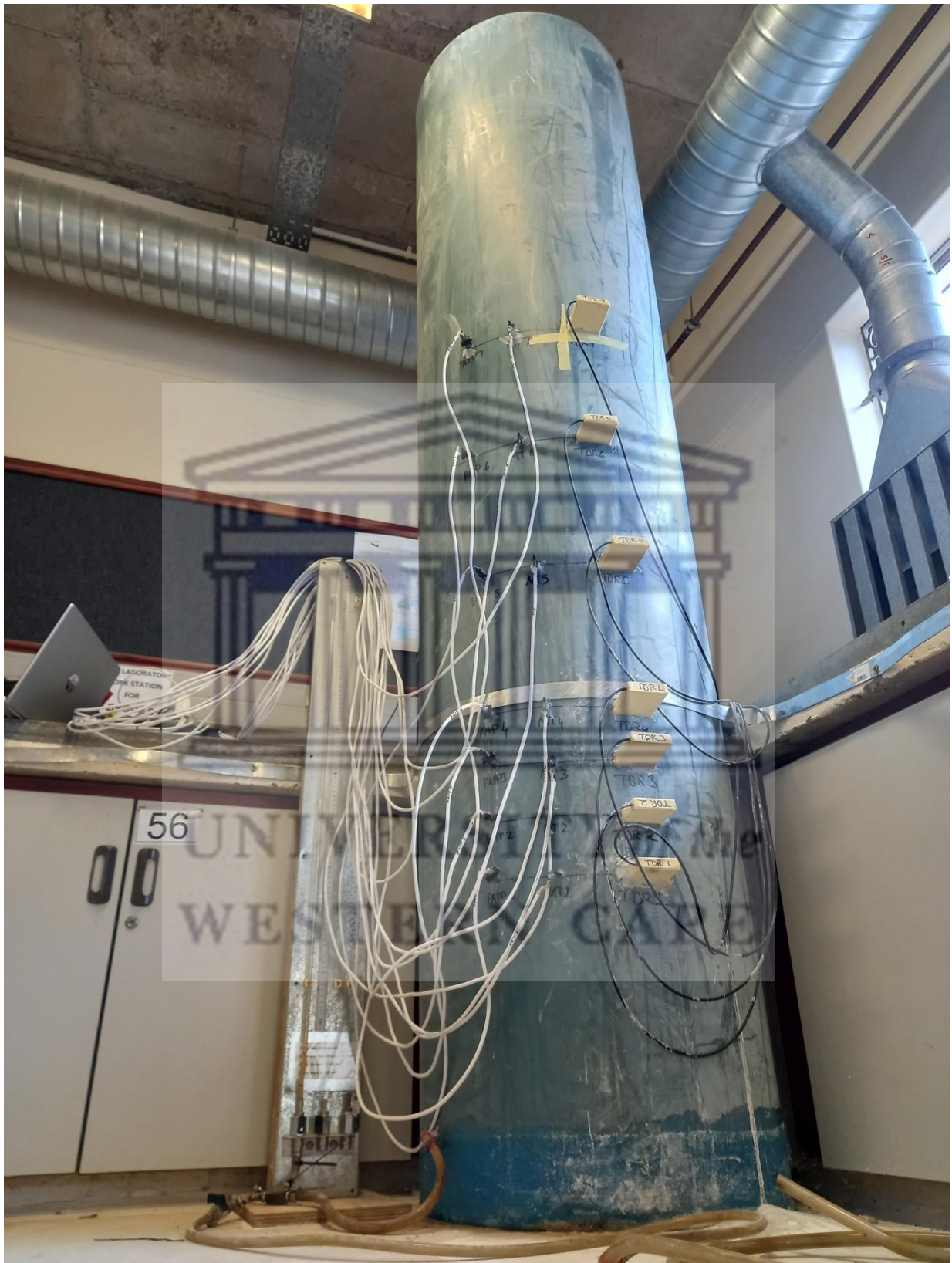


Figure A: complete tall soil column installation

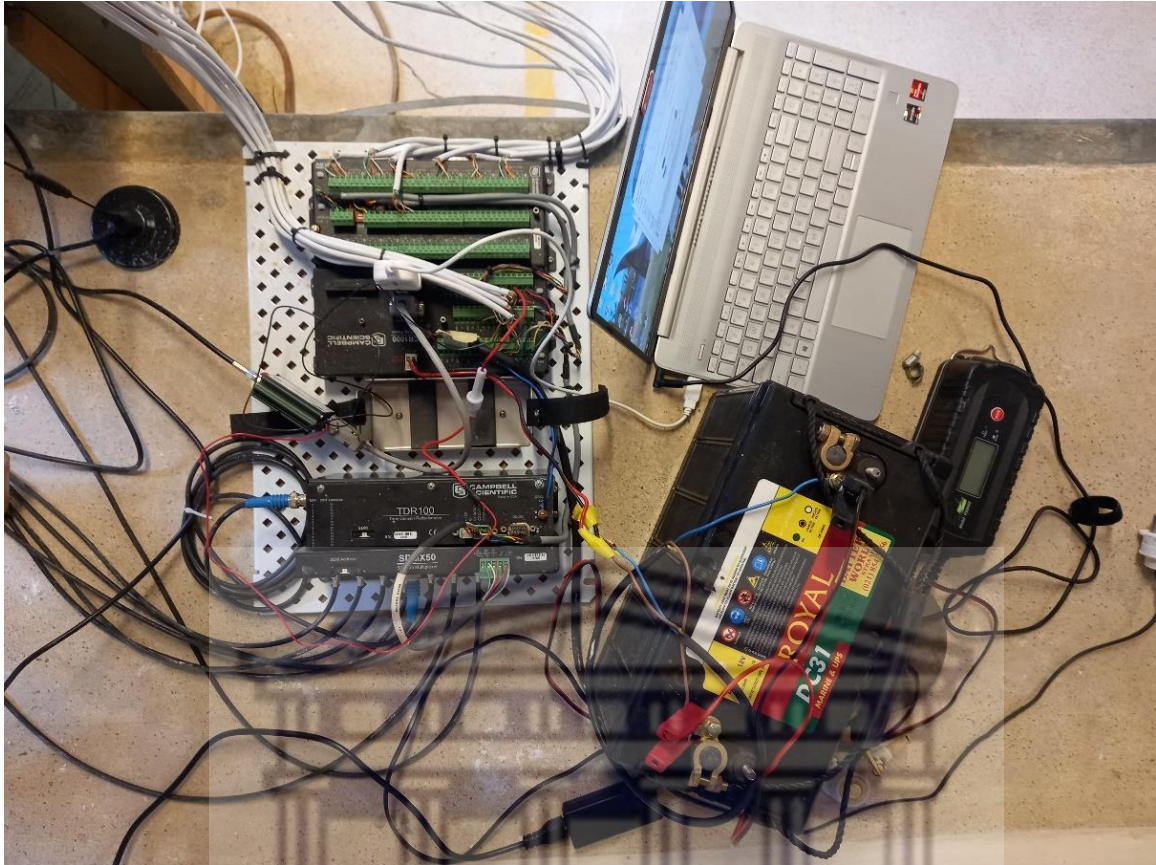


Figure B: Data acquisition equipment layout.



Figure C: Illustration of instruments fitted into tall soil column (from left to right: TDR, PAPP and MTs).



Figure D and E: Course grained aggregate on top of sample and preparation of the sample in predetermined ratios. The soil lab facilities at Cape Peninsula University of Technology was used.



Figure F: Water supply from supply bath, piezometer and inlet

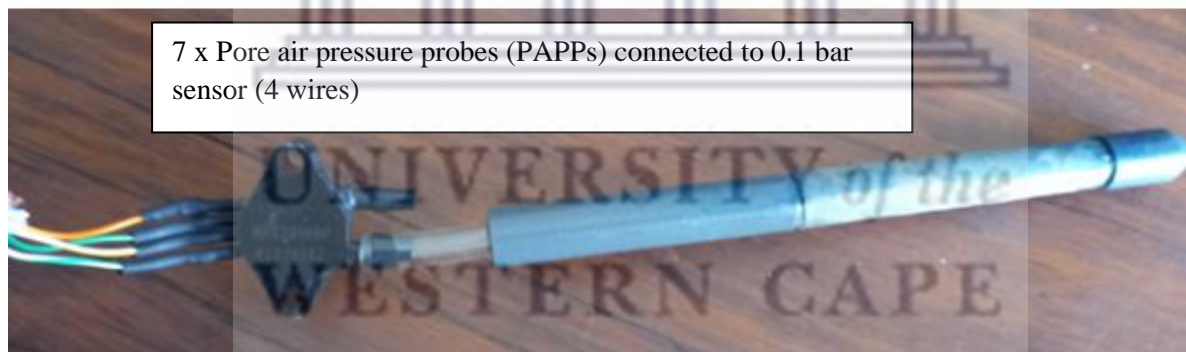
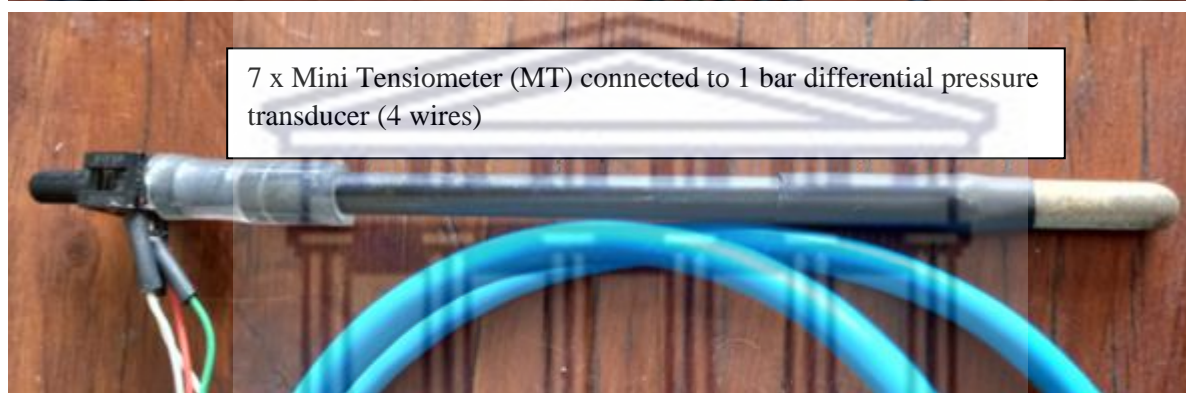


Figure G: Instrumentation at each port consisting of a TDR, MT and PAPP.

APPENDIX B

```
'-----
'-----
' Client:
' StationID: Pressure
' CSA Job: ####
'-----
' Description: Campbell Scientific CR1000 datalogger
'               AM16/32B multiplexer (2 x Mode)
| MUX1           | Common:1H1L   Reset: C1 Clock C2 | Power: 12V
'               Freescale MPX2010DP 0.1 Bar Differential Pressure 40mV
Full Scale 2.5mV/kPA | MPX2010DP_DPress_1 | AM1632B 1H1L
| Powered with 10V
'               Honeywell TSC001BD 1 Bar Differential Pressure 10.2mV/V
Full Scale         | TSC001BD_DPress_1 | AM1632B 1H1L
| Powered with 5V

' Power Supply: ##### AC Charge Controller
'               ##### Solar charge controller
'               ##### Watt Solar Panel
'               ##V/##Ah SLA Battery

' Comms:        ##### Modem with Callback
'-----
' Note all changes made during installation/maintenance and save as new
file with revision and date
' Version: 1 Revision: 0 Date: 20211001 Author: FlR CSAf Description:
Integration and lab test
' Version: # Revision: # Date: YYYYMMDD Author: ### ##### Description:
#####
' Version: # Revision: # Date: YYYYMMDD Author: ### ##### Description:
#####
' Version: # Revision: # Date: YYYYMMDD Author: ### ##### Description:
#####
'-----
'-----
'-Constants-----
-----
AngleDegrees

'-Declare StationID Variables and Units-----
-----
Public Station_ID_Block As String * 12 = "*****"
Public StationID As String * 22 = "_Pressure" : ReadOnly StationID

' Declare MPX2010DP_DPress_1 to 7 Variables, Units and Calibration-----
-----
Public MPX2010DP_DPress_1_Block As String = "*****"
Public MPX2010DP_DPress_1_Slope = 0.4
Public MPX2010DP_DPress_1_Offset = 0
Public MPX2010DP_DPress_1 : Units MPX2010DP_DPress_1 = kPa
Public MPX2010DP_DPress_2 : Units MPX2010DP_DPress_2 = kPa
Public MPX2010DP_DPress_3 : Units MPX2010DP_DPress_3 = kPa
```

```

Public MPX2010DP_DPress_4 : Units MPX2010DP_DPress_4 = kPa
Public MPX2010DP_DPress_5 : Units MPX2010DP_DPress_5 = kPa
Public MPX2010DP_DPress_6 : Units MPX2010DP_DPress_6 = kPa
Public MPX2010DP_DPress_7 : Units MPX2010DP_DPress_7 = kPa

' Declare TSC001BD_DPress_1 Variables, Units and Calibration-----
-----
Public TSC001BD_DPress_1_Block As String = "*****"
Public TSC001BD_DPress_1_Slope = 0.0196
Public TSC001BD_DPress_1_Offset = 0
Public TSC001BD_DPress_(7)
' Units TSC001BD_DPress_1 = bar

'
' Declare TSC001BD_DPress_1 Variables, Units and Calibration-----
-----

Public LAL(8)
Public LedieuVWC(8)
Public flag(1)
Dim il

Dim WavePT(260) 'To conserve datalogger memory, use Dim
                ' instead of Public for waveform data points.
Public MuxChan

'-Declare LoggerInternal Variables and Units-----
-----
Public LoggerInternal_Block As String * 12 = "*****"
Public ProgramName As String * 50
Public ProgramSignature As String * 6
Public LoggerSerialNumber As String * 6
Public LoggerBattery : Units LoggerBattery = V
Public LoggerTemp : Units LoggerTemp = degC
Public LoggerLithiumBatt : Units LoggerLithiumBatt = V
Public ScanTime1 : Units ScanTime1 = mSec
Public ScanTime2 : Units ScanTime2 = mSec
'Public ScanTime3 : Units ScanTime3 = mSec
Public ScanTime4 : Units ScanTime4 = mSec
Dim rTime(9)
Dim LCount

'-Declare Modem Variables and Units-----
-----
Public Modem_Block As String * 12 = "*****"
Dim ModemReset : Units ModemReset = Flag
Dim ModemLowPower : Units ModemLowPower = Flag
Dim PingRetry
Public PingTime As Long : Units PingTime = msec
Public IPFailCount As Long : Units IPFailCount = Count

'-Declare data tables-----
-----
DataTable(TablePressure, True, -1) 'Data table for pressure records
DataInterval(0,1,Min,10)

```



```

'-StationID
Sample(1, StationID,String)

' MPX2010DP_DPress_1
Sample(1,MPX2010DP_DPress_1,ieee4,false)
Average (1,MPX2010DP_DPress_1,IIEEE4,False)
Average (1,MPX2010DP_DPress_2,IIEEE4,False)
Average (1,MPX2010DP_DPress_3,IIEEE4,False)
Average (1,MPX2010DP_DPress_4,IIEEE4,False)
Average (1,MPX2010DP_DPress_5,IIEEE4,False)
Average (1,MPX2010DP_DPress_6,IIEEE4,False)
Average (1,MPX2010DP_DPress_7,IIEEE4,False)

' TSC001BD_DPress_1
Sample(1,TSC001BD_DPress_(1),ieee4,false)
Average (7,TSC001BD_DPress_( ),IIEEE4,False)

'-Logger internal
Sample(1,LoggerSerialNumber,String)
Sample(1,ProgramName,String)
Sample(1,ProgramSignature,String)

Average (1,LoggerBattery,FP2,False)
Average (1,LoggerTemp,FP2,False)
Average(1,LoggerLithiumBatt,fp2,false)

Average(1,PingTime,ieee4,PingTime=0)

Totalize(1,1,ieee4,false)
FieldNames("ScanCount")

EndTable

DataTable(TDR_min,True,-1)
DataInterval(0,1,Min,10)
Sample(8,LAL(),FP2)
Sample(8,LedieuVWC(),FP2)
Sample(1,LoggerTemp,FP2)
EndTable

DataTable (TDR_Wave,1,240) 'Data Table (i.e. Capture TDR Probe
Waveforms)
sample (1,MuxChan,IIEEE4)
sample (260,WavePT(),FP2)
EndTable

'-Main Program-----
-----
BeginProg

' Default Datalogger Battery Voltage at startup
Battery(LoggerBattery)

' Power modem on power up of logger
SW12(1)

```

```

' Wait for sensors to power up
Delay(1,2,Sec)

'-Main Scan-----
-----
Scan(30, Sec, 1, 0) ' Do not change

'-Starting time of processing
Timer (1,mSec,2)

'-Logger internal-----
-----
LoggerSerialNumber = Status.SerialNumber
ProgramName = Status.Progname
ProgramSignature = Status.ProgSignature
Battery(LoggerBattery)
LoggerLithiumBatt = Status.LithiumBattery
PanelTemp(LoggerTemp, _50Hz)
RealTime( rTime)

' MPX2010DP_DPress_1 to 7-----
-----

VoltDiff(MPX2010DP_DPress_1,1,mV250,2,True,0,50,MPX2010DP_DPress_
1_Slope,MPX2010DP_DPress_1_Offset)

VoltDiff(MPX2010DP_DPress_2,1,mV250,3,True,0,50,MPX2010DP_DPress_
1_Slope,MPX2010DP_DPress_1_Offset)

VoltDiff(MPX2010DP_DPress_3,1,mV250,4,True,0,50,MPX2010DP_DPress_
1_Slope,MPX2010DP_DPress_1_Offset)

VoltDiff(MPX2010DP_DPress_4,1,mV250,5,True,0,50,MPX2010DP_DPress_
1_Slope,MPX2010DP_DPress_1_Offset)

VoltDiff(MPX2010DP_DPress_5,1,mV250,6,True,0,50,MPX2010DP_DPress_
1_Slope,MPX2010DP_DPress_1_Offset)

VoltDiff(MPX2010DP_DPress_6,1,mV250,7,True,0,50,MPX2010DP_DPress_
1_Slope,MPX2010DP_DPress_1_Offset)

VoltDiff(MPX2010DP_DPress_7,1,mV250,8,True,0,50,MPX2010DP_DPress_
1_Slope,MPX2010DP_DPress_1_Offset)

'-AM1632B Measurements every 2 minutes
'   If TimeIntoInterval(0,120,sec) Then

'Turn AM16/32 Multiplexer On
PortSet (5,1 )
Delay(0,150,mSec)

LCount=1
SubScan(0,uSec,7)
'Switch to next AM16/32 Multiplexer channel

```

```

PulsePort (6,10000)
  Delay(1,150,msec)

' TSC001BD_DPress_1-----
-----

  VoltDiff(TSC001BD_DPress_(LCount),1,mV250,1,True,0,50,TSC001BD_DP
ress_1_Slope,TSC001BD_DPress_1_Offset)
    LCount=LCount+1
  NextSubScan

' Reset AM1632B
PortSet (5,0 )
Delay(1,150,msec)

'Measure La/L on SDMX50 for all channels and convert to VWC using
TDR100(LAL(1),0,0,1001,4,1.0,251,8.9,5.0,0.2,0.085,1,0)
TDR100(LAL(2),0,0,2001,4,1.0,251,8.9,5.0,0.2,0.085,1,0)
TDR100(LAL(3),0,0,3001,4,1.0,251,8.9,5.0,0.2,0.085,1,0)
TDR100(LAL(4),0,0,4001,4,1.0,251,8.9,5.0,0.2,0.085,1,0)
TDR100(LAL(5),0,0,5001,4,1.0,251,8.9,5.0,0.2,0.085,1,0)
TDR100(LAL(6),0,0,6001,4,1.0,251,8.9,5.0,0.2,0.085,1,0)
TDR100(LAL(7),0,0,7001,4,1.0,251,8.9,5.0,0.2,0.085,1,0)
TDR100(LAL(8),0,0,8001,4,1.0,251,8.9,5.0,0.2,0.085,1,0)

'Perform linear Ledieu conversion to VWC
For il=1 To 8
LedieuVWC(il)=LAL(il)*0.1138-0.1758
Next il

'PortsConfig(andB00000111,andB00000000)
' PortsConfig (andB0111,andB0000)

'-Call tables-----
-----
  CallTable TablePressure
  CallTable(TDR_min)

'          EndIf

' Restart logger on Mondays at 00:00:10 (10 seconds after
midnight) (This can be enabled in remote installations where a logger
restart is the only way to restore comms)
  'If rTime(8) = 2 AND TimeIntoInterval(10,86400,sec) Then
FileManage(Status.ProgName,6)

'-Calculate comms time - all comms must take place in less
than the scan rate
  ScanTime1 = Timer(1,mSec,4)

NextScan

```

```

'-Scan2: ###-----
-----
SlowSequence
Scan(30, Sec, 3, 0)

    '-Starting time of processing
    Timer (2,mSec,2)

    '###-----
-----
    '..
    ,
MuxChan=1001 'store the SDM8X50 channel in variable "MuxChan"
TDR100 (WavePT(),0,1,1001,4,1.0,251,8.9,5.0,0.2,0.085,1,0)
CallTable TDR_Wave()
,
MuxChan=2001 'store the SDM8X50 channel in variable "MuxChan"
TDR100 (WavePT(),0,1,2001,4,1.0,251,8.9,5.0,0.2,0.085,1,0)
CallTable TDR_Wave()
,
MuxChan=3001
TDR100 (WavePT(),0,1,3001,4,1.0,251,8.9,5.0,0.2,0.085,1,0)
CallTable TDR_Wave()
,
MuxChan=4001
TDR100 (WavePT(),0,1,4001,4,1.0,251,8.9,5.0,0.2,0.085,1,0)
CallTable TDR_Wave()
,
MuxChan=5001
TDR100 (WavePT(),0,1,5001,4,1.0,251,8.9,5.0,0.2,0.085,1,0)
CallTable TDR_Wave()
,
MuxChan=6001
TDR100 (WavePT(),0,1,6001,4,1.0,251,8.9,5.0,0.2,0.085,1,0)
CallTable TDR_Wave()
,
MuxChan=7001
TDR100 (WavePT(),0,1,7001,4,1.0,251,8.9,5.0,0.2,0.085,1,0)
CallTable TDR_Wave()
,
MuxChan=8001
TDR100 (WavePT(),0,1,8001,4,1.0,251,8.9,5.0,0.2,0.085,1,0)
CallTable TDR_Wave()

    '-Calculate comms time - all comms must take place in less
than the scan rate
    ScanTime2 = Timer(2,mSec,4)

NextScan
EndSequence

'-Scan3: ###-----
-----
SlowSequence
Scan(60, Sec, 3, 0)
,
    '-Starting time of processing

```



```

'          Timer (3,mSec,2)
'
'          '###-----
-----
'          '..
'
'          '-Calculate comms time - all comms must take place in less
than the scan rate
'          ScanTime3 = Timer(3,mSec,4)
'
'          NextScan
'          EndSequence

' Scan4: Modem power-----
-----
SlowSequence

Scan(1,min,0,0)

'-Starting time of processing
Timer (4,mSec,2)

'-First check if modem is enabled
If status.pppinterface <> 0 Then

    '-Measure battery voltage
    Battery(LoggerBattery)

    '-Power down between 23:57 and 23:59
    If TimeIsBetween(1437,1439,1440,min) Then
        If (ModemReset = false) AND (ModemLowPower =
false) Then
            ModemReset= true
            PPPClose
            Delay(1,5,sec)
            SW12(0)
        EndIf
    Else
        If (ModemReset = true) AND (ModemLowPower =
false) Then
            ModemReset = false
            SW12(1)
            Delay(1,20,sec)
            PPPOpen
        EndIf
    EndIf

    '-Power down below 12V
    If (LoggerBattery < 12) AND (ModemLowPower = false)
AND (ModemReset = false) Then
        ModemLowPower = true
        PPPClose
        Delay(1,5,sec)
        SW12(0)
    EndIf

    '-Power up above 12.2V

```

```

        If (LoggerBattery > 12.2) AND (ModemLowPower = true)
AND (ModemReset = false) Then
            ModemLowPower = false
            SW12(1)
            Delay(1,20,sec)
            PPPOpen
        EndIf

        '-IP Keep alive(30 minute)
        PingTime = 0
        If (ModemReset = false) AND (ModemLowPower = false)
Then
            SetSetting("DNS(2)","8.8.8.8")           'Add google
as secondary DNS
            IPRoute("8.8.8.8",1)                     'Ping test
through modem
            IPRoute("callback.csafrica.co.za",1) 'Callback
through modem
            For PingRetry = 1 To 3
                PingTime = PingIP("8.8.8.8",3000)
                If PingTime > 0 Then ExitFor
            Next PingRetry
            If PingTime = 0 Then IPFailCount += 1 Else
IPFailCount = 0
            If (IPFailCount <> 0) AND (IPFailCount MOD 30 =
0) Then
                PPPClose
                Delay(1,5,sec)
                SW12(0)
                Delay(1,10,Sec)
                SW12(1)
                Delay(1,15,sec)
                PPPOpen
            EndIf
        EndIf
    EndIf
EndIf

        '-Calculate comms time - all comms must take place in less
than the scan rate
        ScanTime4 = Timer(4,mSec,4)

        NextScan
        EndSequence

EndProg

```

APPENDIX C

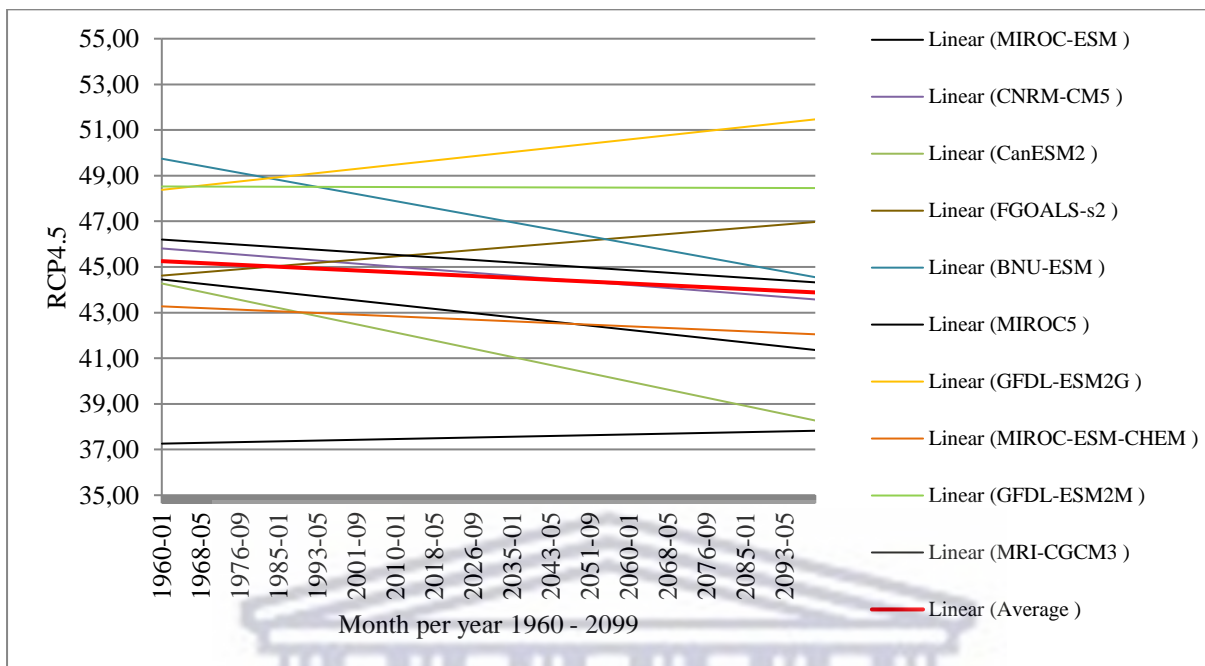


Figure C.1: Total monthly rainfall 1960 – 2099 based on projected future changes across 10 different statistically downscaled CMIP5 GCMs for RCP4.5.

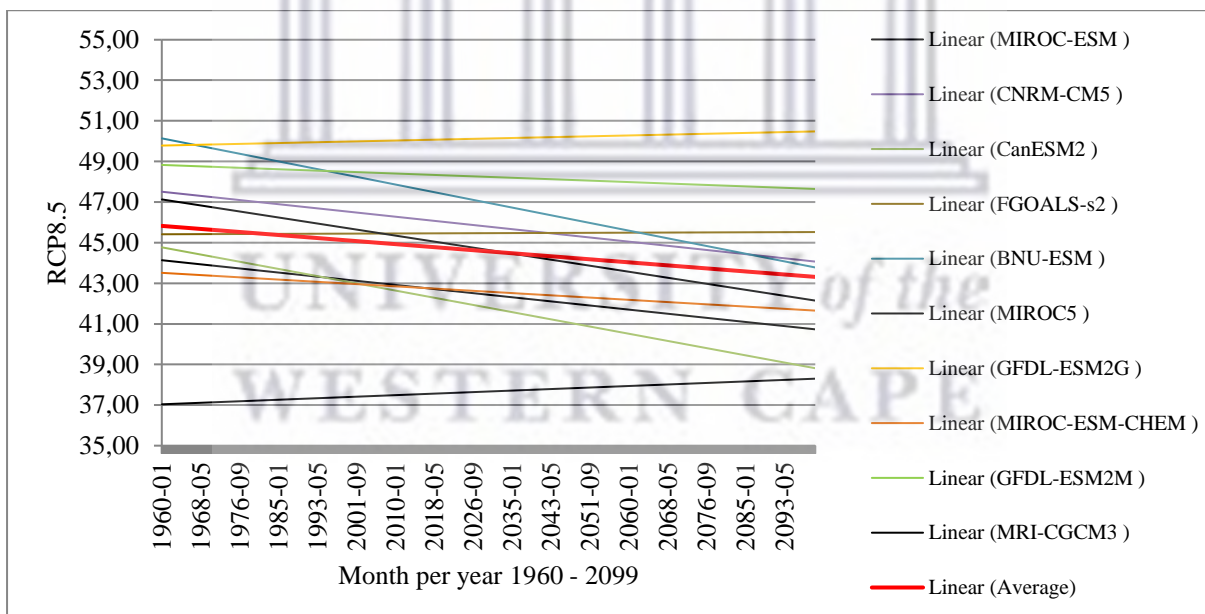
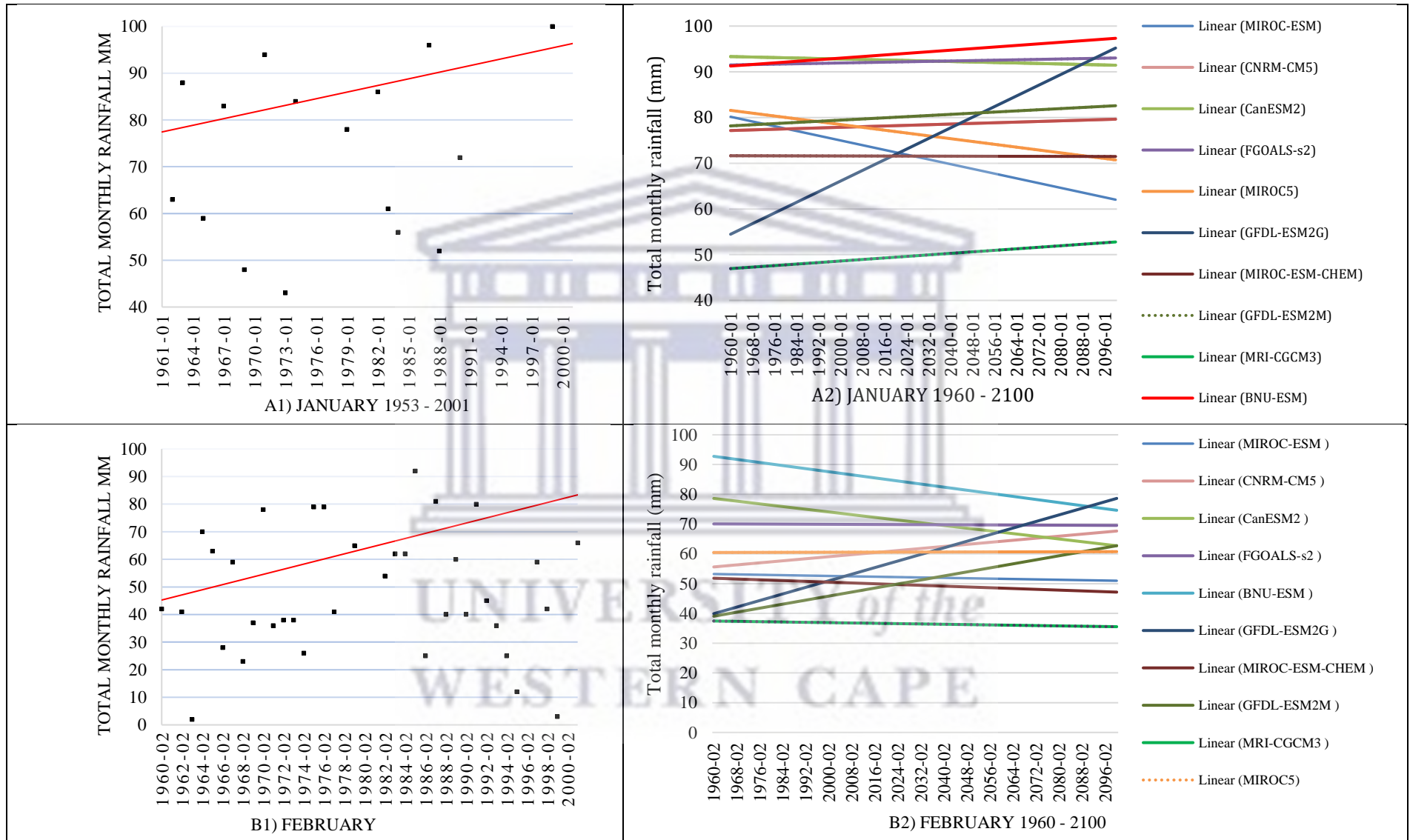
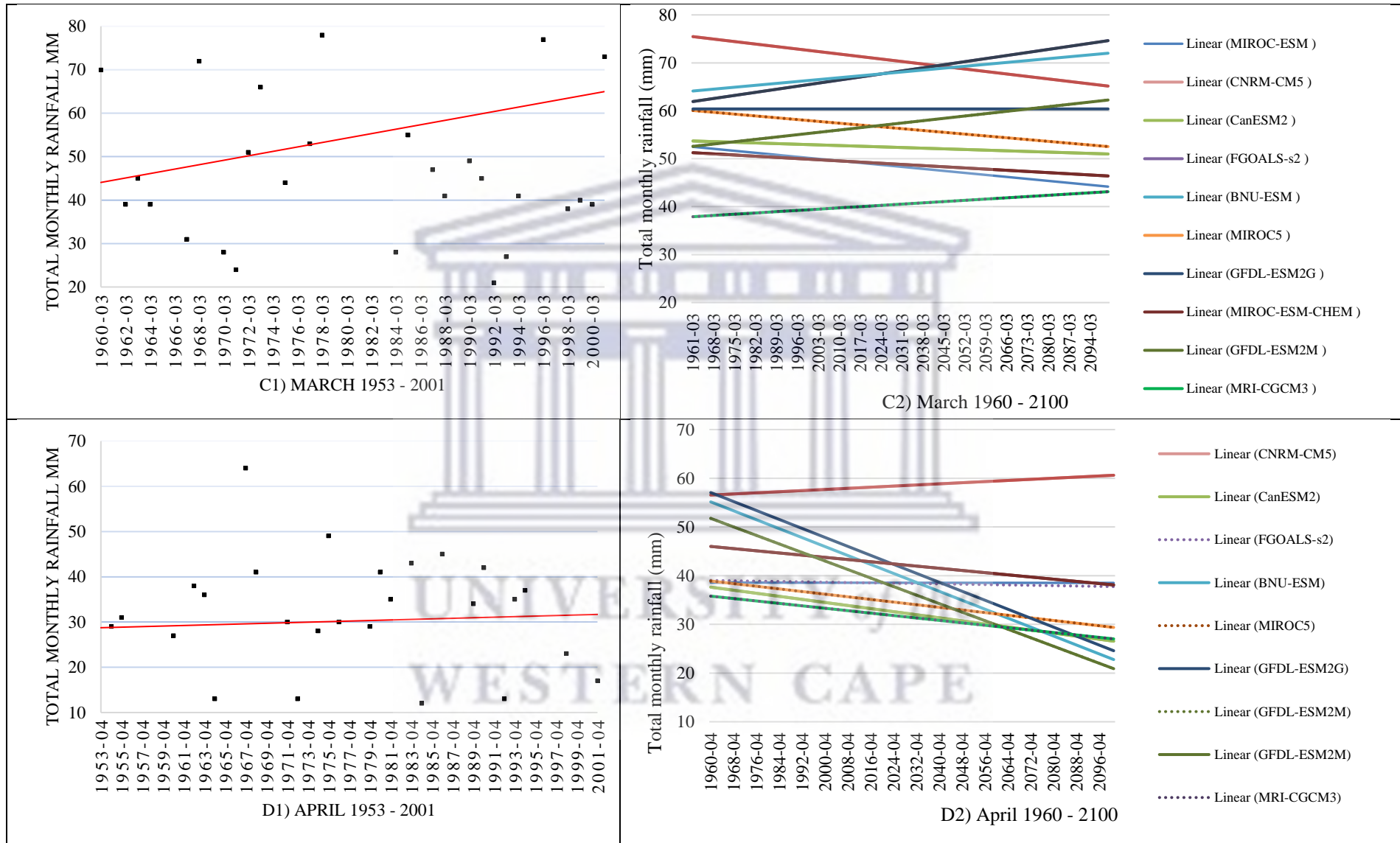
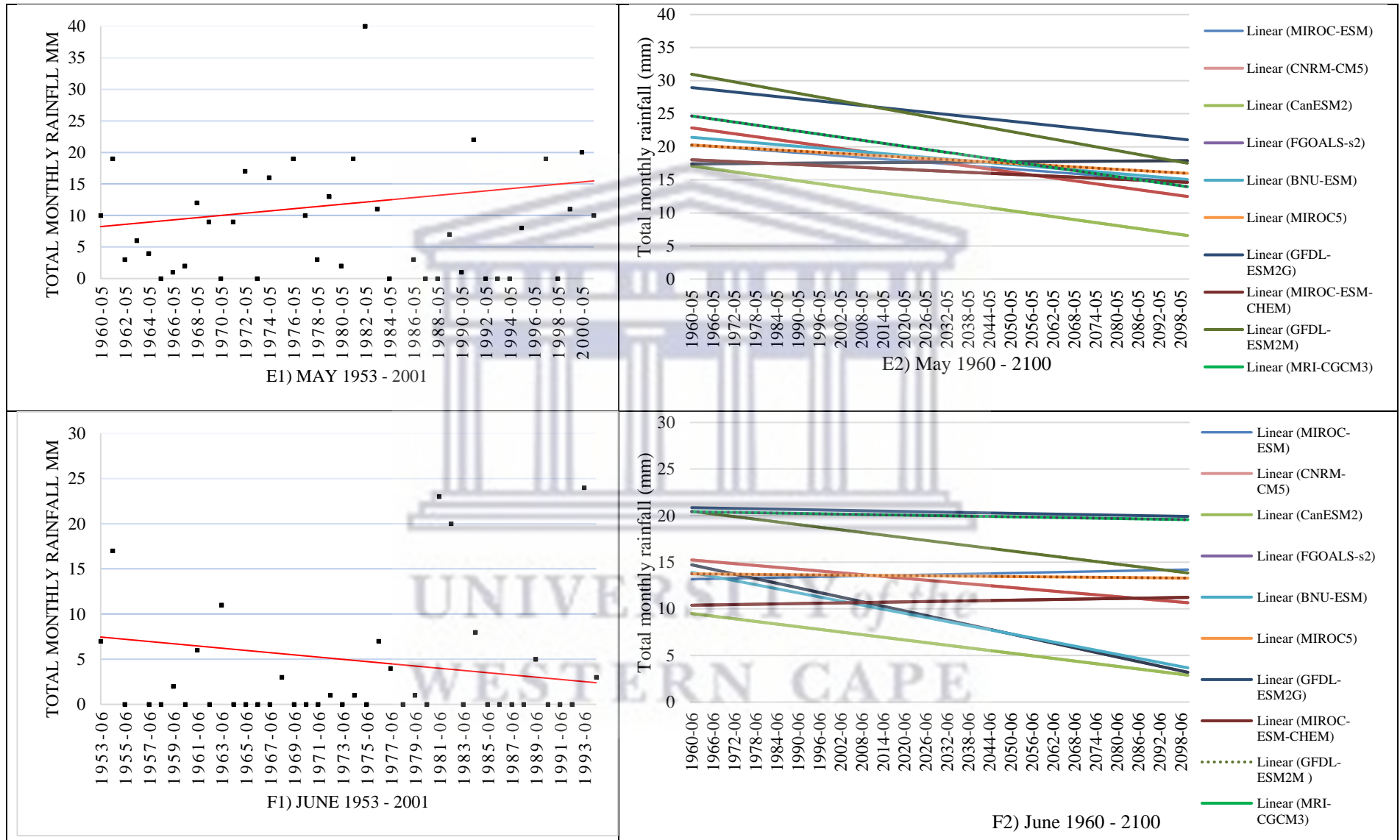
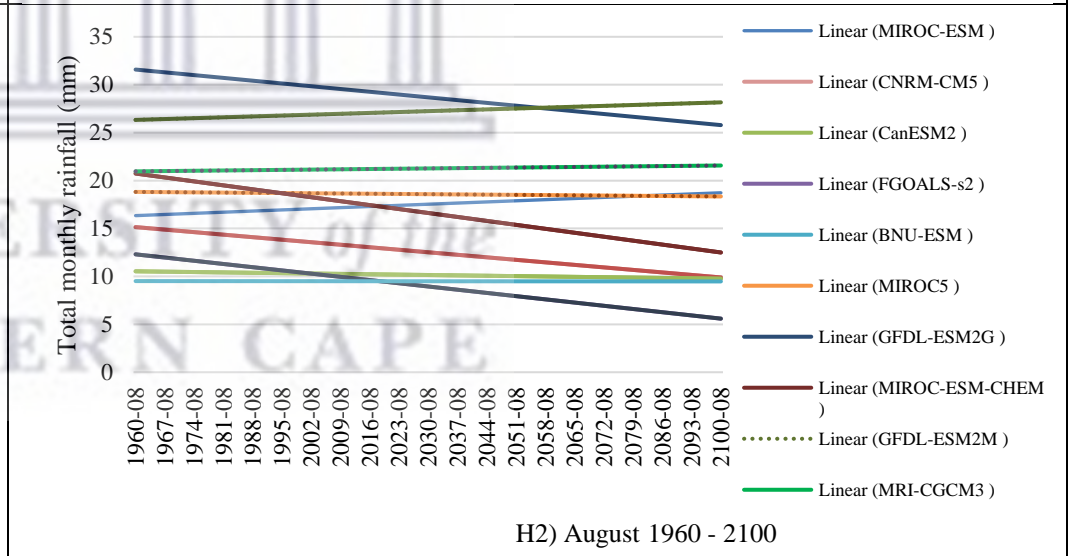
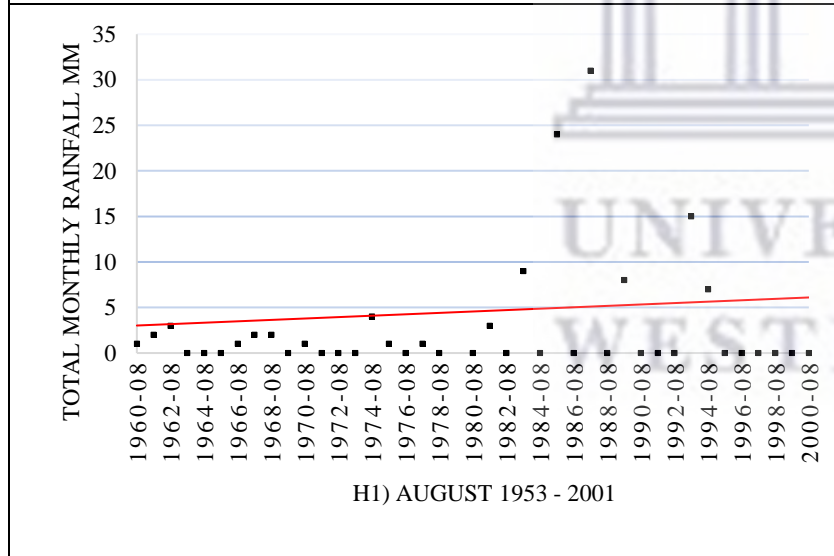
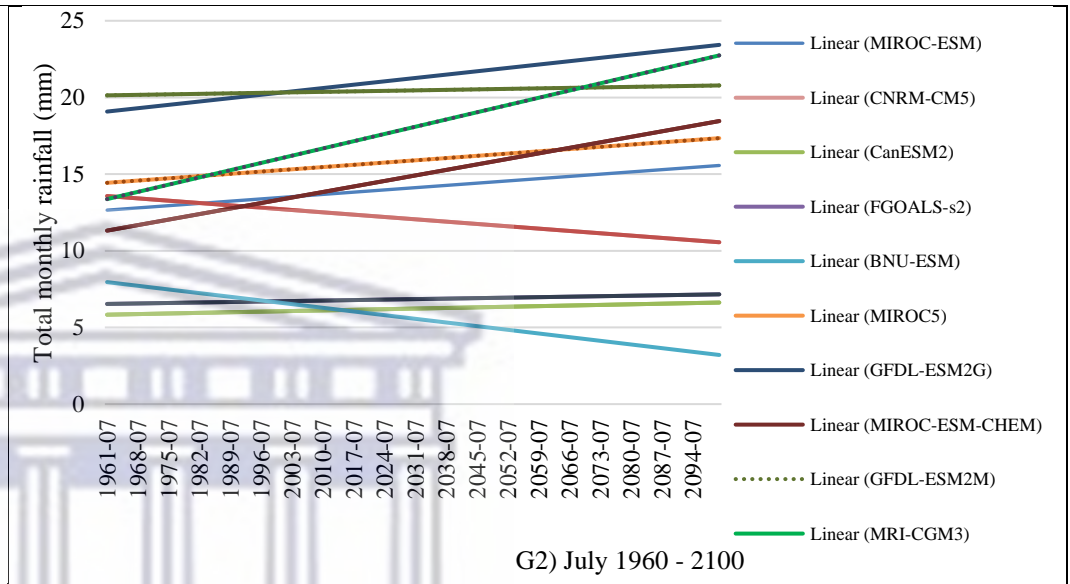
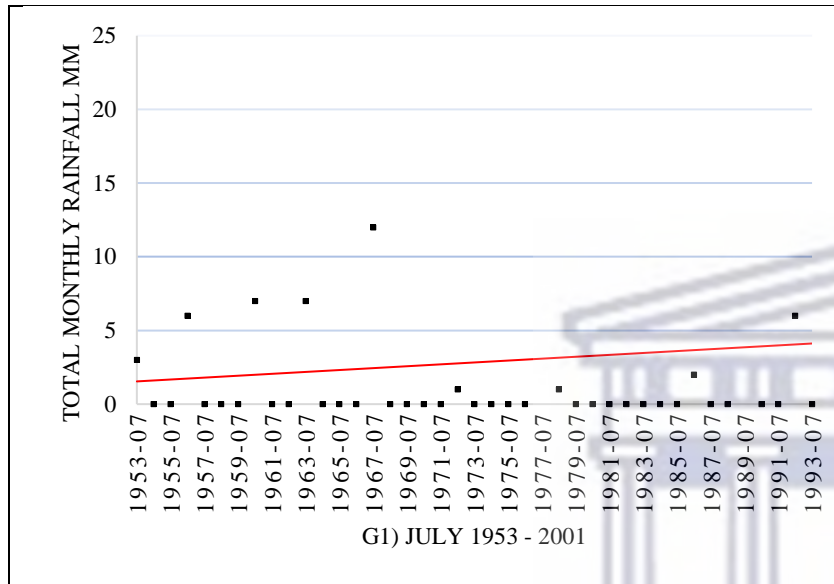


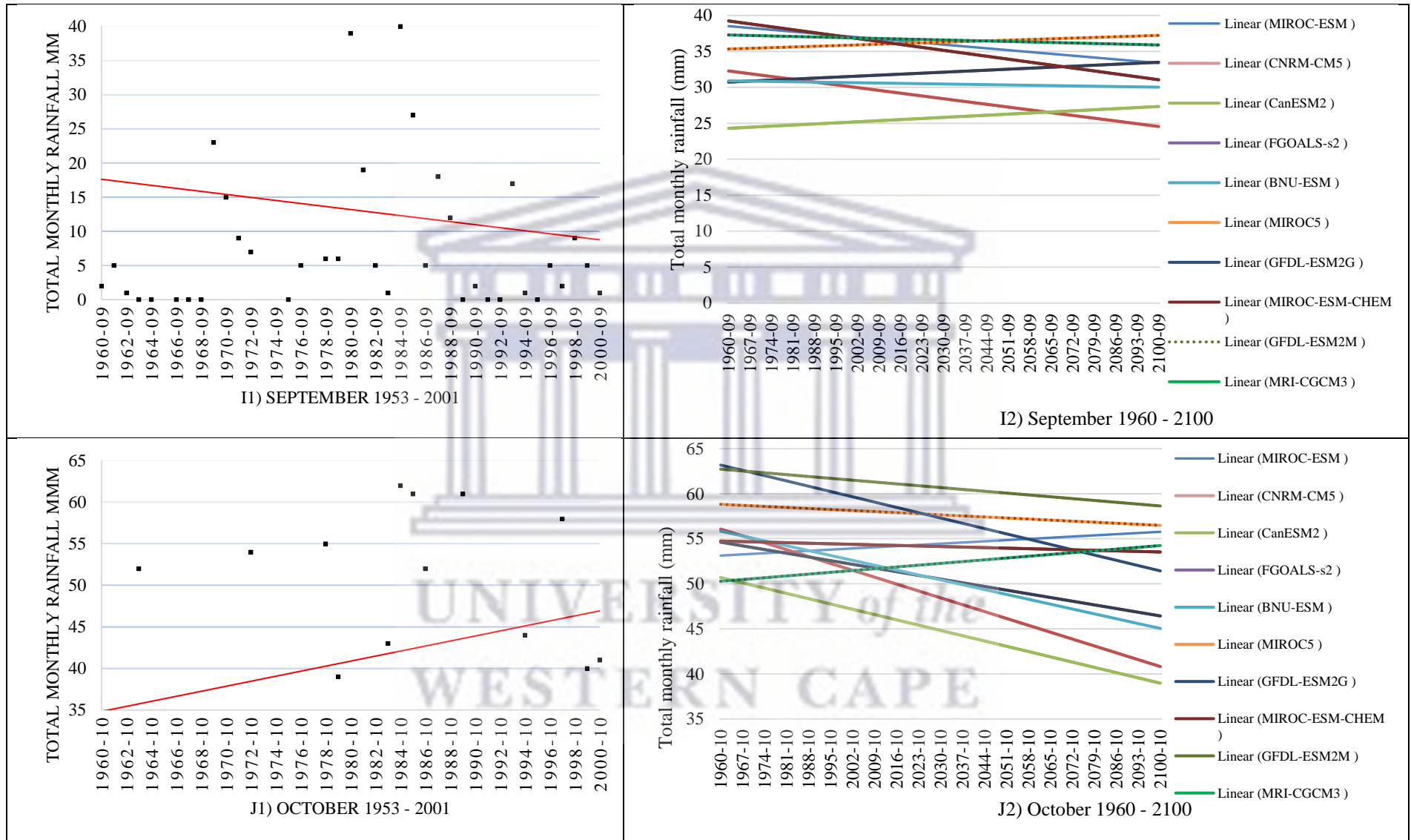
Figure C.2: Total monthly rainfall 1960 – 2099 based on projected future changes across 10 different statistically downscaled CMIP5 GCMs for RCP8.5.











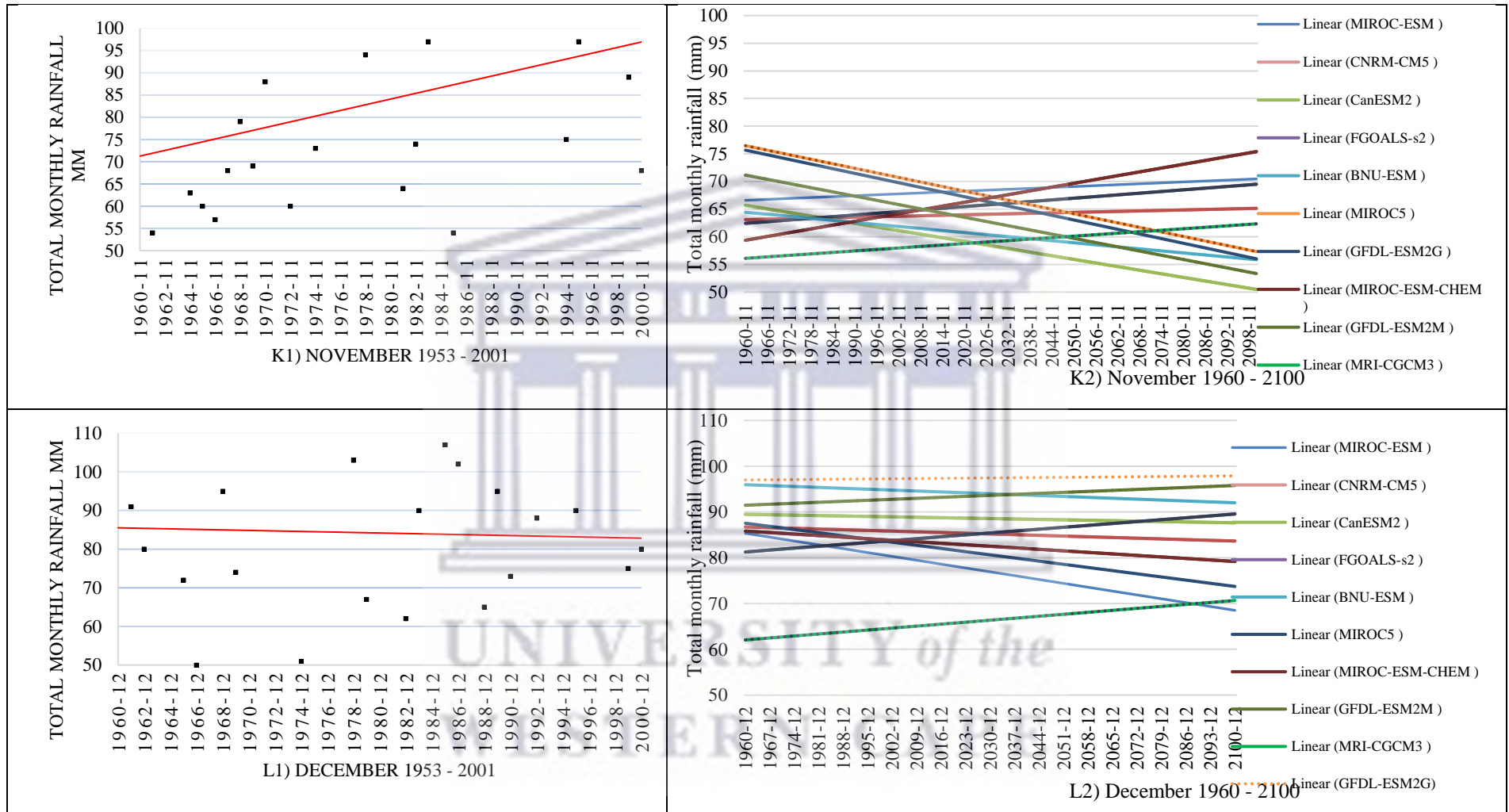


Figure C.3: Observed monthly rainfall totals (A1-L1) 1953 – 2001 compared to predicted total monthly rainfall (a2-l2) based on projected future changes across 10 different statistically downscaled CMIP5 GCMs (RCP8.5).

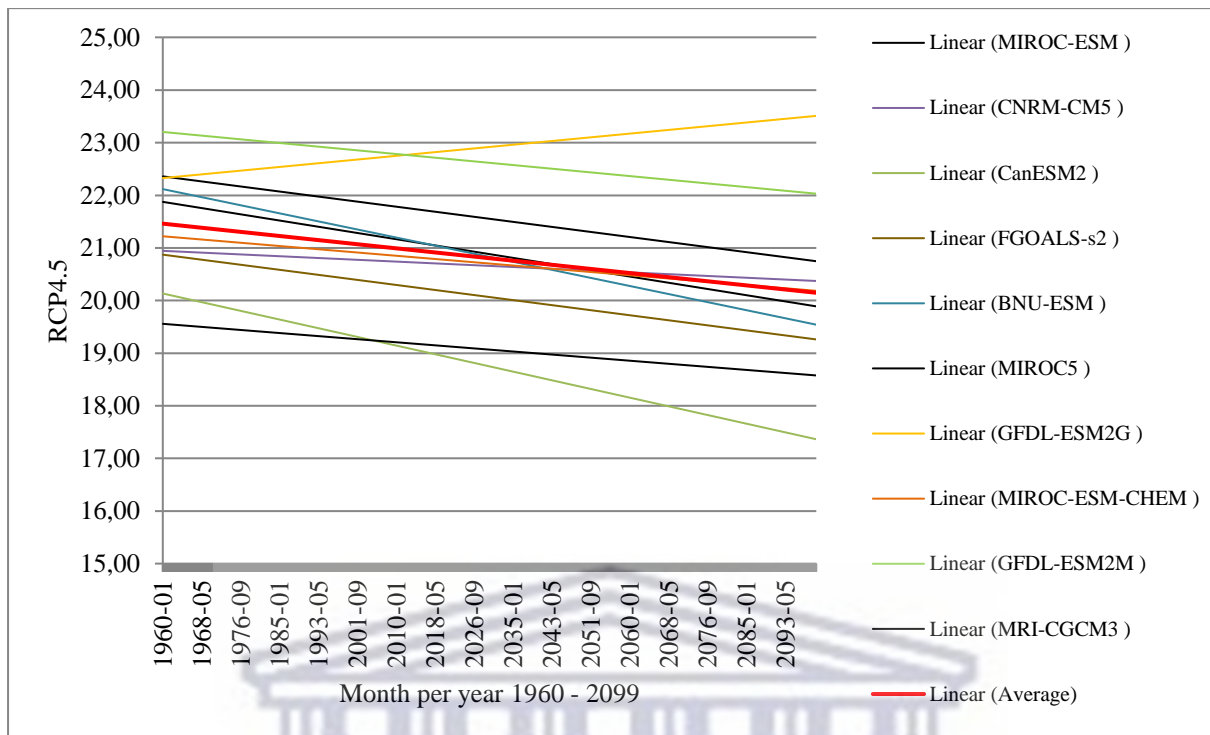


Figure C.4: Maximum daily rainfall per month 1960 – 2099 based on projected future changes across 10 different statistically downscaled CMIP5 GCMs (RCP4.5).

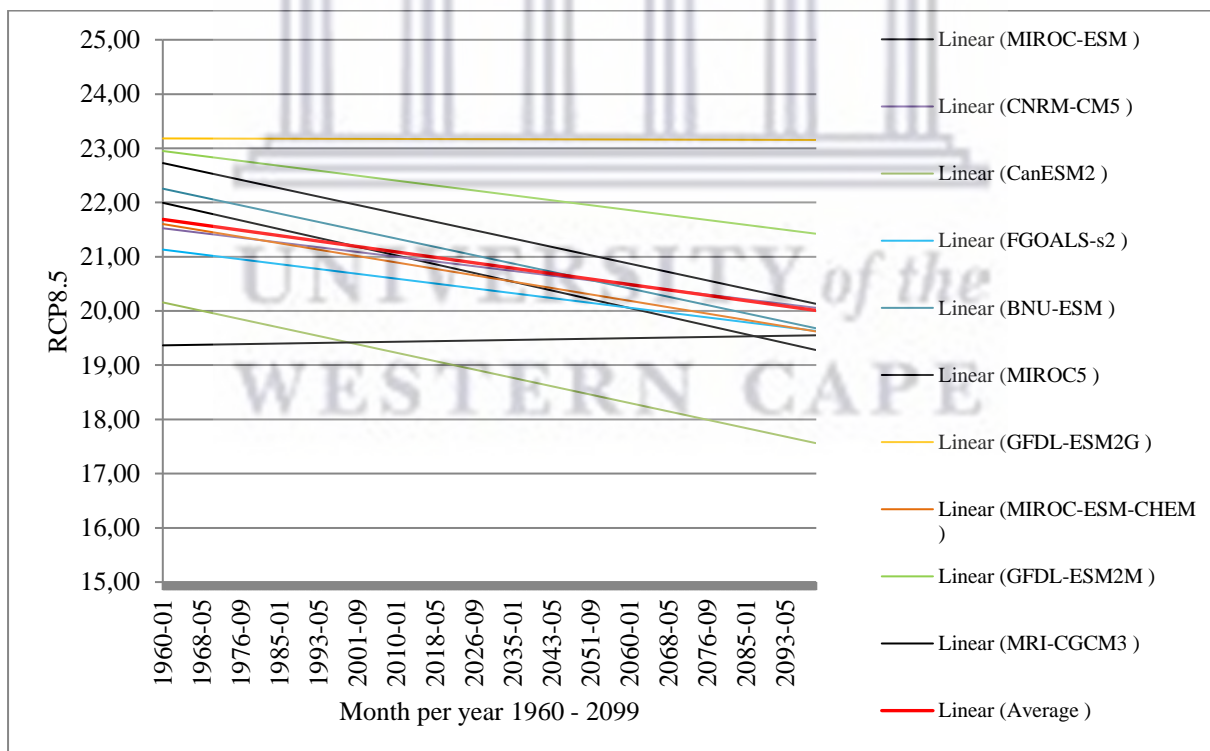


Figure C.5: Maximum daily rainfall per month 1960 – 2099 based on projected future changes across 10 different statistically downscaled CMIP5 GCMs (RCP8.5).

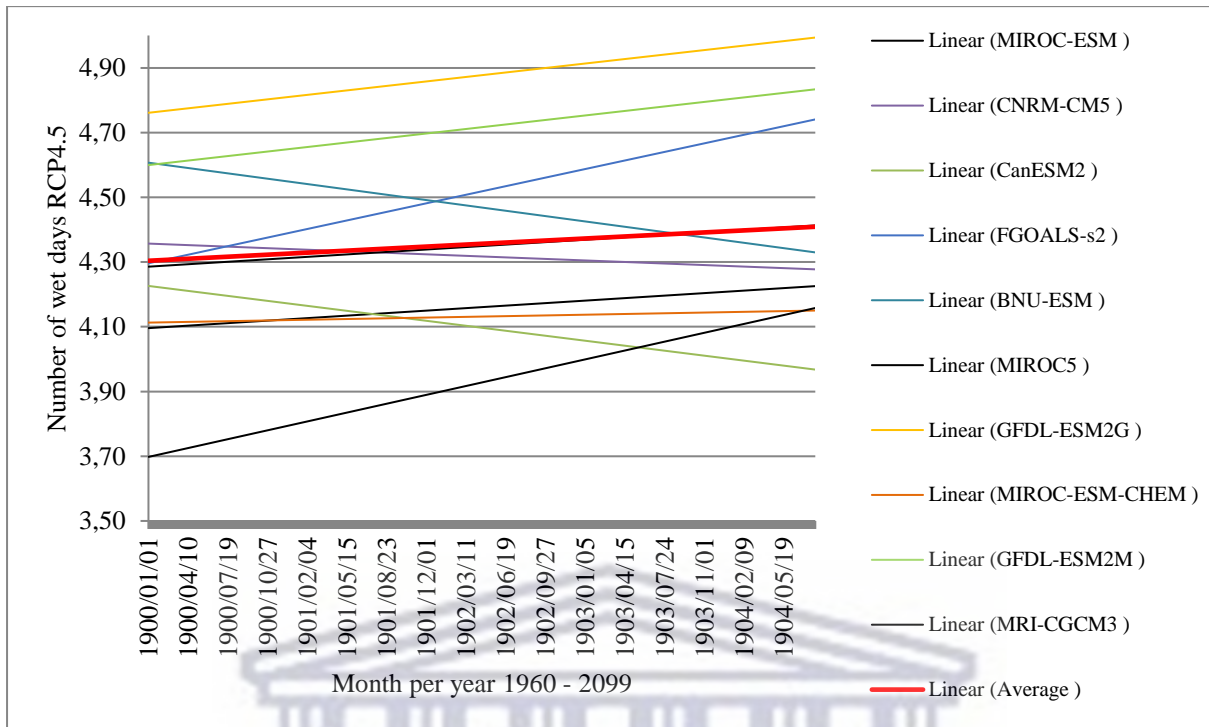


Figure C.6: Number of wet days per month 1960 – 2099 based on projected future changes across 10 different statistically downscaled CMIP5 GCMs (RCP4.5).

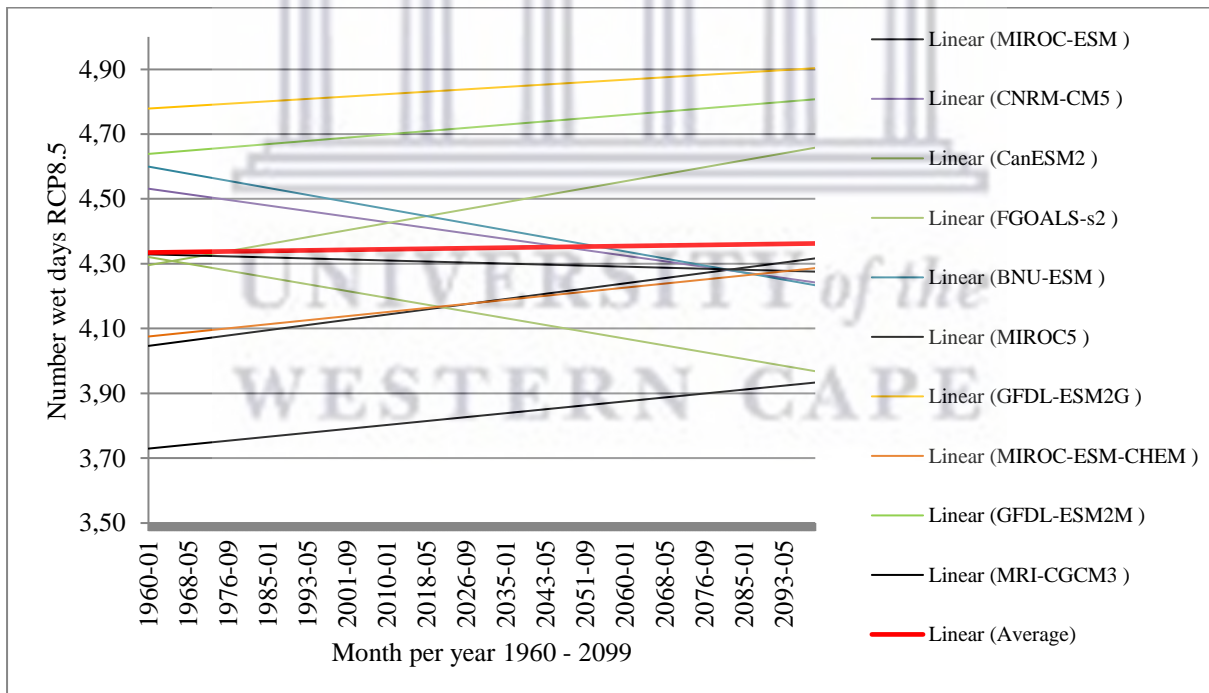


Figure C.7: Number of wet days per month 1960 – 2099 based on projected future changes across 10 different statistically downscaled CMIP5 GCMs (RCP8.5).

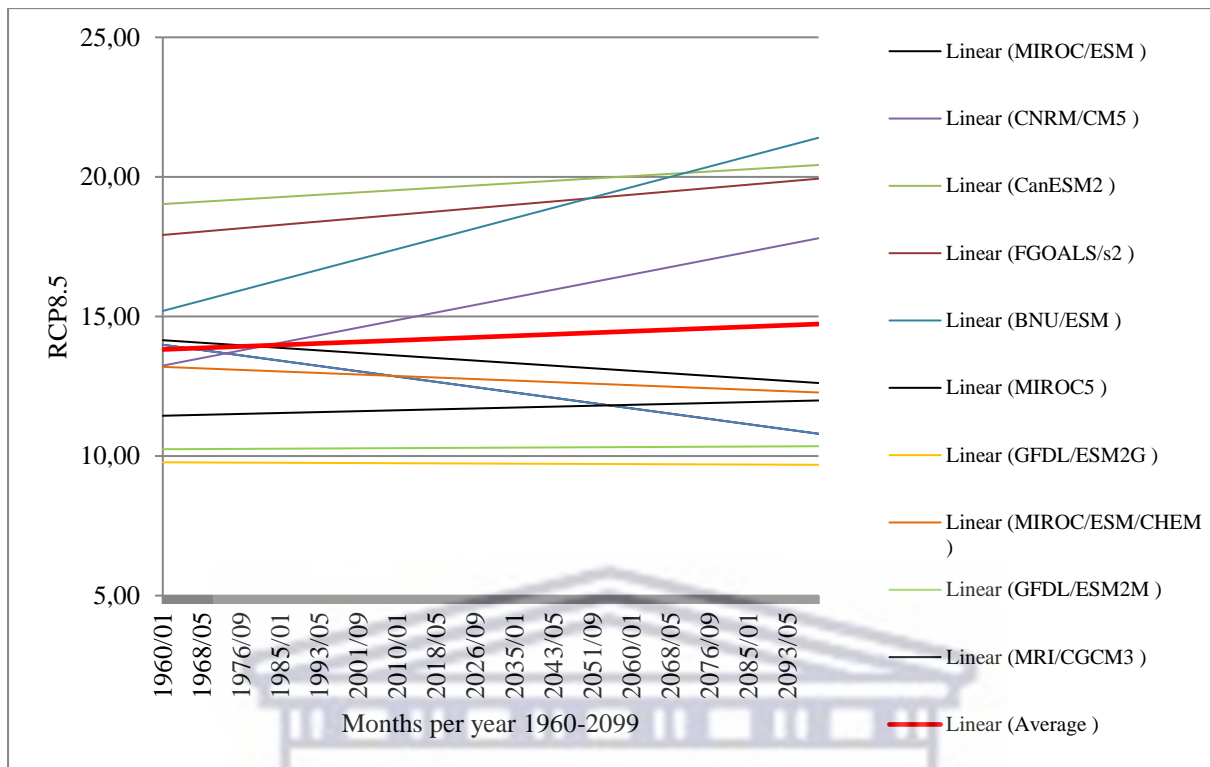
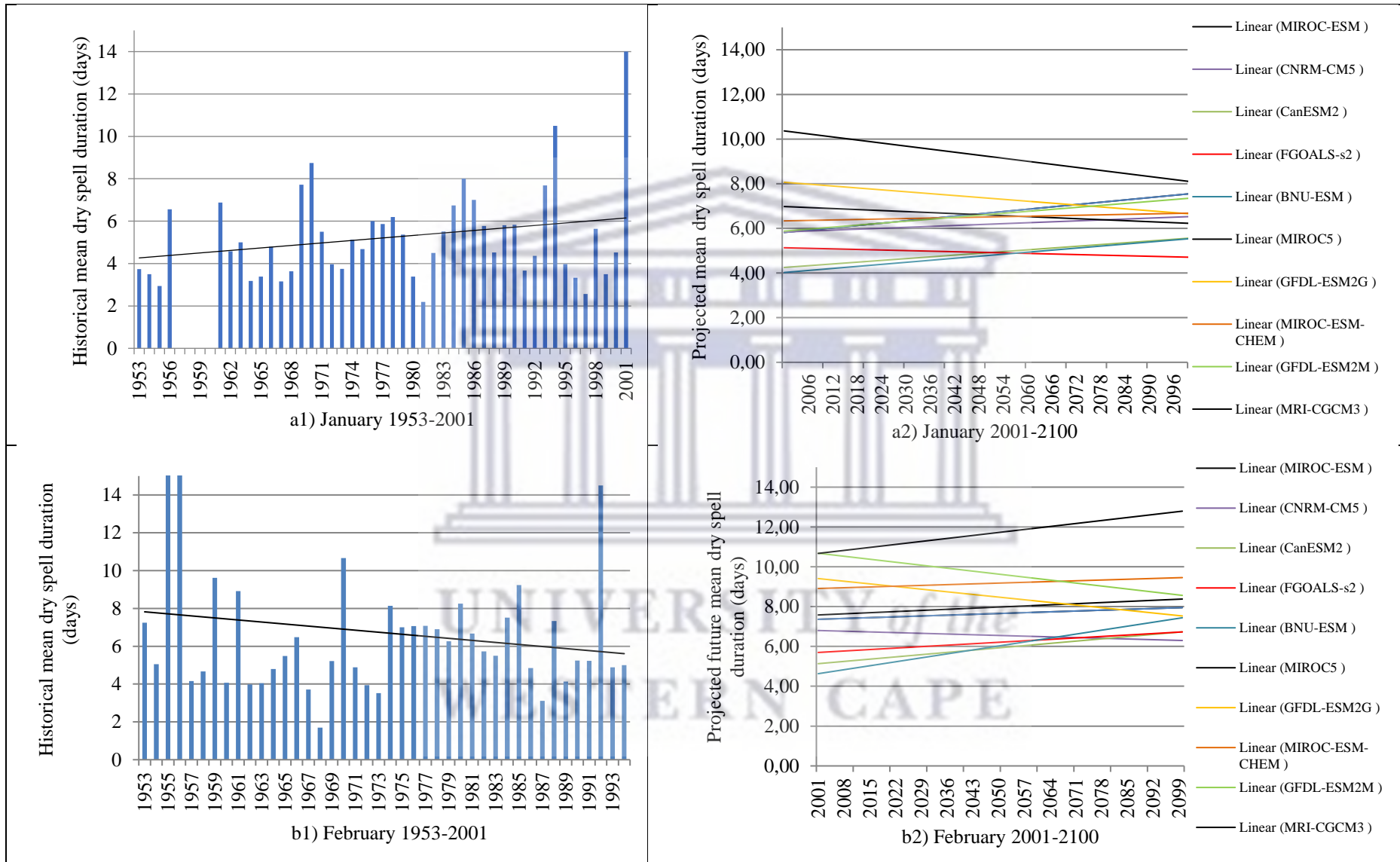
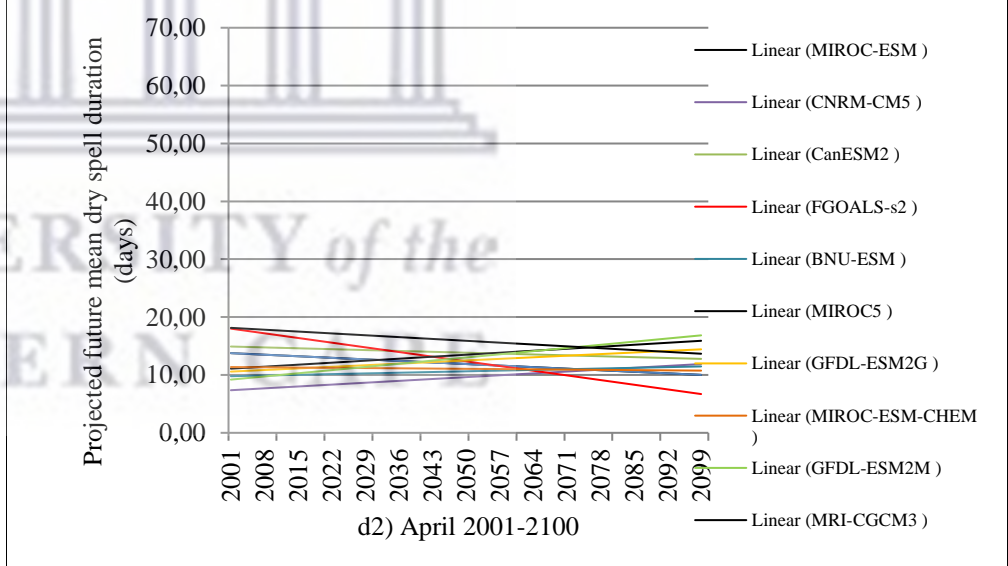
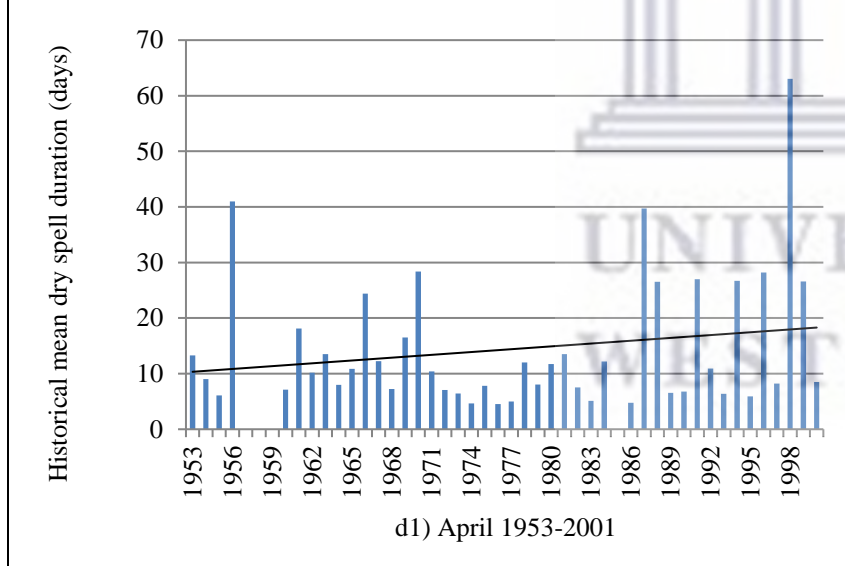
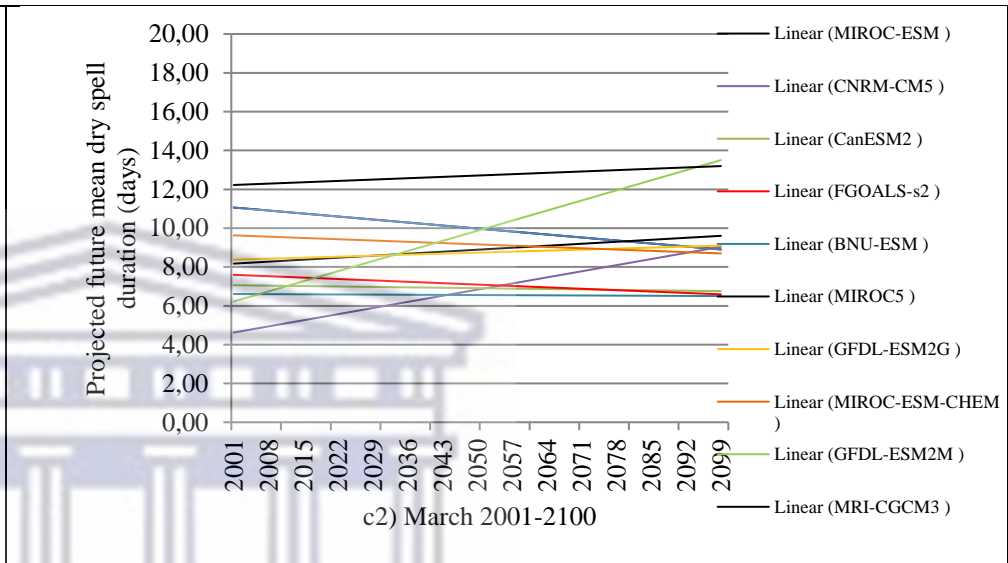
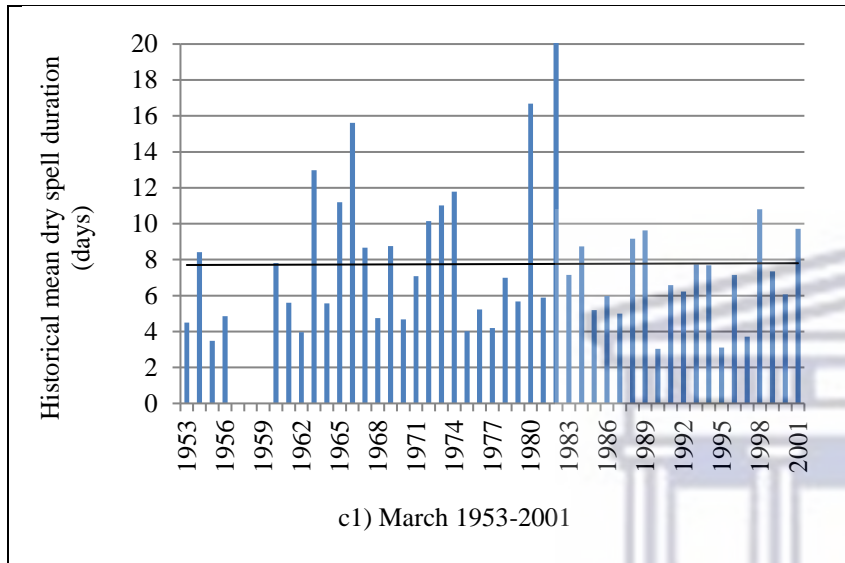
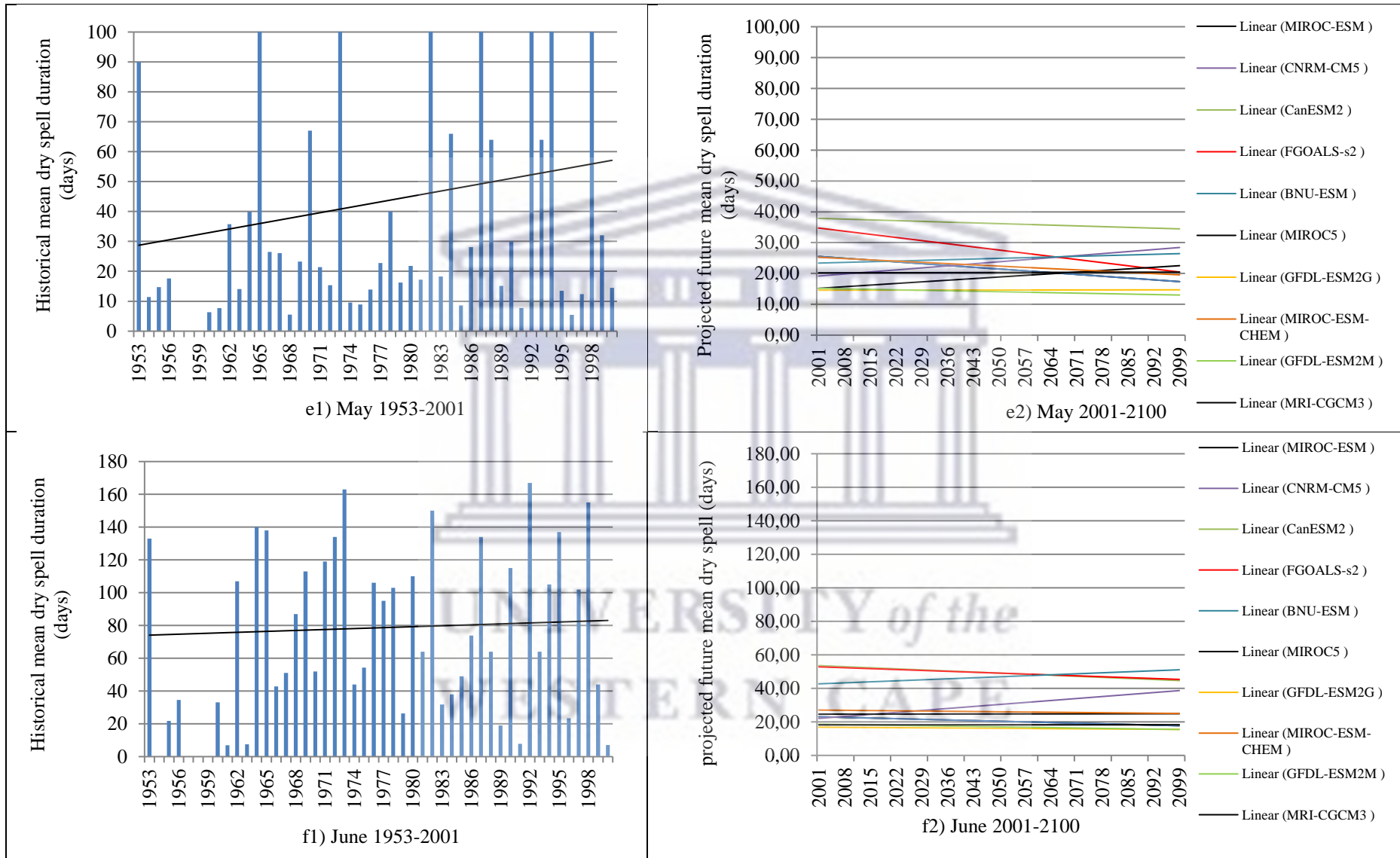
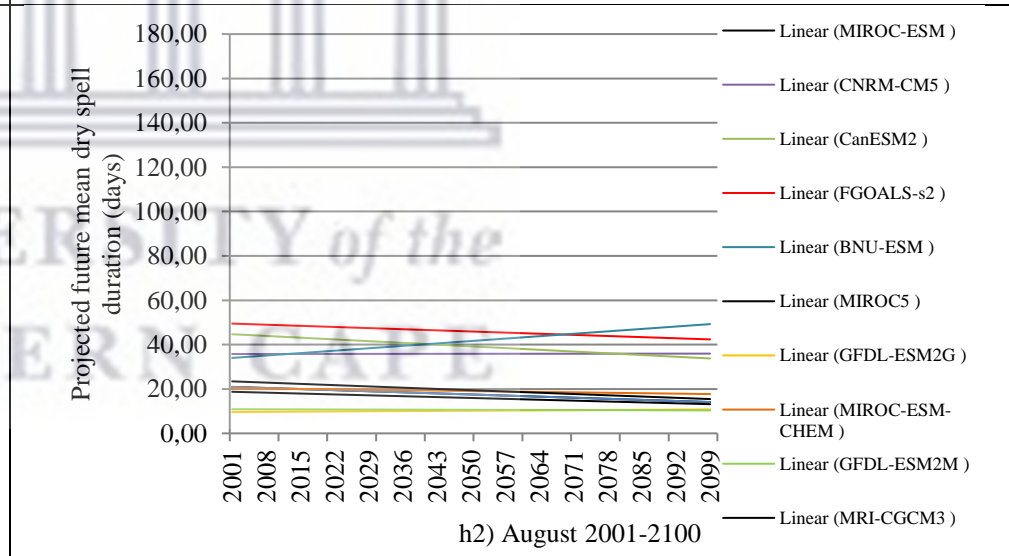
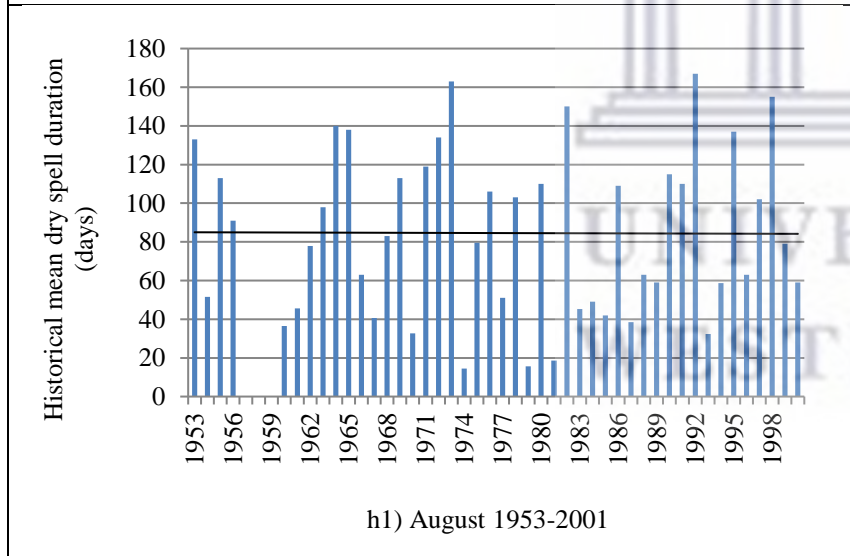
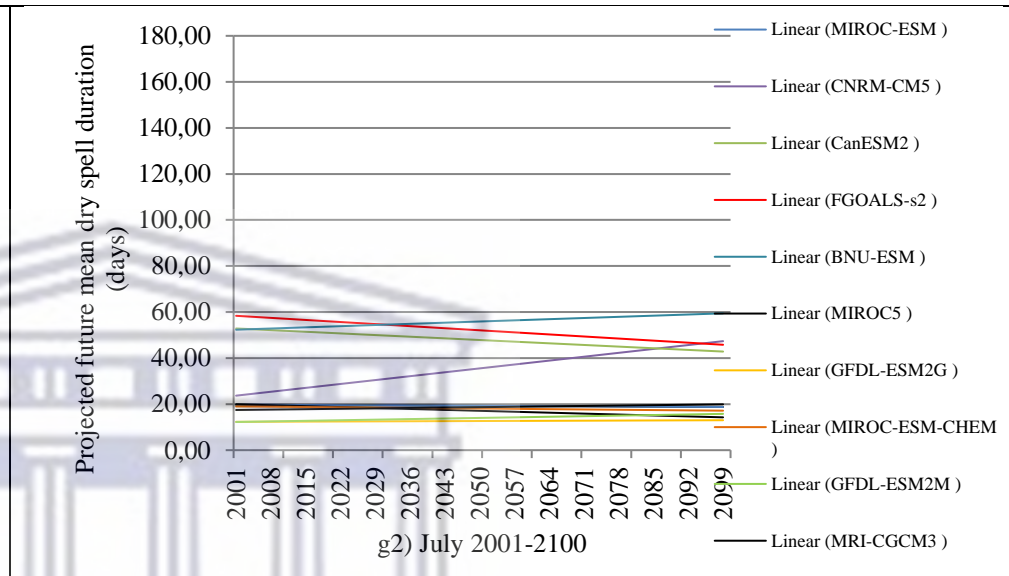
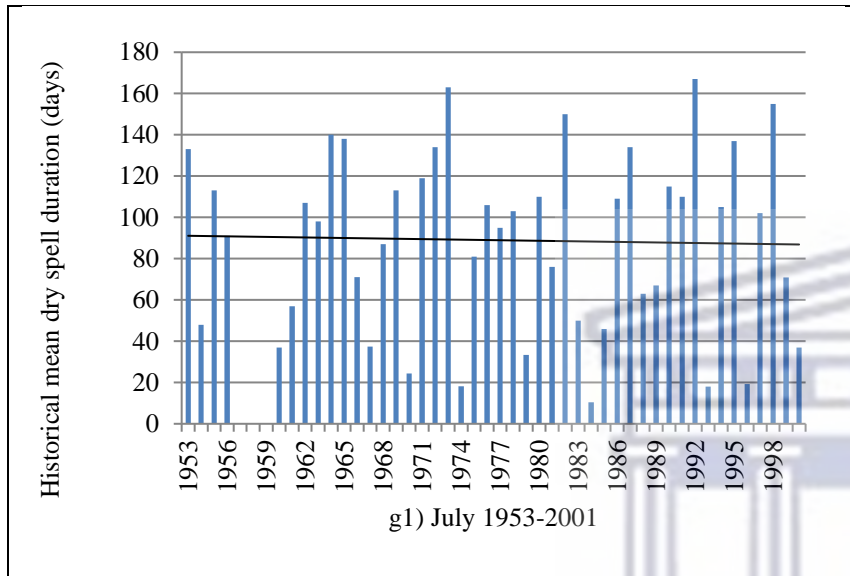


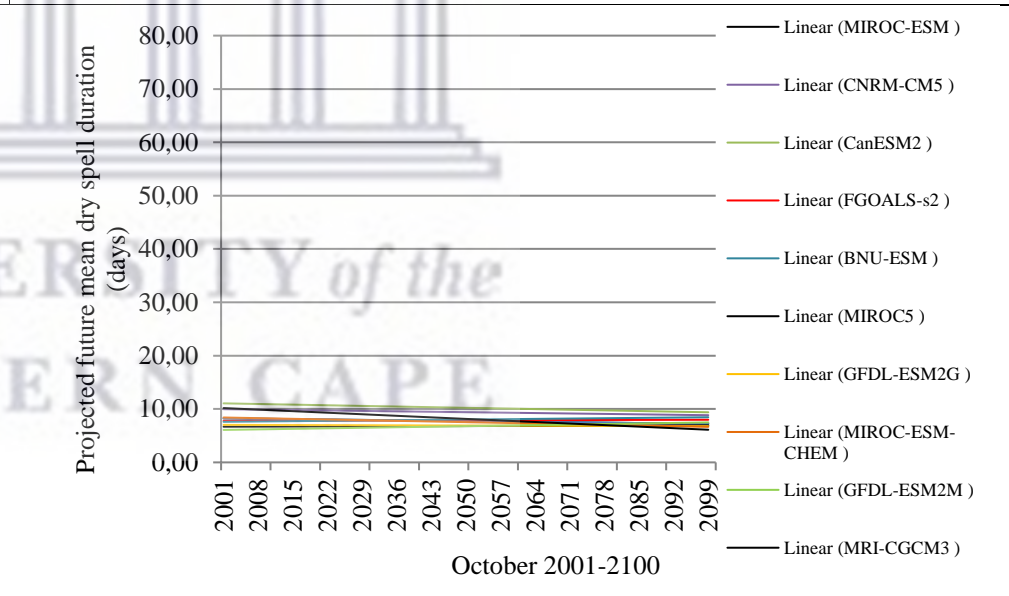
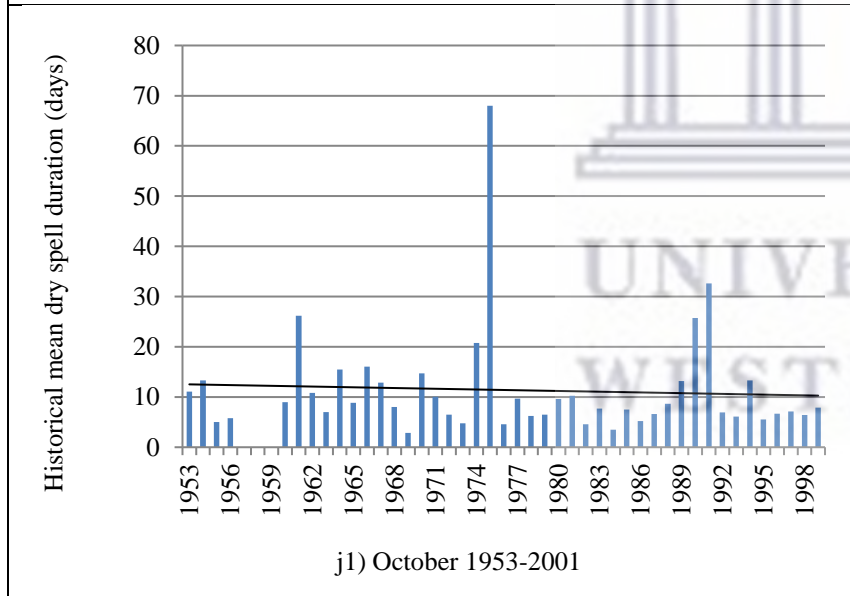
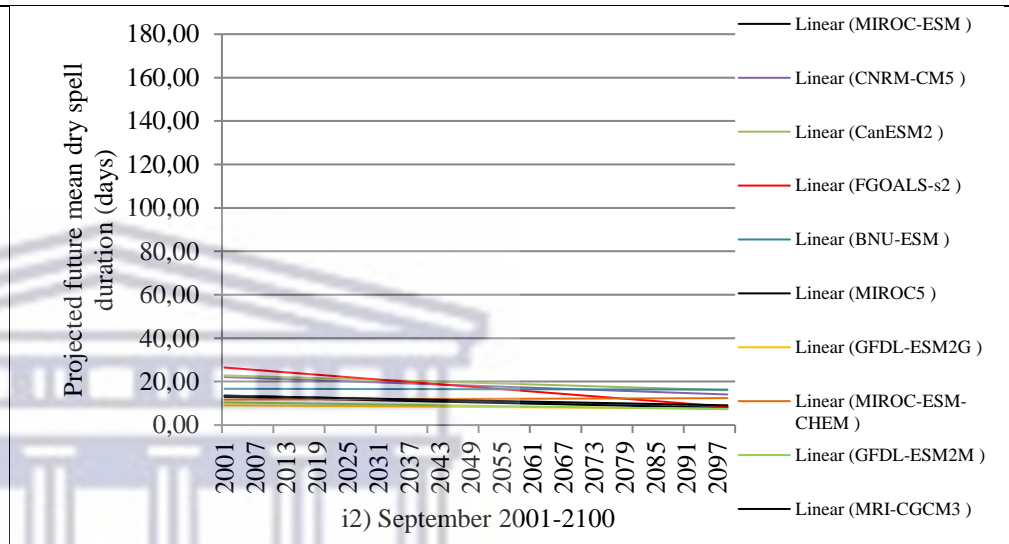
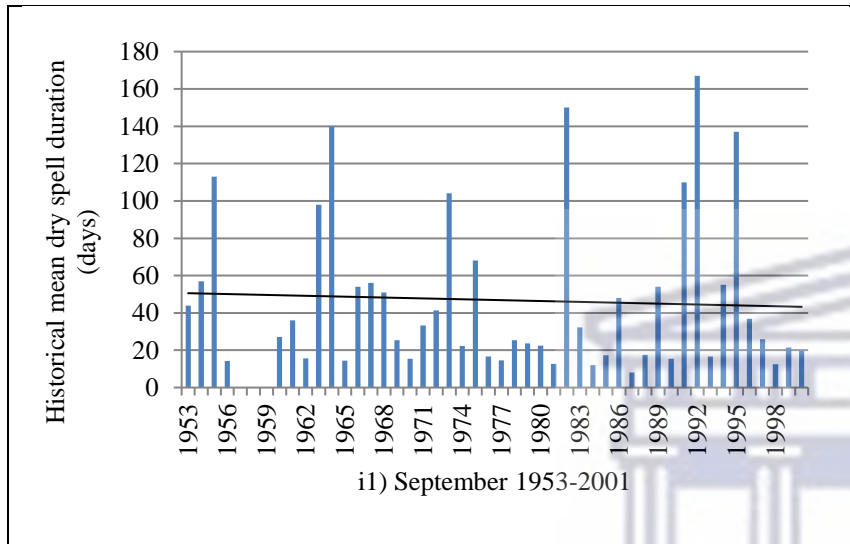
Figure C.8: Mean dry spell duration per month 1960 – 2099 based on projected future changes across 10 different statistically downscaled CMIP5 GCMs (RCP8.5).











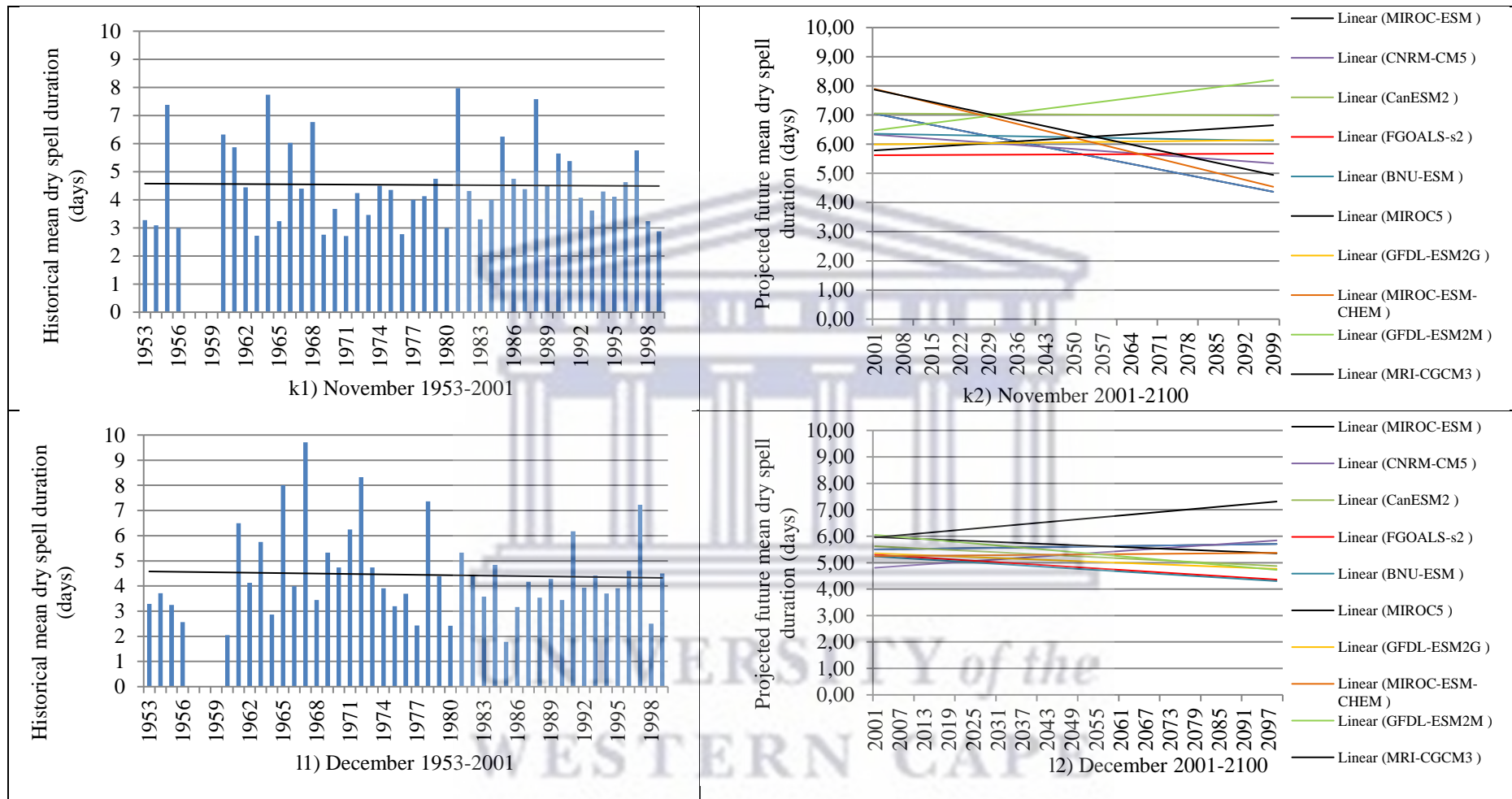


Figure C.9: Observed dry spell duration per month (a1 – l1) 1953 – 2001 compared to predicted dry spell duration (a2-l2) 2001 -2100 based on projected future changes across 10 different statistically downscaled CMIP5 GCMs (RCP8.5).

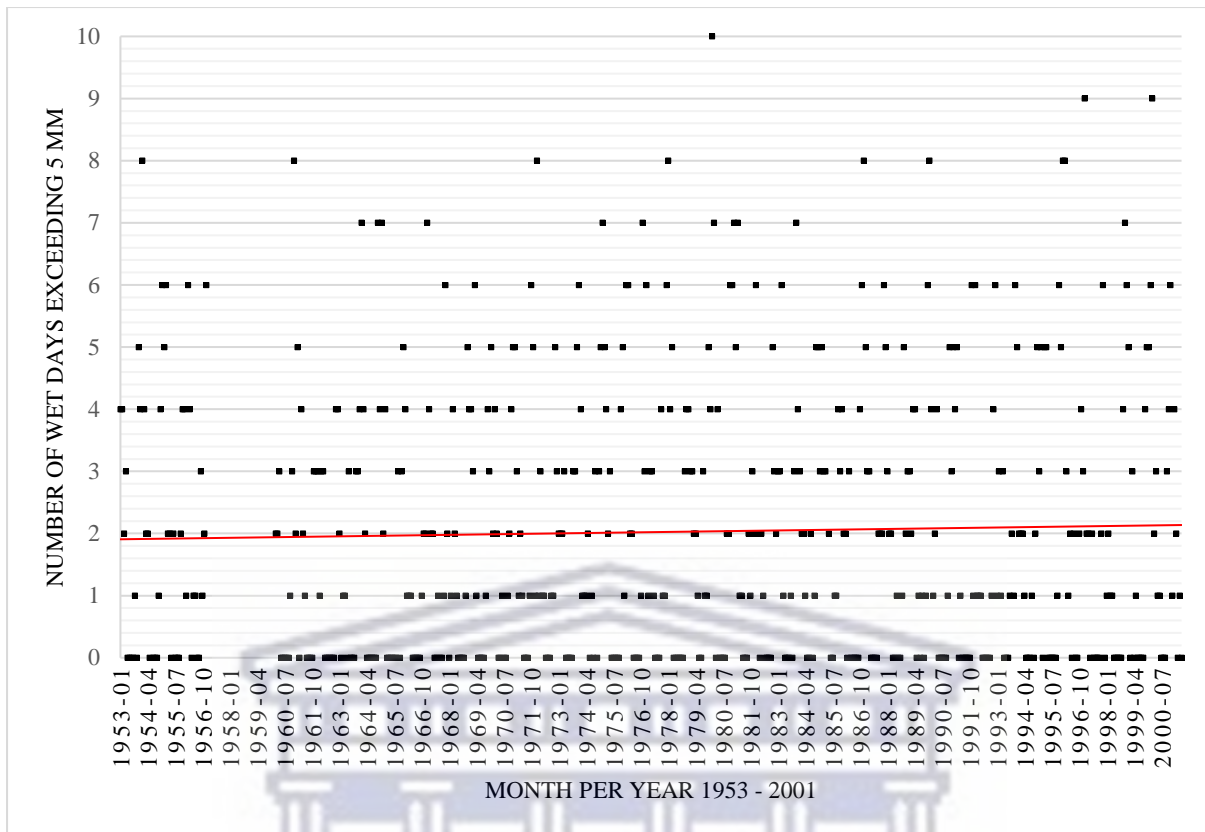


Figure C.10: Observed occurrence of rainfall events exceeding 5 mm 1953 – 2001.

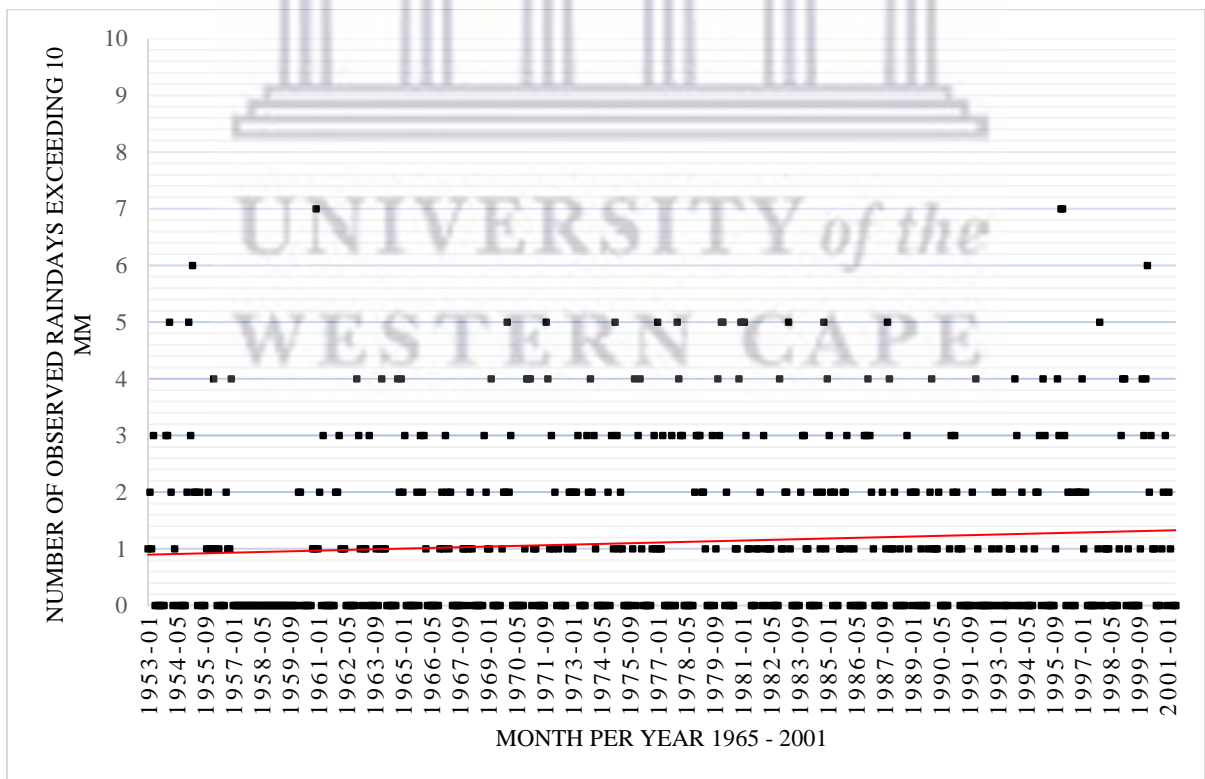


Figure C.11: Observed occurrence of rainfall events exceeding 10 mm 1953 – 2001.

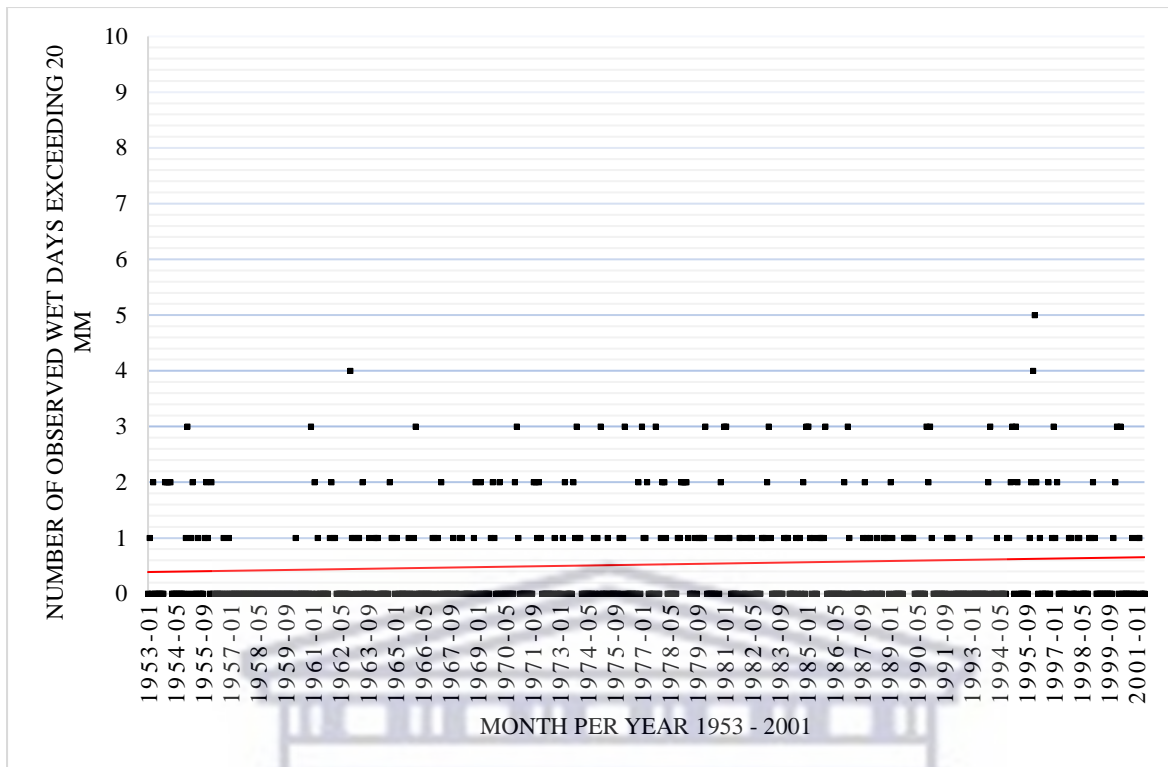


Figure C.12: Observed occurrence of rainfall events exceeding 20 mm 1953 – 2001.